Preface

The Greenland ice sheet is currently losing mass at a significant and accelerating rate. Increased snow and ice melt due to Arctic warming is an important driver; however, other processes such as glacier acceleration and surface albedo reduction also affect the mass loss. In particular, tidewater glaciers are rapidly retreating under the influence of changing ocean conditions. In turn, the increase in freshwater and sediment discharge from the glaciers has an impact on the ocean environment. Such interactions between the ice, the atmosphere and the ocean play important roles in global and Arctic environmental change and affect the living conditions of the Greenlandic population.

This volume of *Low Temperature Science* is inspired by a series of five workshops on the mass balance of the Greenland ice sheet and its relation to global climate change. The workshops were held between 2012 and 2016 at Hokkaido University's Institute of Low Temperature Science (ILTS), supported by the Grant for Joint Research Program of ILTS, the SIGMA (Snow Impurity and Glacial Microbe effects on abrupt warming in the Arctic) project funded by the Japan Society for the Promotion of Science (JSPS), and the Green Network of Excellence (GRENE) Arctic Climate Research Project funded by the Japanese Ministry of Education, Culture, Sports, Science and Technology (MEXT). The volume intends to give an overview of recent research activities on the topics described above, and to provide perspectives for directions of future work.

The research presented here has a strong link to the ongoing Arctic Challenge for Sustainability (ArCS) project, a national flagship project funded by MEXT. In fact, some of the studies have been supported directly by the ArCS project. The scope of ArCS comprises not only the physical science basis of the changing Arctic environment on large and small scales, but also the human dimension. The variety of topics included in this volume is intended to reflect this wide scope.

We are very much indebted to all authors who dedicated their time in order to contribute to this volume. Thanks a lot for your efforts!

Sapporo, Japan
March 2017

Editorial committee of
Low Temperature Science Vol. 75
Ralf Greve
Shin Sugiyama
Yoshinori Iizuka
Ayako Kakugo

はじめに

近年グリーンランド氷床は著しい速度で氷を失っており，質量減少が加速しています。北極域の温暖化による雪氷融解の増加が主な要因のひとつですが，氷河の流動加速や雪氷表面の暗色化など，その他のプロセスも氷の損失に重要な役割を果たしています。特に海洋に流入するカービング氷河は，海洋環境の変化を受けて急速に後退しています。またその結果として氷河から流出する淡水や土砂が増加して，海洋環境に大きな影響を与えています。このような氷床・大気・海洋の相互作用が，北極および地球規模の環境変化に重要な役割を果たし，グリーンランドに暮らす人々の生活環境に影響を与えているのです。

本巻は，低温科学研究所において5回にわたって開催された研究集会「グリーンランド氷床の質量変化と全球気候変動への影響」を受けて出版されるものです。この集会は2012年から2016年にかけて，科学研究費プロジェクトSIGMA（Snow Impurity and Glacial Microbe effects on abrupt warming in the Arctic），文部科学省の助成を受けたGRENE（Green Network of Excellence）北極気候変動研究事業等と連携して，北海道大学低温科学研究所共同利用研究集会（代表：防災科学研究所・山口悟）として開催されました。本巻の出版は，上述の研究分野における近年の研究活動を俯瞰し，研究分野の将来に方向性を与えることを目的としています。

本巻に寄せられた研究成果は，文部科学省が主導するオールジャパンの北極研究プロジェクトArctic Challenge for Sustainability（ArCS）と密接に関連しています。ArCSプロジェクトは，北極域で顕在化する様々なスケールの環境変化に対して，自然科学のみならず，人文社会科学の立場からもその理解を推し進めるものです。本巻の各論文が報告する多様な研究アプローチが，ArCSプロジェクトが目指す研究の視野を示しています。

本巻にご寄稿頂いた著者のみなさま全員に感謝申し上げます。ご尽力をありがとうございました！

2017年3月　札幌にて

「低温科学」75巻編集委員会
グレーベ　ラルフ
杉山　　慎
飯塚　芳徳
角五　綾子

Contents

Preface

低温科学 75 （2017） 1-13
doi: 10.14943/lowtemsci. 75. 1

Recent ice mass loss in northwestern Greenland: Results of the GRENE Greenland project and overview of the ArCS project

Shin Sugiyama[1]*, Shun Tsutaki[1, 2, 3], Daiki Sakakibara[1, 4], Jun Saito[1, 5], Yoshihiko Ohashi[1, 5], Naoki Katayama[1, 5], Evgeny Podolskiy[4], Sumito Matoba[1], Martin Funk[6], Riccardo Genco[7]

Received 24 November 2016, accepted 11 January 2017

The Greenland ice sheet and peripheral ice caps are rapidly losing mass. This mass change has been captured by satellite remote sensing, but more detailed investigations are necessary to understand the spatiotemporal variations and mechanism of the ice loss. It has increased particularly in northwestern Greenland, but in-situ data for northern Greenland are generally sparse. To better understand the ice mass loss in northwestern Greenland, we studied the ice sheet, ice caps and calving glaciers in the Qaanaaq region, as a part of the Green Network of Excellence (GRENE) Arctic Climate Change Research Project. Field and satellite observations were performed to measure the mass loss of the ice caps and calving glaciers in the region. Detailed processes were investigated based on field measurements to understand mechanisms driving the ice loss. The field activities include mass balance monitoring on Qaanaaq Ice Cap since 2012, integrated field observations near the front of Bowdoin Glacier since 2013 and ocean measurements near the calving glaciers. In this contribution, we summarize the results of the GRENE Greenland project, and introduce an overview of the next project to be carried out under the framework of the Arctic Challenge for Sustainability Project (ArCS).

Keywords: Greenland, glacier, ice sheet, ice cap, ice-ocean interaction

1. Introduction

The surface area of Greenland is ~80% covered by ice with a mean ice thickness of 1.7 km. Change in this ice mass is of great importance to the global environment because melting of the entire Greenland ice sheet would cause mean sea level to rise by 7.36 m (Bamber et al., 2013). Recent studies based on satellite remote sensing and regional climate models have shown that ice in Greenland has decreased rapidly over the last few decades (e.g. van den Broeke et al., 2009; Velicogna, 2009; Rignot et al., 2011). The mass change of the Greenland ice sheet, the second largest land ice on Earth, is reported as -229 ± 60 Gt a^{-1}, which is equivalent to the

---

*Corresponding author
e-mail：sugishin@lowtem.hokudai.ac.jp
1）Institute of Low Temperature Science, Hokkaido University, Sapporo, Japan
2）Arctic Environment Research Center, National Institute of Polar Research, Tachikawa, Japan
3）Earth Observation Research Center, Japan Aerospace Exploration Agency, Tsukuba, Japan
4）Arctic Research Center, Hokkaido University, Sapporo, Japan
5）Graduate School of Environmental Science, Hokkaido University, Sapporo, Japan
6）Laboratory of Hydraulics, Hydrology and Glaciology, ETH Zurich, Zurich, Switzerland
7）Department of Earth Science, University of Florence, Florence, Italy

sea level rise of 0.63 mm a^{-1} (IPCC, 2013). Changes are occurring also at peripheral ice caps and glaciers physically separated from the ice sheet, which account for ~7% of the ice-covered area in Greenland (Rastner et al., 2012). They have lost ice at a rate of 41 ± 17 Gt a^{-1} from 2003 to 2008, contributing to sea level rise of 0.12 mm a^{-1} (Bolch et al., 2013). A number of studies have shown acceleration of the ice loss in Greenland since the 1990s, and thus accurate quantification is crucial to predict future sea level change.

These changes are non-uniformly distributed over Greenland. Rapid mass loss has been observed particularly in the coastal regions because snow and ice melt is increasing in lower-elevation areas and calving glaciers are discharging increasing amount of ice into the ocean. These are the two main drivers of the ongoing mass loss of the ice sheet, and ice caps are thinning primarily because of increasingly negative surface mass balance driven by the increasing snow and ice melt at lower elevations (Mernild et al., 2011; Rinne et al., 2011). Snow and ice are melting over a broader area and for a longer period under the influence of enhanced atmospheric warming in the Arctic. As a result of melting, the grain size of snow increases, ice surface areas reach higher elevations and the spatial coverage of light-absorbing glacial microbes increases (e.g. Wientjes and Oerlemans, 2010). These processes contribute to albedo reduction and further enhance melting. Near the front of calving glaciers, acceleration, thinning and retreat have been reported since the beginning of the 21st century. These changes were first discovered at large glaciers in southeastern and western regions (e.g. Joughin et al., 2004; Howat et al., 2005), but were later observed at other glaciers around the ice sheet (e.g. Rignot et al., 2006; Moon et al., 2012). Mechanisms of the glacier changes are not fully understood, but glacier and fjord bed geometry is suggested as a key driver of acceleration and rapid retreat (e.g. Nick et al., 2009). Moreover, subaqueous melting under the influence of changing ocean conditions is suspected as an additional key process, thus intensive research is underway in fjords near the front of calving glaciers (e.g. Rignot et al., 2010; Straneo et al., 2010; Straneo and Heimbach, 2013).

Detailed studies have revealed that ice mass change in Greenland is temporally and spatially heterogeneous (e.g. Schrama and Wouters, 2011; Sasgen et al., 2012; Enderlin et al., 2014). Rapid loss was first reported in the southeastern area, and then spread to other regions along the coast. Mass loss has increased particularly in northwestern Greenland since 2005 (Khan et al., 2010; Kjær et al., 2012), but available data for the northern regions are generally sparse. Therefore, there is an urgent need to increase the reliable data for northwestern Greenland to quantify the mass loss and better understand the mechanisms driving recent changes in the region.

From 2011 to 2016, Arctic researchers in Japan collaborated under the integrated, multidisciplinary Green Network of Excellence (GRENE) Arctic Climate Change Research Project funded by the Japanese Ministry of Education, Culture, Sports, Science and Technology (MEXT). As part of the GRENE research project "The role of Arctic cryosphere in global change", we initiated a glaciological study in the region near Qaanaaq, a village in northwestern Greenland. The aim of the study was to quantify the ice mass loss in the region and understand its driving mechanisms. Here, we provide an overview of the GRENE Greenland project by summarizing the key findings of the study. We also provide an outline of our new project "Interaction of glacier/ice sheet and the ocean in northwestern Greenland", which was launched in 2015 under the framework of the next Japanese national Arctic project "Arctic Challenge for Sustainability" (ArCS).

2. Study site

Qaanaaq is a village populated by ~600 people, located in northwestern Greenland at 77°28'N, 69°14'W (Fig. 1). We selected this region as our study site because of the following factors: i) ice mass loss is increasing in northwestern Greenland; ii) only a few glaciological studies have been conducted in the region in the past; iii) Qaanaaq Airport is accessible by regular flights, and iv) Japanese researchers and explorers have been active in this region. Japanese activities in northwestern Greenland included a glaciological research at Site 2 by Ukichiro Nakaya from 1957 to 1960 (Nakaya, 1959) and pioneering dogsled expeditions by

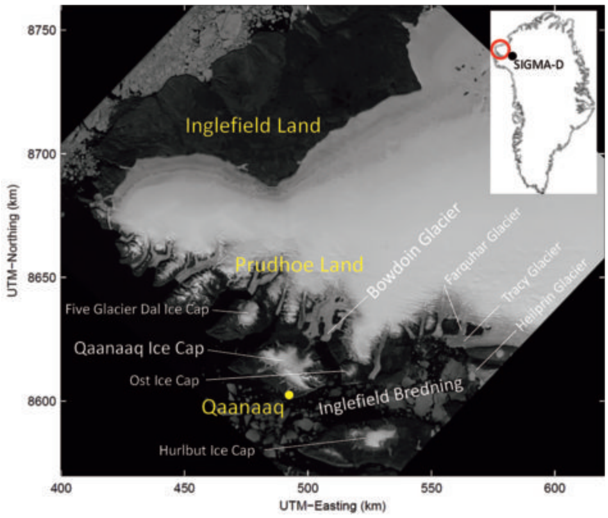

Figure 1 : Satellite image (Landsat 7 on 24 July 1999) of the Qaanaaq region in northwestern Greenland. The inset shows the locations of the study site in Greenland (circle) and the SIGMA-D ice core drilling site (dot).

Naomi Uemura in the 1970s (Uemura, 1974). More recently, a JSPS-funded research project on "Snow impurity and glacial microbe effects on abrupt warming in the Arctic" (SIGMA) has been carried out since 2011 (Aoki et al., 2014). The GRENE and SIGMA projects have closely collaborated over the 5-year period.

Qaanaaq is situated on the southern coast of a peninsula, facing the ~100 km long and ~20 km wide Inglefield Bredning fjord (Fig. 1). The northern bank of the fjord is named Prudhoe Land, where 19 calving glaciers flow into the ocean. Largest among those are Heilprin and Tracy Glaciers, which discharge icebergs into the eastern end of Inglefield Bredning at a rate greater than 1 km a^{-1}. Qaanaaq Ice Cap is located to the north of the village, covers an area of 260 km^2, and feeds numerous land-terminating outlet glaciers. Several other ice caps are situated in the region, including Hurlbut Ice Cap on an island to the southeast of Qaanaaq, and Ost and Five Glacier Dal Ice Caps on the main land adjacent to the ice sheet (Fig. 1).

Only a few scientific research activities have reported on the Qaanaaq region, particularly on its ice sheet and glaciers. Recently, satellite remote sensing on calving glaciers (Porter et al., 2014), airborne ice radar survey over the ice sheet (Palmer et al., 2013) and ocean measurements in Inglefield Bredning (Dybkjaer et al., 2011) have been reported. Climatic data are available from the weather station at Qaanaaq Airport, which has been in operation since 1996.

3. Ice caps

3.1 Ice cap thinning in the Qaanaaq region

The ice caps in the Qaanaaq region are situated at an elevation range of 0–1200 m a.s.l, where snow and ice melt is greatly influenced by recent warming. The rate of ice cap mass loss in northwestern Greenland is reported as 0.6 ± 0.1 m a^{-1} for the period 2003–2008 (Bolch et al., 2013). We utilized a satellite image photogrammetry technique to investigate the mass change during a more recent period, and analyzed its spatial distribution, which was not resolved in the previous study. The focus of our study was six ice caps near Qaanaaq, i.e., Qaanaaq, Hurlbut, Ost, Five Glacier Dal, Kiatak and Steensby Land Ice Caps (Saito, 2015; Saito et al., 2016). We used stereo pair images from the Advanced Land Observing Satellite, Panchromatic Remote-sensing Instrument for Stereo Mapping (ALOS PRISM) to generate digital elevation models (DEMs) of the region for 2006, 2007, 2009 and 2010. Digital photogrammetry software (Leica LPS) and digital map plotting instruments (Planar SD2020 monitor and 3D Topo Mouse) were employed for this purpose. Surface elevation change over the ice caps was computed using the differences in the DEMs over time. DEMs generated by this method have an error of several meters in the vertical direction, but uncertainty in the elevation change decreases when they are averaged over the ice caps.

The result of the analysis revealed pervasive thinning of the ice caps in the Qaanaaq region (Fig. 2) (Saito et al., 2016). Mean elevation change over the six ice caps was -1.1 ± 0.1 m a^{-1} for the period between 2006 and 2010. This thinning rate is approximately twice that reported for 2003–2008 (Bolch et al., 2013), which confirms recent acceleration of the ice cap mass loss in the study area. Thinning is pronounced in the ablation areas, suggesting melt increase as a primary driver of the mass loss. Air temperature record at Qaanaaq Airport indicates an increase in summer temperature at a rate of 0.12 °C a^{-1} over the 1997–2013 period. In addition to the atmospheric warming, albedo reduction also plays a role in the increasing melt rates. Bare ice is

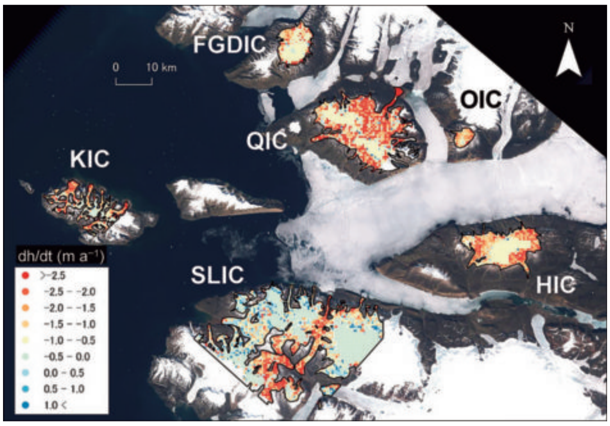

Figure 2 : Rate of surface elevation change for the ice caps (IC) Hurlbut (HIC), Ost (OIC), Kiatak (KIC) (in 2007–2010), Qaanaaq (QIC), Steensby Land (SLIC) (2007–2009) and Five Glacier Dal (FGDIC) (2006–2010). Modified from Saito et al. (2016).

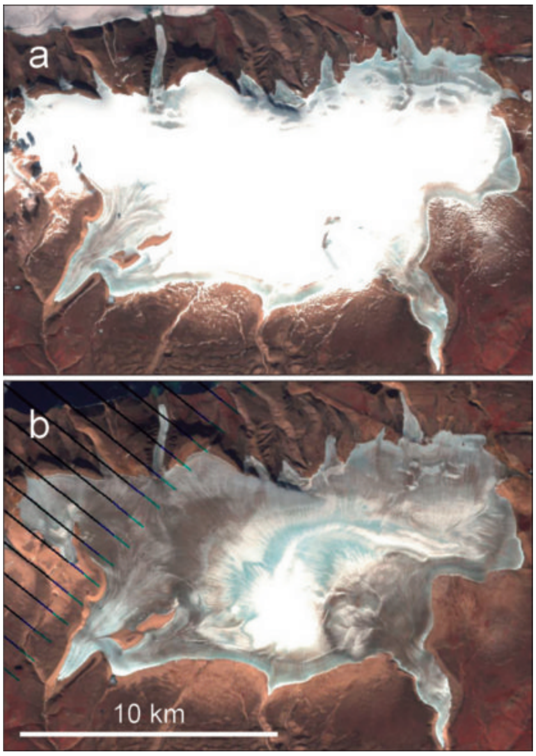

Figure 3 : Satellite images (Landsat 7) of Hurlbut Ice Cap acquired on (a) 2 July 2002 and (b) 6 July 2012.

more exposed as the altitude of the equilibrium line increases, and the spatial coverage of glacial microbes on the ice surface increases (Takeuchi et al., 2014). These changes effectively reduce the surface albedo of the ice caps as represented by satellite images of Hurlbut Ice Cap taken in 2002 and 2012 (Fig. 3). The magnitude of the thinning was substantially different on each ice cap. For example, Qaanaaq Ice Cap thinned at a rate of 1.8 ± 0.1 m a^{-1} from 2007 to 2010, whereas Steensby Land Ice Cap showed a thinning rate of 0.8 ± 0.1 m a^{-1} for the same period. Based on further satellite image analyses, we suggest relatively high albedo as a possible reason for the lower thinning rate observed on Steensby Land Ice Cap. In addition to albedo, regional variations in snow accumulation and glacier dynamics are other possible controls on the surface elevation change.

3.2 Qaanaaq Ice Cap

To monitor long-term variations in the surface mass balance and ice dynamics of Qaanaaq Ice Cap, we installed survey stakes on the ice cap and resurveyed the stakes every summer since 2012 (Maruyama, 2015; Matsuno, 2016). The stakes are located at elevations from 243 to 968 m a.s.l., spanning an area from the terminus of an outlet glacier (Qaanaaq Glacier) to a point inland, slightly higher than the equilibrium line altitude (Fig. 4a). Annual mass balance from 2012 to 2016 showed a large year-to-year fluctuation. During the study period, mass balance was most negative in the 2014/2015 season and most positive in 2012/2013. Specific mass balance at the lower most (243 m a.s.l.) stake was −2.10 and −1.19 m water equivalent (w.e.) a^{-1} in these 2 years, respectively. This result indicates the importance of long-term observations to capturing general trends of climatic and glacier changes. Our data from Qaanaaq Ice Cap form a part of only a few mass balance observations currently operated at marginal parts of Greenland (Machguth et al., 2016). We continue these measurements to help improve the accuracy of our understanding of the impact of changing climate on peripheral glaciers and ice caps in Greenland.

Field observations on Qaanaaq Ice Cap provided valuable information for understanding the processes controlling ice mass loss (Sugiyama et al., 2014). Summer melt rates at the survey stakes showed relatively high melt rates (i.e. large degree-day factors) at 500–900 m a.s.l. (Figs. 4b and c). Brightness intensity of a satellite image showed that ice in this elevation range was darker than in the other regions (Fig. 4c). This observation demonstrated a clear influence of surface albedo on the mass balance of the ice cap. We also determined summer (July) and annual ice motion by surveying the stakes using the global positioning system (GPS) to investigate a possible impact of surface

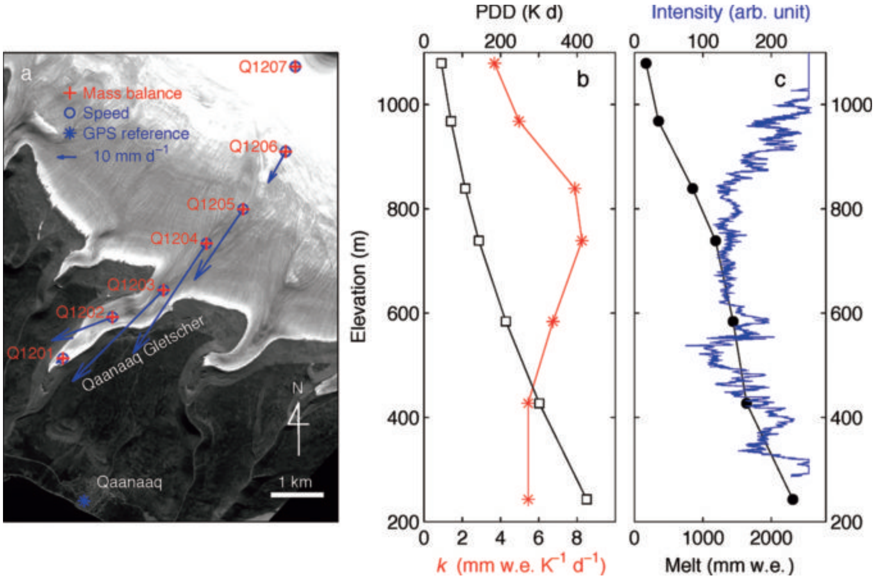

Figure 4 : (a) Satellite image (ALOS PRISM, 25 August 2009) showing the study area of Qaanaaq Ice Cap. Locations of the measurement sites for mass balance (+), ice velocity (○) and the GPS reference station (∗) are indicated. The arrows are horizontal surface flow vectors from 18–29 July 2012. (b) The positive degree-day sum (PDD) (box), degree-day factors (∗) and (c) total melt amount at Q1201–Q1207 computed for the entire summer melt season in 2012 (●). Blue line in (c) is the brightness intensity of the ALOS PRISM image shown in (a) along the survey route. Figures are modified from Sugiyama et al. (2014).

meltwater on basal sliding. Over the 4-year measurement period, ice motion accelerated only in July 2012 when Greenland was hit by an extreme melt event across nearly the entire ice sheet (Nghiem et al., 2012). The lack of summer acceleration in the subsequent years indicates the uniqueness of the meteorological conditions in the summer 2012, and it also suggests that the impact on the ice dynamics would be substantial if similar melt events will occur more frequently in the future.

4. Calving glaciers

4.1 Retreat, thinning and acceleration of calving glaciers

Another focus of our study was calving glaciers (Fig. 5). Most of the outlet glaciers in this region terminate in fjords, forming 0.6–5.0-km wide tidewater calving glaciers. According to our analysis using Landsat satellite images from 1987 to 2014, all of the 19 glaciers in the Qaanaaq region showed retreating trends after 2000 (Sakakibara, 2016). Some of the glaciers retreated more rapidly than the others, as represented

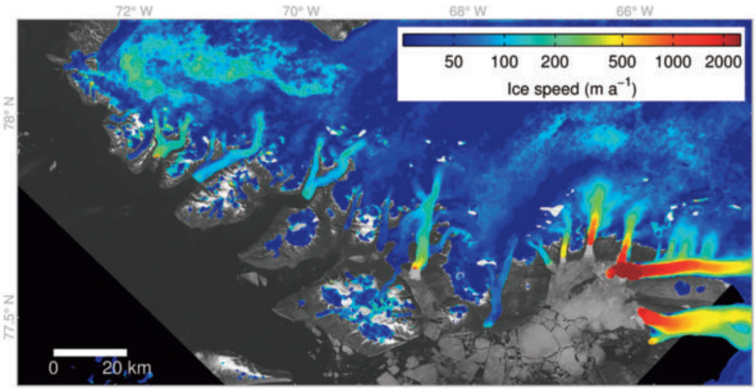

Figure 5 : Ice speed distribution over Prudhoe Land in 1987–2014 (Sakakibara, 2016). The speed was obtained by the feature tracking method applied on Landsat satellite images. Background is a Landsat 8 OLI image acquired on 9 July 2014.

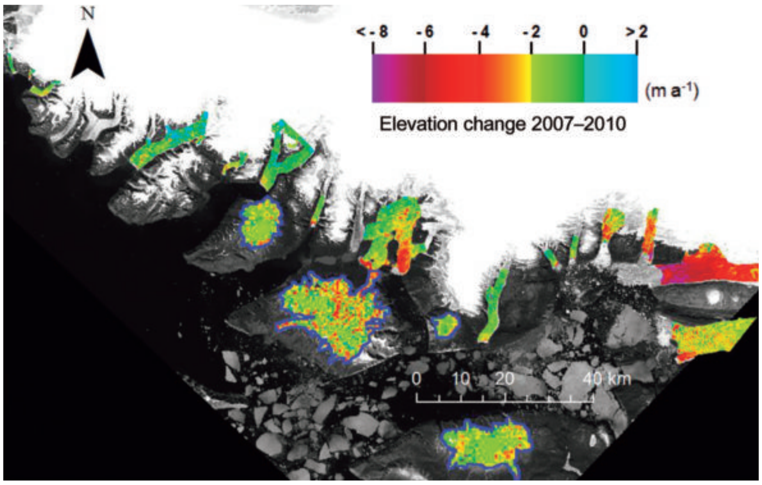

Figure 6 : Surface elevation change of calving glaciers and ice caps in the Qaanaaq region between 2007 and 2010.

by the more than 5-km retreat of Tracy Glacier during the study period. In general, glaciers terminating at the Inglefield Bredning fjord are retreating more quickly than those flowing into smaller fjords directly facing Baffin Bay.

The glacier retreat after 2000 accompanied ice thinning near the calving front. We employed the same DEM generation technique as for the ice caps to measure the surface elevation change of 14 glaciers over the period 2007–2010 (Katayama, 2016). Thinning rates are highly variable on each glacier, and higher thinning rates were observed at more rapidly retreating glaciers (Fig. 6). For example, Tracy and Farquhar Glaciers thinned at a rate of ～8 m a^{-1} from 2007 to 2010, while they retreated by more than 100 m a^{-1} from 2000 to 2014. Several other glaciers were thinning at rates greater than 5 m a^{-1}. These rates are substantially greater than the surface mass balance at the elevation of the glacier termini, which is typically −2 m w.e. a^{-1} in this region (Maruyama, 2015; Tsutaki et al., 2016). The magnitude of the thinning was greater near the glacier fronts. These results imply that the rapid thinning was primarily due to the increase in compressive vertical straining as a result of enhanced extending flow regime, so-called dynamic thinning.

Rapidly retreating and thinning glaciers are accelerating as well. Tracy, Heilprin, and Bowdoin Glaciers accelerated by ＞10 m a^{-2} from 2000 to 2014, and these glaciers retreated rapidly (80–340 m a^{-1}) over the same period (Sakakibara, 2016). The acceleration extended to the region ＞10 km from the calving front, resulting in a large impact on the ice discharge and dynamic thinning. As it has been observed in other regions in Greenland, glacier retreat, thinning and acceleration are occurring concurrently in our study area. To understand the mechanism driving these changes, we performed intensive studies on Bowdoin Glacier.

4.2 Bowdoin Glacier

Bowdoin Glacier is one of the tidewater glaciers in the study area, located ～30 km to the north of Qaanaaq. According to the comparison of an aerial photograph in 1949 and recent satellite images, the glacier front position experienced no significant changes for more than 50 years until it showed a ～200 m retreat in 2000 (Sugiyama et al., 2015). The ice front remained at the same position until 2008, and then it retreated more than 1 km from 2008 to 2013 (Fig. 7). Ice speed showed a twofold increase from 1999 to 2002, and it maintained a fast flowing condition during the following period (Fig. 7b). Meanwhile, the glacier has been thinning at a rate (−4.1 m a^{-1} from 2007 to 2010) substantially greater than that of the nearby land-terminating Tugto Glacier (Tsutaki et al., 2016). Surface ablation in the same region of Bowdoin Glacier was 1.8–2.0 m a^{-1} from 2014 to 2015, which accounts for only ～50% of the observed thinning rate. According to the analysis of the ice flow regime, a large portion of the thinning was due to the dynamic thinning caused by the acceleration after 2000 (Tsutaki et al., 2016).

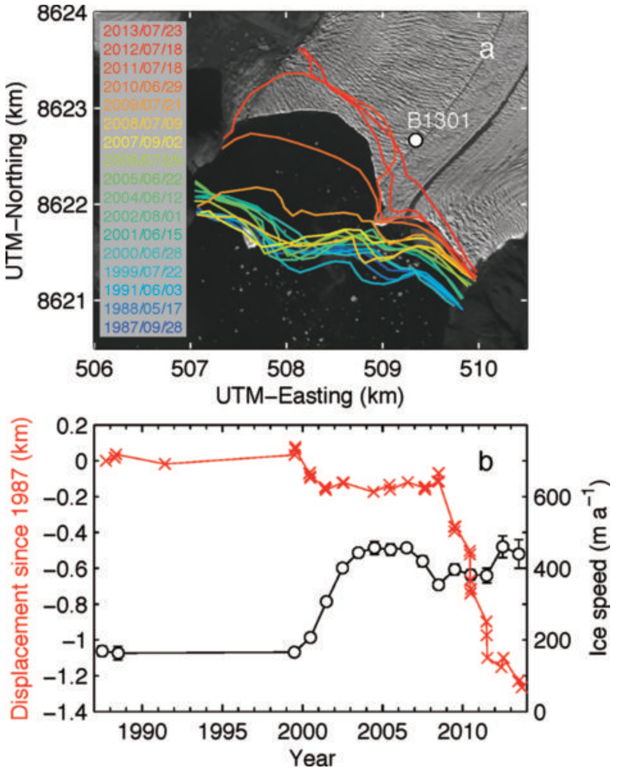

Figure 7 : (a) Frontal margins of Bowdoin Glacier observed from 28 September 1987 to 23 July 2013. Background is an ALOS PRISM image acquired on 25 July 2010. (b) The crosses are mean displacement of the glacier front since 28 September 1987. Negative change in the ordinate represents glacier retreat. The open circles are satellite-derived annual mean ice speed at site B1301 as indicated by the filled circle in (a). Reproduced from Sugiyama et al. (2015).

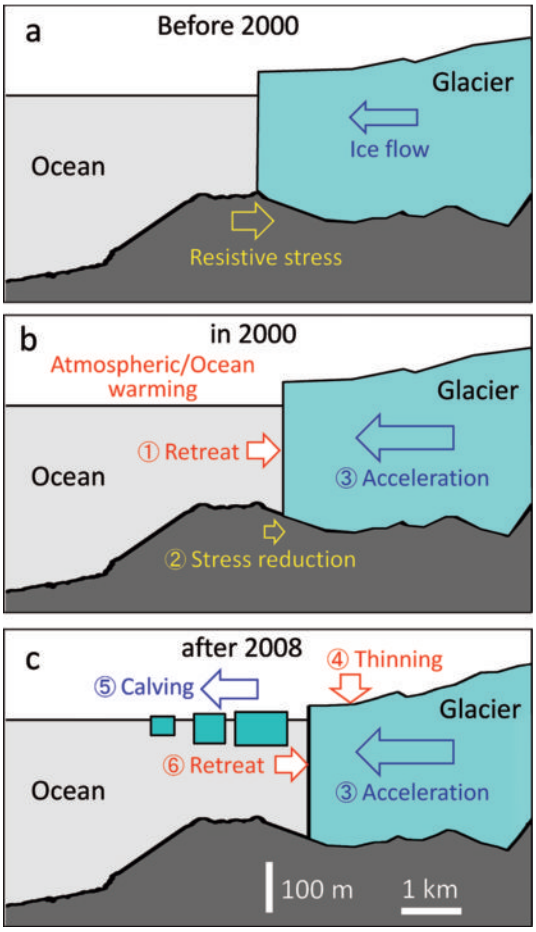

Figure 8 : Schematic diagrams showing the mechanism of the rapid retreat of Bowdoin Glacier since 2008. The diagrams show conditions (a) when the glacier was stable before 2000, (b) when the glacier retreated slightly in 2000 and (c) after the glacier began rapid retreat in 2008. The glacier and fjord geometry in (c) is based on field data.

To obtain detailed information on glacier change, we performed field campaigns on Bowdoin Glacier in the summers 2013–2016. Ice thickness and fjord depth were measured near the glacier front, using a ground-based ice radar system and a sonar mounted on a small boat. The results revealed that the glacier front was very close to flotation (~90% of ice thickness was below sea level) and a ~50 m high ocean bed bump was situated at ~1 km from the ice front (Fig. 8). Ice speed was modulated by tides, surface melt and rain, implying that the force balance was susceptible to small perturbations (Sugiyama et al., 2015). Seismic measurements near the calving front showed that tidally modulated ice flow variation controls the frequency of ice fracture near the surface, which may have important implications for calving (Podolskiy et al., 2016). Infrasonic measurements were also performed to study the timing and locations of calving events (Podolskiy et al., this volume). In 2014, we drilled holes to the glacier bed with a hot-water drilling equipment to explore subglacial and englacial environments. Borehole measurements confirmed that ice is temperate at the bed and that a subglacial hydrological system exists.

Based on the results of the field and satellite observations, we interpret the rapid retreat of Bowdoin Glacier since 2008 as illustrated in Figure 8. Before 2000, the glacier front was situated on the ocean bed bump, which stabilized the glacier front position for more than 50 years (Fig. 8a). Under the influence of atmospheric and ocean warming, the glacier front retreated slightly from the bump in 2000. The retreat distance was small, but the glacier force balance was strongly affected by the retreat of the ice front from the bump towards deeper water in upstream direction, resulting in rapid acceleration observed at the same time (Fig. 8b). After the acceleration, ice discharge increased and the glacier progressively thinned until it reached the threshold of flotation. The rapid retreat initiated in 2008 when the glacier terminus began to float and then collapsed into the ocean (Fig. 8c). The detailed field and satellite data enabled us to propose this interpretation on Bowdoin Glacier. Similar observations on other calving glaciers will provide clues to predict the future evolution of calving glaciers in Greenland.

5. Atmospheric and ocean environments

5.1 Ice core and weather station

Compared with the melt increase clearly observed in lower-elevation areas, the changes in inland snow accumulation are less understood in Greenland. Because of the relatively complex coastal landscape in the Qaanaaq region, precipitation is spatially highly variable, and its temporal variations are not well known. To study snow precipitation and atmospheric conditions in the accumulation area, a 225-m-long ice core was drilled at 2100 m a.s.l, approximately 250 km east of Qaanaaq (Fig. 1 inset) (Matoba et al., 2015; Kadota, 2016). Drilling and other field activities were carried out from 5 to 26 May 2014. In addition to the drilling activities, GPS surveys were performed for surface elevation and ice flow in the region, and an automatic weather station was installed at the drilling site and operated until October 2015.

Figure 9 shows 2-m-height air temperature and snow surface elevation recorded by an ultrasonic ranger at the weather station from May 2014 to October 2015. Annual mean air temperature for the hydrological year 2014/2015 (from 1 October 2014 to 31 September 2015) was −25.9 °C, and summer mean temperatures (June-August) in 2014 and 2015 were −8.1 and −9.0 °C, respectively. Daily mean temperature was below zero throughout the year, suggesting little influence of melt on the ice core. The snow surface rose by 0.8 m over the ~16-month measurement period, showing a highly variable snow deposition rate. For example, summer snow deposition (June-August) in 2014 was 0.36 m, whereas that in 2015 was less than several centimeters during the same period. These weather station data are crucial to analyzing the ice core, as well as to investigating climatological and snow deposition conditions in the accumulation area.

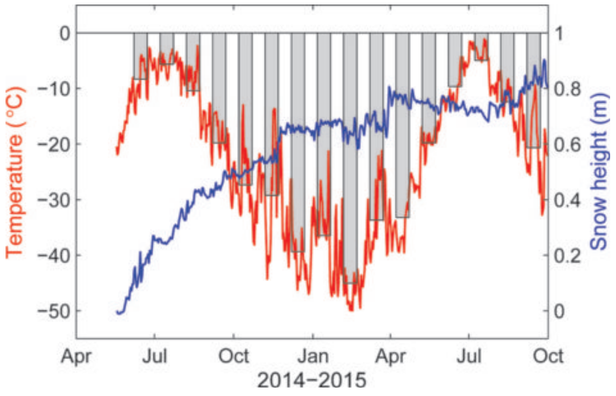

Figure 9 : Daily (red) and monthly (gray bars) mean air temperature, and snow surface height relative to the surface on 18 May 2014 (blue) measured at the SIGMA-D site.

5.2 Ocean measurements

Calving glaciers are affected by ice front melting in the ocean, and in turn glaciers impact the ocean by discharging icebergs, meltwater and sediments. Therefore, it is crucial to investigate glacier-ocean interactions to predict the future of glaciers as well as the coastal environment in Greenland. Increasing numbers of fjord measurements are carried out in other regions of Greenland (e.g. Straneo et al., 2010), but such research is scant in northwestern Greenland. To study water properties in a glacial fjord, we performed conductivity, temperature and depth profiler measurements in Bowdoin Fjord. Temperature and salinity showed typical stratifications for glacier-fed fjords. The deepest region of the fjord (>290 m) was filled with relatively warm and salty water (θ=1.16±0.03 °C, S=34.24±0.10 PSU (practical salinity unit)), indicating intrusion of Atlantic Water into the fjord (Figs 10a and b) (Ohashi, 2015). Temperature and salinity decrease moving upward between the depths of 140–290 m under the influence of freshwater supplied from subaqueous melting. The coldest water, found at a depth of 50–110 m, is attributed to Polar Water originating from the Arctic Ocean. Above the Polar Water layer, highly turbid and fresh water was observed at 20–50 m (Fig. 10c) which we attribute to subglacial meltwater discharge. The turbid water was covered by the warmest and even fresher surface water (0–20 m). These observations are consistent with previously reported structures of Greenlandic fjords in other

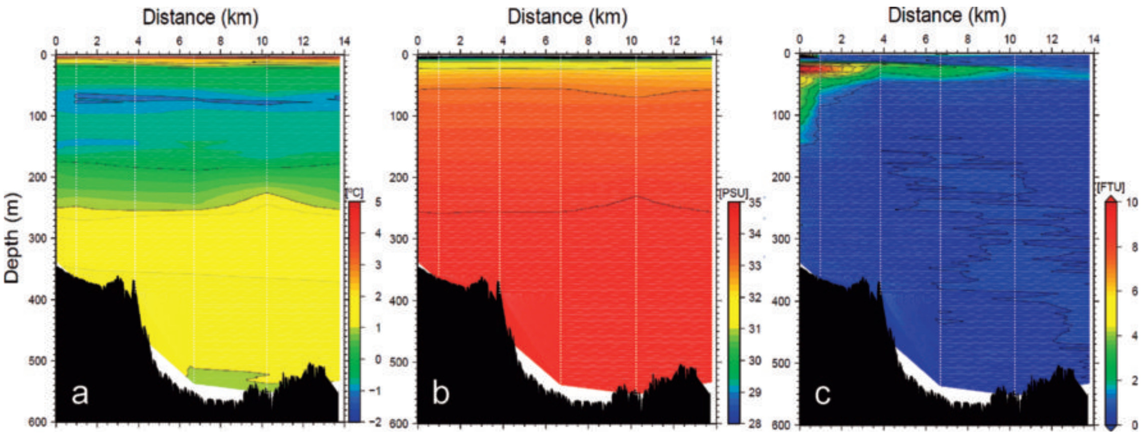

Figure 10 : (a) Potential temperature, (b) salinity in PSU (practical salinity unit) and (c) turbidity in FTU (formazin turbidity unit) measured in Bowdoin Fjord on 4 August 2014.

regions (e.g. Straneo et al., 2012; Chauché et al., 2014). Further measurements are needed in Bowdoin Fjord to understand the processes controlling subaqueous melting of the glacier and to monitor temporal changes in the water properties.

As a possible impact of glacier melt increase on the ocean environment, we studied turbid water discharge from glaciers into the ocean by analyzing satellite data from Moderate Resolution Imaging Spectroradiometer (MODIS) (Ohashi et al., 2016). The remote-sensing reflectance at the wavelength of 555 nm is commonly used to detect turbid water distribution, which we applied to the ocean surface in northwestern Greenland (76–78°N, 65–75°W). Highly turbid water was observed, particularly near the fronts of calving glaciers and the mouths of proglacial streams, indicating that the turbid water originated from sediment-laden glacier meltwater (Fig. 11). The turbid water spreads off the coast during the summer melt season and reaches its maximum extent in mid-July. The area covered by the turbid water showed large annual variations, and the summer maximum extent from 2002 to 2014 is positively correlated with summer mean temperature at Pituffik/Thule Air Base. This result implies that glacier melt controls the turbid water distributions, and sediment discharge into the ocean is likely to increase in the future as the climate continues to warm. We suspect that increasing sediment discharge has an impact on the coastal environment, which further affects the marine ecosystem in the region.

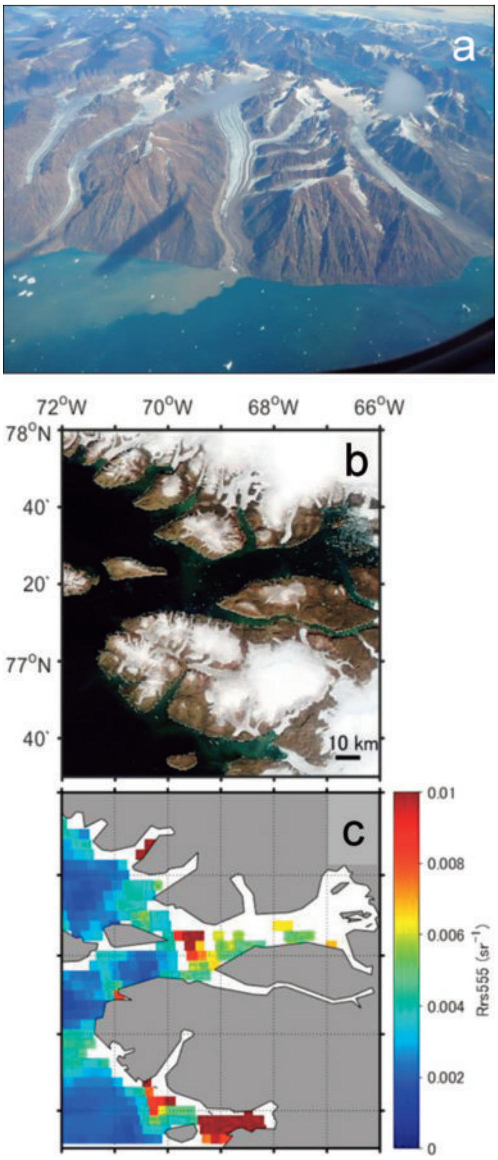

Figure 11 : (a) Turbid water discharge from a glacier in western Greenland (71.3°N, 53.0°W). The glacier length is about 10 km. (b) MODIS true color image of the study area and (c) Rrs 555 (remote sensing reflectance data at a wavelength of 555 nm). Land and ice sheet areas are indicated in gray. Modified from Ohashi et al. (2016).

6. Outlook of the ArCS project

The GRENE Greenland project focused on the changes in the ice sheet, glaciers and ice caps. Over the course of the study in the Qaanaaq region, we realized the importance of the interaction between the ice sheet/glaciers and the ocean. As mentioned above, submarine melting is suspected as a trigger for the recent retreat of the calving glaciers. Recent studies have indicated that ocean heat is efficiently transported to glacier fronts by fjord circulation, and the circulation is driven by subglacial meltwater discharge (Motyka et al., 2003; 2013). Furthermore, subglacial discharge upwells and forms a buoyant plume, which transports nutrient and plankton to the ocean surface, resulting in a unique marine ecosystem in front of calving glaciers (Lydersen et al., 2014). In fact, we observed abundant seabirds near the calving front of Bowdoin Glacier, suggesting that abundant fish and plankton are available in that region. Glacier fronts are also recognized by indigenous people as a good place to hunt sea mammals. Therefore, glacier changes have the potential to produce impacts not only on physical and chemical ocean conditions, but also on the unique fjord ecosystem. Our satellite analysis predicts an increase in sediment discharge into the ocean under warming climate. Such a change would affect the living environment of benthic fish in the fjords such as halibut, which is an important catch for fishermen in Qaanaaq.

After the GRENE project was completed, the Japanese integrated Arctic research was taken over by ArCS, a national project led by National Institute of Polar Research, Japan Agency for Marine-Earth Science and Technology, and Hokkaido University. In this new project, researchers' input is requested to aid stakeholders' and policymakers' decisions on sustainable development in the Arctic region. To achieve this goal, we continue our research in northwestern Greenland with a special emphasis on the ice sheet/glacier-ocean interaction. Furthermore, we investigate ocean environments and marine ecosystems, and the consequences of changes in these environments for the lives of people in Qaanaaq. In July 2016, we organized a workshop in Qaanaaq to present our scientific activities to the local citizens, and to exchange ideas and experiences about coastal environmental changes (Fig. 12). Participants showed great interest in our study and described the impact of the rapidly-changing local environment on their traditional way of life. With a closer collaboration with social scientists, our next project aims to provide clues to help ensure a sustainable future for human activity in Greenland.

Figure 12 : Workshop held in Qaanaaq on 25 July 2016. (a) Introduction of the research project and (b) comment from a local citizen. Photographs taken by Izumi Asaji and Bungo Nishizawa.

7. Conclusion

To quantify recent ice mass loss in northwestern Greenland, research was carried out in 2011–2016 in the Qaanaaq region under the framework of the GRENE project. Satellite image photogrammetry revealed thinning of ice caps in the region at a rate of -1.1 ± 0.1 m a^{-1} from 2006 to 2010, which is nearly twice the rate reported for 2003–2008. Atmospheric warming is the primary driver of the acceleration of mass loss, but other processes including albedo reduction also play roles. Mass balance and ice speed measured on Qaanaaq Ice Cap have added to our understanding of the physical processes causing ice cap mass loss, and measurements will continue to monitor these ongoing changes into the future.

Calving glaciers are retreating, thinning and accelerating. Some glaciers show rapid mass loss near the ice front, which indicates the importance of ice-ocean interaction for the glacier recession. Field campaigns and satellite data analyses on Bowdoin Glacier provided a comprehensive data set, which contributes to a better understanding of the mechanisms involved in the dynamics of calving glaciers in Greenland. Based on the observational data, we proposed a mechanism of the rapid retreat of Bowdoin Glacier that began in 2008. We also performed ocean measurements in Bowdoin Fjord and satellite analysis on turbid glacial meltwater discharge into the ocean. Our results demonstrated impacts of glacier discharge on the ocean environment. Further investigation is necessary on the interaction between ice sheet/glaciers and the ocean to understand ongoing changes in the coastal environment.

To investigate the ice sheet/glacier-ocean interaction and its consequences to the ocean environment and marine ecosystems, we initiated our next project under the framework of ArCS. In this project, we continue our research on the ice sheet and glaciers, and expand it further to the field of physical/chemical oceanography and marine biology. We collaborate with social scientists to determine the influence of environmental changes on human activities in Qaanaaq. Our project aims to acquire accurate data and improve understanding of ongoing change in the coastal environment, which should contribute to a sustainable future of the region.

Acknowledgements

We thank all the members of the GRENE Greenland project, particularly those who participated in the Qaanaaq field campaigns from 2012 to 2016 for their help in the field. Hiroyuki Enomoto supported our study as a principal investigator of the GRENE Snow and Ice Project. The research activity was carried out in close collaboration with the SIGMA project led by Teruo Aoki. Special thanks are due to Saki Daorana and Toku Oshima for their logistical support in Qaanaaq. Ralf Greve provided helpful comments on the manuscript. This study was funded by the Japanese Ministry of Education, Culture, Sports, Science and Technology through the GRENE Arctic Climate Research Project and ArCS Arctic Challenge for Sustainability Project. A part of the research was carried out under JSPS KAKENHI grant number 26550001 (FY2014–2016). This paper benefited from discussion in the workshops organized under the Joint Research Program of the Institute of Low Temperature Science, Hokkaido University.

References

Aoki, T., S. Matoba, J. Uetake, N. Takeuchi, and H. Motoyama (2014) Field activities of the “Snow Impurity and Glacial microbe effects on abrupt warming in the Arctic” (SIGMA) project in Greenland in 2011–2013. *Bull. Glaciol. Res.*, **32**, 3–20.

Bamber, J. L., J. A. Griggs, R. T. W. L. Hurkmans, J. A. Dowdeswell, S. P. Gogineni, I. Howat, J. Mouginot, J. Paden, S. Palmer, E. Rignot, and D. Steinhage (2013) A new bed elevation dataset for Greenland. *Cryosphere*, **7**, 499–510.

Bolch, T., L. Sandberg Sørensen, S. B. Simonsen, N. Mölg, H. Machguth, P. Rastner, and F. Paul (2013) Mass loss of Greenland’s glaciers and ice caps 2003–2008 revealed from ICESat data. *Geophys. Res. Lett.*, **40**, 875–881.

Chauché, N., A. Hubbard, J.-C. Gascard, J. E. Box, R. Bates, M. Koppes, A. Sole, P. Christoffersen, and H. Patton (2014) Ice-ocean interaction and calving front morphology at two west Greenland tidewater outlet glaciers. *Cryosphere*, **8**, 1457–1468.

Dybkjaer, G., J. Hoyer, R. Tonboe, S. Olsen, S. Rodwell, W. Wimmer, and S. Sobjaerg (2011) *QASITEEX-2011: The Qaanaaq Sea Ice Thermal Emission EXperiment Field and data report.* Danish Meteorological Institute, Copenhagen, Denmark.

Enderlin, E. M., I. M. Howat, S. Jeong, M.-J. Noh, J. H. van Angelen, and M. R. van den Broeke (2014) An improved mass budget for the Greenland ice sheet. *Geophys. Res. Lett.*, **41**, 866–872.

Howat, I. M., I. Joughin, S. Tulaczyk, and S. Gogineni (2005) Rapid retreat and acceleration of Helheim Glacier, east Greenland. *Geophys. Res. Lett.*, **32**, L22502.

IPCC (2013) *Climate Change 2013: The Physical Science Basis, Contribution of Working Group I to the Fifth Assessment Report of the Intergovernmental Panel on Climate Change.* Cambridge University Press, Cambridge, UK.

Joughin, I., W. Abdalati, and M. Fahnestock (2004) Large fluctuations in speed on Greenland’s Jakobshavn Isbrae glacier. *Nature*, **432**, 608–610.

Kadota, M. (2016) Environmental changes since Little Ice Age reconstructed from SIGMA-D ice core drilled in northwestern Greenland ice sheet. M.S. thesis, Hokkaido University.

Katayama, N. (2016) Surface elevation change on calving glaciers in northwestern Greenland. M.S. thesis, Hokkaido University.

Khan, S. A., J. Wahr, M. Bevis, I. Velicogna, and E. Kendrick (2010) Spread of ice mass loss into northwest Greenland observed by GRACE and GPS. *Geophys. Res. Lett.*, **37**, L06501.

Kjær, K. H., S. A. Khan, N. J. Korsgaard, J. Wahr, J. L. Bamber, R. Hurkmans, M. van den Broeke, L. H. Timm, K. K. Kjeldsen, A. A. Bjørk, N. K. Larsen, L. T. Jørgensen, A. Færch-Jensen, and E. Willerslev (2012) Aerial photographs reveal late-20th-century dynamic ice loss in northwestern Greenland. *Science*, **337**, 596–573.

Lydersen, C., P. Assmy, S. Falk-Petersen, J. Kohler, K. M. Kovacs, M. Reigstad, H. Steen, H. Strøm, A. Sundfjord, Ø. Varpe, W. Walczowski, J. M. Weslawski, and M. Zajaczkowsk (2014) The importance of tidewater glaciers for marine mammals and seabirds in Svalbard, Norway. *J. Marine Syst.*, **129**, 452–471.

Machguth, H., H. H. Thomsen, A. Weidick, A. P. Ahlstrøm, J. Abermann, M. L. Andersen, S. B. Andersen, A. A. Bjørk, J. E. Box, R. J. Braithwaite, C. E. Bøggild, M. Citterio, P. Clement, W. Colgan, R. S. Fausto, K. Gleie, S. Gubler, B. Hasholt, B. Hynek, N. T. Knudsen, S. H. Larsen, S. H. Mernild, J. Oerlemans, H. Oerter, O. B. Olesen, C. J. P. P. Smeets, K. Steffen, M. Stober, S. Sugiyama, D. van As, M. R. van den Broeke, and R. S. W. van de Wal (2016) Greenland surface mass-balance observations from the ice-sheet ablation area and local glaciers. *J. Glaciol.,* **62** (235), 861–887.

Maruyama, M. (2015) Elevation change, mass balance and ice speed in Qaanaaq Ice Cap, northwestern Greenland. M.S. thesis, Hokkaido University.

Matoba, T., H. Motoyama, K. Fujita, T. Yamasaki, M. Minowa, Y. Onuma, Y. Komuro, T. Aoki, S. Yamaguchi, S. Sugiyama, and H. Enomoto (2015) Glaciological and meteorological observations at the SIGMA-D site, northwestern Greenland Ice Sheet. *Bull. Glaciol. Res.,* **33**, 7–14.

Matsuno, S. (2016) Melt water runoff from the Greenland ice sheet to the ocean in northwestern Greenland. M.S. thesis, Hokkaido University.

Mernild, S. H., N. T. Knudsen, W. H. Lipscomb, J. C. Yde, J. K. Malmros, B. Hasholt, and B. H. Jakobsen (2011) Increasing mass loss from Greenland's Mittivakkat Gletscher. *Cryosphere,* **5** (2), 341–348.

Moon, T., I. Joughin, B. Smith, and I. Howat (2012) 21st-century evolution of Greenland outlet glacier velocities. *Science*, **336** (6081), 576–578.

Motyka, R. J., L. Hunter, K. A. Echelmeyer, and C. Connor (2003) Submarine melting at the terminus of a temperate tidewater glacier, LeConte Glacier, Alaska, U.S.A. *Ann. Glaciol.*, **36** (1), 57–65.

Motyka, R. J., W. P. Dryer, J. Amundson, M. Truffer, and M. Fahnestock (2013) Rapid submarine melting driven by subglacial discharge, LeConte Glacier, Alaska. *Geophys. Res. Lett.*, **40**, 5153–5158.

Nakaya, U. (1959) Visco-elastic properties of snow and ice in the Greenland ice cap. *SIPRE Report*, **46**.

Nghiem, S. V., D. K. Hall, T. L. Mote, M. Tedesco, M. R. Albert, K. Keegan, C. A. Shuman, N. E. DiGirolamo, and G. Neumann (2012) The extreme melt across the Greenland ice sheet in 2012. *Geophys. Res. Lett.*, **39**, L20502.

Nick, F., A. Vieli, I. M. Howat, and I. Joughin (2009) Large-scale changes in Greenland outlet glacier dynamics triggered at the terminus. *Nat. Geosci.*, **2** (2), 110–114.

Ohashi, Y. (2015) Variations in high turbidity ocean surface water in northwestern Greenland. M.S. thesis, Hokkaido University.

Ohashi, Y., T. Iida, S. Sugiyama, S. Aoki (2016) Spatial and temporal variations in high turbidity surface water off the Thule region, northwestern Greenland. *Polar Sci.,* **10**, 270–277.

Palmer, S. J., J. A. Dowdeswell, P. Christoffersen, D. A. Young, D. D. Blankenship, J. S. Greenbaum, T. Benham, J. Bamber, and M. J. Siegert (2013) Greenland subglacial lakes detected by radar. *Geophys. Res. Lett.*, **40**, 6154–6159.

Podolskiy, E. A., S. Sugiyama, M. Funk, F. Walter, R. Genco, S. Tsutaki, M. Minowa, and M. Ripepe (2016) Tide-modulated ice flow variations drive seismicity near the calving front of Bowdoin Glacier, Greenland. *Geophys. Res. Lett.*, **43**, 2036–2044.

Podolskiy, E. A., R. Genco, S. Sugiyama, F. Walter, M. Funk, M. Minowa, S. Tsutaki, and M. Ripepe (2017) Seismic and infrasound monitoring of Bowdoin Glacier, Greenland. *Low Temp. Sci.,* **75** (this volume).

Porter, D. F., K. J. Tinto, A. Boghosian, J. R. Cochran, R. E. Bell, S. S. Manizade, and J. G. Sonntag (2014) Bathymetric control of tidewater glacier mass loss in northwest Greenland. *Earth Planet. Sci. Lett.*, **401**, 40–46.

Rastner, P., T. Bolch, N. Mælg, H. Machguth, R. Le Bris, and F. Paul (2012) The first complete inventory of the local glaciers and ice caps on Greenland. *Cryosphere,* **6**, 1483–1495.

Rignot, E., and P. Kanagaratnam (2006) Changes in the velocity structure of the Greenland ice sheet. *Science*, **311**, 986–990.

Rignot, E., M. Koppes, and I. Velicogna (2010) Rapid submarine melting of the calving faces of West Greenland glaciers. *Nat. Geosci.*, **3** (3), 187–191.

Rignot, E., I. Velicogna, M. R. van den Broeke, A. Monaghan, and J. T. M. Lenaerts (2011) Acceleration of the contribution of the Greenland and Antarctic ice sheets to sea level rise. *Geophys. Res. Lett.*, **38**, L05503.

Rinne, E. J., A. Shepherd, S. Palmer, M. R. van den Broeke, A. Muir, J. Ettema, and D. Wingham (2011) On the recent elevation changes at the Flade Isblink Ice Cap, northern Greenland. *J. Geophys. Res.*, **116**, F03024.

Saito, J. (2015) Surface elevation change on ice caps in northwestern Greenland. M.S. thesis, Hokkaido University.

Saito, J., S. Sugiyama, S. Tsutaki, T. Sawagaki (2016) Surface elevation change on ice caps in the Qaanaaq region, northwestern Greenland. *Polar Sci.,* **10**, 239–248.

Sakakibara, D. (2016) Ice front variations and velocity changes of calving glaciers in the Southern Patagonia Icefield and northwestern Greenland. Ph. D. thesis, Hokkaido University.

Sasgen, I., M. van den Broeke, J. L. Bamber, E. Rignot, L. S. Sorensen, B. Wouters, Z. Martinec, I. Velicogna, and S. B. Simonsen (2012) Timing and origin of recent regional ice-mass loss in Greenland. *Earth Planet. Sci. Lett.*, **333–334**, 293–303.

Schrama, E. J. O., and B. Wouters (2011) Revisiting Greenland ice sheet mass loss observed by GRACE. *J. Geophys. Res.*, **116**, B02407.

Straneo, F., and P. Heimbach (2013) North Atlantic warming and the retreat of Greenland's outlet glaciers. *Nature*, **504**, 36–43.

Straneo, F., G. S. Hamilton, D. A. Sutherland, L. A. Stearns, F. Davidson, M. O. Hammill, G. B. Stenson, and A. Rosing-Asvid (2010) Rapid circulation of warm subtropical waters in a major glacial fjord in East Greenland. *Nat. Geosci.*, **3**, 182–186.

Straneo, F., D. A. Sutherland, D. Holland, C. Gladish, G. S. Hamilton, H. L. Johnson, E. Rignot, Y. Xu, and M. Koppes (2012) Characteristics of ocean waters reaching Greenland's glaciers. *Ann. Glaciol.*, **53** (60), 202–210.

Sugiyama, S., D. Sakakibara, S. Matsuno, S. Yamaguchi, S. Matoba, and T. Aoki (2014) Initial field observations on Qaanaaq Ice Cap in northwestern Greenland. *Ann. Glaciol.*, **55** (66), 25–33.

Sugiyama, S., D. Sakakibara, S. Tsutaki, M. Maruyama, and T. Sawagaki (2015) Glacier dynamics near the calving front of Bowdoin Glacier, northwestern Greenland. *J. Glaciol.,* **61** (226), 223–232.

Takeuchi, N., N. Nagatsuka, J. Uetake, and R. Shimada (2014) Spatial variations in impurities (cryoconite) on glaciers in northwest Greenland. *Bull. Glaciol. Res.,* **32**, 85–94.

Tsutaki, S., S. Sugiyama, D. Sakakibara, and T. Sawagaki (2016) Surface elevation changes during 2007–13 on Bowdoin and Tugto Glaciers, northwestern Greenland. *J. Glaciol.,* **62** (236), 1083–1092.

Uemura, N. (1976) *Kyokuhoku ni kakeru*. Bungeishunju, 262 pp., ISBN 4167178028.

van den Broeke, M., J. Bamber, J. Ettema, E. Rignot, E. Schrama, W. J. van de Berg, E. van Meijgaard, I. Velicogna, and B. Wouters (2009) Partitioning recent Greenland mass loss. *Science*, **326**, 984–986.

Velicogna, I. (2009) Increasing rates of ice mass loss from the Greenland and Antarctic ice sheets revealed by GRACE. *Geophys. Res. Lett.*, **36**, L19503.

Wientjes, I. G. M., and J. Oerlemans (2010) An explanation for the dark region in the western melt zone of the Greenland ice sheet. *Cryosphere*, **4** (3), 261–268.

低温科学 75 （2017） 15-36
doi: 10.14943/lowtemsci. 75. 15

Seismic and infrasound monitoring of Bowdoin Glacier, Greenland

Evgeny A. Podolskiy[1]*, Riccardo Genco[2], Shin Sugiyama[3], Fabian Walter[4], Martin Funk[4], Masahiro Minowa[3], Shun Tsutaki[5, 6], Maurizio Ripepe[2]

Received 28 October 2016, accepted 11 January 2017

Outlet glaciers in Greenland have retreated and lost mass over the past decade. Understanding the dynamics of tidewater glaciers is crucial for forecasting sea-level rise and for understanding the future of the Greenland Ice Sheet, given the buttressing support that tidewater glaciers provide to inland ice. However, the mechanisms controlling glacier-front location and the role played by external forcings (e.g., meltwater input and tidal oscillation) in basal motion and fracture formation leading to iceberg calving are poorly understood. Today it is known that glaciers generate seismic and infrasound signals that are detectable at local and teleseismic distances and can be used to monitor glacier dynamics. Here, we present examples of data recorded by a temporary network of seismic and infrasound instruments deployed at a tidewater glacier (Bowdoin Glacier, Greenland) in July 2015. Some stations were installed on ice at distances as close as ～ 250 m from the calving front, representing the closest deployments to the calving front that have been made to date. Multiple seismic and infrasound events were recorded by five seismic and six infrasound sensors, and linked to surface crevassing, calving, and ice-cliff collapses, and presumably also hydrofracturing, iceberg rotations, teleseismic earthquakes, and helicopter-induced tremors. Using classic seismological and array analysis approaches (e.g., "short-term averaging/long-term averaging" and "*f–k*" analysis), as well as image processing techniques, we explore this unique dataset to understand the glacial response to external forcings. Our observations, supported by GPS measurements of ice velocity, local weather-station records, and time-lapse photography, provide a valuable resource for studying seismogenic glacial processes and their dependence on ocean tides and other environmental factors.

Keywords: Seismicity, infrasound, array, tidewater glacier, Greenland

1. Introduction

> *"Beneath our feet a continuous trembling sensation was felt … Quick, sharp, deep-tingling, ringing, shrieking sounds frightful enough, came, not as sound usually does, horizontally, but vertically up to our ears, seeming to vibrate through our feet, our limbs, our very bodies, spitefully shouting in our ears: Why, presump-*

---

*Corresponding author
e-mail：e.podolskiy@arc.hokudai.ac.jp
1）Arctic Research Center, Hokkaido University, Sapporo, Japan
2）Dipartimento di Scienze della Terra, Università di Firenze, Florence, Italy
3）Institute of Low Temperature Science, Hokkaido University, Sapporo, Japan
4）Laboratory of Hydraulics, Hydrology and Glaciology, ETH Zürich, Zurich, Switzerland
5）Earth Observation Research Center, Japan Aerospace Exploration Agency, Tsukuba, Japan
6）Arctic Environment Research Center, National Institute of Polar Research, Tachikawa, Japan

tuous man, hast thou set disturbing foot upon my chaste bosom? Beware! Beware! Beware! Split-jingle-crash-Off! Away! Away!"

E. B. Baldwin about his crossing of the Bowdoin Glacier in the summer 1894 (Baldwin, 1896)

Polar glaciers are difficult and expensive to access for scientific research purposes. Moreover, glacier interiors are difficult environments in which to study and monitor important glacial phenomena such as the dynamics of ice fracturing, the mechanisms of basal movement, and the material properties of ice and sub-glacial till, as well as the evolution of sub-glacial drainage systems. Similarly, the observation of calving-rates remains challenging and is one of the most uncertain inputs in predictions of future sea-level rise (IPCC, 2013).

In this light, passive seismology enables monitoring of near- and sub-surface processes at high spatial and temporal resolutions in regions that are difficult to access or hard to monitor. Recent observational studies have shown that monitoring the natural seismicity of ice is useful for many glaciological applications (for a comprehensive review, see Podolskiy and Walter, 2016). In particular, seismological techniques have been applied to the study of the Greenland Ice Sheet (GrIS) and its marginal ice and glaciers, which are known to have experienced retreat and intense mass loss in the last decade (Khan et al., 2015). For example, if we limit ourselves only to Greenland-related research, Ekström et al. (2003) reported previously unknown tele-seismic events that differ from tectonic earthquakes, termed "glacier earthquakes", which are generated by large-scale iceberg calving and capsizing events. These events have increased in frequency since 1990 (Ekström et al., 2006), and their locations have spread into northwest Greenland during the last decade (Veitch and Nettles, 2012). In another context, Walter et al. (2014) showed that the properties and thickness of sub-glacial sediments, which influence basal movement, could be estimated beneath the margin of western Greenland via analysis of natural seismicity. Bartholomaus et al. (2015) demonstrated the possibility of quantifying sub-glacial discharge using continuous seismic tremor as a proxy. Carmichael et al. (2015) analyzed seismic and GPS signals related to the rapid draining of a supra-glacial lake, and associated the signals with an increase in ice-flow speed in western Greenland. Their results suggested that the ice-quake activity peak was associated with vertical hydro-fracturing that enhanced ice flow by supplying meltwater from the lake to the bed at a depth of almost 1 km. Roeoesli et al. (2016) discovered small stick-slip events that are influenced by meltwater input, which were previously never observed near the base of the Greenland Ice Sheet. Furthermore, most recently, Mordret et al. (2016) demonstrated that the mass balance of Southern Greenland could be inferred from ambient seismic-noise analysis. This innovative approach is based on measurements of seismic-velocity variations in the crust due to changes in ice-mass loading. According to the authors, this technique presents an opportunity for near-real-time mass-balance monitoring as an alternative to satellite observations, which have limited temporal resolution.

Glacial seismic sources corresponding to sudden mass acceleration also emit energy into the atmosphere in the form of infrasound waves; i. e., as air-pressure oscillations at frequencies below 20 Hz, which can propagate for thousands of kilometers with little attenuation. In particular, calving and iceberg capsizing events are the most prominent sources of local and regional infrasound and seismic wave fields at regional and tele-seismic scales (e. g., Richardson et al., 2010). Analysis of both types of signals allows for a comprehensive understanding of the source mechanisms and source location in time and space. Specifically, the different information carried by seismic waves propagating through solid ice and infrasound waves propagating through air from the same event, which may involve impacts and mass acceleration, has the potential to provide additional insights. Moreover, infrasound data can be a useful complement to seismic data as it helps to better differentiate surface events like iceberg calving from signals emanating from other parts of the glacier. To our knowledge, the possibility of glacial and cryosphere monitoring with infrasound remains to be explored, and has only rarely been applied previously (Richardson et al., 2010; Maruyama et al., 2015; Preiswerk et al., 2016).

The internationally funded Greenland Ice Sheet

Monitoring Network (GLISN) currently provides continuous regional seismic observations in Greenland, including near-real-time data from some of its stations. These data are freely distributed by Incorporated Research Institutions for Seismology (IRIS). However, local observations are needed to obtain a comprehensive understanding of glacier dynamics and glacier seismic sources, especially because the magnitude of most events is too weak (i.e., $M<1$) to be detected at epicentral distances greater than a few kilometers (Podolskiy and Walter, 2016). Moreover, a long-term Comprehensive Nuclear-Test-Ban Treaty Organization (CTBTO) infrasound installation (IS18) for real-time nuclear and atmospheric monitoring, located near Qaanaaq village in northwestern Greenland, provides detailed in-situ infrasound observations that are valuable for assessing the potential, and limitations, of using this geophysical approach for cryospheric studies.

Against this background, in this paper we briefly introduce the seismic and infrasound monitoring campaign that we conducted at Bowdoin Glacier in northwestern Greenland in July 2015. This work formed part of a comprehensive set of glaciological observations, organized as a collaboration among Hokkaido University (Japan), ETH Zürich (Switzerland), and the University of Florence (Italy). A similar field campaign was performed in July 2016, and the results will be published elsewhere, along with a detailed analysis of the present results.

2. Site and instrumentation set-up

2.1 Study site

Bowdoin Glacier (77°41′N, 68°35′W) is located ~ 125 km from Pituffic and more than 25 km from Qaanaaq. The glacier was named after Bowdoin College, USA, by its famous 1877 graduate, Arctic explorer Admiral Robert Peary. It is a grounded tide-water glacier with a calving front that is 3 km wide. The first scientific observations of the glacier were performed during Peary's expedition of 1894, and included, surprisingly, time-lapse photography. These observations are described in the corresponding expedition reports (Chamberlin, 1895; Chamberlin, 1897). The latter report presented photographs of the glacier front, near-front ice-speed measurements of up to 84 cm per day at the center and 57 cm per day on average, and other detailed, mostly qualitative descriptions. Since 2013, the dynamics of Bowdoin Glacier and the properties of its fjord have being intensively studied through annual Japanese expeditions and from satellite imagery (Sugiyama et al., 2015). These more recent observations have found that the terminus of the glacier remained relatively stable until 2008, when it started to retreat from an elongate submarine bump oriented perpendicular to the fjord. Close to the calving front, ice thickness measured with ground-penetrating radar is known to be less than 280 m. Precise GPS measurements show that the horizontal ice speed is tide-modulated and reaches a maximum of ~ 2 m per day at low tide (Sugiyama et al., 2015).

2.2 Instrumentation

Despite some heavily crevassed zones, conditions in the lower parts of the glacier surface enable many locations to be accessed by foot, thus permitting direct access to the calving front and creating various unique opportunities for deploying monitoring instruments. In July 2015, several sites (both on the ice and on nearby rock outcrops along the eastern side of the glacier) were selected for observations, to enable near-source monitoring of calving front dynamics (Fig. 1). A helicopter was used to transport instrumentation to monitoring sites and to deliver seismic-array equipment to a location on the central moraine a few hundred meters from the calving front (Fig. 2). The ability to land a helicopter near the calving front on the loose boulders of the moraine and the availability of human resources to manually move heavy equipment over the rough ice surface with backpacks were crucial to the successful and safe installation of the on-ice seismic array. This seismic deployment is closer to the calving front than any previous set-up.

A Guralp CMG40T triaxial broadband seismometer, sensitive to periods up to 30 s, was installed on the rocky coast forward of the calving front, along with a Guralp CMG-DAS-S6 recorder operating at a sampling rate of 100 Hz and a GoPro time-lapse camera operating at 6 frames per minute. An Onset HOBO U-20 water-pressure sensor, operating at a sampling rate of 0.5 Hz,

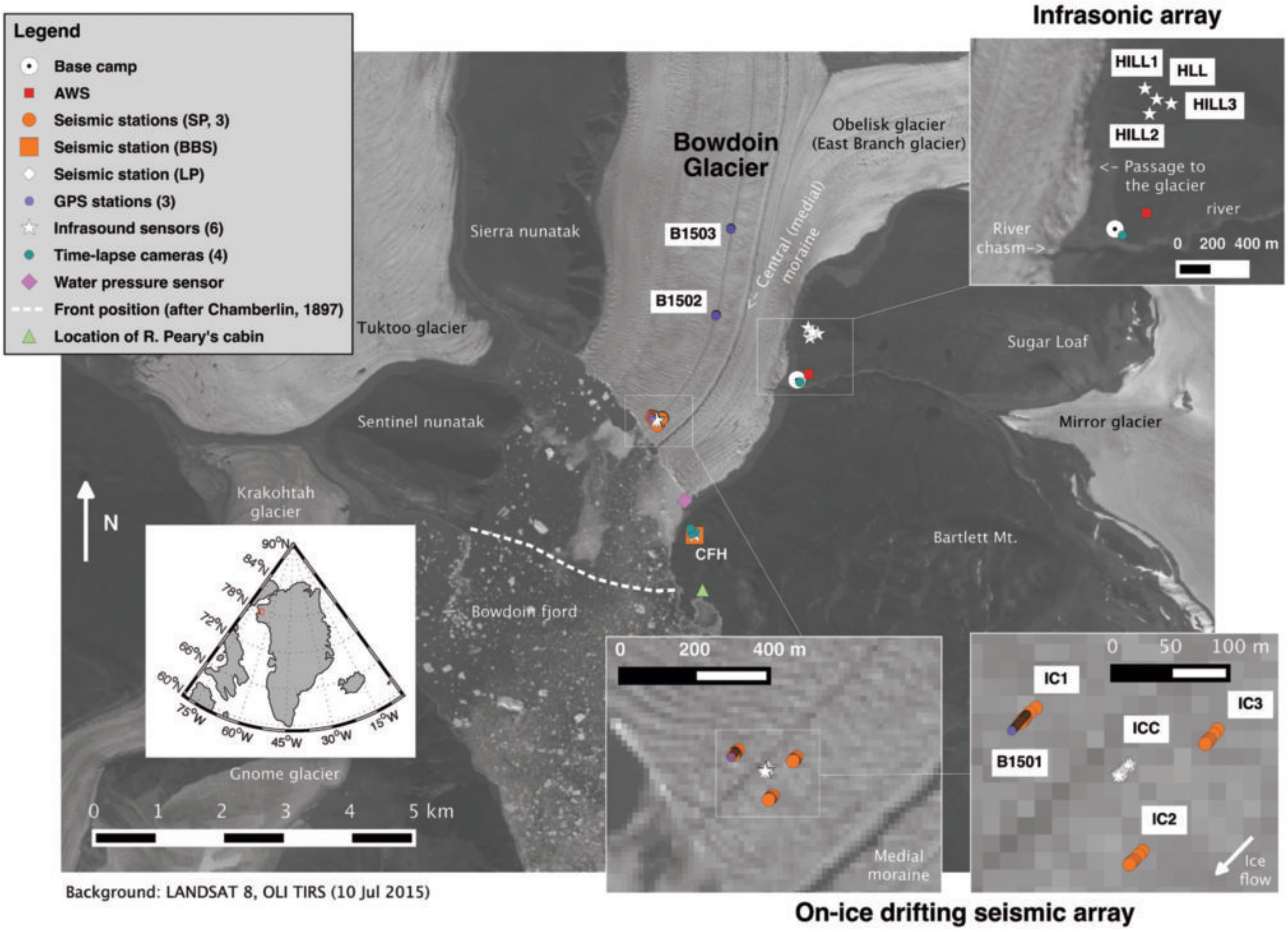

Figure 1 : Map of the Bowdoin Glacier geophysical experiment setup of July 7–19, 2015. The insets at lower right show close-up views of the seismic array. Note that a drift in the position of the on-ice stations is apparent due to the ice flow. Depending on the station, these shifts corresponds to ~ 14–18 m of horizontal displacement in total. The inset at lower left shows a map of Greenland with Bowdoin's location.

was deployed in the fjord to record micro-tsunamis generated by calving events. Four Lennartz LE-3D short-period (SP) and long-period (LP) seismometers, connected to Taurus/Nanometrics and Guralp data loggers, were arranged on the glacier ice in a triangular array located ~ 250 m from the marginal ice cliff, where icebergs are discharged into the fjord. The three SP stations (named "IC1", "IC2", and "IC3") used seismometers with a natural frequency of 1 Hz, and formed the vertices of the triangular array. The instruments were seated on tripods, as used typically for installations into soft soil. The central LP station ("ICC") used an instrument with a natural frequency of 0.2 Hz that was placed on a ceramic tile. All stations operated at a sampling rate of 500 Hz. Each sensor was placed in an ice pit with a drainage channel for removing meltwater; each pit was covered with a metal mesh and a high-albedo blanket to protect the stations from wind, rain, and solar radiation (Fig. 2).

An infrasound array, comprising four absolute pressure transducers (from iTem geophysics) with a sensitivity of 0.01 Pa in the 0.01–100 Hz frequency band, was installed on a hill located close to the base camp, 3 km behind the calving front and at an elevation of 270 m. Three pressure sensors were connected via 100 m cables to a Guralp data-logger (7 channels, 24 bits Guralp CMG-DM24 A/D converter), operating at a sampling frequency of 500 Hz, located at the central station. Another two infrasound sensors were co-located with the central station of the on-ice seismic array, ICC, and the broadband seismic station, recording at sampling rates of 500 and 100 Hz, respectively. The aperture of both arrays was ~ 150 m. In addition, three dual-frequency GPS stations (Global Navigation Satellite Systems, GEM-1) were deployed on the ice, and a reference station was positioned on bedrock to establish

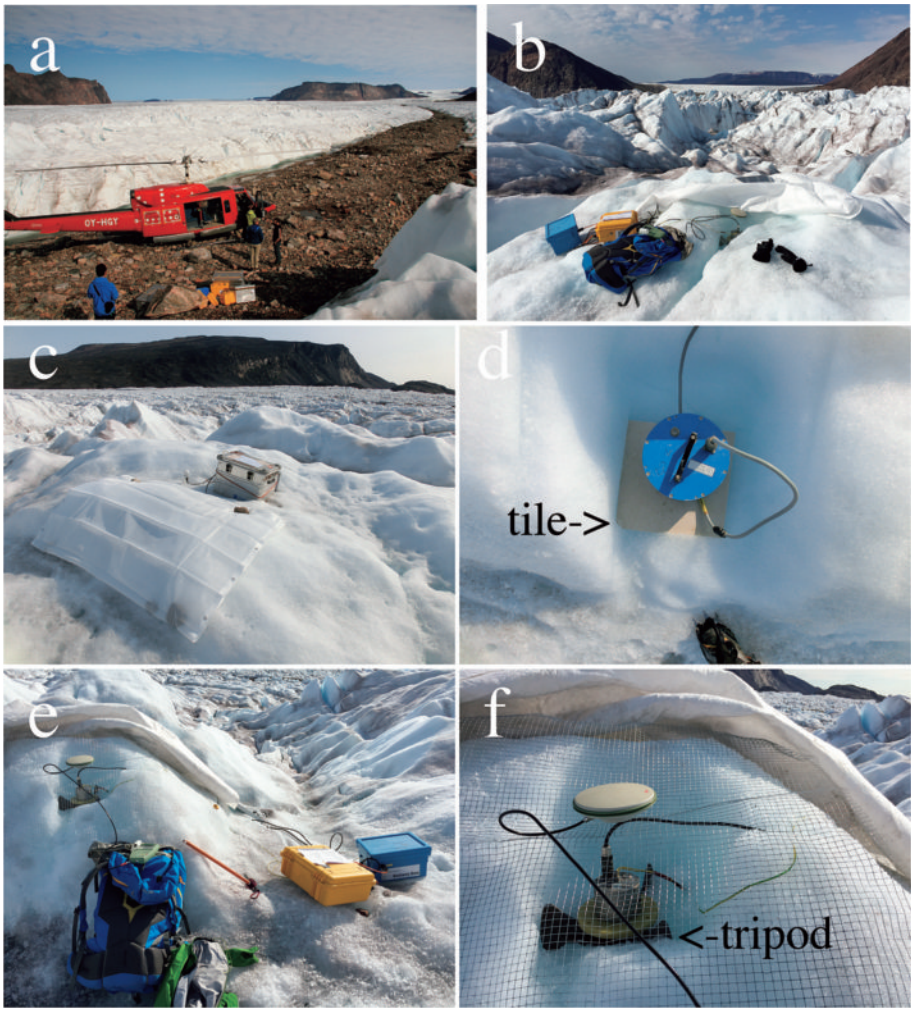

Figure 2 : (a) Staging area for seismic equipment on the central moraine, unloaded from the helicopter. (b) Seismic station IC1. An SP seismometer was screwed to a disk and placed on a metal tripod. Note the drainage channel for removing meltwater from the ice pit. The yellow watertight box contains the Taurus recorder, GPS antenna, and solar panel regulator. This box is connected to one external battery (Cyclon; 12V, 46 Ah) and a solar panel. (c) Seismic station ICC. An LP seismometer was placed in an ice pit and covered with a mesh and protective blanket. The aluminum Zarges box contains the Guralp recorder, battery (Fiamm, 12V, 42 Ah), and solar panel regulator. The solar panel and GPS antenna are located at the sides of the box. (d) LP seismometer at station ICC deployed on a ceramic tile. (e) Seismic station IC2; setup is as for station IC1 — see (b) above. (f) SP seismometer at station IC2, deployed on a metal tripod. Note that the Leica Geosystems dual-frequency GPS antenna is placed into an intentionally formed depression in the mesh so that a consistent measurement position can be obtained. This strategy was also employed at station IC1. Efforts were always made to ensure that other parts of the mesh were kept away from direct contact with the cable.

a longitudinal profile of ice speed along Bowdoin Glacier. Seismic station IC1 was co-located with one of these GPS stations. Finally, Vaisala WXT520 and Campbell CR1000 automatic weather stations (AWS) were used to record meteorological conditions near the base camp, east of the glacier. A second time-lapse camera operating at 6 frames per hour was deployed at the base camp to monitor erosion of a glacier margin due to the river from the Mirror Glacier. All instruments were powered with 12 V batteries that were constantly charged by solar panels.

Finally, we note that all four on-ice seismic stations were visited on a daily basis to enable maintenance tasks such as leveling, orientation, and data back-up to be performed. This ongoing effort was required due to intense ablation of the glacier surface of up to 45 mm w.e. per day, which is approximately equivalent to 5 cm of ice per day. Because the receivers moved with the ice flow a total distance of ~ 18 m during the campaign (Fig. 1), the precise location of each seismometer was re-measured with a dual-frequency GPS receiver every couple of days (Fig. 2e and f). We also note that calm weather conditions with almost no wind prevailed during our survey, providing a low-noise environment for observations. These calm weather conditions were especially favorable for the acquisition of infrasound records, which are strongly affected by wind.

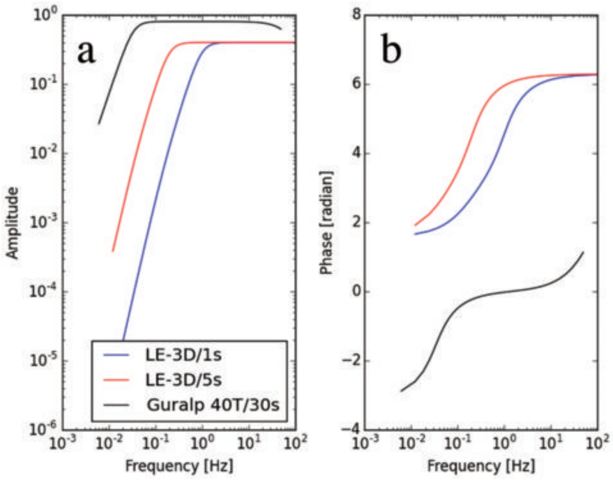

Figure 3：Frequency response of the seismometers used in this study: (a) amplitude response; (b) phase response.

3. Results and discussion

3.1 Instrument performance

Maintenance of on-ice seismometers deployed in a zone of ablation is known to be a challenging and laborious task (Pomeroy et al., 2013). During our campaign, for example, we walked an >8 km round trip every day between the base camp and the seismic array to maintain the array. This maintenance work is dramatically different to the annual station visit that is typically required in classical seismology. Nevertheless, it is valuable if on-ice installations can be sustained via such regular visits, as they can provide superior data to that obtained at nearby stations deployed on bedrock. This difference in data quality arises because seismic arrivals recorded by on-ice stations have not experienced changes due to propagation through the complex ice-sediment-rock interface, whose seismic velocity structure is poorly understood. Finally, considering the relatively short duration of the campaign, daily visits guaranteed the success of data collection by reducing the risk of data loss due to possible troubles with the instruments, as well as allowed to continuously re-evaluate the performance of our setup.

Some difference was noted between the performance of the tripod and ceramic tile seismometer-supports, which are shown for comparison in Figures 2d and 2f. A tile was used only for the LP seismometer (Fig. 2d), simply because the latter was larger and heavier than the more compact SP sensors. On the one hand, tripods have sharp legs (Fig. 2f) that favor heterogeneous pressure-melting of the ice, potentially resulting in rapid loss of proper instrument leveling and orientation. On the other hand, tripods provide relatively stable conditions that reduce the risk of the sensor falling. The tile, however, in our opinion better preserves the level of the instrument, because the load is distributed more evenly and thus pressure melt is fairly homogeneous under the tile area. Nevertheless, the flat and smooth bottom of the tile may allow the instrument to slowly drift to the side of a pit, which creates a risk of the sensor toppling if the pit has an open side. A further benefit of using tripods over tiles is that seismometers attached to disks and seated on tripods can be easily and quickly leveled and oriented. Seismometers deployed on tiles, however, require each of the three leveling screws to be adjusted individually. (It is worth mentioning that there is also the possibility to place the tripod on the tile, a practice adopted on Alpine glaciers).

We found that for all on-ice stations, degradations in instrument levels and rotations of up to ±10–30° from north can sometimes occur within 24 hours, thereby reducing the fidelity of horizontal components for further analysis. For this reason, we discuss only the vertical-component traces recorded by the instruments (the vertical component is affected too, although less so).

The instrument response functions of the SP, LP, and broadband sensors used in this study differ from one another (Fig. 3), which means our dataset spans a wide frequency band with flat instrument response ranging from 0.033 to 100 Hz. Although most seismic signals were at frequencies above 0.5 Hz, the broadband instrument was valuable for documenting low-frequency events, as well as tele-seismic earthquakes that would otherwise have been missed. Moreover, the LP sensor installed on the glacier surface provided an opportunity to expand the frequency band of the seismic observations and, therefore, to obtain a more complete dataset.

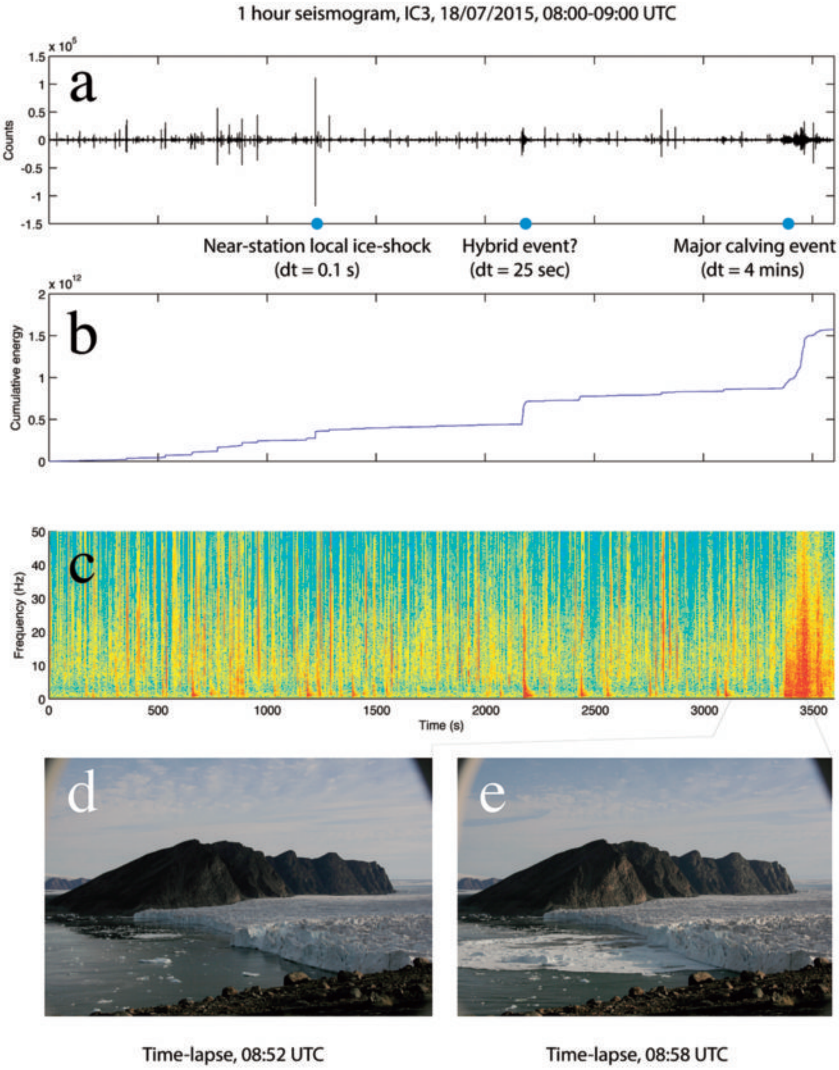

Time-lapse, 08:52 UTC

Time-lapse, 08:58 UTC

Figure 4 : Example of typical seismic activity recorded in an hour-long period by the on-ice seismometer IC3 (18 July 2015, 08 : 00–09 : 00 UTC). (a) Raw vertical-component seismic trace with markers indicating the three most common types of events: short impulsive ice-quakes, LP or hybrid events (the foot-like signals; see text for details), and major calving events. (b) Cumulative energy (i.e., cumulative squared amplitude of a trace). (c) Spectrogram of the trace shown in (a). (d, e) Photographs taken by time-lapse cameras covering a six minute interval before (d) and after (e) the calving event on 18 July 2015, 08 : 56–09 : 00 UTC.

3.2 Seismic events

Multiple seismic events were recorded and associated with various processes, including surface crevassing, iceberg calving, iceberg rotations, tele-seismic earthquakes, harmonic tremors, lateral ice-cliff collapses onto rock, and presumably also hydro-fracturing.

A representative segment of a vertical-component seismic trace of 1 hour duration, together with its cumulative energy and spectrogram, is shown in Fig. 4. Hundreds of short, high-frequency (>10 Hz) events with spiky waveforms are the most common and prominent feature of the seismic data (Fig. 4a). Another type of event, which occurs more rarely, has a low characteristic frequency of ∼ 1 Hz with high frequency onset (thus we can call these long-period events as “hybrid” events) and is followed by a monochromatic coda lasting up to 30 s. Finally, calving events took place several times a day; they are visible in the data as emergent, high-amplitude tremors with dominant frequencies between 0.2 and 5 Hz that last for a few minutes (Fig. 4d and e).

A time-lapse video showing an example of the largest calving event, which occurred at 08 : 56–09 : 00 UTC on 18 July 2015, and small ice-quakes is available online at https: //www. youtube. com/watch? v = U3F6kv3To3Y. This video was produced by synchronizing one hour of time-lapse photographs with the corresponding seismic record from the on-ice station IC2, after the seismogram had been converted into an audible

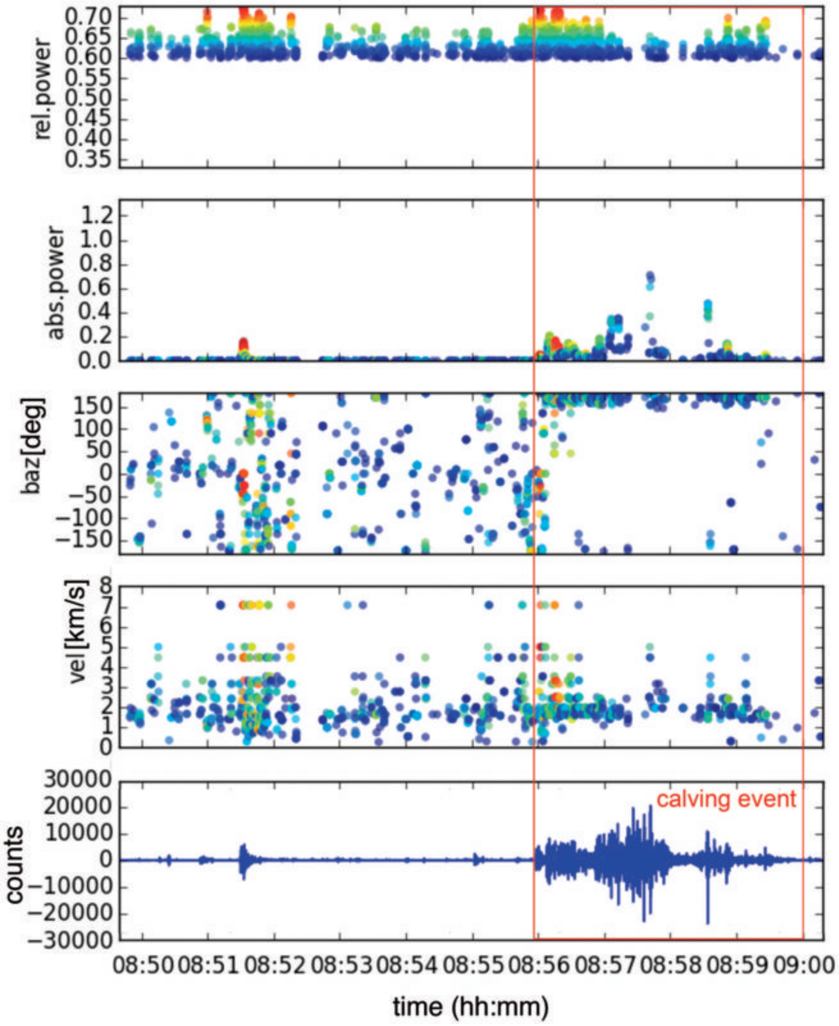

Figure 5 : Results of *f–k* analysis of a calving event for data in the interval 08 : 50 : 00–09 : 00 : 00 UTC on 18 July 2015 (using a sliding window of duration 1 s, a window fraction of 0.1 s, and frequency band of 1–10 Hz). Panels from top to bottom respectively show: relative power (i.e., equivalent of coherence); absolute power ($\times 10^{14}$; related to an amplitude of a signal) back-azimuth relative to north; apparent velocity (km/s); and the low-pass filtered (i.e., <10 Hz) data trace. Marker colors in the upper four sub-panels correspond to the relative power from the top sub-plot (high relative power implies more reliable result).

synthetic sound. Multiple smaller-amplitude signals corresponding to ice-quakes are apparent in the video, in addition to the major event due to calving. Following the calving event, note the tsunami that is generated at the coast and the brownish melt-water plume that emanates from beneath the central part of the glacier. As shown by this video and Fig. 4c, the majority of seismic-energy release is due to long-period events and calving; however, the time-lapse video confirms that only calving can be observed visually and all other seismic activity is not accompanied by any recognizable processes at the calving front.

Array analysis, in particular frequency-wavenumber or *f–k* analysis, can be used to obtain the so-called back-azimuth; i. e., the angle of wave-front approach relative to north, together with slowness (i.e., the inverse of apparent velocity, $1/V_{app}$) at which the wave-front propagates through the array (Schweitzer et al., 2002; Rost and Thomas, 2002). Calving and other events recorded using our array can be analyzed using this method. A description of limits of the array resolution can be found in Appendix A.

An example of *f–k* analysis performed for four stations is shown in Fig. 5. The estimated back-azimuth (Fig. 6, energy in the direction 150–170° clockwise from north) points to the real location of the calving event of 18 July 2015, which is known from time-lapse photography. Further analysis of data for the full duration of the campaign will be published elsewhere.

Here, it is also worth mentioning that, according to

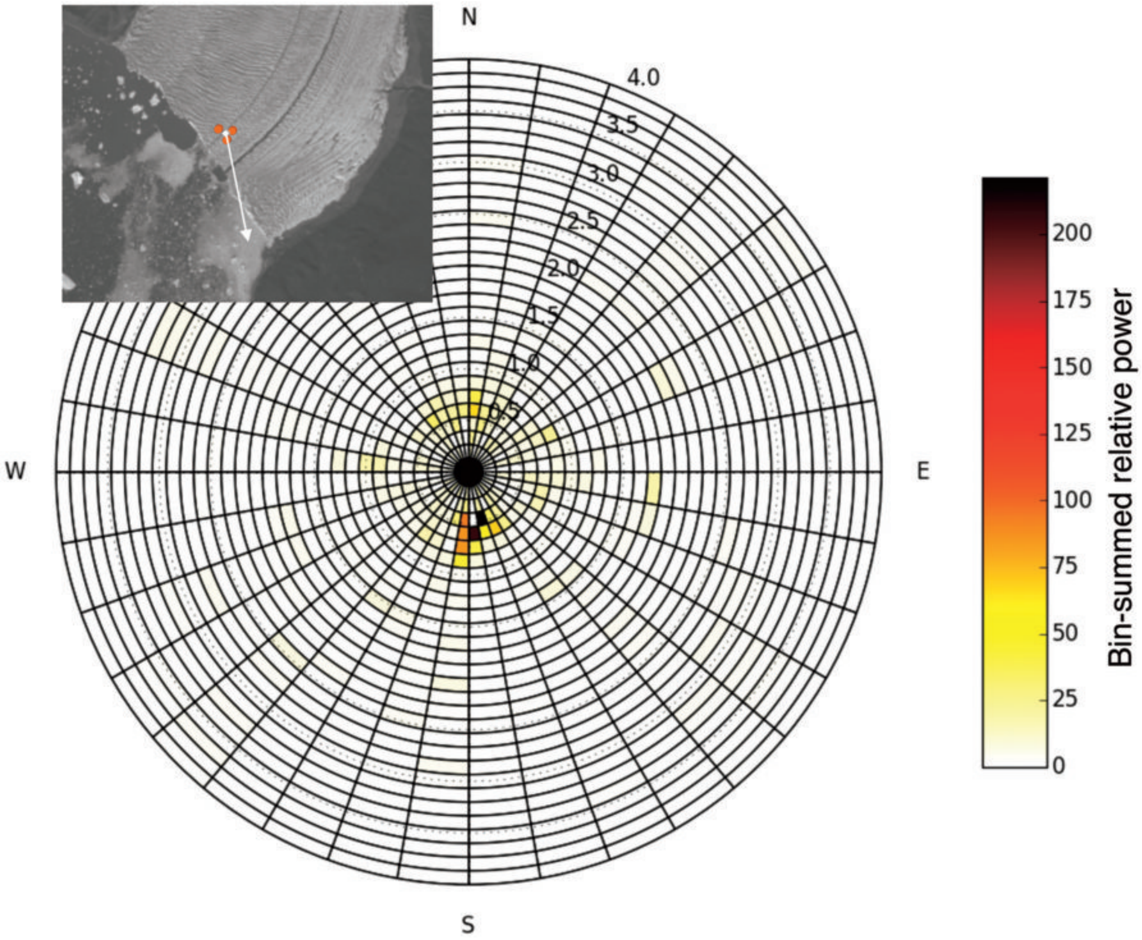

Figure 6 : Polar plot showing back-azimuth and slowness calculated using *f–k* analysis of the calving event of 08 : 50 : 00–09 : 00 : 00 UTC on 18 July 2015, with cumulative relative power in gridded bins. The inset indicates the back-azimuth on the map.

our time-lapse records, some seismic tremor-like signals that are followed by micro-tsunamis (e.g., after 06 : 04 : 00 UTC on 17 July 2015) may not originate at the calving front, but from iceberg capsize in the fjord, which generates similar signals. The signals can be misinterpreted as calving, as was also reported by Richardson et al. (2010), who detected many false "calving events".

3.2.1 Long-period events

Long-period (hereafter LP) events, with frequencies below 5 Hz, have puzzled seismologists and glaciologists since they were first detected, when it was realized that signals of glacial origin emanating from glacier-covered volcanoes can be confused with volcanic events (Weaver and Malone, 1976; St. Lawrence and Qamar, 1979). This type of event has regularly resurfaced in the literature over the last 40 years, and the debate surrounding the underlying mechanism is ongoing. Their source mechanism is usually explained as an analogy to volcanic events, with brittle fracture-opening followed by resonance of a water-filled cavity or rapid flow of water into a newly opened space (Metaxian, 2003; West et al., 2010). Recently, LP events near Ekström and Roi Baudoin ice shelfs, Antarctica, were found to occur exclusively on the rising tide and interpreted as basal fracturing due to upward bending of the ice shelf under tidal forcing (Hammer et al., 2015; Lombardi et al., 2016). The most recent Antarctic study by Lombardi et al. (2016) has encouraged further research into these LP events and their long-term variation. We observe a significant number of signals in our data set that resemble LP events (Fig. 7). The key features of LP events at Bowdoin Glacier are as follows:

- low-frequency content (i.e., <10 Hz),
- long duration (up to 30 s and longer),
- monochromatic coda tail (around and below 1 Hz).

Furthermore, the amplitude of LP signals is larger than that of the majority of high-frequency events.

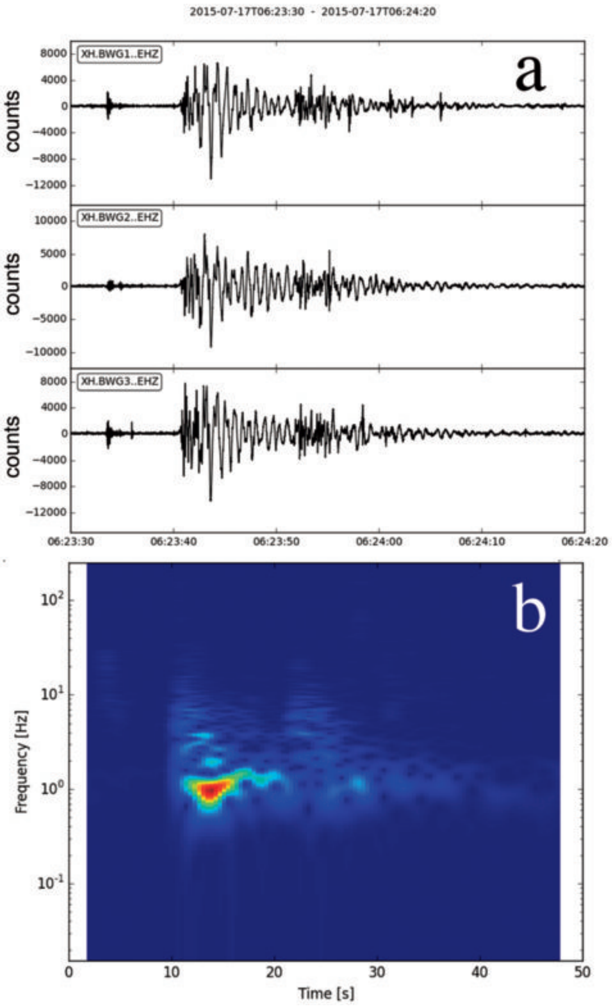

Figure 7 : (a) Example of a long-period event that occurred on 17 July 2015, which was recorded on the vertical component of three SP seismometers deployed on the glacier. (b) Spectrogram from station IC1 for the corresponding time interval.

Therefore, LP events can be seen at all seismic stations, including the broadband seismometer located on rock (Fig. 8). The true source mechanisms of LP events at Bowdoin Glacier remain to be understood, but should be obtainable through further analysis of long-term observations, as explained below.

3.2.2 Anomalous events

Amongst other noticeable events, two tele-seismic earthquakes were recorded, as well as several tremors with distinct gliding spectral lines (as illustrated below). These types of cryospheric phenomena are important for two reasons: (i) it is known that the passage of surface-wave arrivals from large tele-seismic earthquakes through the Antarctic ice sheet can trigger bursts of ice-quakes due to dynamic induced strains (Peng et al., 2014); and (ii) it has been observed that ice sheet sliding and icebergs can produce long-duration tremors (e.g., with duration from 20 mins to 16 hours) with multiple harmonics. This latter phenomenon was previously interpreted as scratching of the ocean floor by icebergs (MacAyeal et al., 2008), or as the overlap of many small stick-slip events during large-scale slip of the Willans Ice Stream in Antarctica (Winberry et al., 2013; Lipovsky and Dunham, 2015). Similar tremors have also been reported in volcanic environments. Moreover, it is known that this type of event can be easily confused with helicopter tremors produced by rotor blade noise (Eibl et al., 2015), and we find this to be exactly the case in our records from Bowdoin Glacier, as shown in the analysis below.

3.2.2.1 Tele-seismic earthquakes

The vertical-component traces of two tele-seismic earthquakes recorded by broadband seismometer CFH on July 10 and 18 are shown in Fig. 9a and b. The parts of the signal with highest amplitude are associated with surface wave arrivals. These earthquakes can also be seen in records from the Thule permanent broadband station (station code: DK TULEG, GLISN), which is located ~ 125 km away (Fig. 9c and d). According to the European-Mediterranean Seismological Centre global event catalogue (www.emsc-csem.org), these earthquakes originated from an area to the east of Papua New Guinea (for details see Appendix B), at a distance of ~ 12,000 km from Bowdoin (i.e., an epicentral distance of ~ 107°):

10 July 2015 04:12:41 UTC: M6.8 - Solomon Islands,

18 July 2015 02:27:33 UTC: M6.9 - Santa Cruz Islands.

The tele-seismic signals are dominated by low frequencies, meaning that the on-ice seismometers recorded only the ballistic, high-frequency-rich first-arrivals, as the rest of the signal bandwidth was below the instrument response (Fig. 10). At this preliminary stage of analysis we have not observed any evidence for increased ice-quake activity triggered by the tele-seismic surface-wave arrivals, which have previously been hypothesized as corresponding to the largest amplitude strains (Peng et al., 2014). Moreover, according to the time-lapse

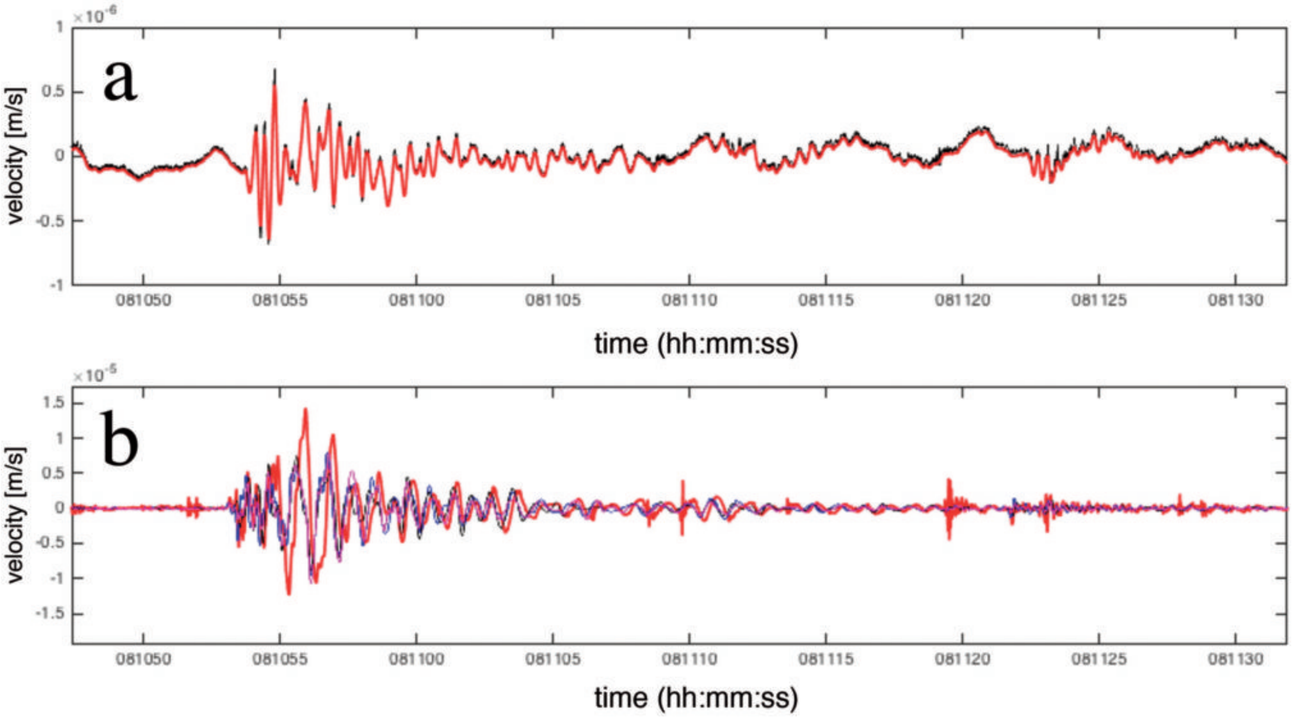

Figure 8 : (a) Long-period event that occurred on 18 July 2015, recorded at the broadband seismometer station CFH. Raw and lowpass-filtered (i.e., <5 Hz) data are shown by black and red lines, respectively. (b) The same event as recorded by the on-ice stations, after application of the same lowpass filter. Data from the LP sensor are shown in red, with SP sensor data shown in other colors.

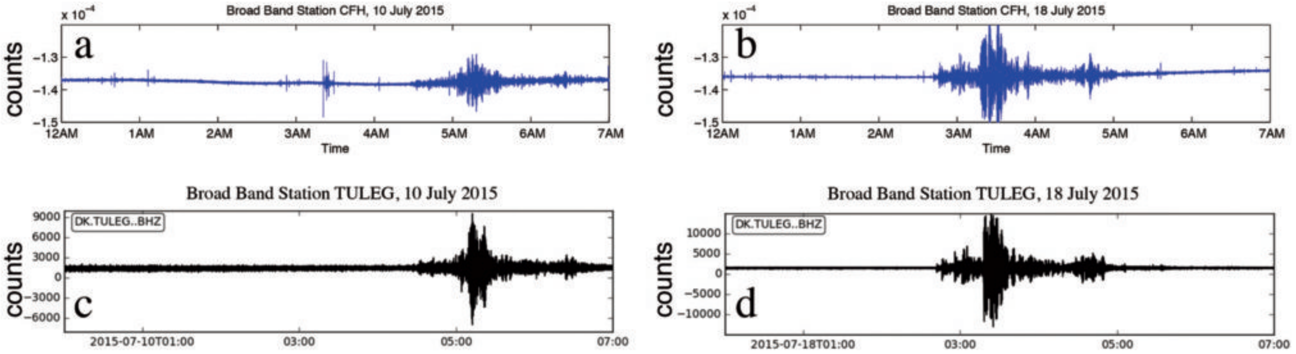

Figure 9 : (a, b) Raw traces recorded by temporary broadband station CFH for two tele-seismic earthquakes that occurred on 10 and 18 July 2015. This station was deployed on bedrock close to the calving front of Bowdoin Glacier. (c, d) Raw traces recorded on the same two days at the closest permanent broadband station TULEG (operated as part of Danish Seismological Network and GLISN), which is located ～ 120 km from the glacier (http://ds.iris.edu/SeismiQuery/by_station.html).

camera records, no calving events were observed during the passage of these long duration seismic trains through the site.

3.2.2.2 Harmonic tremor with spectral gliding

On 13 July 2015 a calving event was preceded by high-frequency harmonic tremor accompanied by spectral gliding (Fig. 11). This tremor event lasted for at least 175 s and was observed at all on-ice stations. The tremor and calving events overlapped in time for half of the calving-tremor duration (i.e., ～ 80 s). The tremor shows a downward dip in the time-frequency plane, with between ～ 16 and 19 overtones being apparent beneath the Nyquist frequency of 250 Hz. In general, the overtones were regularly spaced as $f/f_0 = $[integer]; the interval between overtones was ～ 12.2±0.7 Hz.

Previous studies of helicopter-induced tremors (e.g., Eibl et al., 2015) reported that "helicopter-generated tremor consists of regularly repeating pulses", has "fundamental frequencies above 10 Hz and overtones at integer multiples", that the "Doppler Effect causes the frequency gliding", and that "signals could be misinter-

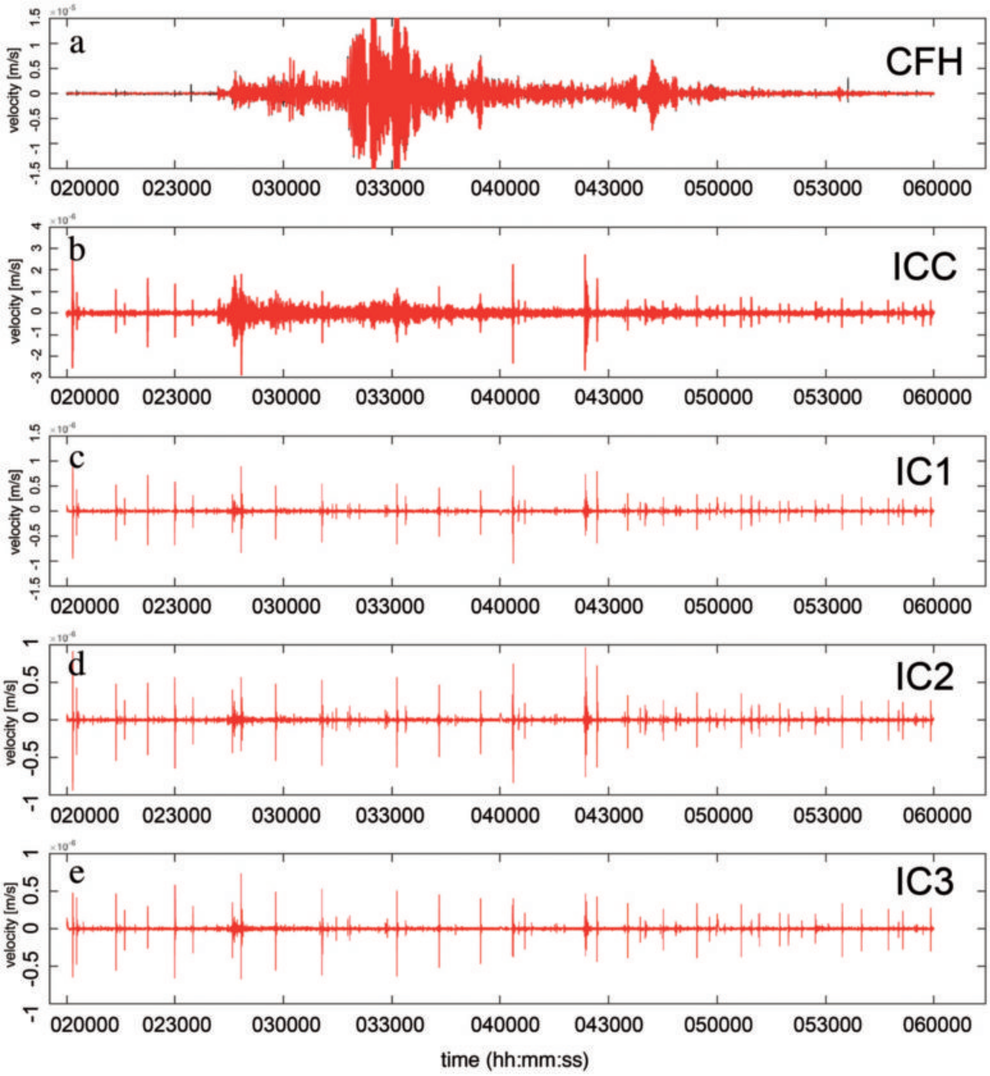

Figure 10: Low-pass filtered seismogram (i.e., <0.5 Hz) showing the tele-seismic earthquake of 18 July 2015 as recorded by the Bowdoin seismic network at (a) broadband station CFH; (b) LP on-ice station ICC; and (c, d, e) SP on-ice seismometers IC1, IC2 and IC3, respectively. The step-like impulsive feature that is visible at 4 : 00 a.m., especially in sub-panels c and d, is a boundary effect due to filtering in hourly segments and is therefore an artifact.

preted as volcanic tremor on poorly monitored volcanoes.” In this light, all of the aforementioned features indicate that this tremor was artificially generated by a helicopter’s rotor.

Helicopter activity on 13 July 2015 can be reconstructed from a diary kept by the first author and the time-lapse camera, from which the following time line can be obtained. On this day, an Air Greenland Bell 212 helicopter, with an 1800 H.P. power unit and a rotor diameter of 14.63 m, arrived at the base camp at around 15 : 58 UTC. It would appear that this initial approach towards the base camp generated the tremor that overlapped the calving event. The helicopter arrived to pick up a Swiss TV crew to fly them over the glacier terminus to film two of our members standing near the ice cliff. Later, between 16 : 32 and 16 : 45 UTC, the helicopter flew over the team members in a series of three loops. During the second fly-by, which occurred close to the seismic array, harmonic tremors were again observed (Fig. 12). It appears that before 16 : 00 UTC the calving front was partially covered with fog, which obscured this calving event from being recorded by the time-lapse camera. Members of the expedition who were staying at the central moraine near to the ice cliff (MF and SS) noted that they heard a loud calving noise. This noise emanated from a direction consistent with the back-azimuth derived from *f–k* analysis, which was directed approximately towards the section of the calving front located between the western margin and the central moraine (Fig. 13).

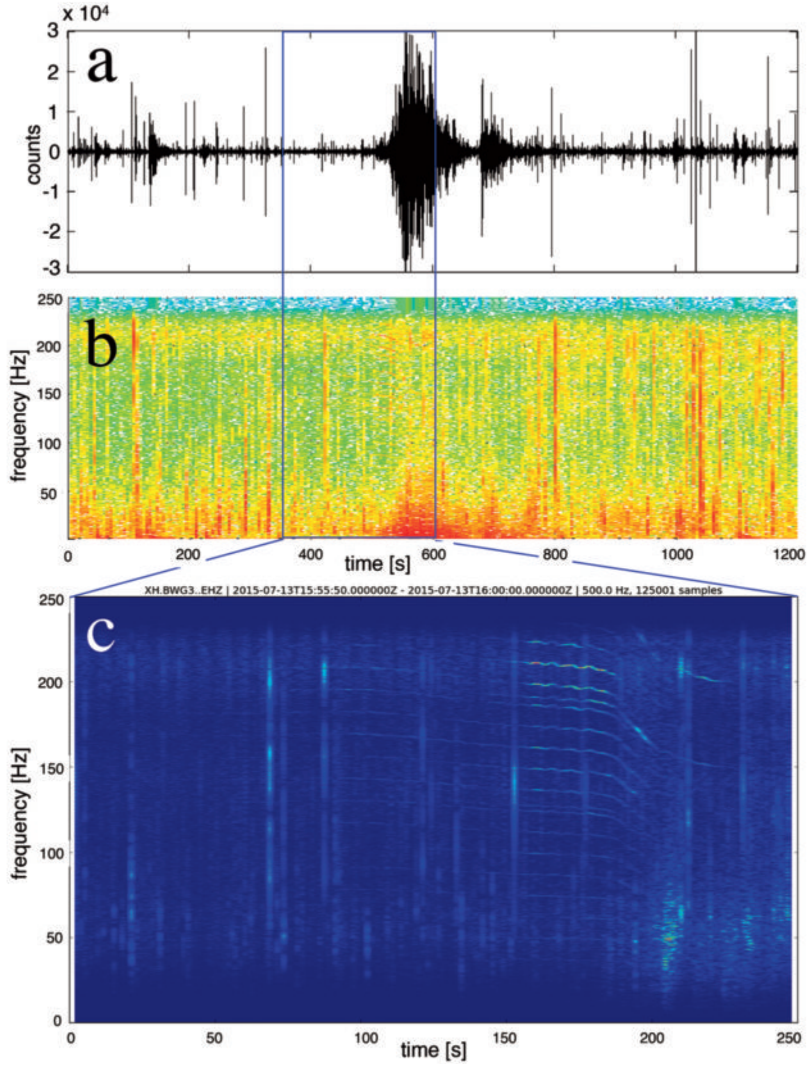

Figure 11：Raw seismic trace (a) for the interval 15 : 50–16 : 10 UTC on 13 July 2015 from station IC1, and its spectrogram (b) showing the emergent signal of the calving tremor, which is preceded by a harmonic gliding tremor with overtones. (c) Close-up of the spectrogram of the same signal after it has been bandpass filtered between 50 and 250 Hz.

3.3 Temporal variations in seismic activity

Using the classic seismological technique of short-term averaging/long-term averaging (STA/LTA), we investigate and compare the temporal variations in seismic activity detected by the SP seismometers. Details of this analysis have recently been reported by Podolskiy et al. (2016). The most striking feature was the distinct tidal modulation of micro-seismic activity over a period of two weeks. The results show a double-peak diurnal oscillation in the number of events, with a maximum of up to 600 events per hour occurring during falling or low tides. Using high-resolution GPS measurements of surface displacement, we showed that the correlation between the number of events and tidal activity is transmitted through strain-rate variation (Fig. 14). The strain rate corresponds to local extensional stretching of the glacial surface, occurring mainly in response to increases in air temperature and falling tide velocity, which reduce back-pressure on the ice cliff. The increase in extensional strain rate is favorable for tensile co-seismic fracturing. A cartoon depicting this mechanism is shown in Fig. 15. Additional details are available in the original paper (Podolskiy et al., 2016).

3.4 Infrasound events

The infrasound array (Fig. 1) operated continuously from 8 to 19 July 2015, during which time several thousand infrasound coherent signals (hereafter called "events") were recorded, emanating from various sources and directions. Analysis of these events reveals the existence of three main types of signal, with distinctive waveforms and source areas (Fig. 16). Here,

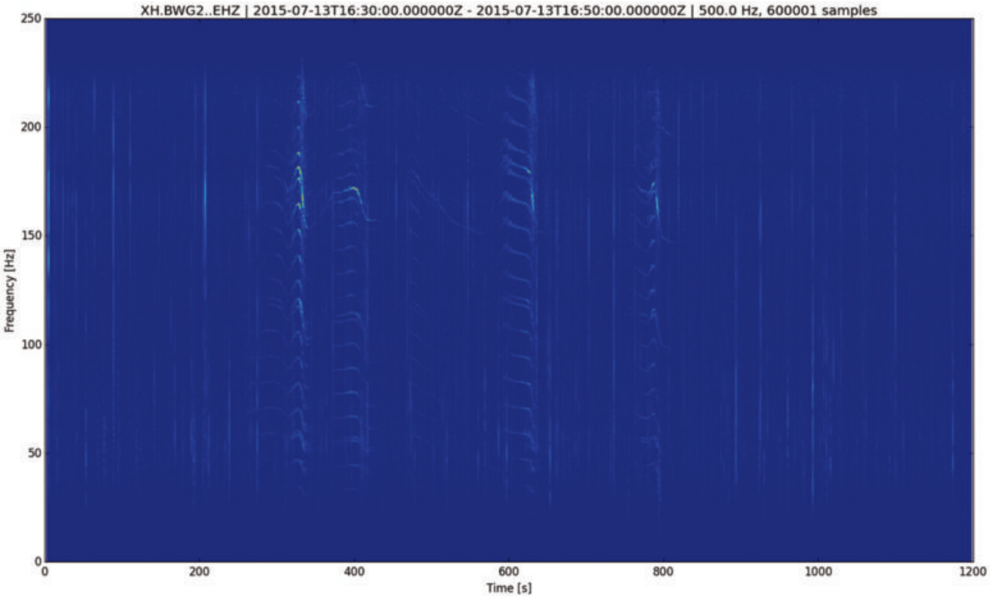

Figure 12：Spectrogram of the harmonic gliding tremor signal generated by a helicopter (recorded at station IC2 for the period 16 : 30–16 : 50 UTC on 13 July 2015 after bandpass filtering between 50 and 250 Hz).

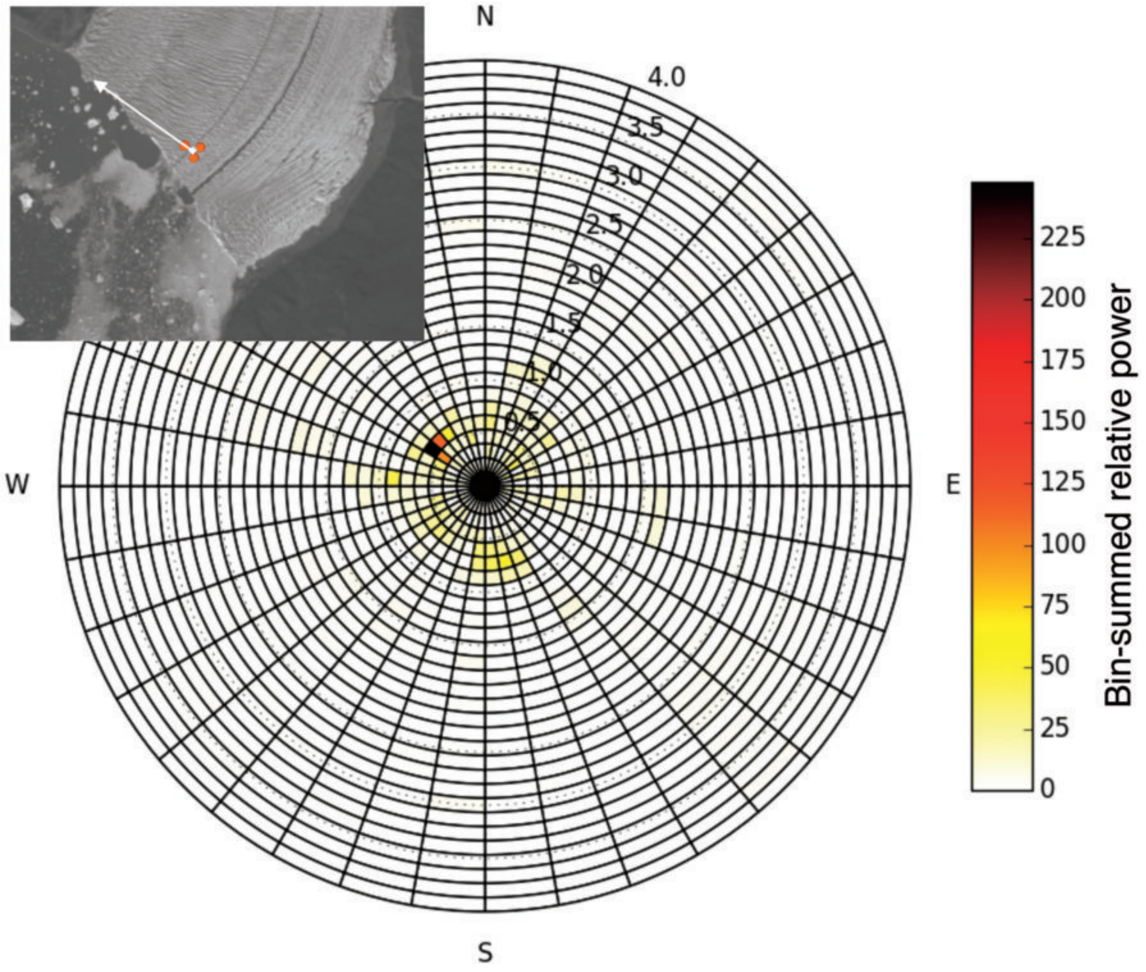

Figure 13：Polar plot showing back-azimuth and slowness for the calving event of 15 : 50 : 00–16 : 00 : 00 UTC on 13 July 2015, determined from *f–k* analysis with cumulative relative power plotted in gridded bins. The inset indicates the back-azimuth on the map.

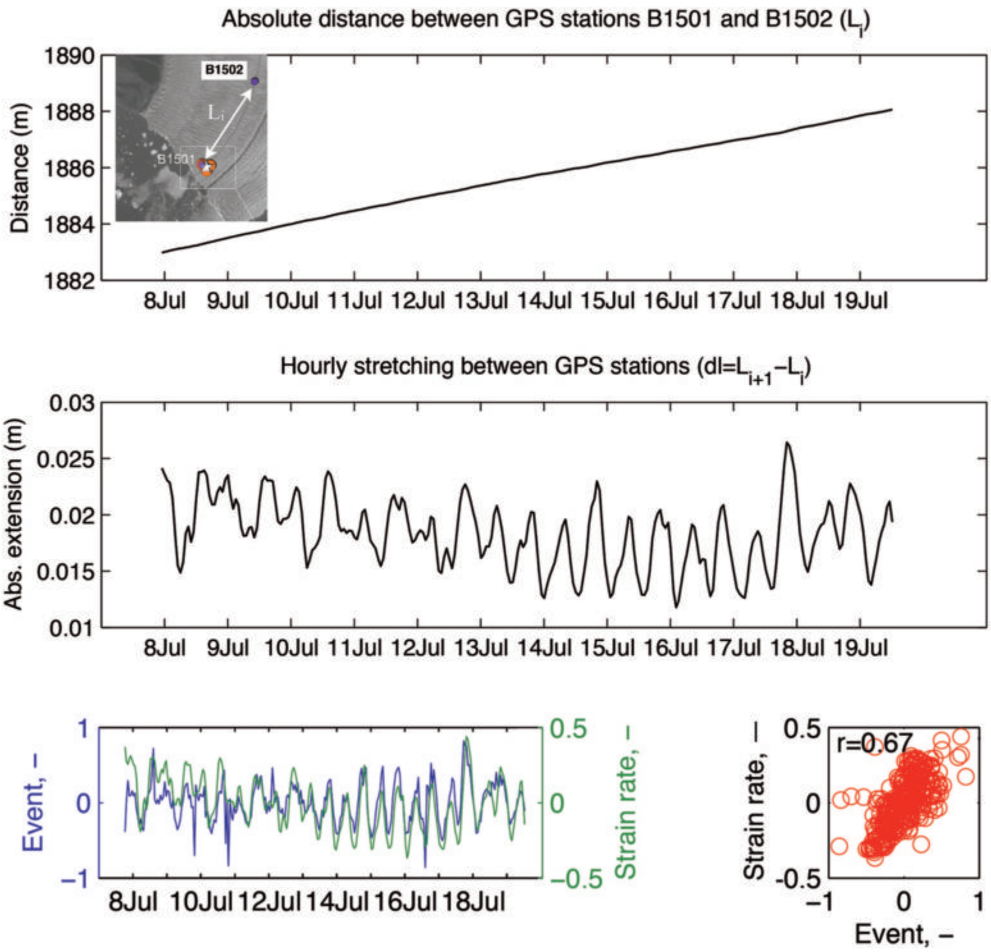

Figure 14: Absolute and hourly extension of the glacier ice surface between GPS stations B1501 and B1502. The plot at lower left shows this extensional strain as an anomaly (i.e., a deviation from the mean) against the anomaly in a number of seismic events; the scatter plot at lower right shows that the correlation coefficient between the strain and the seismic activity is 0.67 (after Podolskiy et al., 2016).

several examples of the most typical (i.e., frequent) types of infrasound events and their characteristic waveforms are briefly introduced. More detailed analyses of the infrasound activity will be published elsewhere (Genco et al., in prep.).

3.4.1 Infrasound array analysis

The full infrasound dataset was processed using multichannel cross-correlation analysis. This method allows for the automatic discrimination of coherent signals from noise using a coherency threshold (e.g., Ripepe and Marchetti, 2002) and is based on the assumption that real infrasound signals will be coherently recorded at the different sensors of the array, while noise will not show any correlation across the array (Marchetti et al., 2015). This procedure was applied to the entire dataset using a sliding window of length 3 s and a 0.3 s shift between successive windows. The data in each window are characterized in terms of the back-azimuth and apparent velocity of the energy contained within the window as well as a coherency index, which can be used to discriminate between windows containing signal and noise (Ulivieri et al., 2011). Examples of the results produced using this technique are shown in Figure 17.

The array processing technique was repeated using infrasound data filtered in different frequency bands, which revealed that the coherent signal is concentrated in the 0.5–10 Hz frequency range and shows a peak in the 1–5 Hz band, as is consistent with other observations on mass-movement-related phenomena, such as snow/ice avalanches (e.g., Bedard, 1989; Ulivieri et al., 2011) or calving events (Richardson et al., 2010). A total of ~ 13,000 detections (i.e., individual three-second windows with a coherency index exceeding the threshold) were extracted from the ~ 260 hours of continuous

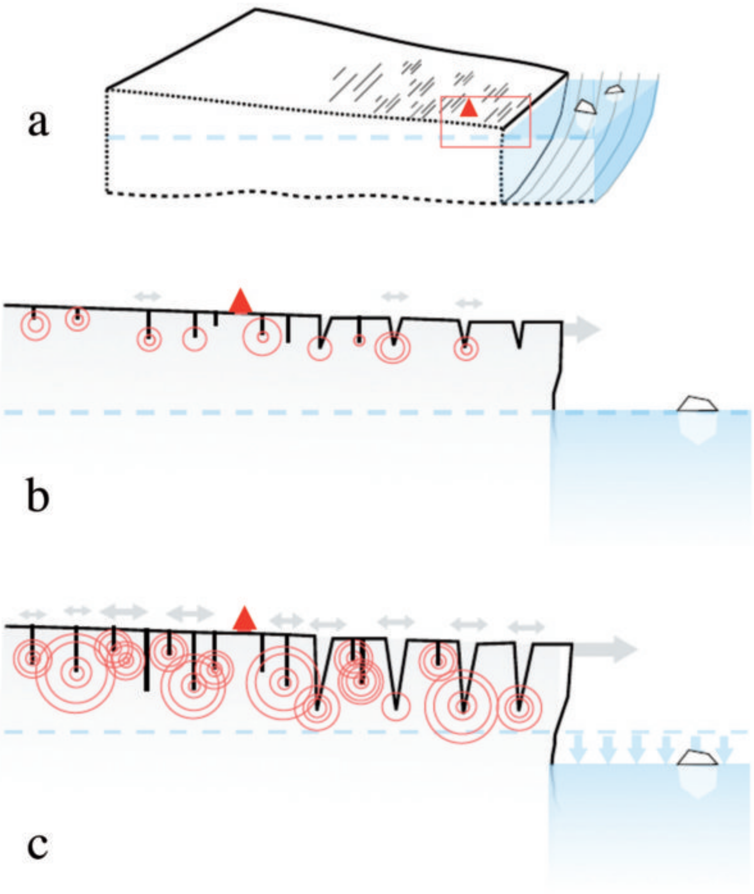

Figure 15 : Cartoon showing the dominant mechanism driving micro-seismic activity at Bowdoin Glacier: (a) longitudinal cross-section of the glacier with an on-ice seismometer shown by the red triangle; (b) the crevassed area near the calving front at high tide; (c) the same area near the calving front at low tide.

infrasound recording. Over 90% of the detections fall into three distinct back-azimuth sectors, suggesting three main source areas (Fig. 16a). Differences in waveforms, durations, and amplitudes of signals originating from these different sectors suggest the existence of different source processes for each of the observed signal types, as also confirmed by seismic data, time-lapse photography, and direct observations (Fig. 16b–c). In the following subsections, these three sources are introduced and discussed. We note that the aforementioned helicopter traverse (section 3.2.2) over some stations of our infrasound network (e.g., ICC at 16 : 34–16 : 44 UTC on 13 July 2015) also produced distinct artificial signals with clear monochromatic spectral content.

3.4.2 Calving-front events

Before introducing calving-front events, we need to remind that infrasound and seismic waves are sensitive to different source physics (Richardson et al., 2010). In general, infrasound is generated by mass acceleration leading to displacement of air volume, while seismic signals are mainly produced by release of elastic energy through brittle failure of material or slip, and, in case of calving, an interaction of icebergs with water, ice and the ocean floor (for a detailed discussion of calving seismic emissions see Podolskiy and Walter, 2016).

The largest azimuthal sector from which infrasound signals are observed, spanning back-azimuths of 220°–266° (Fig. 16c), coincides with the full extent of the Bowdoin Glacier calving front, which is situated between 2950 and 3700 m from the center of the infrasound array (Fig. 1). Despite the limited number of signals recorded in this sector (i.e., 2.2% of the total number of detections), this class of event is interesting in terms of the complexity of the recorded waveforms, duration of the events, and the amount of energy released. Analysis of the infrasound-array data identified 33 calving-front events with durations spanning from a few seconds to several minutes. Sixteen of these events are clustered

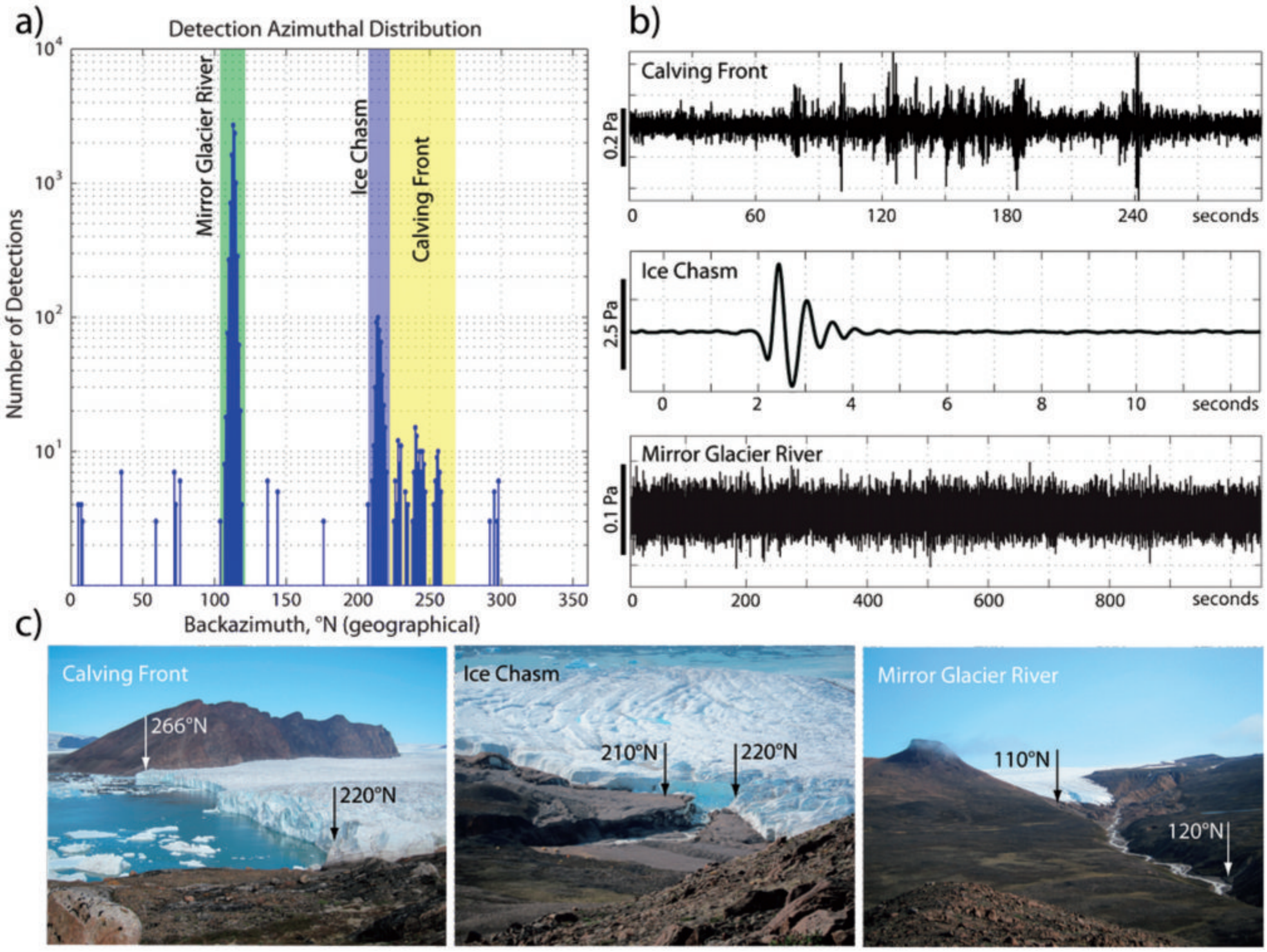

Figure 16 : (a) Number of detected infrasound events as a function of back-azimuth, with different source sectors highlighted by colored bars. (b) Example of infrasound signals produced by calving-front (top), ice-chasm (middle) and Mirror Glacier River (bottom) events. (c) Photographs of the identified source areas, annotated with back-azimuth ranges with respect to the array center, for the calving-front (left), ice-chasm (center) and Mirror Glacier River (right) events.

in three main calving episodes: July 10, 03 : 21–03 : 26 UTC; July 13, 15 : 58–16 : 03 UTC; July 18, 08 : 56–09 : 00 UTC. The other 17 events are shorter in duration and often consist of a single pulse or only a few pulses. All of the recorded events show amplitudes below 1 Pa at the HLL array, but are also clearly recorded at stations ICC and CFH with comparable amplitudes. Assuming a sound velocity of 320–330 m/s, which is reasonable for air temperatures between 0 and 10℃, the time delay between the three sites (Fig. 18) and source back-azimuth with respect to the array are compatible with a source located on the calving front. This analysis therefore provides strong evidence that calving is the process generating these events. Seismic records, time-lapse camera images and direct field observations confirmed that these infrasound signals were generated by calving events. For example, Figure 17 shows the infrasound signature of the seismic event presented in Figure 5 (i.e., July 18, 2015) for the same time window. The infrasound-array analysis provides a back-azimuth of 225–230°N, which is comparable with the source position obtained from *f–k* analysis of seismic-array data that was also validated using time-lapse photography (see section 3.2). Closer inspection of the infrasound traces reveals that each calving event, and particularly those with longer durations, consists of multiple discrete pulses of short duration that repeat at intervals of a few seconds, and sometimes merge into a continuous oscillatory phase with a duration of a few seconds. Spectral analysis shows that the main frequency content of these signals is between 0.5 and 5 Hz, peaking at ～ 2 Hz, which is consistent with seismic observations.

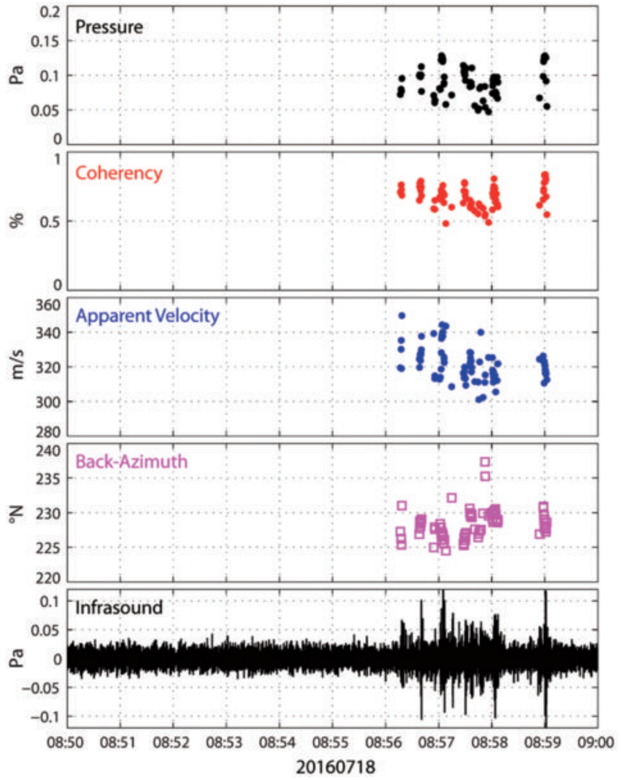

Figure 17 : Results of the multichannel cross-correlation analysis performed on infrasound data in the 1–10 Hz frequency band using a sliding window of length 3 s and a 0.3 s shift between successive windows. Acoustic pressure, coherency, apparent velocity, back-azimuth and infrasound trace data (band-pass filtered in the 1–10 Hz band) are plotted for the same time period as shown in Figure 5 (i.e., 08 : 50 : 00–09 : 00 : 00 UTC, 18 July 2015).

3.4.3 Ice-chasm events

Close to base camp, at the location where the proglacial stream emanating from the terminus of Mirror Glacier enters Bowdoin Glacier to become a subglacial stream, an ice chasm and a gorge have formed that are prone to collapse (Fig. 16c). The morphology of this ice chasm area evolved during the observation period via repeated serac falls, which produced clearly audible sounds, as well as sharp infrasound pulses that were recorded by the nearby HLL array. The more energetic ice-falls were also recorded at the more distant stations ICC and CFH. These ice-chasm events are characterized by simple waveforms that consist mainly of a single pulse, sometimes followed by a short coda of a few oscillations, with a maximum total duration of a few seconds (Fig. 16b). Peak amplitudes are generally higher than those seen for calving-related events, but are significantly reduced at stations ICC and CFH, where signals from ice-chasm events are often barely observable. Infrasound signals from these events have a spectral content that shows a strong peak at frequencies between 2 and 3 Hz. The relationship between recorded infrasound signals and this ice-chasm source process was confirmed by direct observations, which were easily made due to the proximity of the ice-chasm to the base camp.

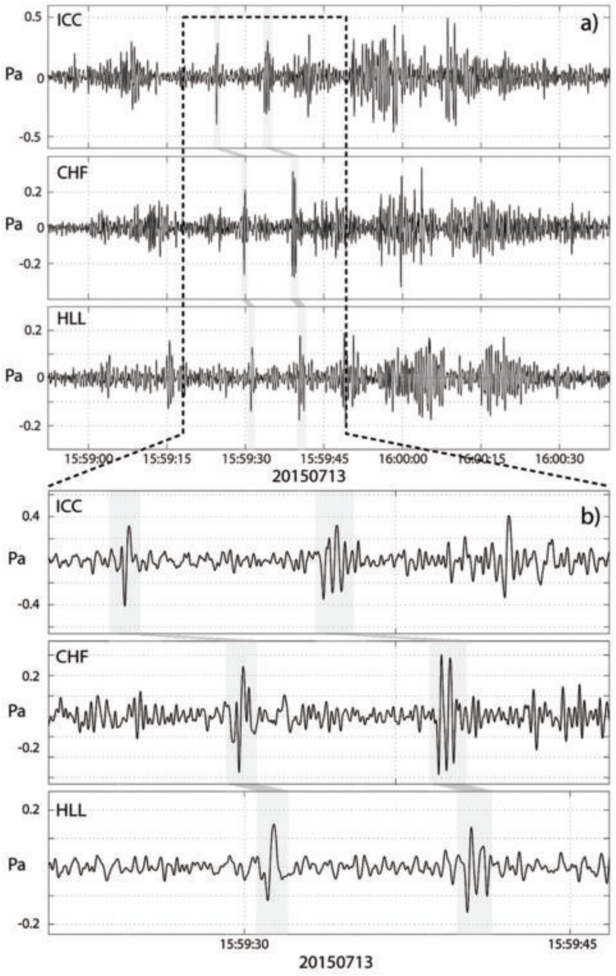

Figure 18 : (a) Infrasound signals (i.e., pressure) for the calving event of July 13, 2015 recorded at the ICC and CFH single-sensor stations and the HLL array. (b) Close-up view of the infrasound data for the highlighted time interval. Despite small differences in the character of the signal, the traces recorded at each of the three locations clearly show correlated pulses with constant time lags caused by the different source-receiver distances.

3.4.4 Mirror Glacier River events

Surprisingly, the vast majority of detected events (i.e., 87%) are associated with signals that have very small amplitudes and back-azimuths between 110 and 120°N. These azimuths are consistent with the position of a turbulent river that flows from the terminus of

Mirror Glacier (Fig. 16c). These signals are barely detectable, lack a characteristic waveform signature, have amplitudes that are comparable to the noise level, and are not continuously detected over the observation period. Rather, these signals are detected from time to time in episodes lasting a few hours, whereby the events increase in number and amplitude before eventually subsiding (detailed analysis will be published elsewhere). These events have a relatively broad frequency content in the 1–20 Hz band. The absence of a well-defined waveform signature and the emergent nature of these signals seem to suggest that these events are related to changes in stream flow, and may in fact reflect changes in the melting rate of Mirror Glacier. However, this hypothesis needs further investigation.

4. Summary and outlook

This paper presents examples of seismic and infrasound records obtained during a short but fruitful geophysical experiment in July 2015 at Bowdoin Glacier in northwest Greenland. This data set has already provided important and novel insights into glacier dynamics (Podolskiy et al., 2016). Further analysis of the unique combination of seismic, infrasound, tsunami, and geodetic time series is ongoing, and will be published elsewhere (Genco et al., in prep.; Minowa et al., in prep.; Podolskiy et al., in prep.).

Seismic signatures (or lack thereof) from a variety of processes remain to be analyzed, including subglacial water tremor, since the array was located close to a turbulent meltwater plume, and a large-scale rifting event, which presumably started on 14 July 2015 and led to the major calving event of 27 July that occurred after the field campaign was concluded (Fig. 19). The plume and the rift activity may be related through subglacial melting, which could induce an additional downward bending moment on the overhanging ice cliff.

In July 2016 a more ambitious geophysical experiment was performed at Bowdoin Glacier, with a larger number of seismic and infrasound stations, deployed near or at the glacier to obtain short- and long-term observations. Eight infrasound sensors were arranged in pairs, forming an approximately triangular array at an elevation of 460 m at Sentinel Nunatak in front of the glacier. Three time-lapse cameras and a radar were also installed. At the same time, eight seismic stations were deployed directly onto the ice in two triangular arrays. One array, consisting of four short-period Lennartz LE-3D/1s seismometers, was located approximately at the same location as in 2015 (Podolskiy et al., 2016); the other was set ~ 1.5 km up-flow of the first. This second 'upper' seismic array included one Lennartz LE-3Dlite MkIII/1s placed at the glacier surface and three Lennartz LE-3D/BHs borehole seismometers deployed at a depth of slightly less than 3 m. This depth was chosen to assure melt out in the next summer season. The seismometers were connected to DATA-CUBE[3] recorders produced by Omnirecs (a GFZ spin-off company in Potsdam, Germany), two large Cyclon or Block-Power 65 Ah batteries, and solar panels. The borehole seismic array had an aperture of ~ 250 m and will be left in situ during winter 2016/17, with the recording system switched to energy- and memory-saving modes (i.e., cycled GPS recording at 50 samples

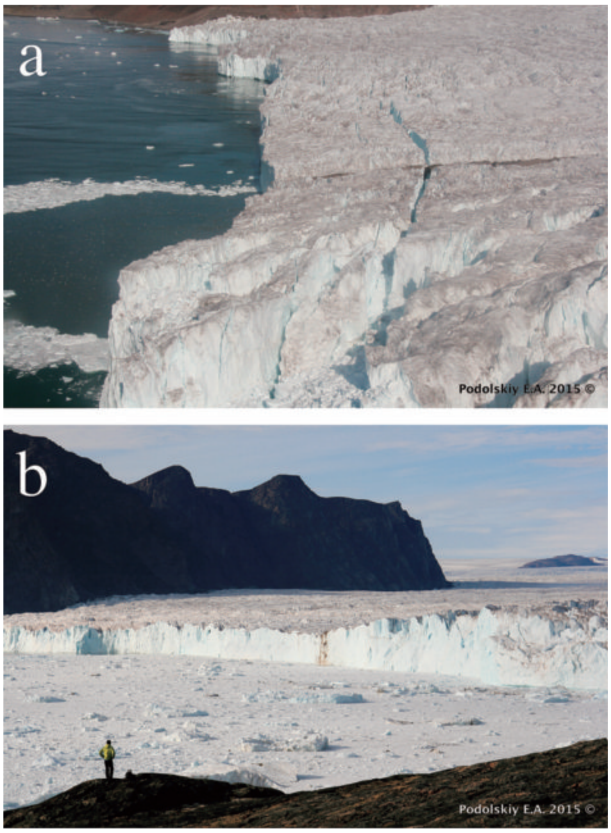

Figure 19 : Photographs of the calving front before and after the major calving event. (a) Meltwater plume and newly formed rift as seen from a helicopter on 20 July 2015; the white spots over the plume are feeding birds. (b) Calving front of Bowdoin Glacier after the calving event (28 July 2015).

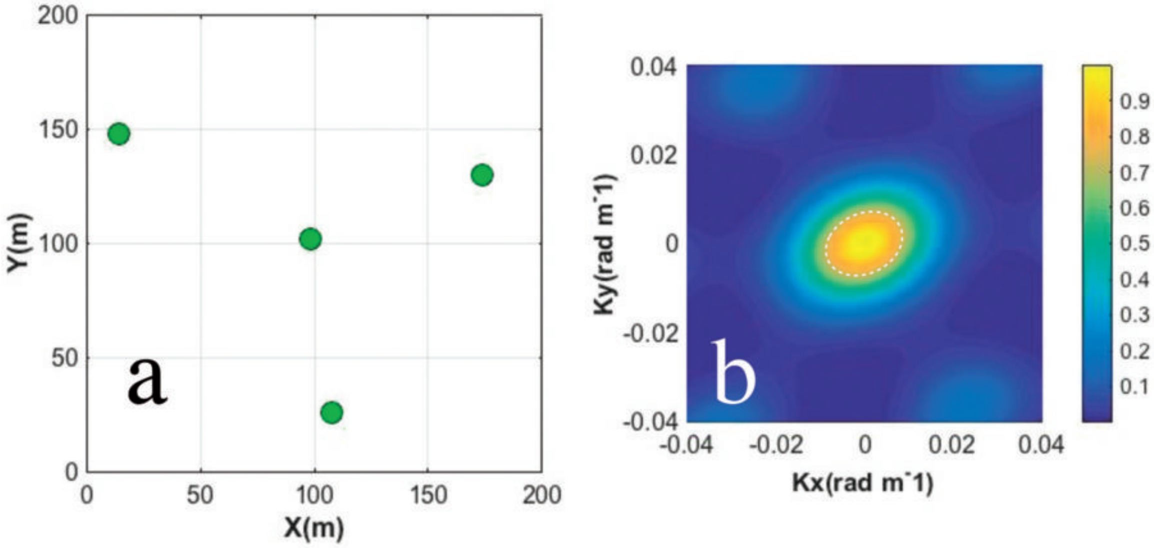

Figure A1 : (a) Geometry and (b) array response function of the Bowdoin Glacier on-ice seismic array computed at 1 Hz. Dashed ellipse indicates the resolution bounds.

per second for 4 out of every 40 minutes). Contrary to surface seismometers, the borehole sensors do not need maintenance. If the array performs well under the harsh polar-winter conditions, and instruments can be safely retrieved in July 2017, we anticipate gaining further valuable insights into long-term seasonal variations in glacier seismicity, especially related to changes in subglacial hydraulics and LP events. The experiment will also serve as an assessment of the performance of the compact, lightweight, and low-cost DATA-CUBE^3 recorders in the challenging polar environment.

Appendix A: Bowdoin array response function

For understanding examples of array analysis and its limitations, we need to introduce the array response function (ARF) of our array (Fig. A1). This function represents the resolution quality of the array for signals of different frequency and slowness (e.g., Schweitzer et al., 2002; Rost and Thomas, 2002). For the geometry of our array (Fig. A1a), the largest observable (i.e., Nyquist) wavenumber k is, in theory, less than 0.04 rad m^{-1}, which corresponds to a shortest observable wavelength of 25 m (i.e., any shorter wavelengths will alias). The shape of the main ARF lobe (Fig. A1b) indicates that the relative power of the array response shows a rapid drop in the center, meaning that energy falling into the yellow region (<0.006 rad m^{-1}) is suppressed. The longest observable wavelength is approximately equivalent to the aperture of the array, or to ~ 160 m, which means that at larger wavelengths the response of our array is equivalent to the response of any one station (i. e., all sensors are excited at the same time).

Appendix B: Tele-seismic earthquakes

The association of aforementioned tele-seismic earthquakes with particular recorded events at Bowdoin Glacier can be verified by estimating the arrival time of the fastest P wave arrivals, which were diffracted along the core-mantle boundary (i. e., the P_{diff} phase). For example, the first arrival at Thule for the signal seen on 10 July 2015 was at around 04:26:53 UTC (Fig. 10a), which is consistent with the ~ 14 minute travel-time that is predicted by the IASP91 Earth model (Fig. B1). Similarly, the first arrival at Thule on 18 July 2015 is seen at 02:41:53 UTC (Fig. 10b), which also corresponds to the expected 14 minute delay.

Acknowledgments

Some of the contents of this paper were presented by EAP and RG at the international workshop "Greenland Ice Sheet Mass Loss and its Impact on Global Climate Change", held at the Institute of Low Temperature Science, Hokkaido University (Sapporo, Japan; 22–24 March 2016). The authors acknowledge

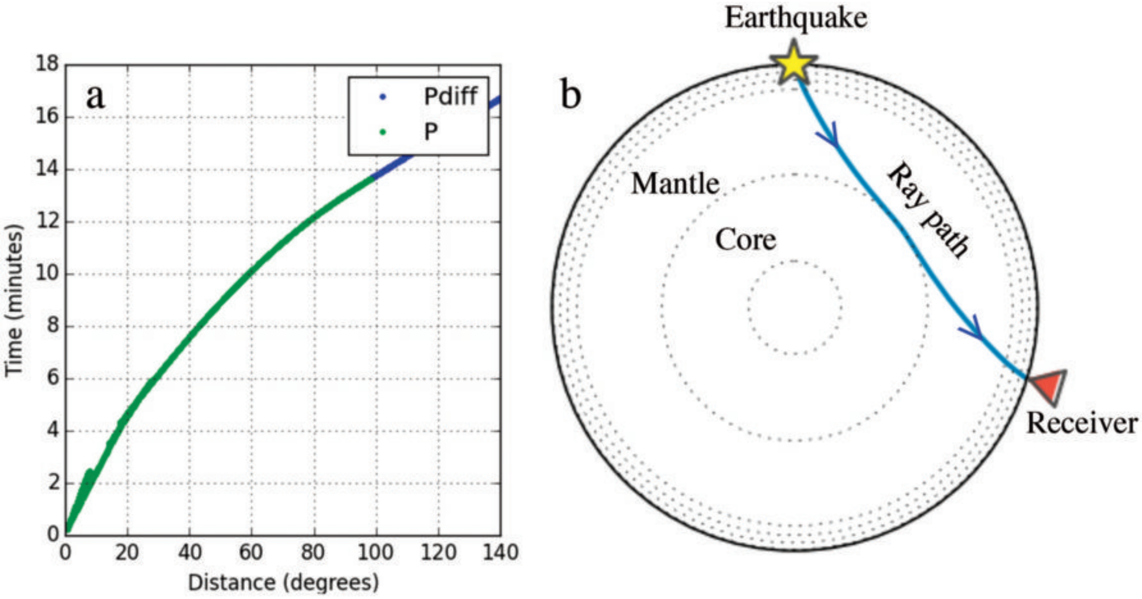

Figure B1 : (a) Travel-time curve predicting arrival time of the first seismic phase from an earthquake at a particular epicentral distance calculated using the IASP91 velocity model. In our case, source-receiver distance between epicenters in Oceania and seismic stations in the Qaanaaq region was around 107°, and the first arrival corresponded to the P_{diff} seismic phase. (b) The P and P_{diff} ray paths traced through the IASP91 velocity model.

funding from a JSPS fellowship (Grant-in-Aid PU15901), SNF grant 200021_153179/1, and the GREEN and ArCS projects. We also thank G. Lombardi for field support and the helicopter pilots of Air Greenland for their skills and logistical assistance in carrying out complex operations over the glacier surface. Signal processing and preparation of figures presented in this manuscript were performed using ObsPy, QGIS, and MATLAB software.

References

Baldwin, E. B. (1896) *The Search for the North Pole or Life in the Great White World*. Chicago, Illinois, USA.

Bartholomaus, T. C., J. M. Amundson, J. I. Walter, S. O'Neel, M. E. West, and C. F. Larsen (2015) Subglacial discharge at tidewater glaciers revealed by seismic tremor. *Geophys. Res. Lett.*, **42** (15), 6391–6398, doi: 10.1002/2015GL064590.

Bedard, A. (1989) Detection of avalanches using atmospheric infrasound. In: *Proceedings of the Western Snow Conference*, B. Shafer (ed.), Western Snow Conference, April 1989, Colorado State University, Fort Collins, CO, USA, 52–58.

Carmichael, J. D., I. Joughin, M. D. Behn, S. Das, M. A. King, L. Stevens, and D. Lizarralde (2015) Seismicity on the western Greenland Ice Sheet: Surface fracture in the vicinity of active moulins. *J. Geophys. Res. Earth Surf.*, **120** (6), 1082–1106, doi: 10.1002/2014JF003398.

Chamberlin, T. C. (1895) Appendix A: Geology. In: H. G. Bryant, *The Peary Auxiliary Expedition of 1894* (reprint from *Bulletin of Geographical Club*, No.**5**), pp.29–56.

Chamberlin, T. C. (1897) Glacial studies in Greenland. X. *J. Geol.*, **5** (3), 229–240.

Eibl, E. P. S., I. Lokmer, C. J. Bean, E. Akerlie, and K. S. Vogfjörd (2015) Helicopter vs. volcanic tremor: Characteristic features of seismic harmonic tremor on volcanoes. *J. Volcanol. Geotherm. Res.*, **304**, 108–117, doi: 10.1016/j.jvolgeores.2015.08.002.

Ekström, G., M. Nettles, and G. A. Abers (2003) Glacial earthquakes. *Science*, **302** (5645), 622–624, doi: 10.1126/science.1088057.

Ekström, G., M. Nettles, and V. C. Tsai (2006) Seasonality and increasing frequency of Greenland glacial earthquakes. *Science*, **311** (5768), 1756–1758, doi: 10.1126/science.1122112.

Hammer, C., M. Ohrnberger, and V. Schlindwein (2015) Pattern of cryospheric seismic events observed at Ekstrom Ice Shelf, Antarctica. *Geophys. Res. Lett.*, **42** (10), 3936–3943, doi: 10.1002/2015GL064029.

IPCC (2013) *Climate Change 2013: The Physical Science Basis. Contribution of Working Group I to the Fifth Assessment Report of the Intergovernmental Panel on Climate Change* (eds. T. F. Stocker, D. Qin, G. -K. Plattner, M. Tignor, S. K. Allen, J. Boschung, A. Nauels, Y. Xia, V. Bex and P. M. Midgley). Cambridge University Press, Cambridge, United Kingdom and New York, NY, USA, 1535 pp.

Khan, S. A., A. Aschwanden, A. A. Bjork, J. Wahr, K. K. Kjeldsen, and K. H. Kjaer (2015) Greenland ice sheet mass balance: a review. *Rep. Prog. Phys.*, **78** (4), 046801, doi:

10.1088/0034-4885/78/4/046801.

Kogelnig, A., E. Suriñach, I. Vilajosana, J. Hübl, B. Sovilla, M. Hiller, and F. Dufour (2011) On the complementariness of infrasound and seismic sensors for monitoring snow avalanches. *Nat. Hazards Earth Syst. Sci.*, **11**, 2355–2370, doi: 10.5194/nhess-11-2355-2011.

Lipovsky, B. P., and E. M. Dunham (2015) Tremor during ice stream stick-slip. *Cryosphere Discuss.*, **9** (5), 5253–5289, doi: 10.5194/tcd-9-5253-2015.

MacAyeal, D. R., E. A. Okal, R. C. Aster, and J. N. Bassis (2008) Seismic and hydroacoustic tremor generated by colliding icebergs. *J. Geophys. Res.*, **113** (F3), F03011, doi: 10.1029/2008JF001005.

Marchetti, E., M. Ripepe, G. Ulivieri, and A. Kiogelnig (2015) Infrasound array criteria for automatic detection and front velocity estimation of snow avalanches: towards a realtime early warning system. *Nat. Hazards Earth Syst. Sci.*, **15**, 2545–2555, doi: 10.5194/chess-15-2545-2015.

Metaxian, J. -P. (2003) Seismicity related to the glacier of Cotopaxi Volcano, Ecuador. *Geophys. Res. Lett.*, **30** (9), 1483, doi: 10.1029/2002GL016773.

Mordret, A., T. D. Mikesell, C. Harig, B. P. Lipovsky, and G. A. Prieto (2016) Monitoring southwest Greenland's ice sheet melt with ambient seismic noise. *Sci. Adv.*, **2** (5), doi: 10.1126/sciadv.1501538.

Murayama, T., M. Kanao, M. Yamamoto, Y. Ishihara, T. Matsushima, and Y. Kakinami (2015) Infrasound array observations in the Lützow-Holm Bay region, East Antarctica. *Polar Sci.*, **9** (1), 35–50, doi: 10.1016/j.polar.2014.07.005.

Lombardi, D., L. Benoit, T. Camelbeeck, O. Martin, C. Meynard, and C. Thom (2016) Bimodal pattern of seismicity detected at the ocean margin of an Antarctic ice shelf. *Geophys. J. Int.*, **206** (2), 1375–1381, doi: 10.1093/gji/ggw214.

Peng, Z. G., J. I. Walter, R. C. Aster, A. Nyblade, D. A. Wiens, and S. Anandakrishnan (2014) Antarctic icequakes triggered by the 2010 Maule earthquake in Chile. *Nat. Geosci.*, **7** (9), 677–681, doi: 10.1038/ngeo2212.

Preiswerk, L. E., F. Walter, S. Anandakrishnan, G. Barfucci, J. Beutel, P. G. Burkett, P. Dalban Canassy, M. Funk, P. Limpach, E. Marchetti, L. Meier, and F. Neyer (2016) Monitoring unstable parts in the ice-covered Weissmies northwest face. *INTERPRAEVENT 2016 – Conference Proceedings*, pp.434–443.

Podolskiy E. A. and F. Walter (2016) Cryoseismology. *Rev. Geophys.*, **54** (4), 708–758, doi: 10.1002/2016RG000526.

Podolskiy, E. A., S. Sugiyama, M. Funk, F. Walter, R. Genco, S. Tsutaki, M. Minowa, and M. Ripepe (2016) Tide-modulated ice flow variations drive seismicity near the calving front of Bowdoin Glacier, Greenland. *Geophys. Res. Lett.*, **43**, 2036–2044, doi: 10.1002/2016GL067743.

Pomeroy, J., A. Brisbourne, J. Evans, and D. Graham (2013) The search for seismic signatures of movement at the glacier bed in a polythermal valley glacier. *Ann. Glaciol.*, **54** (64), 149–156, doi: 10.3189/2013AoG64A203.

Richardson, J. P., G. P. Waite, K. A. FitzGerald, and W. D. Pennington (2010) Characteristics of seismic and acoustic signals produced by calving, Bering Glacier, Alaska. *Geophys. Res. Lett.,* **37** (3), L03503, doi: 10.1029/2009GL041113.

Ripepe, M., and E. Marchetti (2002) Array tracking of infrasonic sources at Stromboli volcano. *Geophys. Res. Lett.*, **29**, 2076, doi: 10.1029/2002GL015452.

Roeoesli, C., A. Helmstetter, F. Walter, and E. Kissling (2016) Meltwater influences on deep stick-slip icequakes near the base of the Greenland Ice Sheet. *J. Geophys. Res. Earth Surf.*, **121** (2), 223–240, doi: 10.1002/2015JF003601.

Rost, S., and C. Thomas (2002) Array seismology: Methods and applications. *Rev. Geophys.*, **40** (3), 1008, doi: 10.1029/2000RG000100.

Schweitzer, J., J. Fyen, S. Mykkeltveit, S. J. Gibbons, M. Pirli, D. Kühn, and T. Kvaerna (2012) Chapter 9: Seismic Arrays. In: Bormann, P. (ed.), *New Manual of Seismological Observatory Practice* (NMSOP-2), IASPEI, GFZ German Research Centre for Geosciences, Potsdam, doi: 10.2312/GFZ.NMSOP-2_CH9.

Sugiyama, S., D. Sakakibara, S. Tsutaki, M. Maruyama, and T. Sawagaki (2015) Glacier dynamics near the calving front of Bowdoin Glacier, northwestern Greenland. *J. Glaciol.*, **61** (226), 223–232, doi: 10.3189/2015JoG14J127.

St. Lawrence, W., and A. Qamar (1979) Hydraulic transients: a seismic source in volcanoes and glaciers. *Science*, **203** (4381), 654–656.

Ulivieri, G., E. Marchetti, M. Ripepe, I. Chiambretti, G. De Rosa, and V. Segor (2011) Monitoring snow avalanches in Northwestern Italian Alps using an infrasound array. *Cold Reg. Sci. Technol.*, **69**, 177–183, doi: 10.1016/j.coldregions.2011.09.006.

Veitch, S. A., and M. Nettles (2012) Spatial and temporal variations in Greenland glacial-earthquake activity, 1993–2010. *J. Geophys. Res.*, **117** (F4), F04007, doi: 10.1029/2012JF002412.

Walter, F., J. Chaput, and M. P. Lüthi (2014) Thick sediments beneath Greenland's ablation zone and their potential role in future ice sheet dynamics. *Geology*, **42** (6), 487–490, doi: 10.1130/G35492.1.

Weaver, C. S., and S. D. Malone (1976) Mt. Saint Helens seismic events: volcanic earthquakes or glacial noises? *Geophys. Res. Lett.*, **3** (3), 197–200.

West, M. E., C. F. Larsen, M. Truffer, S. O'Neel, and L. LeBlanc (2010) Glacier microseismicity. *Geology*, **38** (4), 319–322, doi: 10.1130/G30606.1.

Winberry, J. P., S. Anandakrishnan, D. A. Wiens, and R. B. Alley (2013) Nucleation and seismic tremor associated with the glacial earthquakes of Whillans Ice Stream, Antarctica. *Geophys. Res. Lett.*, **40** (2), 312–315, doi: 10.1002/grl.50130.

低温科学 75 （2017） 37-44
doi: 10.14943/lowtemsci. 75. 37

グリーンランド氷床北西部沿岸部における表面質量収支の変動

的場　澄人1)，山口　悟2)，對馬　あかね3)，青木　輝夫4)，杉山　慎1)

2017 年 1 月 23 日受付，2017 年 2 月 13 日受理

グリーンランド氷床北西部における数十年間の表面質量収支を明らかにすることを目的に標高 1490 m 地点と 1750 m 地点においてそれぞれ 19 m と 6.5 m 長のアイスコアを採取した．1750 m で採取されたアイスコアは全層乾雪で構成されていた．一方，1490 m 地点で採取されたアイスコアは，浅部は表面融解の影響を受けた氷板やザラメ雪層で構成されているのに対し，深部は乾雪で構成されていた．1490 m 地点の年間の表面質量収支は，融解の影響が大きくなる 2001 年以降に減少していた．この地域では，近年降水量の増加が観測されていることから，1490 m 地点では表面融解水の流出が生じている可能性が示された．

Surface mass balance variations in a maritime area of the northwestern Greenland Ice Sheet

Sumito Matoba1*, Satoru Yamaguchi2, Akane Tsushima3, Teruo Aoki4, Shin Sugiyama1

We conducted shallow ice core drillings at two sites (SIGMA-A: 1490 m a.s.l., SIGMA-A2: 1750 m a.s.l.) on the Greenland Ice Sheet to estimate the past surface mass balance for several decades. The ice cores obtained from the site SIGMA-A2 were composed of dry snow layers. In contrast, the shallower parts of the ice cores obtained from the site SIGMA-A were composed of ice layers and wet snow layers influenced by surface melt water, and the deeper parts were composed of dry snow layers. The reconstructed surface mass balance at the site SIGMA-A decreased since 2001 when melt water influence increased. Because the amount of precipitation in this region has increased recently, we suggest that the low surface mass balance since 2001 indicates that run-off of melt water from the ice sheet has occurred.

キーワード： グリーンランド氷床，表面質量収支，アイスコア，SIGMA，GRENE-北極事業
Greenland Ice Sheet, surface mass balance, ice core, SIGMA, GRENE-Arctic

1. はじめに

グリーンランド氷床の質量は，近年の温暖化の影響で減少していることが指摘されている（e.g. Rignot et al., 2011）．氷床の質量は，涵養と消耗の収支によって変化する．涵養の主要素は降水（雪）である．グリーンランド氷床の積雪および表面質量収支の観測は，1930 年代のアルフレッド・ヴェゲナーによるトラバース観測の頃から行われ，第二次世界大戦後の 1950 年代には雪上車を使用した広域な観測が行われるようになった．例えば，Benson（1960）は，氷床北西部から中部にかけて広域の観測を行い，積雪中の密度や水の安定同位体比の季節変

連絡先
的場　澄人
e-mail：matoba@pop.lowtem.hokudai.ac.jp
１）北海道大学低温科学研究所
Institute of Low Temperature Science, Hokkaido University, Sapporo, Japan
２）防災科学技術研究所雪氷防災研究センター
Snow and Ice Research Center, National Research Institute for Earth Science and Disaster Resilience, Nagaoka, Japan
３）総合地球環境学研究所
Research Institute for Humanity and Nature, Kyoto, Japan
４）岡山大学理学部
Faculty of Science, Okayama University, Okayama, Japan

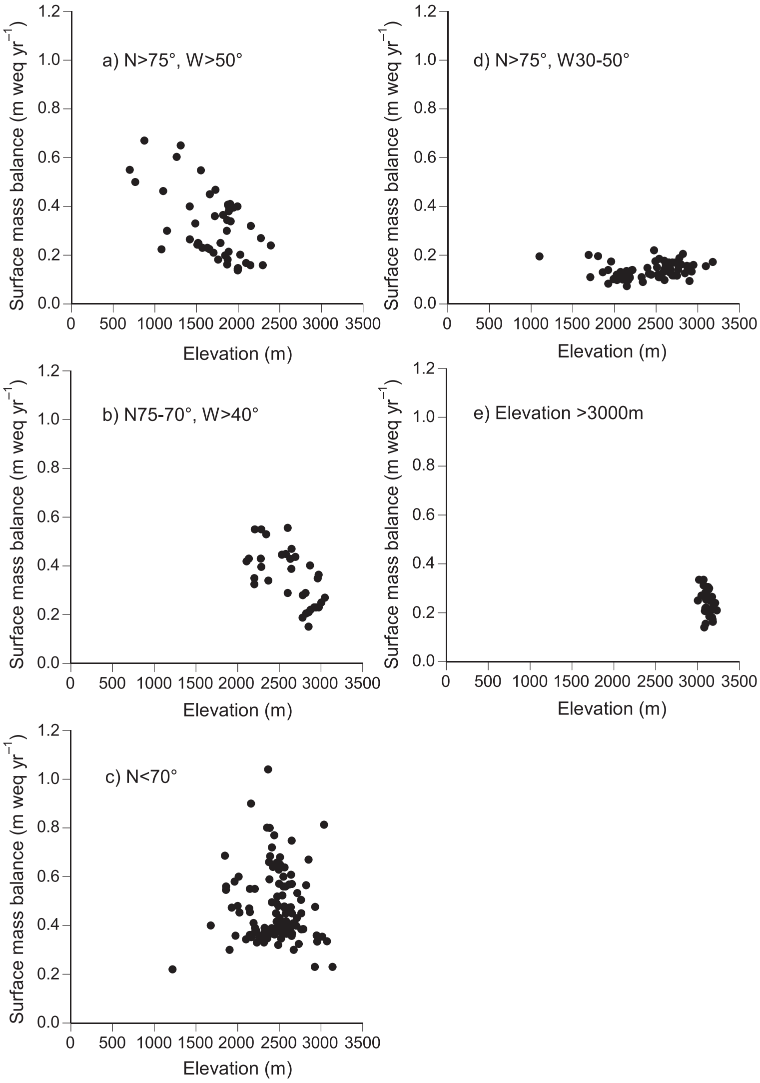

図 1：グリーンランド氷床上の標高と年間表面質量収支の関係．(a)北西部（北緯 75 度以北，西経 50 度以西），(b)中西部（北緯 70〜75 度，西経 40 度以西），(c)南部（北緯 70 度以下），(d)北東部（北緯 75 度以北，西経 30〜50 度），(e)高標高部（標高 3000 m 以上）．データは Bales et al.（2001）から引用した．

Figure 1：Relationship between elevation and annual surface mass balance of the sites in the (a) northwestern region (latitude＞75°N, longitude＞50°W), (b) central western region (latitude 70–75°N, longitude＞40°W), (c) south region (latitude＜70°N), (d) northeastern region (latitude＞75°N, longitude 30–50°W) and (e) high-elevation region (elevation＞3000 m) on the Greenland Ice Sheet. Data by Bales et al. (2001).

動からその地点の年間表面質量収支を求め，その空間分布を示した．Ohmura and Reeh（1991）は，これらの積雪観測やアイスコア解析のデータを集積し，グリーンランド氷床上の表面質量収支の空間分布を示し，気象場の季節変動との関係を議論した．1990 年代後半には，グリーンランド氷床の表面質量収支の詳細な把握を目的とした PARCA プロジェクトが実施され（e.g. Mothly-Thompson et al., 2001），アイスコアの掘削と積雪観測が新たに実施され，グリーンランド氷床の表面質量収支の新たな空間分布が示された（Bales et al., 2001）．

図 1 に，Bales et al.（2001）によって整えられたデータを用い，標高と年間表面質量収支の関係の地域的な特性を示す．北西部（北緯 75 度以北，西経 50 度以西）および西部（北緯 70〜75 度，西経 40 度以西）では標高が高くなるにつれて年間表面質量収支が減少する傾向がみられた．北東部（北緯 75 度以北，西経 30〜50 度）は標高に無関係に年間表面質量収支は低かった．南部（北緯 70 度以南）は，標高に無関係に年間表面質量収支は大きく変化した．図 2 に，Bales et al.（2001）によって報告されたグリーンランド北西部（カナック地域）の年間表面質

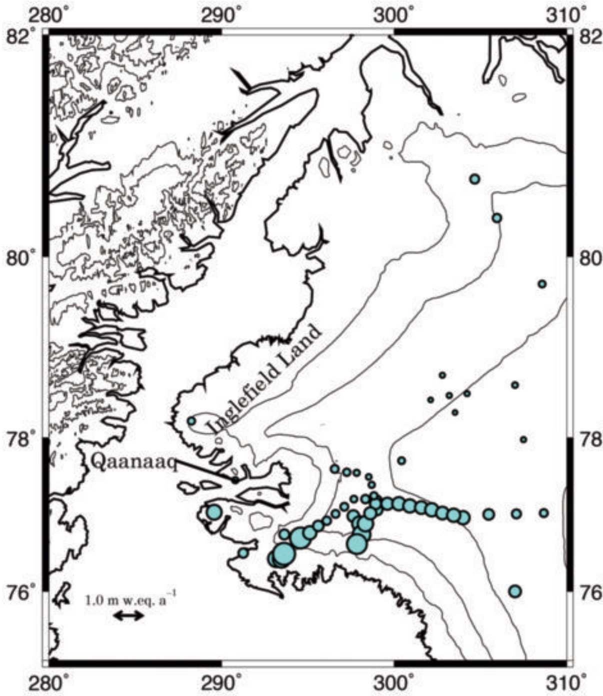

図 2：グリーンランド氷床北西部の年間表面質量収支の空間分布．図中の円の大きさはその地点の年間質量収支を示す．データは Bales et al.（2001）から引用した．

Figure 2：Spatial distribution of the annual surface mass balance of the northwestern Greenland Ice Sheet. The annual surface mass balance is indicated by the size of the circles. Data by Bales et al. (2001).

量収支の観測値の空間分布を示す．年間表面質量収支は南側の半島（Hays 半島）において高く，緯度が上がるにつれて減少する傾向を示した．これは，Ohmura and Reeh（1991）で示された，メルビル湾に発達する低気圧によって南から水蒸気が輸送されて降水が生じる大気循環場と整合的である．また，この地域の表面積雪中の水同位体比と化学成分濃度の広域分布から水と物質の循環を議論した Matoba et al.（2014）の結果とも整合的である．

この地域では，2011 年から，氷床の質量収支とそれに関連する氷床表面融解プロセスや氷山分離に着目した研究プロジェクト，SIGMA（Snow impurity and glacial microbe effect on abrupt warming in the Arctic）プロジェクトと GRENE 北極事業（Green network of excellence Arctic climate change research project）が開始された（Aoki et al., 2014; Sugimaya et al., 2014, 2015）．図 2 に示された年間表面質量収支の観測データは，チューレ米空軍基地から南へ進んだトラバースルート上に集中しており，これらのプロジェクトが対象としているカナック村やシオラパルク村がある北側の Inglefield Land を含む半島では観測データが殆どない．これらのプロジェクトの元では，2012 年から 2013 年にかけてグリーンランド氷床北西部において積雪・気象観測が行われ，この地域における過去数十年間の環境変動復元を目的に，ハンドオーガーを用いて 2 カ所でアイスコアが掘削された（Aoki et al., 2014; Yamaguchi et al., 2014）．本研究は，これらのアイスコアの解析結果から復元されたこの地域の過去数十年間の表面質量収支の変化について議論する．

2．試料採取と化学分析

図 3 に観測サイトを示す．2012 年 6，7 月に，グリーンランド氷床北西部 SIGMA-A サイト（北緯 78 度 3 分 6 秒，西経 67 度 37 分 42 秒，標高 1490 m）において実施された積雪・気象観測において（e.g. Aoki et al., 2014），この地点における過去数十年間の環境復元を目的に，ハンド-オーガーを用いて 19 m 長の表層アイスコアが採取された（Yamaguchi et al., 2014）．掘削後，アイスコアの密度を測定し，氷板の分布を記載した後，清浄なナイフで試料を 5 から 10 cm 長に分割し，作業中に試料の表面に付着した汚染を除去した後，清浄なポリエチレン袋（Whirl-pak）内で融解させ，清浄なポリプロピレン瓶に保存した．アイスコアは，2 日間に分けて採取され，測定と融解処理は掘削後直ちに行われた．

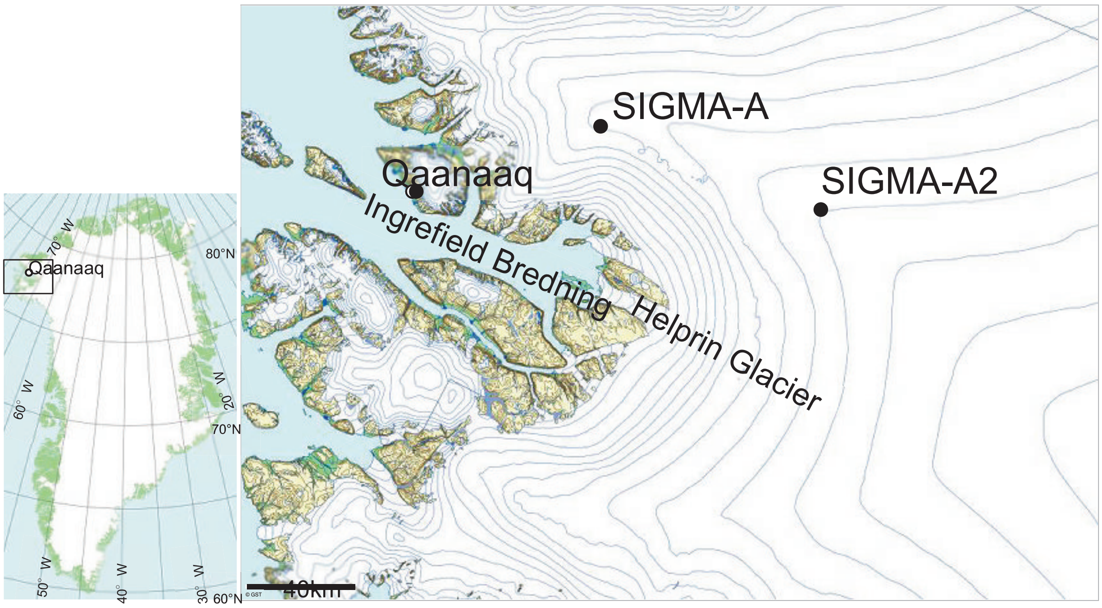

図3：観測サイトの位置.
Figure 3：Location of the study area.

2013年7月には，SIGMA-A2サイト（北緯78度6分13秒，西経64度4分59秒，標高1750 m）において，ハンドオーガーを用いて6.5 m長のアイスコアが採取された（Aoki et al., 2014）．掘削後，密度を測定し，氷板の分布を記載した後，ステンレス製のナイフで試料を5から10 cm長に分割し，作業中に試料の表面に付着した汚染を除去した後，清浄なポリエチレン袋（Whirl-pak）に密封した．掘削及び処理はヘリコプターを氷床上に待機させ，2時間あまりの間に行った．試料はカナック村に持ち帰り，室内で融解させ，清浄なポリプロピレン瓶に保存した．

試料は常温でグリーンランドから日本まで輸送し，日本に到着後直ちに凍らせ，化学分析まで冷凍で保存された．

試料中の溶存イオン種濃度は，イオンクロマトグラフィー（ICS-2100，Thermo Scientific社）によって測定した．陽イオンの測定には，分離カラムにCS-12A（Thermo Scientific社）を用い，溶離液には20 mMのメタンスルホン酸を用いた．試料はオートサンプラーで1 mL注入した．これらの条件において検出限界は約5 μg L^{-1}である．陰イオンの測定には，分離カラムにAS-14A（Thermo Scientific社）を用い，溶離液には23 mM水酸化ナトリウム溶液を用いた．試料はオートサンプラーで500 μL注入した．これらの条件おいて検出限界は約10 μg L^{-1}である．

試料中の水の安定同位体比は，レーザーキャビティーリングダウン分光法を用いた同位体比分析装置（Picarro社，L-2120i）に高速蒸気化装置（Picarro社，A0212）にて蒸気化させた試料を導入して測定した．分析精度はδDが±0.6～1.0‰，δ^{18}Oが±0.08～0.1‰であった．

3. 結果と考察

図4にSIMGA-Aサイトで採取されたアイスコアの約5 m深（水当量深度2.4 m）と約15 m深（水当量深度8.0 m）で採取されたアイスコアの写真を示す．また，図5にアイスコア10 cm中に含まれる氷板の厚さの割合の鉛直プロファイルを示す．5 m深のアイスコアの写真が示すように，アイスコアの浅層部は融解水の影響で氷板が形成され，フィルンの部分も粒径の大きいザラメ雪で構成されていた．一方，深部のアイスコアには氷板は殆ど観察されず，フィルンを形成する積雪の粒径も小さい「乾いた」雪で構成されていた．

図6にSIGMA-Aサイトで採取されたアイスコア中のδDの深さプロファイルを示す．一般的に極域の降雪中の水同位体比は気温によって変動し，夏に高い値を示すことが知られている．このサイトにおいても，同様な変動を示すことが考えられ，δDは明瞭な季節変動を示していると考えることができる．水素同位体比の負のピークを一年の始まりとしてアイスコアの年代を推定した．その結果，19 m深までのアイスコアは1974年から2011年までの期間に堆積した積雪であると推定された．負のピークと負のピークの距離を，アイスコアの密度を用いて水当量に換算した値を年間の質量収支とした．

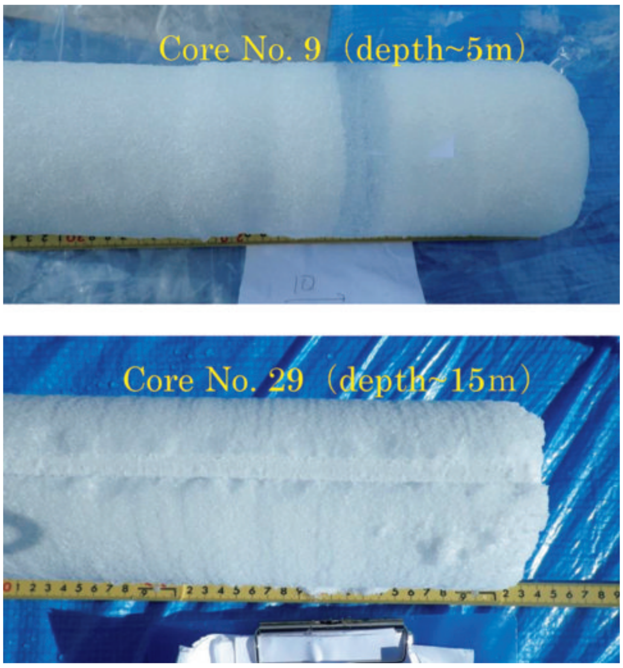

図 4：SIGMA-A サイトで採取されたアイスコアの約 5 m 深（上）と約 15 m 深（下）の接写写真.
Figure 4：Photographs of ice cores at 5 m depth (top) and 15 m depth (bottom) obtained from the SIGMA-A site.

図 7 に SIGMA-A2 サイトで採取されたアイスコア中の δD のプロファイルを示す．SIGMA-A コアに比べ，試料の採取間隔が広いために季節変動は明瞭ではないが確認することができ，2011 年から 2002 年に堆積した積雪であると推定された．

図 8a，b に SIGMA-A コアの各年層中に含まれる氷板の厚さの総量と年層厚の経年変化を示す．融解再凍結が生じたことを示す氷板は，1985 年以前には殆ど観察されず，1990 年代以降，氷板の厚さの総量が増加する傾向が現れた．また氷床の表面融解を生じた面積が大きかったと報告されている 2007 年に最大値を示した．表面質量収支に相当する年層厚は 1975 年から 2010 年までの平均値が 0.27 m w.eq. yr^{-1} であり，1975 年から現在にかけて減少する傾向を示し，特に 2001 年以降は低い値を示した．氷板が観察されなかった 1985 年以前の平均年層厚は 0.36 m w.eq. yr^{-1}，2001 年以降は 0.18 m w.eq. yr^{-1} だった．図 8c に SIGMA-A2 サイトで採取されたアイスコアから復元した年層厚の経年変化を示す．2002 年から 2011 年までの平均表面質量収支は 0.24 w.eq. yr^{-1} だった．SIMGA-A コアと復元される期間が異なるため，単純に比較はできないが，SIMGA-A コアで見られた 2001 年以降の年層厚の急激な減少に対応する変化は

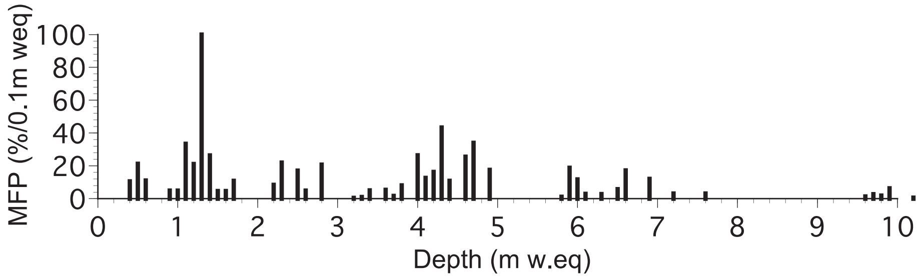

図 5：SIGMA-A で採取されたアイスコアの MFP（Melt Feature Percentage）のプロファイル．MFP は，アイスコア 0.1 m 水当量深度あたりの氷板の厚さを示す．
Figure 5：Vertical profile of MFP (Melt Feature Percentage) of the ice core obtained from the SIGMA-A site. MFP is shown by percentage of ice layer thickness in 0.1 m weq. of the ice core.

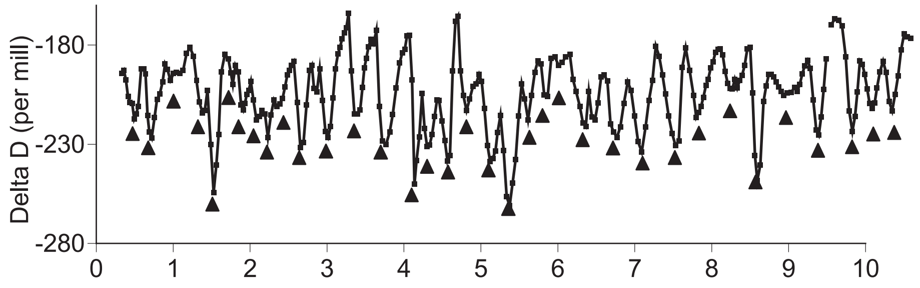

図 6：SIGMA-A サイトで採取されたアイスコア中の δD のプロファイル．図中の三角形（▲）は年層の境界として同定された δD の負のピークを表す．
Figure 6：δD profile of the ice core obtained from the SIGMA-A site. Solid triangles indicate minimum δD peaks identified as annual boundary layers.

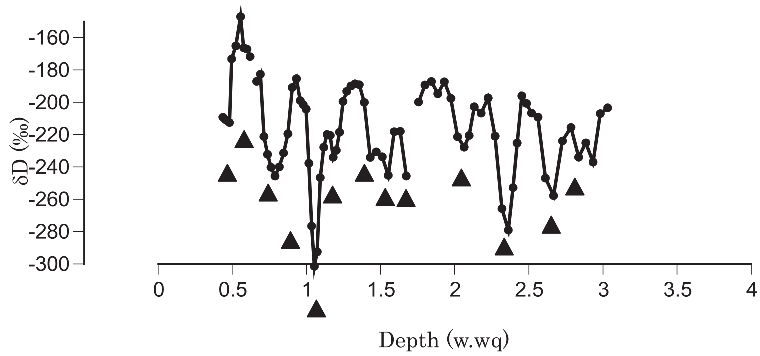

図 7：SIMGA-A2 サイトで採取されたアイスコア中の δD のプロファイル．図中の三角形（▲）は年層の境界として同定された δD の負のピークを表す．
Figure 7：δD profile of the ice core obtained from the SIGMA-A2 site. Solid triangles indicate minimum δD peaks identified as annual boundary layers.

見られず，2006～2009 年の期間に年層厚が減少する傾向が見られた．両サイトで復元された年間表面質量収支の値は，図 1 に示した先行研究で報告された値の範囲内にある（e.g. Bales et al., 2001）．

図 8d にグリーンランドチューレ空軍基地（サイト名 Pituffik，北緯 76 度 31 分 59 分，西経 68 度 45 分 00 秒，標高 77 m）で観測された年間降水量の経年変化を示す．この年間降水量は，米国海洋大気庁の National Center for Environmental Information のウェブサイトで公開されている降水量の月平均値のデータから算出した．取得されているデータは 1982 年から 2006 年まであるが，SIGMA-A コアの年層厚に見られたような減少傾向はなく，むしろ増加している傾向が現れた．

チューレ空軍基地で観測された降水量の増加傾向が北西グリーンランド全域で見られるトレンドだとすると，SIGMA-A サイトのアイスコアで見られた年層厚の減少傾向は，SIGMA-A サイトで消耗量が増加していることを示している．SIGMA-A サイトにおいて消耗に関与する現象は，融解水の流出，昇華，削剥が考えられる．昇華と削剥については，詳細な気象データを用いた解析が必要であり，現時点ではそのような解析に足るデータがないため，ここでは融解水の流出についてのみ考察をする．SIGMA-A サイトは，20 m 深の雪温は −20℃と充分に低く（Yamaguchi et al., 2014），夏季に表面で生じた融解水が積雪内に浸透して再凍結して氷板を形成する，いわゆる浸透帯に属する（Benson, 1960; Müller, 1962）．氷体温度が充分低いため，融解水が積雪カラムから流出することは通常は考えづらい．しかし，2012 年 7 月に行われた観測では，前年に形成された氷板の上の 2011 年冬期から 2012 年春期に堆積した積雪層が，激しい表面融解のために融解水が浸透し，全層がザラメ雪層になり全層にわたり雪温が 0 度になることが観測された（Yamaguchi et al., 2014）．そのとき，2011 年に形成された氷板は浸透した融解水によって融解することはなく，融解水が氷板上に帯水していた．つまり，表面融解水の一部はその年の積雪層内で再凍結せず，前年に形成された氷板上を移動し，積雪カラムから流出していた可能性がある．従って，SIGMA-A アイスコアから復元された年層厚の近年の減少は，この地域では表面融解量が増加し，融解水の一部が積雪層内から流失したことが要因であると推測できる．

謝辞

SIGMA-A，SIGMA-A2 での観測に参加された皆様に感謝いたします．この研究は，SIGMA プロジェクト（代表：青木輝夫，JSPS 科研費 JP23221004）及び GRENE 事業北極気候変動分野の共同研究にて行われた．また，JSPS 科研費 JP26400460 及び北海道大学低温科学研究所共同研究の助成をうけた．

References

Aoki, T., S. Matoba, J. Uetake, N. Takeuchi, and H. Motoyama (2014) Field activities of the “Snow Impurity and Glacial Microbe effects on abrupt warming in the Arctic” (SIGMA) project in Greenland in 2011-2013. *Bull. Glaciol. Res.*, **32**, 3-20.

Bales, R. C., J. R. McConnell, E. Mosley-Thompson, and B. Csatho (2001) Accumulation over the Greenland ice sheet from historical and recent records. *J. Geophys. Res.*, **106** (D24), 33813-33825.

Benson, C. S. (1960) Stratigraphic studies in the snow and firn of the Greenland Ice Sheet. Ph. D. thesis, California Institute of Technology.

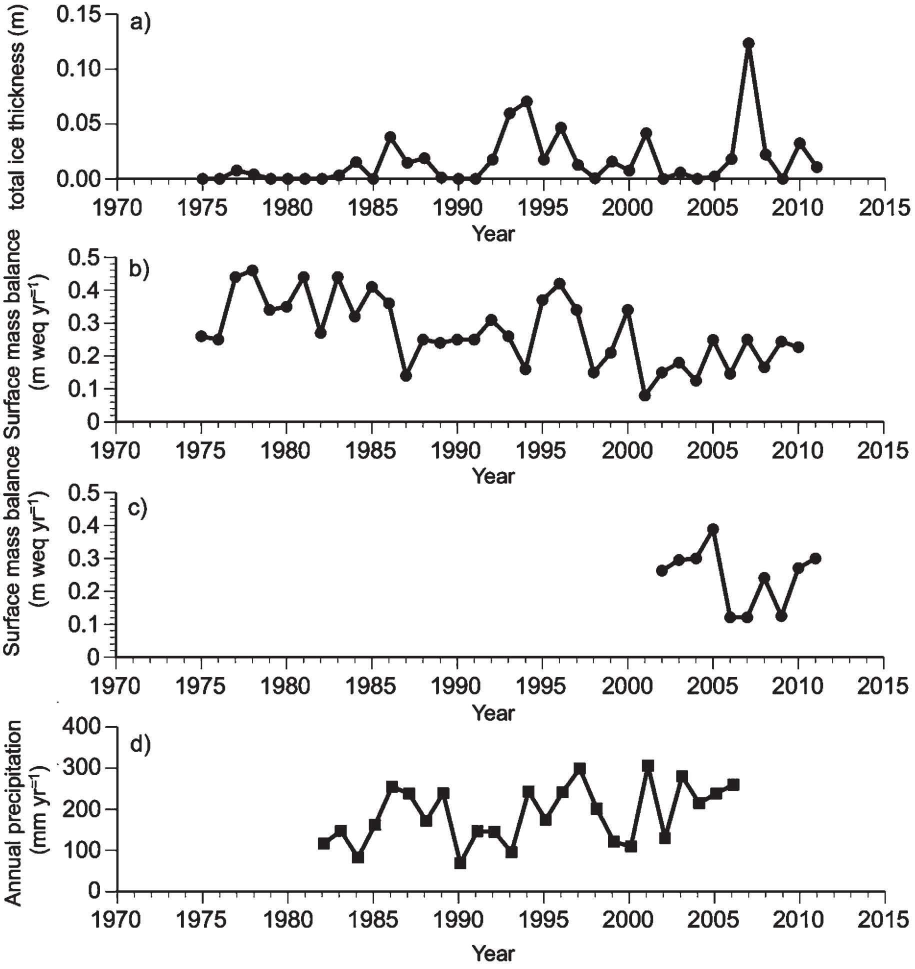

図 8：SIGMA-A サイトで採取されたアイスコアから復元された，(a)年層に含まれる総氷板厚さ，(b)年間表面質量収支，(c)SIGMA-A2 サイトで採取されたアイスコアから復元された年間表面質量収支，(d)チューレ空軍基地（北緯 76 度 31 分 59 秒，西経 68 度 45 分 00 秒，標高 77 m）で観測された年間降水量の時系列変化．チューレ空軍基地の降水量データは，アメリカ合衆国のアメリカ海洋大気庁 National Center for Environmental Information が提供しているデータ（観測サイト名 Pituffik，サイト番号 GHCND：GLE00146841）を使用した．

Figure 8：Temporal variations of (a) total ice layer thickness in annual layers, (b) reconstructed annual surface mass balance at the SIGMA-A site by the ice core, (c) reconstructed annual surface mass balance at the SIGMA-A2 site by the ice core, and (d) annual precipitation at Thule Air Base (76°31′59″N, 68°45′00″W, elevation 77 m, station name: Pituffik, station number: GHCND: GLE00146841 of the National Center for Environmental Information, National Oceanic and Atmospheric Administration, United States of America).

Matoba S., T. Yamasaki, and H. Motoyama (2014) Spatial variations of δ^{18}O and ion species in the snowpack of the northwestern Greenland ice sheet. *Bull. Glaciol. Res.*, **32**, 79–84.

Mosley-Thompson, E., J. R. McConnell, R. C. Bales, Z. Li, P.-N. Lin, K. Steffen, L. G. Thompson, R. Edward, and D. Bathke (2001) Local to regional-scale variability of annual net accumulation on the Greenland ice sheet from PARCA cores. *J. Geophys. Res.*, **106** (D24), 33839–33851.

Müller, F. (1962) Zonation in the accumulation area of the glaciers of Axel Heiberg Island, N. W. T., Canada. *J. Glaciol.*, **4**, 301–313.

Ohmura, A. and N. Reeh (1991) New precipitation and accumulation maps for Greenland. *J. Glaciol.*, **37**(125), 140–148.

Rignot, E., I. Velicogna, M. R. van den Broeke, A. Monaghan, and J. T. M. Lenaerts (2011) Acceleration of the contribution of the Greenland and Antarctic ice sheets to sea level rise. *Geophys. Res. Lett.*, **38**, L05503.

Sugiyama, S., D. Sakakibara, S. Matsuno, S. Yamaguchi, S. Matoba, and T. Aoki (2014) Initial field observations on Qaanaaq Ice Cap in northwestern Greenland. *Ann.*

Glaciol., **55**(66), 25–33.

Sugiyama, S., D. Sakakibara, S. Tsutaki, M. Maruyama, and T. Sawagaki (2015) Glacier dynamics near the calving front of Bowdoin Glacier, northwestern Greenland. *J. Glaciol.*, **61** (226), 223–232.

Yamaguchi, S., S. Matoba, T. Yamasaki, A. Tsushima, M. Niwano, T. Tanikawa, and T. Aoki (2014) Glaciological observation in 2012 and 2013 at SIMGA-A site, Northwest Greenland. *Bull. Glaciol. Res.*, **32**, 95–105.

低温科学 75 （2017） 45-52
doi: 10.14943/lowtemsci. 75. 45

グリーンランド南東ドームにおける浅層アイスコア掘削と初期物理解析

飯塚　芳徳1)，的場　澄人1)，藤田　秀二2)，新堀　邦夫1)，山崎　哲秀3)，宮本　淳4)，
堀　彰5)，斉藤　健1)，古川　崚仁1)，杉山　慎1)，青木　輝夫6)

2016 年 10 月 28 日受付，2017 年 1 月 16 日受理

グリーンランドにおける高涵養量域の圧密氷化過程の特徴の解明や近年の人為起源エアロゾルの変遷の解読を目的として，2015 年 5 月にグリーンランド南東ドームにおいて，90.45 m の浅層コア掘削を実施した．掘削地点はタシーラク（アンマサリック）から 185 km 北に位置している（SE-Dome；67.18°N，36.37°W，3170 m a.s.l.）．掘削孔の氷温は 20 m 深において－20.9℃であった．2015 年 8 月にコアが日本に輸送され，低温科学研究所の低温室において密度測定や電気伝導度測定などの初期コア解析が行われた．その結果，SE-Dome コアの氷化深度は 83-86 m，涵養量は約 1.0 m w.e. yr^{-1} であった．SE-Dome コアは氷床のドームとしては最も高涵養量の地域の一つである．圧密氷化過程を調べたところ，750 kg m^{-3} 以上の密度域において，SE-Dome コアは通常の涵養量地域の浅層コアよりも変形しやすい特徴を持つことが分かった．

Shallow ice core drilling and preliminary analysis at South-East Dome, Greenland

Yoshinori Iizuka[1]*, Sumito Matoba[1], Shuji Fujita[2], Kunio Shinbori[1], Tetsuhisa Yamasaki[3],
Atsushi Miyamoto[4], Akira Hori[5], Takeshi Saito[1], Ryoto Furukawa[1], Shin Sugiyama[1], Teruo Aoki[6]

In order to understand 1) temporal variations of anthropogenic aerosols from European regions under the Icelandic Low with high time resolution, and 2) the snow densification mechanism at a high accumulation dome in Greenland, we drilled a 90.45 m ice core in a high accumulation area of the southeastern Greenland Ice Sheet. The drilling site (SE-Dome; 67.18°N, 36.37°W, 3170 m a.s.l.) is located 185 km north of the town of Tasiilaq in southeastern Greenland. The ice temperature is −20.9℃ at 20 m depth, and the site has an average accumulation rate of 1.0 m w.e. yr^{-1} in water equivalent. The ice core exhibits distinct firn densification. The close-off density of 830 kg m^{-3} occurs at 83.4-86.8 m depth, which is about 20 m shallower than predicted from an empirical model. In the region where the density $\rho > 750$ kg m^{-3}, the densification appears faster than according to the empirical model.

キーワード：グリーンランド氷床，南東ドーム，アイスコア，圧密氷化
Greenland Ice Sheet, South-East Dome, ice core, snow densification

---

連絡先
飯塚　芳徳
e-mail：iizuka@lowtem.hokudai.ac.jp
１）北海道大学低温科学研究所
Institute of Low Temperature Science, Hokkaido University, Sapporo, Japan
２）大学共同利用機関法人　情報・システム研究機構　国立極地研究所
National Institute of Polar Research, Tachikawa, Japan
３）アバンナット
Avangnaq, Takatsuki, Japan
４）北海道大学高等教育推進機構
Institute for the Advancement of Higher Education, Hokkaido University, Sapporo, Japan
５）北見工業大学社会環境工学科
Kitami Institute of Technology, Kitami, Japan
６）岡山大学大学院自然科学研究科
Okayama University, Okayama, Japan

1．はじめに

極地氷床で掘削されるアイスコアは古環境を復元する有力なツールである．極地氷床の高標高地域は広域の環境情報を記録している．特にドームと呼ばれる氷床の頂上は他からの氷の移流がないために精度の良い古環境復元をするうえで良い場所である．こういった背景からこれまで多くの氷床コア掘削が行われてきた．南極においては Dome Fuji（Watanabe et al., 2003），EPICA DML（EPICA community members, 2006），EPICA Dome C（EPICA community members, 2004），グリーンランドにおいては GRIP（Greenland Ice-core Project Members, 1993），GISP2（Grootes et al., 1993），NGRIP（North Greenland Ice Core Project Members, 2004）などが代表的な代表的な氷床ドームコアの掘削地であるである．一般的にこれらの氷床ドームコアは 1）乾燥しているために低涵養地域，2）高緯度で標高が高いために低温地域という特徴がある．こういった低温低涵養量地域の氷床コアは融解の影響が少なく，数十万年にわたる古環境の復元を可能にする．しかしながら，低涵養量は古環境を復元できる時間分解能を粗くし，極端に低涵養量な地域に於いては一年間堆積が欠損しうる（Kameda et al., 2008）という短所がある．

グリーンランド氷床は北半球の人間活動圏に近く，過去の人為起源物質を保存している．代表的な人為起源物質は硫酸塩，硝酸塩，有機物，ブラックカーボンなどが挙げられる（IPCC, 2013）．これらのエアロゾルはグリーンランドの各地域で堆積環境が異なる（e.g. Fischer et al., 1998）．北西部では偏西風の影響を受け，南東部ではアイスランド低気圧の影響を受けやすい（Buchardt et al., 2012）．北西部のアイスコアはアジアなどから長距離輸送される人為起源物質を含んでいる（Bory et al., 2014）．他方で，南東部ではいわゆる産業革命後の欧州や北米由来の人為起源物質を保存している（McConnell et al., 2008）．数十年スケールの気候変動としては北極振動（Arctic Oscillation）や北大西洋振動（North Atlantic Oscillation）が地域的な気象状態，気温，降水量に影響を与えていると考えられる．こういったグリーンランドの地域による堆積環境や気候の違いについては，多点浅層掘削によるプロジェクトが行われている（United States, PARCA project; German, NGT project; e.g. McConnell et al., 2006）．しかしながら，南東部は多点浅層掘削があまり行われていない地域であり，古環境復元研究が不十分である．

我々はグリーンランド南東部の高涵養ドームにおいて，浅層掘削を実施した．この掘削の目的はグリーンランドにおける高涵養量域の圧密氷化過程の特徴を解明し，近年の人為起源エアロゾルの変遷を解読するためである．この地域は日本の雪氷学コミュニティーにとってフロンティアであり，ロジスティクスからの取り組みとなった．本稿では，すでに学術誌に掲載されている論文（Iizuka et al., 2016a; 2016b）を参考にし，掘削プロジェクトと国内初期解析の概要を報告する．

2．研究地域

観測地点（67.18°N, 36.37°W, 3170 m a.s.l.）は東グリーンランド最大の都市タシーラクから北に約 185 km に位置する（図 1）．グリーンランド氷床の最高地点は Summit（GRIP/GISP2）で Summit から南に分水嶺が伸

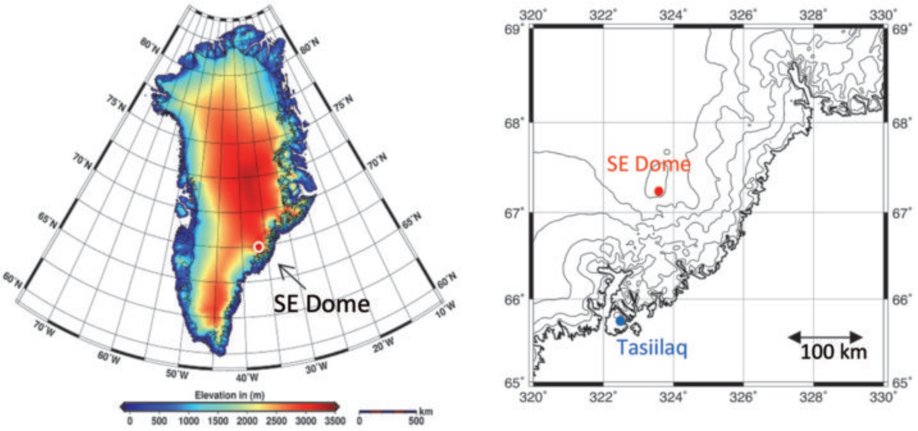

図 1：左：南東ドーム（SE-Dome）の位置．（Helm et al.（2014）のグリーンランド氷床等高線を使用）．右：南東ドーム近傍．

Figure 1：Left: Location of the SE-Dome region. The base map was produced from Helm et al. (2014). Right: Contour map of the SE-Dome region.

びている．この分氷嶺は南東方向，南西方向に分岐し，南西方向の分氷嶺はDye 3を通りNarsarsuaq近くまで南下する．南東方向の分氷嶺の端に標高3170 mのドームが形成されており，このドームが今回の観測地点である（以後，南東ドームまたはSE-Domeという）．標高3000 m以上の南東ドームが維持されている原因は，この氷床の下に山が形成されていること（Bamber et al., 2013）や涵養量が大きいこと（Burgess et al., 2010）が考えられる．南東ドームの下流にはHelheim Glacier, Fenris Glacier, MIdård Glacierが流れ，これらの氷河はSermilik Fjordに流出する．

デンマークの気象研究所（Danish Meteorological Institute）によれば，タシーラクの降水の特徴は他のグリーンランドの都市とは異なっており，膨大な年降水量を示すとともに冬季に降水の極大がある．南東部の気候は北大西洋に起因するアイスランド低気圧によって支配されている（Pedro et al., 2012）．南東ドームはタシーラクと同様の降水特性を持っていると考えられる．

いくつかのモデルや衛星解析が南東ドームの気候状態や涵養量を推定している（Bales et al., 2009; Burgess et al., 2010; Hall et al., 2013; Howat et al., 2014; Helm et al., 2014）．これらの研究は南東ドームの特徴として，1）グリーンランド氷床上で有数の海抜3000 m以上の高地；2）67°Nにしては比較的寒冷であり年平均気温が－20℃以下；3）グリーンランドのドームの一つで涵養量は0.6～0.8 m water equivalent（w.e）yr^{-1}などを挙げている．南東ドームで採取されたアイスコアはグリーンランドのドームで最も高涵養量でかつ比較的低温の特徴を持つ．これらの特徴は近年の人為起源物質の変動を高時間分解能で追跡できる長所がある．

南東ドームの北30 kmの地点（67.5 N，36.1 W）に於いて，2002年に浅層コアが掘削されている．このアイスコアはDAS2コアと呼ばれており，1936～2002の期間の水等量は約0.9 m w.e.であり（Pedro et al., 2012），冬季の海塩物質（海域起源）の極大と春季の炭酸塩とアルミ鉱物（陸域起源）の極大がみられている（Banta et al., 2008）．

3．旅程

観測隊員はタシーラクのエアーグリーンランド社からヘリコプター（Bell 212）をチャーターし，物資をタシーラクから南東ドームに輸送した．総輸送量は装備や食料約700 kg，発電機用ガソリン180 L，調理用の灯油80 Lであった．2015年5月18日観測隊員3名がドリル一式，燃料，食料，居住用テントとともに南東ドームに移動し，2つの居住テントと掘削テントを設置した．その後，18日夜から20日までブリザードであり，掘削テントが半壊した．翌21日掘削テントを再設置した．21日夕方，観測隊員2名が装備，燃料，食糧，居住テントとともに南東ドームに移動した．22日から27日まで調査・掘削をした．28日に撤収を開始したが，6月2日までブリザードのためにピックアップフライトがなく，停滞した．6月2日に観測隊員5名と装備と一部のアイスコアをタシーラクに輸送した．追加のピックアップフライトが6月4日に実施され，残りのアイスコアと試料がすべてタシーラクに輸送された．アイスコアと氷試料はタシーラクのスーパーマーケット（the Pilersuisoq general store）の－20℃の低温室に保管された．アイスコアと氷試料は20 ftの冷凍コンテナに移され，輸送船HEUNG-A AKITA 0013によって，タシーラクからAalborg，Denmarkを経由し，石狩湾まで輸送され，8月24日に北海道大学低温科学研究所の－50℃の低温室に保管された．アイスコアや試料は－25℃以下の環境で輸送された．低温科学研究所の低温室において，アイスコアが輸送中の破損がなく良質の状態で輸送されたことを確認した．

4．アイスコア掘削

掘削テントや掘削ドリルのセッティング後，アイスコアの掘削を始めた．掘削機は低温科学研究所の技術部が2002年に開発した軽量の電動駆動アイスコア掘削システム「どこでもドリル2」である（Shiraiwa et al., 2003; Matoba et al., 2014）．掘削の総重量は約100 kgである．掘削機はガイドがなく，3本のパントグラフ型のアンチトルクがついている．コアバレルは掘削機の長さを短くするために，チップ室とコア室に分かれている．また軽量化のため，ドリルマストはコアバレルの輸送箱として使用できる．我々は4気筒シングルシリンダー型のガソリン発電機を2機（HONDA model EU16i; YAMAHA model EF2300i）掘削に用いた．高地で使用するために燃料噴射ノイズを小さく加工した．5月27日，我々は195回の掘削を経て深度90.45 mのアイスコア掘削を終了した．平均のアイスコア長は0.479 mであり，54.95時間を要した．コア採取速度は1.65 m h^{-1}である．掘削後，アイスコアの層位観測を行い，層構造とアイスコアの長さを記録した．アイスコアはいくつかの氷板を含んでいたが，そのほとんどは0.02 m以下であった．

掘削後，我々は掘削孔内温度を測定した．孔内温度測

定にはサーミスターセンタつきの温度計（Techno-seven model BYE-64 T and D corporation model TR-52）を用いた．温度計の精度は0.1℃である．掘削孔温度測定を行ったときの掘削テント内の室温は－15.2℃であった．深度20 mに25分間放置した温度は－20.9℃であった．

5．低温室処理と密度分析

2015年9月から12月にかけて，低温研低温室において,いくつかの基本分析を行った．測定項目は層位観察，バルク密度測定，X線密度測定，電気伝導度測定，可視写真撮影，近赤外写真撮影である．本稿ではこのうち層位観察，バルク密度測定，X線密度測定，電気伝導度測定について述べる．バルク密度は189本の各アイスコアセクションの体積と重量を測定し，算出した．X線透過法（Hori et al., 1999）によってSE-Domeコアの連続密度プロファイルを得た．この方法では，フィルンコアを透過するX線の強度をコア試料の反対側につけられたX線検出器で測定する．氷の厚さに基づいたX線吸収量の補正式を用いて，X線の強度を密度に変換する．密度プロファイルの空間分解能は1 mmである．火山イベントとそれに基づいた年代を推定するために電気伝導度を連続誘電プロファイル（DEP）法で分析した（Fujita et al. 2016）．この方法は250 MHzの交流電気伝導度の連続プロファイルを得ることができる．電気伝導度プロファイルの空間分解能は20 mmである．

6．密度プロファイル

図2にバルク密度プロファイルが示されている．バルク密度は．深さ13.8 mで550 kg m^{-3}になり，深さ20.2 mで600 kg m^{-3}になった．密度550 kg m^{-3}は古典的な圧密氷化理論において重要な密度であり，機械的な雪粒子の再配分機構から転位クリープによる雪粒の変形機構に主なメカニズムが変化する密度と考えられている．また，密度600 kg m^{-3}は機械的な雪粒子の再配分機構が起きなくなる密度と近年考えられている（Fujita et al., 2014）．その後，バルク密度は．深さ64.0 mで760 kg m^{-3}になった．密度760 kg m^{-3}は，氷化するまでのより高密度フィルンにおいて，転位クリープ機構が主なメカニズムとなると考えられている密度である（Salamatin et al., 2009）．バルク密度は，深さ86.8 mで830 kg m^{-3}になり，氷化した．X線密度もバルク密度とほぼ同じ結果となり，深さ83.4 mで830 kg m^{-3}になった．他のグリーンランドで掘削されたアイスコアと比較すると，SE-Domeコアはより深く，より短期間で氷化している特徴をもつ．

7．SE-Domeコアの涵養量

X線密度プロファイルが図3に示されている．X線密度は周期1～1.5 mで変動をしている．この短周期変動は冬の高密度と夏の低密度による季節変動である．DEP深さプロファイルが図3に示されている．深さ11.745 mと43.420 mに電気伝導度ピークが見つかる．X線密度による年層カウントから，深さ11.745 mの電気伝導度ピークは2010年の3月から6月に起きたアイスランドのEyjafjallajökull火山噴火によると考えられる．深さ11.745 mは水等量で5.27 m w.e.に相当する．起源からの輸送時間を無視すると，2010年春から2015年春の涵養量は1.05 m w.e. yr^{-1}である．深さ43.420 mの電気伝導度ピークは1991年6月15日に起きたフィリピンのPinatubo火山噴火によると考えられる．深さ43.420 mは水等量で24.89 m w.e.に相当する．起源からの輸送時間を無視すると，1991年夏から2015年春の涵養量は1.04 m w.e. yr^{-1}である．まとめとして，SE-Domeコアの涵養量は約1.0 m w.e. yr^{-1}であった．今後，SE-Domeコアの涵養量は1.0 m w.e. yr^{-1}，氷温は

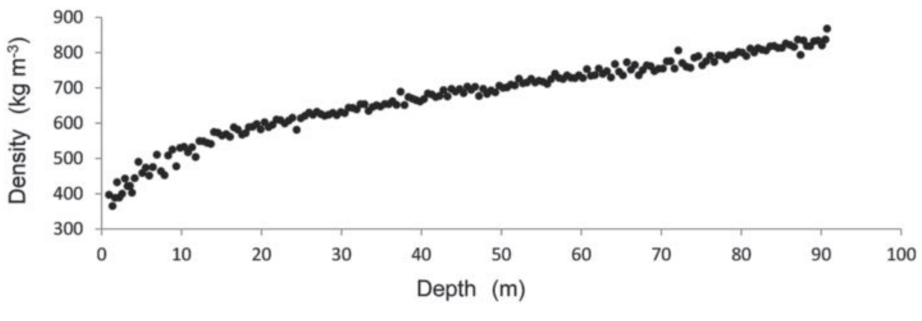

図2：南東ドームアイスコアのバルク密度の深さプロファイル．
Figure 2：Density profile of the SE-Dome ice core.

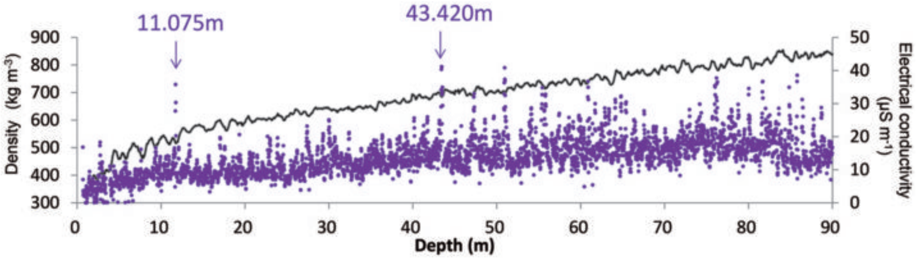

図 3：南東ドームアイスコアの X 線密度（40 mm 移動平均）（実線）と交流電気伝導度（250 MHz）（点）の深さプロファイル

Figure 3：X-ray density (thick line; 40 mm running mean) and alternating-current electrical-conductivity (circle; 250MHz) profiles of the SE-Dome ice core.

−20.9℃として議論を進める．

8．SE-Dome コアと圧密モデルの深さ-密度曲線の比較

経験的な圧密氷化モデルが通常のアイスコアの深さ-密度曲線をよく再現することが知られている（Sorge 1935; Schytt 1958; Herron and Langway, 1980）．代表的で良く使用される経験的な圧密氷化モデルに Herron and Langway's model（Herron and Langway, 1980）がある．表面密度（Surface density; ρ_s＝0.36 kg m^{-3}），氷の密度（Ice density; ρ_i＝0.83 kg m^{-3}），とすると，密度 0.55 kg m^{-3} 未満（$\rho<0.55$ kg m^{-3}）の浅層の深さ h（m）における密度（ρ_h）は以下の式で表される．

$$\rho_h=\frac{\rho_i Z_0}{1+Z_0} \qquad \cdots (1)$$

ここで，

$$Z_0=\exp\left[\rho_i k_0 h+\ln\left(\frac{\rho_s}{\rho_i-\rho_s}\right)\right] \qquad \cdots (2)$$

k_0 は定数であり，−20.9℃において 0.0862 である．

密度 0.55 kg m^{-3} より高密度（$\rho>0.55$ kg m^{-3}）の深層の深さ（h）における密度（ρ_h）は以下の式で表される．

$$\rho_h=\frac{\rho_i Z_1}{1+Z_1}, \qquad \cdots (3)$$

ここで，

$$Z_1=\exp\left[\frac{\rho_i k_1(h-h_{0.55})}{A^{0.5}}h+\ln\left(\frac{\rho_{0.55}}{\rho_i-\rho_{0.55}}\right)\right] \cdots (4)$$

k_1 は定数であり，−20.9℃において 0.0211 である．A は涵養量である（1.0 m w.e. yr^{-1}）．

図 4 に SE-Dome コアの密度測定値およびモデルによる深さ-密度曲線を示す．密度 0.55 kg m^{-3} 未満において，SE-Dome コア測定値とモデルによる深さ-密度曲線はよく一致している．しかしながら，密度 0.55 kg m^{-3} より高密度において，測定された深さ-密度曲線は涵養量が 1.0 m w.e. yr^{-1} としたときのモデルの曲線とはあわない．涵養量が 1.0 m w.e. yr^{-1} であれば，圧密氷化深度は 107-108 m と計算された．実際の圧密氷化深度は 83-86 m であり，経験式によるモデル深度よりも 20 m 以上浅い結果となった．

9．SE-Dome コアの圧密氷化メカニズム

なぜ SE-Dome コアの氷化深度が経験式によるモデル深度よりも 20 m 以上浅い結果となったのか考察する．SE-Dome コアの圧縮粘性係数は以下の式で表される．

$$\eta_c=\sigma\cdot\rho\cdot\left(\frac{d\rho}{dt}\right)^{-1}, \qquad \cdots (5)$$

ここで，ρ, σ, t はそれぞれ密度（kg m^{-3}），積載荷重（Pa），時間（s）である．

他方で，経験的な圧縮粘性係数の密度依存性は以下の式で表される（Nishimura et al., 1983）．

$$\eta=\eta_0\cdot\exp(K\cdot\rho)\cdot\exp\left(\frac{\Delta E}{k_B T}\right), \qquad \cdots (6)$$

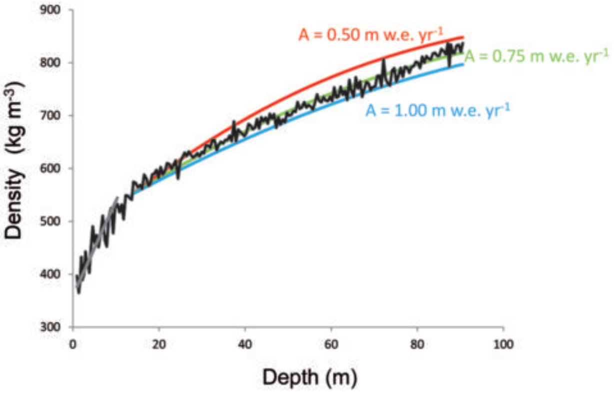

図 4：南東ドームアイスコアのバルク密度（黒）と Herron and Langway's model の深さプロファイル（赤，緑，水色）．涵養量の違いによる曲線の変化をみるために，Herron and Langway's model からは 3 曲線を示した．

Figure 4：Density profiles of the SE-Dome ice core (black) and Herron and Langway's model (red, green, blue).

ここで，η_0 は定数で 0.001〜0.007 $\mathrm{N \cdot s\,m^{-2}}$ の値をとる．K は $2.57\times10^{-3}\ \mathrm{m^3\,kg^{-1}}$，$\Delta E$ は活性化エネルギーで 51.6 $\mathrm{kJ\,mol^{-1}}$，k_b はボルツマン定数，T は温度である．図 5 に密度測定値を式（4）に適用して得られた SE-Dome コアの圧縮粘性係数と式（6）によって求めた経験的な圧縮粘性係数を示した．低密度域において，両者はよく一致しているが，$\rho>750\ \mathrm{kg\,m^{-3}}$ の密度域において，SE-Dome コアの圧縮粘性係数は密度によらずほぼ一定の値をとり，経験的な圧縮粘性係数よりも低い値をとる．つまり，$\rho>750\ \mathrm{kg\,m^{-3}}$ の密度域において，SE-Dome コアは経験式よりも変形しやすいといえる．

750 $\mathrm{kg\,m^{-3}}$ 以上の密度域において，SE-Dome コアが経験式よりも変形しやすい理由として二つのメカニズムが考えられる．先ず一つは，高涵養量であるためである．高涵養量は，短期間で大きな積載荷重をもたらす．短期間であることは粒子間の結合が十分に行われないことを意味し，通常の涵養量地域の圧密氷化に比べて，同様の積載荷重であってもより変形が生じやすく（圧密が進みやすく）なる．もう一つは，高涵養量地域のフィルンが短期間で大きな荷重の変化を生み出すために，通常の圧密氷化に比べて高い転位密度の氷が存在しやすいということである．750 $\mathrm{kg\,m^{-3}}$ 以上の密度域における圧密氷化には転位クリープが重要である（Salamatin et al., 2009）．どちらのメカニズムにせよ，高涵養量という物理現象が経験的なモデルとの不整合を生み出していると考えられる．

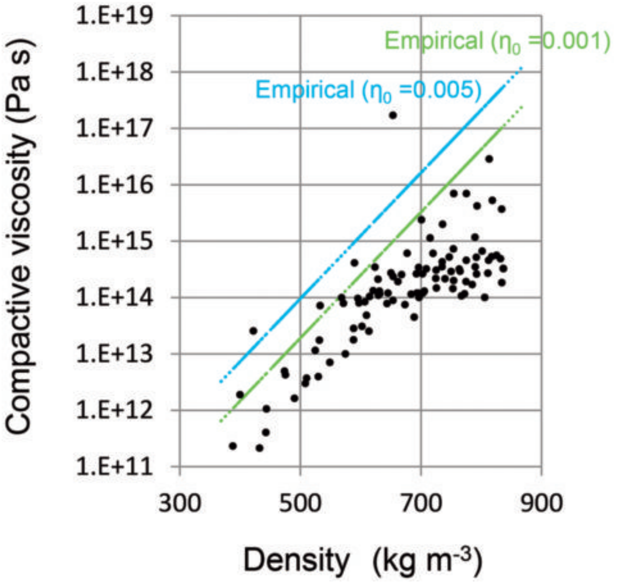

図 5：南東ドームアイスコアの深さ–密度曲線から求めた圧密粘性係数（黒点）と Nishimura et al.,（1983）による経験的な深さ–密度曲線による密度と圧縮粘性係数（水色，緑）．
Figure 5：Compactive viscosity from the SE-Dome ice core (black circle) and an empirical model (blue and green; (Nishimura et al., 1983))

まとめ

2015 年 5 月にグリーンランド氷床南東ドーム（SE-Dome）において浅層掘削に成功し，同 8 月には SE-Dome コア 189 セクションを氷のまま日本に輸送した．SE-Dome コアの涵養量は約 1.0 m w.e. $\mathrm{yr^{-1}}$，氷温は −20.9℃であった．SE-Dome コアは氷床のドームとしては最も高涵養量の地域の一つである．高涵養量地域の圧密氷化過程について精査された研究例は少なく，Herron and Langway’s model のような優れたモデルですら深さ−密度の関係を再現できなかった．この理由は主に 750 $\mathrm{kg\,m^{-3}}$ 以上の密度域において，SE-Dome コアは経験式よりもつぶれやすい特徴を持つためである．今後，高涵養量地域の圧密氷化メカニズムを明らかにすることで，より包括的な圧密氷化モデルを提案できる可能性がある．

謝辞

SE-Dome コアプロジェクトに関与したすべての皆様に感謝いたします．このプロジェクトの主財源は MEXT/JSPS KAKENHI Grant Number 26257201 と 16K12573，低温科学研究所共同研究経費です．一部 ArCS（Arctic Challenge for Sustainability Project）から助成を受けました．また，低温科学研究所からは共同研究経費だけではなく，多くのサポートをいただいています．心からお礼申し上げます．

References

Bales, R. C., Q. Guo, D. Shen, J. R. McConnell, G. Du, J. F. Burkhart, V. B. Spikes, E. Hanna, and J. Cappelen (2009) Annual accumulation for Greenland updated using ice core data developed during 2000–2006 and analysis of daily coastal meteorological data. *J. Geophys. Res.*, **114**, D06116, doi: 10.1029/2008JD011208.

Bamber, J. L., J. A. Griggs, R. T. W. L. Hurkmans, J. A. Dowdeswell, S. P. Gogineni, I. Howat, J. Mouginot, J. Paden, S. Palmer, E. Rignot, and D. Steinhage (2013) A new bed elevation data-set for Greenland. *Cryosphere*, **7**, 499–510, doi: 10.5194/tc-7-499-2013.

Banta, J. R., J. R. McConnell, R. Edwards, and J. P. Engelbrecht (2008) Delineation of carbonate dust, aluminous dust, and sea salt deposition in a Greenland glaciochemical array using positive matrix factorization. *Geochem. Geophys. Geosyst.*, **9**, Q07013, doi: 10.1029/2007GC001908.

Bory, A. J. M., W. Abouchami, S. J. G. Galer, A. Svensson, J. N. Christensen, and P. E. Biscaye (2014) A Chinese Imprint in Insoluble Pollutants Recently Deposited in Central Greenland As Indicated by Lead Isotopes. *Environ. Sci. Technol.*, **48**, 1451–1457, dx.doi.org/10.1021/es4035655.

Buchardt, S. L., H. B. Clausen, B. M. Vinther, and D. Dahl-Jensen (2012) Investigating the past and recent δ^{18} O-accumulation relationship seen in Greenland ice cores. *Clim. Past*, **8**, 2053–2059, doi: 10.5194/cp-8-2053-2012.

Burgess, E. W., R. R. Forster, J. E. Box, E. Mosley-Thompson, D. H. Bromwich, R. C. Bales, and L. C. Smith, (2010) A spatially calibrated model of annual accumulation rate on the Greenland Ice Sheet (1958–2007). *J. Geophys. Res.*, **115**, F02004, doi: 10.1029/2009JF001293.

Cappelen. J., B. V. Jørgense, E. V. Laursen, L. S. Stannius, and R. S. Thomsen (2001) The observed climate of Greenland, 1958–99 - with climatological Standard Normals, 1961–90. *Danish Meteorological Institute Technical Report*, 00–18.

EPICA community members (2004) Eight glacial cycles from an Antarctic ice core. *Nature*, **429**, 623–628, doi: 10.1038/nature02599.

EPICA community members (2006) One-to-one coupling of glacial climate variability in Greenland and Antarctica. *Nature*, **444**, 195–198, doi: 10.1038/nature05301.

Fischer, H., D. Wagenbach, and J. Kipfstuhl, (1998) Sulfate and nitrate firn concentrations on the Greenland Ice Sheet: 1. Large scale geographical deposition changes. *J. Geophys. Res.*, **103** (D17): 21927–21934, doi: 10.1029/98JD01885.

Fujita, S, M. Hirabayashi, K. Goto-Azuma, R. Dallmayr, K. Satow, J. Zheng, and D. Dahl-Jensen (2014) Densification of layered firn of the ice sheet at NEEM, Greenland. *J. Glaciol.*, **60** (223), 905–921, doi: 10.3189/2014JoG14J006.

Fujita, S., K. Goto-Azuma, M. Hirabayashi, A. Hori, Y. Iizuka, Y. Motizuki, H. Motoyama, and K. Takahashi (2016) Densification of layered firn in the ice sheet at Dome Fuji, Antarctica. *J. Glaciol.*, **62** (231), 103–123, doi: 10.1017/jog.2016.16.

Greenland Ice-core Project Members (1993) Climate instability during the last interglacial period recorded in the GRIP ice core. *Nature*, **364**, 203–207.

Grootes, P. M., M. Stuiver, J. W. C. White, S. Johnsen, and J. Jouzel, (1993) Comparison of oxygen isotope records from the GISP2 and GRIP Greenland ice cores. *Nature*, **366**, 552–554, doi: 10.1038/366552a0.

Hall, D. K., J. C. Comiso, N. E. DiGirolamo, C. A. Shuman, J. E. Box, and L. S. Koenig, (2013), Variability in the surface temperature and melt extent of the Greenland ice sheet from MODIS. *Geophys. Res. Lett.*, **40**, 1–7, doi: 10.1002/grl.50240.

Helm, V., A. Humbert, and H. Miller (2014) Elevation and elevation change of Greenland and Antarctica derived from CryoSat-2. *Cryosphere*, **8**, 1539–1559, doi: 10.5194/tc-8-1539-2014.

Herron, M. M. and C. C. Langway (1980) Firn densification: an empirical model. *J. Glaciol.*, **25** (93), 373–385.

Hori, A., K. Tayuki, H. Narita, T. Hondoh, S. Fujita, T. Kameda, H. Shoji, N. Azuma, K. Kamiyama, Y. Fujii, H. Motoyama and O. Watanabe (1999) A detailed density profile of the Dome Fuji (Antarctica) shallow ice core by X-ray transmission method. *Ann. Glaciol.*, **29**, 211–214.

Howat, I. M., A. Negrete, and B. E. Smith (2014), The Greenland Ice Mapping Project (GIMP) land classification and surface elevation data sets. *Cryosphere*, **8**, 1509–1518, doi: 10.5194/tc-8-1509-2014.

IPCC (2013) Climate Change 2013: The Physical Science Basis. Contribution of Working Group I to the Fifth Assessment Report of the Intergovernmental Panel on Climate Change [Stocker, T. F., Qin, D., Plattner, G.-K., Tignor, M., Allen, S. K., Boschung, J., Nauels, A., Xia, Y., Bex, V. and Midgley, P. M. (eds.)]. Cambridge University Press, Cambridge, United Kingdom and New York, NY, USA, 1535 pp, doi: 10.1017/CBO9781107415324.

Iizuka, Y., S. Matoba, T. Yamasaki, I. Oyabu, M. Kadota, and T. Aoki, (2016a) Glaciological and meteorological observations at the SE-Dome site, southeastern Greenland Ice Sheet. *Bull. Glaciol. Res.*, **34**, 1–10, 10.5331/bgr.15R03

Iizuka, Y., A. Miyamoto, A. Hori, S. Matoba, R. Furukawa, T. Saito, S. Fujita, M. Hirabayashi, S. Yamaguchi, K. Fujita, and N. Takeuchi (2016b) A firn densification process in the high accumulation dome of southeastern Greenland. *Arc. Ant. Alp. Res.*, in press.

Kameda, T., H. Motoyama, S. Fujita, and S. Takahashi (2008) Temporal and spatial variability of surface mass balance at Dome Fuji, East Antarctica, by the stake method from 1995 to 2006. *J. Glaciol.*, **54**, 107–116, doi: 10.3189/002214308784409062.

Matoba, S., K. Shimbori, and T. Shiraiwa (2014) Alpine ice-core drilling in the North Pacific region. *Ann. Glaciol.*, **55** (68), 83–87, doi: 10.3189/2014AoG68A020.

McConnell, J. R. and R. Edwards (2008) Coal burning leaves toxic heavy metal legacy in the Arctic. *PNAS*, **105**, 34, 12141, doi: 10.1073/pnas.0803564105.

McConnell, J. R., S. Kipfstuhl, and H. Fischer (2006) The NGT and PARCA shallow ice core arrays in Greenland: A brief overview. *PAGES NEWS*, **14**, 1, hdl: 10013/epic.24999.

Nishimura, H, N. Maeno, and K. Satow (1983) Snow structure and depth hoar formation in Mizuho Plateau, Antarctica. *Mem. Natl. Inst. Polar Res.*, **29**, 149–158.

North Greenland Ice Core Project Members (2004) High-resolution record of Northern Hemisphere climate extending into the last interglacial period. *Nature*, **431**, 147–151, doi: 10.1038/nature02805.

Pedro, J. B., J. R. McConnell, T. D. van Ommen, D. Fink, M. A. J. Curran, A. M. Smith, K. J. Simon, A. D. Moy, and S. B. Das (2012) Solar and climate influences on ice core 10Be records from Antarctica and Greenland during the neutron monitor era. *Earth Planet. Sci. Lett.*, **355-356**, 174-186, doi: 10.1016/j.epsl.2012.08.038.

Salamatin, A. N., V. Y. Lipenkov, J. M. Barnola, A. Hori, P. Duval, and T. Hondoh (2009) Snow/firn densification in polar ice sheets. *Low Temp. Sci.*, **68** (Suppl.), 195-222.

Schytt, V. (1958) Glaciology II. A: Snow studies at Maudheim. Glaciology. B: Snow studies inland. Glaciology. C: The inner structure of the ice shelf at Maudheim as shown by core drilling. Norwegian- British- Swedish Antarctic Expedition, 1949-52. Sci. Results, Vol.IV.

Shiraiwa, T., K. Goto-Azuma, S. Matoba, T. Yamasaki, T. Segawa, S. Kanamori, K. Matsuoka, and Y. Fujii (2003) Ice core drilling at King Col, Mount Logan 2002. *Bull. Glaciol. Res.*, **20**, 57-63.

Sorge, E. (1935) Glaziologische Untersuchungen in Eismitte. In Brockamp, B., H. Jülg, F. Loewe and E. Sorge, eds. Wissenschaflliche Ergebnisse der Deutschen Grönland-Expedition Alfred Wegener 1929 und 1930/1931. Band III. Glaziologie. Leipzig, F. A. Brockhaus, 62-270.

Watanabe, O., J. Jouzel, S. Johnsen, F. Parrenin, H. Shoji, and N. Yoshida (2003) Homogeneous climate variability across East Antarctica over the past three glacial cycles. *Nature*, **422** (6931), 509-512, doi: 10.1038/nature01525.

低温科学 75 (2017) 53-65
doi: 10.14943/lowtemsci. 75. 53

北極域氷河の雪氷藻類群集と暗色化

竹内　望[1)]

2016 年 11 月 11 日受付，2017 年 1 月 16 日受理

雪氷藻類は，氷河や積雪上で繁殖する光合成微生物である．本稿では，北極域氷河の生物学的な暗色化過程を理解するために，近年明らかになったアラスカ，スンタルハヤタ，スバールバル，グリーンランドの各氷河上の雪氷藻類群集を比較する．氷河裸氷域の藻類による暗色化には，2つのプロセスがあることがわかってきた．一つは暗色の色素を持った緑藻の繁殖によるもので，もう一つはシアノバクテリアによるクリオコナイト形成によるものである．さらに積雪域では，赤雪を引き起こす緑藻の繁殖が，アルベド低下の一因であることがわかってきた．それぞれの雪氷藻類の繁殖に関わる環境要因の解明と繁殖のモデル化，さらに物理モデルに基づいたアルベドへの影響評価が，今後の課題である．

Snow and ice algal communities and their effect on surface darkening of Arctic glaciers

Nozomu Takeuchi[1]

Snow and ice algae are cold-tolerant photosynthetic microbes and grow on glaciers and snowfields worldwide. Organic matter derived from the algae possibly causes recent darkening of the Greenland Ice Sheet. To understand the relationship between Arctic warming and biological glacier darkening, it is necessary to know the geographical distribution and ecology of snow and ice algae on glaciers in the Arctic region. In this paper, I review recent studies on snow and ice algae on glaciers in various parts of the Arctic, including Alaska, Suntar-Khayata (eastern Siberia), Svalbard, and Greenland. Comparison of the algal communities and their darkening effect revealed that there are two processes to darken the glacial ice surface associated with algae. One is the darkening by the bloom of green algae with dark-colored pigments (mainly *Ancylonema* (*A.*) *nordenskioldii*). Another is darkening by the cyanobacteria (*Phormidesmis* (*P.*) *priestleyi*) forming dark-colored cryoconite granules. The darkening observed on the studied glaciers was due to either one. Furthermore, red snow algae frequently bloom on the melting snow surface of the upper accumulation area of the glaciers and enhance its melting. For future work on the bio-albedo studies, we need to determine the environmental factors controlling the algal growth, to create a numerical model to reconstruct the algal temporal change, and to evaluate their quantitative impact on the melting based on a physical model of snow and ice albedo.

キーワード：氷河，雪氷藻類，暗色化，クリオコナイト，北極
Glacier, snow and ice algae, darkening, cryoconite, Arctic

1．はじめに

雪氷微生物は，氷河や積雪で繁殖する寒冷環境に特殊化した微生物で，世界各地の氷河から報告されている．特に北極域の氷河では，古くからグリーンランドやアラスカを中心に，その微生物の存在が知られてきた．氷河上微生物の中で光合成によって有機物を生成する役割を

連絡先
竹内　望
e-mail：ntakeuch@faculty.chiba-u.jp
１）千葉大学大学院理学研究科地球科学コース
Department of Earth Sciences, Graduate School of Science, Chiba University, Chiba, Japan

持つものが，緑藻やシアノバクテリアといった雪氷藻類である．雪氷藻類は，二酸化炭素，水，日射から有機物を生成する微生物で，融解期の雪氷の表面で日射を浴びて繁殖する．このうち緑藻は，細胞中に核を持つ真核生物の仲間で，細胞は直径数十 μm の球または円筒形をしたものが多く，細胞内に緑色をした葉緑素（クロロフィル）の他，赤や黄色のカロチノイド類など様々な色素を持つ（図 1a，e.g. Hoham and Duval, 2001）．一方，シアノバクテリアは，細胞内に核がない細菌（バクテリア）の仲間で，細胞は直径数 μm と緑藻よりも小さく，複数の細胞が糸のように連なった形態であるものが多い（図 1b）．シアノバクテリアは，鉱物粒子や他の有機物と絡み合いクリオコナイト粒とよばれる暗色をした粒状の構造体を氷河上で形成する（図 1c，e.g. Cook et al., 2015）．このような色素を持った緑藻の細胞や，シアノバクテリアが形成する暗色のクリオコナイト粒が氷河上に蓄積すると，もともと白くアルベドの高い雪や氷が暗色化するのである．

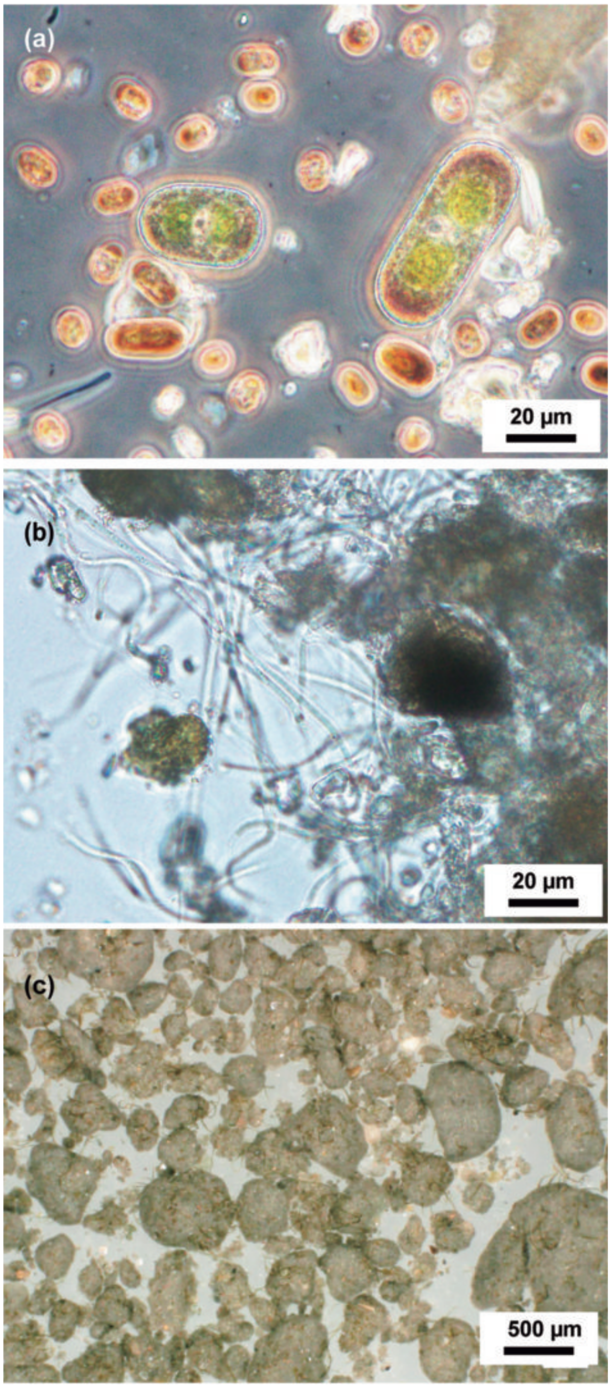

図 1：代表的な雪氷藻類である（a）緑藻と（b）シアノバクテリア（糸状），およびシアノバクテリアが形成する（c）クリオコナイト粒．写真はすべてグリーンランドのサンプル．

Figure 1：Two major groups of snow and ice algae. (a) green algae, (b) cyanobacteria, (c) cryoconite granules formed by filamentous cyanobacteria. All samples in the photographs are from Greenland.

雪氷藻類由来の有機物による氷河の暗色化が特に顕著であることが指摘されたのは，ヒマラヤを中心としたアジア山岳域の氷河である．例えば，ネパールヒマラヤのヤラ氷河では，糸状のシアノバクテリアを含む暗色のクリオコナイト粒が消耗域表面に大量に堆積し，その量は乾燥重量の平均で約 $300\ \mathrm{g\ m^{-2}}$ に達し，氷河全面を見た目にも黒くしている（Takeuchi et al., 2001）．このクリオコナイトによるアルベド低下によって，融解速度は約 3 倍も加速されていることが明らかになっている（Kohshima et al., 1993）．このようなクリオコナイトの堆積は，ヒマラヤだけでなく，天山山脈や祁連山脈ほか，アジア全域の氷河でみられることが明らかになり，シアノバクテリアを中心とした雪氷藻類の繁殖が，氷河融解を大きく加速していることが明らかになった（Takeuchi and Li, 2008）．

一方，最近になって注目されているのが，北極域のグリーンランド氷床の暗色化である．北極域の氷河は，もともとアジア山岳域の氷河に比べて繁殖する微生物量が少なく，氷河表面もきれいでアルベドも比較的高いと考えられてきた．しかしながら，グリーンランド氷床の衛星画像の解析によって，21 世紀に入ってから氷床全域にわたってアルベドが低下していることが明らかになり，氷床の質量減少の一因となっていることがわかってきた（e.g. Box et al., 2012）．アルベドの低下は特に氷床辺縁部で顕著であり，これは単にアルベドの高い積雪の融解が速くなったためだけではなく，暗色の裸氷面が拡大しているためであることが明らかになった（Shimada et al., 2016）．このような雪氷の暗色化の要因として，従来，大気を介して供給される黒色炭素や鉱物粒子の雪氷への混入が考えられることが多かったが，実際氷河上の不純物を分析すると，シアノバクテリアを含むクリオコナイトであった（Wientjes and Oerlemans, 2010; Takeuchi et al.,

2014）．したがって，近年の氷床の暗色域の拡大の要因は，氷床の生態系の変化による微生物の繁殖域の拡大である可能性が高い．

このような北極域氷河の微生物活動の変化の考えられる原因の一つは，近年の地球温暖化に伴う北極圏の気温上昇である．20 世紀以降，全球平均気温が上昇していることが明らかになっているが，北極圏の気温上昇率は他の地域に比べても大きいことが指摘されている（e.g. Screen and Simmonds, 2010）．気温の上昇は，融解期間の延長や大気循環に影響し，氷河上の微生物に影響を与える可能性が高い．北極域が温暖化しているとすれば，グリーンランドだけでなく他の北極域の氷河の生態系でも同じような変化が起きているのだろうか．しかしながら，いままで北極圏の氷河の雪氷微生物に関する定量的な情報はほとんどなかった．

北極域の氷河の微生物に関しては，21 世紀以降スバールバルやグリーンランド，アラスカの氷河を中心に，欧米や日本，インドのグループによって研究が進み様々なことが明らかになってきた．さらに，2011 年より 5 年間行われた日本のプロジェクト，積雪汚染及び雪氷微生物が北極域の環境変動に及ぼす影響（SIGMA）及びグリーン・ネットワーク・オブ・エクセレンス北極気候変動研究事業（GRENE 北極）では，グリーンランド氷床のほか，東シベリアのスンタルハヤタ地域の氷河の微生物調査が行われた（Aoki et al., 2014; Shirakawa et al., 2016）．これらの北極を取り囲む氷河にはそれぞれどのような雪氷藻類が生息し，それぞれどのように温暖化の影響を受けているのだろうか．グリーンランドの暗色化の理解のためには，北極域の雪氷藻類および暗色化現象の地理的な比較が欠かすことができない．本稿では，北極を取り囲むアラスカ，東シベリア，スバールバル，グリーンランド（図 2）の順に，近年明らかになってきたそれぞれの地域の氷河上の雪氷藻類を整理して，北極の氷河の暗色化過程の理解と今後の展望を述べてみたい．

2．アラスカの氷河の雪氷藻類

北米大陸の北西に位置するアラスカには，東西に走る山脈が大きく三つ存在し，それぞれの山脈に数多くの山岳氷河が発達している．その三つの山脈とは，アラスカ北部のブルックス山脈，中部のアラスカ山脈，そして南部の海岸山脈である．北部のブルックス山脈は，北極圏に位置しているが，降水量が少ないため氷河の規模は小さい．一方，南部の山岳地帯は，太平洋からの豊富な水蒸気供給があるために巨大な氷河が発達している．南部の海岸山脈や中部のアラスカ山脈の氷河は，比較的アクセスがよいことから，古くから氷河の質量収支観測をはじめ，さまざまな研究が行われてきた．質量観測の記録によれば，どの氷河も特に 1990 年代以降大幅に縮小している（e.g. Josberger et al., 2007）．

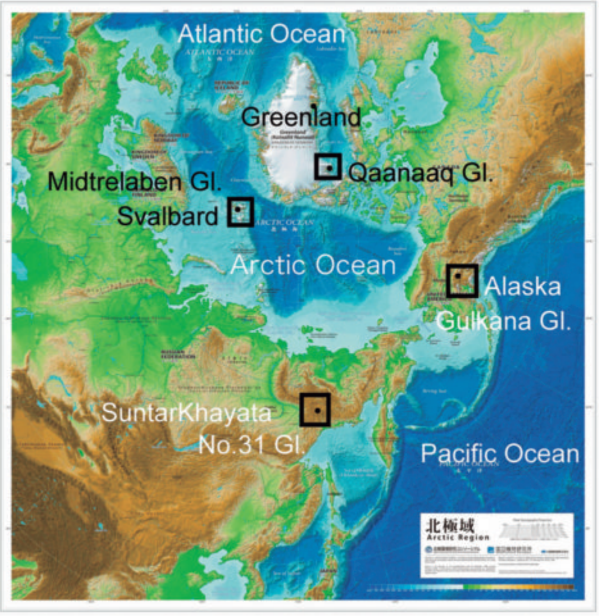

図 2：北極域の地図．本稿で扱うアラスカ，スンタルハヤタ，スバールバル，グリーンランドの氷河の位置を示した．地図は北極コンソーシアムより．

Figure 2：Map of the Arctic region, showing the locations of Alaska, Suntar-Khayata, Svalbard, and Greenland, where the algal communities are described in this paper.

アラスカの雪氷藻類についての最初の包括的な報告は，20 世紀前半のハンガリーの藻類学者エリザベート・コル（Erzsébet Kol）によるものである．コルはアラスカ南部の海岸山脈から中部アラスカ山脈にかけて氷河や残雪を採取し，顕微鏡観察に基づく雪氷藻類の分類を行った（Kol, 1942）．彼女の記載によれば，緑藻やシアノバクテリアを含む数十種の多様な藻類が，氷河や積雪上で観察されている．

2000 年以降，著者のグループはアラスカの氷河上の雪氷藻類について，より定量的な調査を行ってきた．主な調査対象としたのは，アラスカ中部アラスカ山脈に位置し，長期の質量収支観測が行われているグルカナ氷河である（図 3a）．グルカナ氷河は，標高 2400 m から 1220 m を南向きに流れる面積 21.8 km^2，全長 4 km の小型氷河である．この氷河は，車と徒歩によるアクセス，さらに徒歩による末端の消耗域から涵養域までの連続的な調査が可能な氷河である．高度別に 6 サイトの表面の氷または雪を採取し，顕微鏡分析により雪氷藻類のバイオマス（藻類細胞体積）を測定した結果，33–2211 μL m^{-2} の

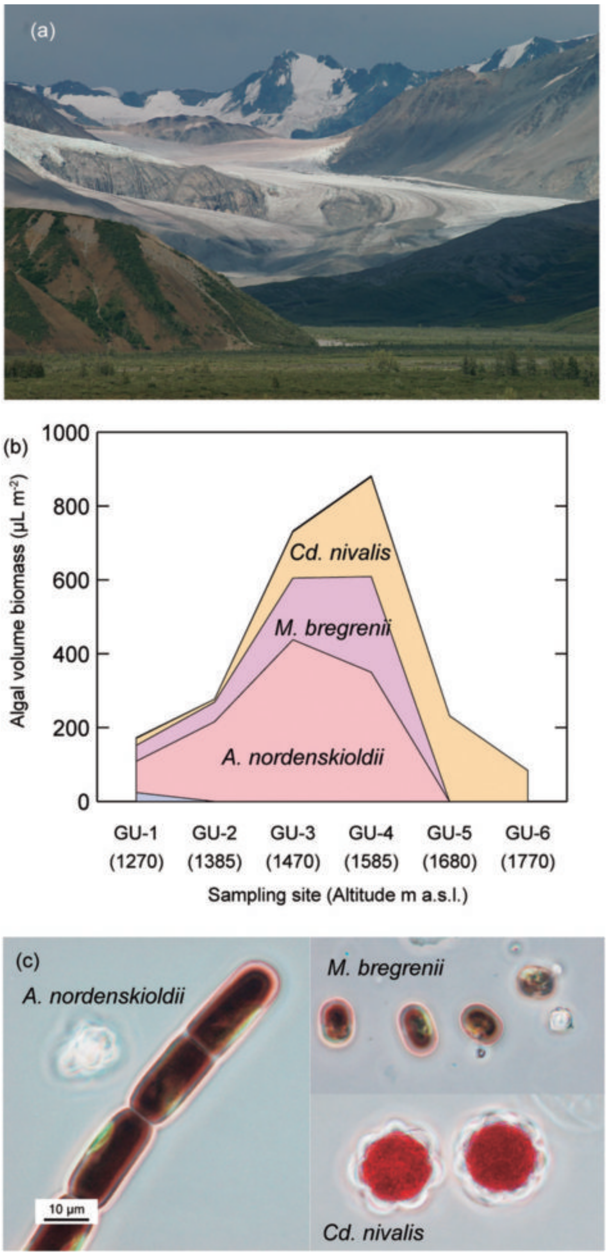

図 3：アラスカの（a）グルカナ氷河（2010.8），（b）グルカナ氷河の雪氷藻類の高度分布，（c）グルカナ氷河の雪氷藻類の優占種 3 種．Takeuchi（2001）から改変．

Figure 3：(a) Photograph of Gulkana Glacier in Alaska (Aug. 2010), (b) altitudinal distribution of snow algal communities on the glacier, (3) photographs of three major algae on the glacier.　The data are by Takeuchi (2001).

範囲で高度によって変化し，中流部付近で最も多いことが明らかになった（図 3b，Takeuchi, 2001）．このバイオマスは，ヒマラヤの氷河などアジア山岳氷河に匹敵する量である一方，藻類の構成（群集構造）はアジアの氷河とは全く異なっていた．アジアの氷河では，シアノバクテリアが優占種することが多いが，グルカナ氷河では緑藻の *Ancylonema*（*A.*）*nordenskioldii*，*Mesotaenium*（*M.*）*bregrenii*，という 2 種が優占種で全バイオマスの 8 割近くをしめていた．*A. nordenskioldii* は複数の円筒形の細胞が連なった藻類で，*M. bregrenii* はより小型の円筒形の単細胞の藻類である（図 3c）．両藻類ともに深紅の色素で細胞内が満たされていることから，これらの藻類の繁殖は氷河表面を赤または紫色に着色し，アルベド低下の原因にもなる（Takeuchi, 2013; Remias et al., 2011; 2009）．氷河上流部の積雪域では，赤い色素をもつ藻類として知られる *Chlamydomonas*（*Cd.*）*nivalis* が優占し，肉眼でもはっきりわかる鮮やかな赤雪が広がっていた．この積雪域の *Cd. nivalis* の大規模な繁殖もアジア山岳域ではみられない特徴である．さらに融雪初期の 5 月から末期の 9 月までの藻類群集の季節変化を観測した結果，氷河上の雪線の上昇とともに藻類の分布範囲が上流部へ広がっていくこと，雪線付近には常に *Cd. nivalis* の赤雪がみられること，露出した裸氷域にはすぐに *A. nordenskioldii* と *M. bregrenii* の 2 種が繁殖し，融雪期末期までバイオマスが増加することなど，季節によって氷河上の藻類分布が変化していく様子が初めて明らかになった（Takeuchi, 2013）．

一方，氷河表面に堆積している全不純物の量は，乾燥重量で 1.0–102 g m^{-2}（平均 23 g m^{-2}）となり，ヒマラヤの氷河の約 10 分の 1 程度の量しかないことがわかった（Takeuchi, 2002）．藻類バイオマスとしては，アラスカもアジアの氷河に匹敵する量であったが，全不純物量でみるとやはりアラスカはアジアに比べて少なく，このことはアラスカの氷河表面の暗色化の程度も小さいことを示している．不純物の顕微鏡観察の結果は，藻類細胞と鉱物粒子のほか，黒色のクリオコナイト粒も含まれていた．有機物の含有量は平均で 7.1% であった．表面の反射率を測定した結果は，消耗域表面は 0.3–0.5 で，表面不純物量と負の相関があること，また不純物量の多い中流域では比較的低いことを示した．しかしながら，アジアの氷河のアルベド（0.1–0.2）に比べるとその反射率は全体的に高い値であり，不純物の暗色化への寄与は限定的であるといえる（Takeuchi, 2009）．

アラスカの南部の海岸山脈では，ハーディング氷原，ワーシントン氷河，マタヌスカ氷河で，限定的であるが雪氷生物の調査が行われ，これらの氷河にもほぼ同様の藻類が観察されている（Takeuchi et al., 2003; 2006）．したがって，グルカナ氷河での微生物と不純物およびアルベドの特徴は，広くアラスカの氷河でみられる特徴としてもほぼ問題ないと思われる．海岸山脈の氷河には，コオリミミズ（ice worm）という珍しい無脊椎動物が生息していることが知られ，氷河上の藻類やバクテリアを捕食していることから，氷河上の微生物群集への影響があ

るかもしれない（e.g. Murakami et al., 2015）．以上のように，アラスカの雪氷藻類は，緑藻が優占するというアジア山岳氷河とは明確に異なる特徴をもっていることが明らかになった．

3．東シベリア，スンタルハヤタの氷河の雪氷藻類

シベリアの東部を流れるレナ川の東側には，数多くの氷河が分布する山岳地帯が広がっている．その中でもスンタルハヤタ山域（北緯62°-63°，東経140°-142°）には，総面積163 km^2，合計195の氷河が存在している（Ananicheva and Koreisha, 2005）．この山域は，サハ共和国の首都ヤクーツクから550 km，オホーツク海沿岸の街マガダンからも550 kmも離れた場所にあり，アクセスの難しい地域であるが，国際地球観測年（IGY）の期間に旧ソ連の研究者によって集中的な氷河の観測が行われた．その後，21世紀に入って日本とロシアの共同調査が断続的に行われ，氷河変動に関するデータが蓄積されてきた．2011年から始まった日本のGRENE北極プロジェクトでは，再びこの地域が観測対象地となり，ロシア凍土研究所との共同研究として集中的な観測が行われた．スンタルハヤタ地域は，北半球最寒気温の記録をもつ街であるオイミヤコンがあるなど，シベリア特有の寒冷な気候で特徴づけられるが，近年の温暖化の影響はここでもはっきりと現れてきている．1945年からの60年間の間に1.9℃の気温上昇（Takahashi et. al., 2011）と，20.8％の全氷河群の総面積減少が報告されている（Ananicheva and Koreisha, 2005）．IGYの観測からの調査対象氷河であるNo.31氷河は，IGY時には面積3.20 km^2，全長3.85 kmであったが（Koreisha, 1963）．GRENE北極プロジェクトによる2012年の再測量の結果，面積は2.27 km^2，全長は3.38 kmにまで縮小したことが明らかになった（Shirakawa et al., 2016）．No.31氷河は，標高2730 mから2020 mまで北西方向へ流れる山岳氷河で，アラスカのグルカナ氷河とほぼ同じ面積をもつ（図4a）．GRENE北極プロジェクトでは，No.31氷河を中心に氷河観測とともに雪氷生物の調査も行われた．

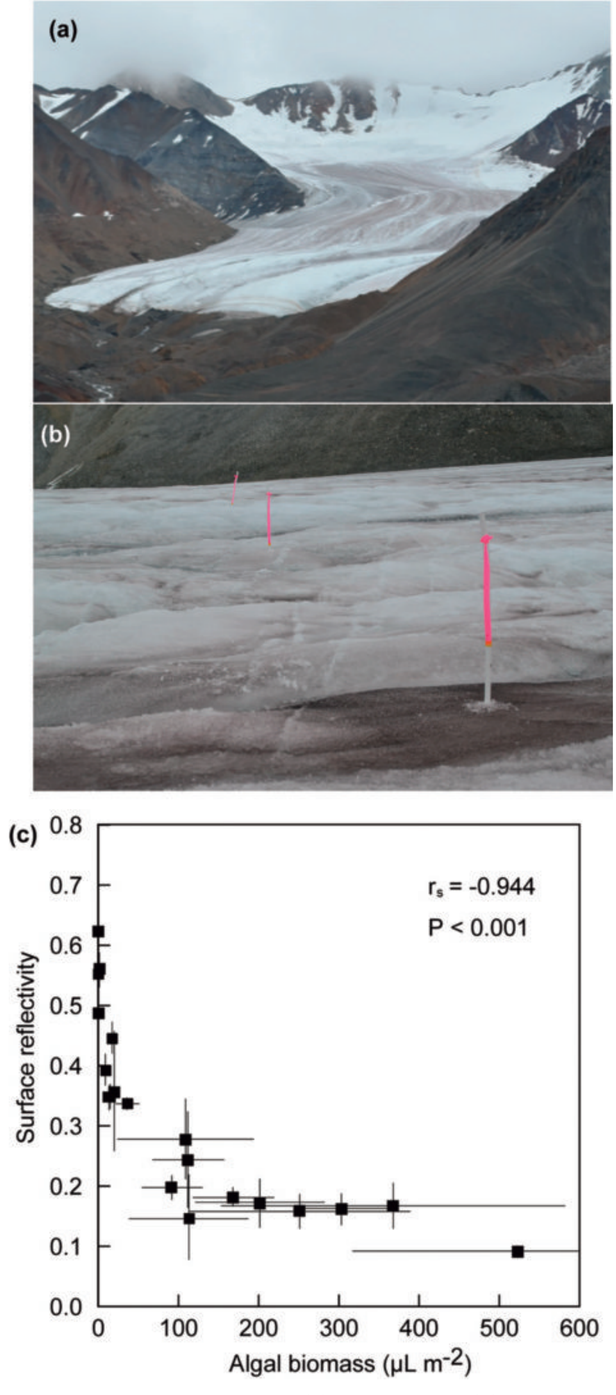

図4：スンタルハヤタ地域の（a）No.31氷河，（b）No.31氷河裸氷域の融解速度測定のために設置したステーク，（c）No.31氷河の表面反射率と雪氷藻類*A. nordensholdii*のバイオマスとの負の相関．Takeuchi et al.（2015）より引用．

Figure 4：(a) Photograph of No.31 Glacier in Suntar-Khayata, eastern Siberia, (b) stakes for melt rate measurement on the bare ice area of the glacier, (c) significant negative correlation between surface reflectivity and algal biomass of *A. nordensholdii*. The data are by Takeuchi et al. (2015).

雪氷藻類群集を調査した結果，スンタルハヤタ山域の氷河には7種の藻類が生息していることが確認された（Tanaka et al., 2016）．藻類バイオマスは，30-3968 μL m^{-2}の範囲で，アラスカ同様に中流域で高くなる高度分布を示したが，全体的にバイオマスは高く，アラスカよりも3倍以上高い場所もあることがわかった．裸氷域ではアラスカの氷河で優占種であった*A. nordenskioldii*がバイオマスの9割近くを占めていた．一方，アラスカの氷河で*A. nordenskioldii*と並んで優占種であった*M. bregrenii*は，スンタルハヤタ山域の氷河では見られなかった．積雪域では*Chloromonas* sp.という緑藻が優占

し，アラスカ同様に肉眼で確認できる赤雪が氷河上に広がっていた．No.31 氷河の表面の全不純物量は，裸氷域で 14–142 $\mathrm{g\,m^{-2}}$（平均：47 $\mathrm{g\,m^{-2}}$）とほぼアラスカと同レベルで，高度分布も中流部で高い傾向であった．不純物の構成も，藻類の他，鉱物粒子とクリオコナイト粒であり，アラスカの氷河と同様である．ただし，有機物含有量は平均で 13.5%とアラスカよりも高い傾向にあった．

スンタルハヤタ山域では，2012 から 2014 年の 3 年間を通して雪氷藻類の観測を行っている（Tanaka et al., 2016）．その結果，氷河上に現れる藻類の群集構造には年によって大きな変化はないことがわかった．一方，バイオマスは年によって異なり，観測を行った 3 年間の中で，2012 年がもっとも大きく，その年は最も気温が高く融解が進んだ年に一致した．このことは，藻類の繁殖量は，融解期の気温に依存することを示唆している．

No.31 氷河ではさらに，氷河表面の融解速度を氷河上の多地点で 10 日間観測し，融解速度を決めている要因は不純物の中でもどの成分なのかについて検討した（図 4b，Takeuchi et al., 2015）．氷河表面の 20 地点の融解速度を，正の気温 1℃かつ 1 日あたりの融解量に基準化した Positive Degree-Day Factors（PDDF）として表したところ，観測表面によって 3.00 から 8.55 mm w.e. $\mathrm{K^{-1}\,day^{-1}}$ の範囲をとることがわかった．この融解速度は，各地点で測定した表面反射率と負の有意な相関があり，これは表面のアルベド，つまり暗色化の程度が融解速度を決めていることを示している．さらに表面反射率と氷河表面不純物の各構成物と相関をとった結果，反射率は全不純物量とは有意な相関がなかった一方，不純物の構成物の中でも，有機物量および藻類群集の優占種である *A. nordenskioldii* のバイオマスと有意な負の相関を示した（図 4c）．これは，氷河表面の *A. nordenskioldii* の繁殖量が，表面の暗色の程度を決め，融解を加速していることを示している．氷河全体の平均反射率に基づくと，この暗色化によって融解速度は 1.6 から 2.6 倍に大きくなっていることがわかった．この氷河の暗色の程度は，単に全不純物量が決めているのではなく，暗色の色素を持つ緑藻の *A. nordenskioldii* が決めていることが，重要な点である．

4．スバールバルの氷河の雪氷藻類

スバールバルはノルウェーの北西バレンツ海に浮かぶ北極圏の群島で，各島には数多くの氷河・氷帽が存在する．スバールバル諸島の定住地であるニーオルスンやロングイヤービエンには研究をサポートする設備が充実し，世界各地から多くの研究者が訪れ周辺の氷河で様々な観測が行われてきた（図 5）．

図 5：スバールバル，（a）ニーオルスンと周辺の氷河，（b）ミドトレラーベン氷河の裸氷面．不純物で色がついているのがわかる．

Figure 5：(a) The scientific station Ny-Alesund and nearby glaciers in Svalbard, (b) the bare ice surface with biogenic impurities on Midtrelaben Glacier (Aug. 2013).

スバールバルの雪氷微生物について最初の詳しい報告は，アラスカ同様コルによるものである．Kol and Eurola（1974）による報告では，観察された藻類は細胞形態を基に 12 種に分類され，アラスカやスンタルハヤタの氷河裸氷域の優占種 *A. nordenskioldii* や *M. bregrenii* のほか，積雪域の赤雪の優占種 *Cd. nivalis* など，北極圏の他の地域にも見られる共通種が記載されている．その後 1990 年代後半には，雪氷藻類の種の同定や分布，分散過程，栄養塩との関係など，様々な研究が行われた．スバールバル北西部を中心に多地点で赤雪を調査した結果では，赤雪には *Chlamydomonas* spp. および *Chloromonas* spp. の 2 種が含まれ（Müller et al, 1998; 2001），これらの藻類の起源は，前年の表面からの移動ではなく，土壌での胞子が大気を介して積雪上に飛来し始まることを明らかにした（Müller et al., 2001; Stibal et al., 2006）．氷河の裸氷域表面では，クリオコナイト粒の形成が確認され，その氷河上の構造と成長過程についても詳しく調べられている（Hodson et al., 2010）．

氷河上の雪氷藻類群集について，アラスカやスンタル

ハヤタの氷河の藻類と比較できるようなバイオマスのデータは，まだ未公表であるが著者らによる2011年および2013年の調査で得られている．スバールバル北西部ニーオルスン周辺の氷河裸氷域で調査した結果，藻類バイオマスは14–473 µL m^{-2}で，ほぼアラスカのグルカナ氷河と同程度であった．藻類群集の構成もアラスカと同様で，*A. nordenskioldii*がほとんどの地点で優占種であったが，一部の氷河ではシアノバクテリアの割合が高い場所もあった．氷河表面の全不純物量は，14–91 g m^{-2}（平均：30.5 g m^{-2}）で，アラスカやスンタルハヤタと同レベルであった．不純物の構成も同様であったが，有機物含有量は平均5.9%で他の地域と比べて少なめであった．これは，不純物中の鉱物粒子の割合が高いことを意味するが，後述する通り一部シアノバクテリアが藻類群集の優占種となっていることと関係がある可能性がある．

スバールバルでは雪氷微生物の氷河表面アルベドや氷河融解量に対する影響についての定量的な研究例はまだないが，氷河融解については多くのモデルが提案されている．その中の一つ，気温を指数化した（PDDF法）モデルによる氷河融解量の見積もりでは，モデルと観測の結果の一部の不一致について，スンタルハヤタで明らかになったような，生物由来不純物によるアルベドの空間分布が関わっていることが指摘されている（Irvine-Fynn et al., 2014）．したがって，スバールバルの氷河でも雪氷藻類による暗色化が起きていることは間違いなく，今後詳しい研究が進むことが期待される．

5．グリーンランドの雪氷藻類

グリーンランド氷床は，他の北極圏の氷河と比べて圧倒的にその規模が大きい．氷床面積は約180万km^2，質量は2657兆トンで，前章まで見てきた面積わずか数km^{2}の氷河とは桁違いの氷河である．しかし，このような巨大氷床も，雪の涵養と氷の融解，流動などといった物理的プロセスは小型氷河と等しく，グリーンランド氷床の表面にも小型氷河と同様の微生物現象があっても不思議なことではない．グリーンランドの雪氷微生物は，19世紀の北極探検の時代に発見され，数は少ないものの古くから記載的な研究が行われてきた．しかし，グリーンランド氷床のような巨大な氷河では，全域の把握はほぼ不可能に近く，調査は集落が存在するアクセスの良い地域に限られている．例えば主な雪氷微生物の調査は，北西部のチューレ，中西部のカンゲルスアーク，北東部のクロンプリンツ・クリスチャンランド，南東部のタシラック等の周辺に限られる．グリーンランドの雪氷微生物の歴史的な経緯の詳しくは永塚ほか（2012）や竹内（2011）にまとめられているが，19世紀のノルデンショルドによるクリオコナイトの発見とジョン・ロス（John Ross）による赤雪の発見に始まり，2000年代以降は最もアクセスの良いカンゲルサークの地域で集中的な調査が行われ，藻類の生産量（Cook et al., 2012），バクテリア群集（Cameron et al., 2016），栄養塩循環（Telling et al., 2012），氷河表面有機物の起源と収支（Stibal et al., 2012），緑藻による裸氷域の暗色化（Yallop et al., 2012）などが明らかになっている．

2011年より始まった日本のSIGMA及びGRENEプロジェクトでは，グリーンランド北西部カナック氷帽周辺および中西部カンゲルサーク周辺の地域を中心に調査が行われた．北西部の半島に位置するカナック氷帽は，グリーンランド氷床とは独立した面積286 km^{2}の氷帽である．定期便でアクセス可能な集落であるカナックから，徒歩でアクセスできることから，2011年からこの氷帽で集中的な観測が行われた．これらの調査によって，前述のアラスカ等と比較可能な藻類群集のデータが得られた（Uetake et al. 2016）．

カナック氷河の雪氷藻類の高度分布は，42–584 µL m^{-2}（平均：337 µL m^{-2}）の範囲で変動し，バイオマスが比較的高いのは氷河の中流から下流部であった（Uetake et al., 2016）．藻類群集構造も他の北極地域の氷河と概ね同様で，裸氷域では*A. nordenskioldii*が44–83%を占める優占種で，積雪域では*Cd. nivalis*が優占し，雪線近くには赤雪が広がっていた．中流部の一部の表面では，シアノバクテリアの割合が高くなっている場所があった．これは，スバールバルにも見られたことで，後に述べるクリオコナイトの分布と関わっている．

氷河表面の全不純物量は，裸氷域で1.2–32.7 g m^{-2}（平均14.7 g m^{-2}）で，他の北極域の氷河よりも若干少ない程度である（Takeuchi et al., 2014）．最も不純物が多かったのは，氷河中流域の地点である．不純物の有機物含有量は平均5.2%で，スバールバルに近く，低めの値であった．不純物量の高度分布は，衛星画像でみたカナック氷河の表面の反射率と一致する．衛星画像では，氷河末端部や上流部では白く反射率が比較的高いが，中流部は暗色で反射率が低いことがわかる（図6a）．さらにこの氷河表面の反射率の高度分布は，カナック氷河の融解速度の観測結果にも一致する（Sugiyama et al., 2014）．カナック氷河の上流から下流にかけての融解量の観測をもとに求められたPDDFは，氷河下流部では5.44–5.45mm w.e. K^{-1} day^{-1}であるのに対し，中流部では

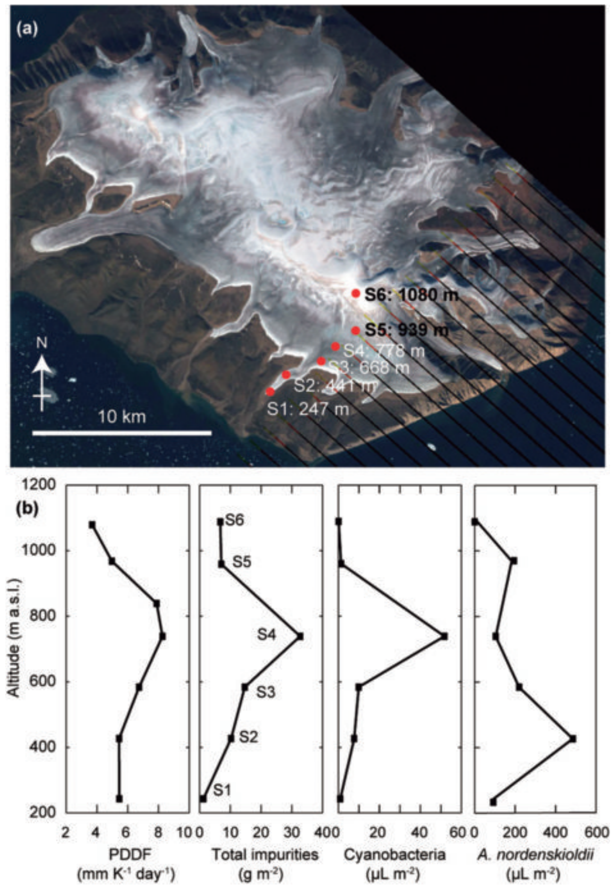

図 6：グリーンランド，(a) カナック氷帽の衛星画像（Landsat 7, 2011.8）．カナック氷河上の観測サイトを示した．（b）カナック氷河上の融解速度（PDDF），全不純物量，シアノバクテリアと緑藻 *A. nordensholdii* の各バイオマスの高度分布．Sugiyama et al.（2014），Takeuchi et al.（2014），Uetake et al.（2016）から引用．

Figure 6：(a) Landsat-7 satellite image of Qaanaaq Ice Cap in northwest Greenland (Aug. 2011), showing the study site along the Qaanaaq Glacier profile. (b) Altitudinal distribution of PDDF, total impurity abundance, and biomass of cyanobacteria and green algae (*A. nordenshioldii*) on Qaanaaq Glacier. The data are by Sugiyama et al. (2014), Takeuchi et al. (2014), and Uetake et al. (2016).

6.74–8.26 mm w.e. K^{-1} day^{-1} と大きい値を示した（図 6b）．この結果は，暗色化によって中流部の融解速度が 1.2 から 1.5 倍に加速されていることを示している．

スンタルハヤタの氷河では暗色化の要因は，全不純物量というよりも緑藻 *A. nordenskioldii* のバイオマスであったが，カナック氷河では暗色化している領域は，全不純物量が多い場所に一致した．*A. nordenskioldii* はカナック氷河でも優占種ではあったが，その高度分布と暗色域は一致せず，むしろシアノバクテリアの分布が暗色域に一致した（図 6b）．このことは，カナック氷河での暗色化は，暗色色素を持つ *A. nordenskioldii* の繁殖によるのではなく，シアノバクテリアの繁殖によってクリオコナイト粒が形成されることによって引き起こされていることを示唆している．シアノバクテリアのバイオマスは，*A. nordenskioldii* に比べて 1 桁小さいが，シアノバクテリアは鉱物粒子と有機物とでクリオコナイト粒を形成するため，その効果によるアルベド低下への寄与が *A. nordenskioldii* を上回るのである．不純物量が多い中流部では，実際クリオコナイト粒が発達していた．クリオコナイト粒の大きさと微生物量との関係を分析した結果からは，シアノバクテリアの中でも，*Phormidesmis* (*P.*) *priestleyi* という種が粒の成長に重要な役割を果たしていること，さらにシアノバクテリアが繁殖する条件は，鉱物粒子の供給が多いことであることが示唆された（Uetake et al., 2016）．

以上明らかになったカナック氷河の暗色化のプロセスは，広大なグリーンランド氷床の北西部の 1 点の調査であり，必ずしも全域にあてはまることではないかもしれない．グリーンランド氷床で，最も裸氷域が広がり表面融解が大きいのは中西部であり，この地域の暗色化の要因を理解することが重要であるが，カナック氷河と同様にシアノバクテリアによるクリオコナイト粒の発達によるという意見（Chandler et al., 2015）や，スンタルハヤタの氷河と同様に暗色色素の緑藻によるという意見（Yallop et al., 2012）もある．グリーンランド氷床全域の特徴を理解するためには，今後より多くの地点で調査を進める必要がある．

6．北極域の雪氷藻類と氷河の暗色化

北極周辺の 4 地域の氷河上の雪氷藻類群集，およびその暗色化と融解への影響について，以上の通り整理した結果，藻類が関わる氷河の暗色化には大きく 2 つのプロセスがあることがわかった．一つは，暗色色素をもつ緑藻 *A. nordenskioldii* による氷河の暗色化である．スンタルハヤタ地域の氷河では，この藻類のバイオマスと表面反射率の間に負の相関があり，バイオマスの高い表面で実際に融解が加速されていることが明らかになった．このような暗色色素を持つ緑藻による裸氷域の暗色化は，Yallop et al.（2012）によりグリーンランド氷床中西部でも顕著であることが報告されている．*A. nordenskioldii* は，アジアの氷河ではほとんど観察されることはないが，北極圏の 4 地域のどの氷河でも全藻類バイオマスの 50％以上を占める優占種であった（図 7）．これはこの藻類が北極圏の特徴的な種であることを示している．しかし，*A. nordenskioldii* のバイオマスを 4 地域で比較すると，スンタルハヤタ地域の氷河では平均 1600 μL m^{-2} で，アラスカやグリーンランドの 5 倍近い値であ

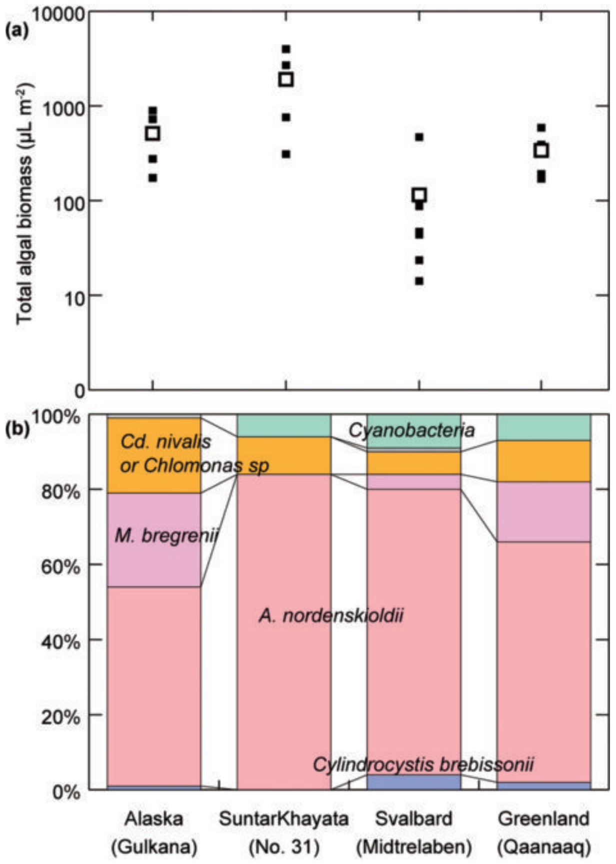

図７：本稿で扱った北極域４地域（アラスカ，スンタルハヤタ，スバールバル，グリーンランド）の各氷河裸氷域の（a）雪氷藻類バイオマス（■：観測値，□：平均）と（b）雪氷藻類群集構造の比較．各データは，Takeuchi（2001），Tanaka et al.（2016），Uetake et al.（2017）と竹内の未公表データから引用した．

Figure 7：Comparison of (a) total algal biomass (open and solid squares represent mean and study site values), (b) algal community structure among the four glaciers in the Arctic region. The data are by Takeuchi (2001), Tanaka et al. (2016), Uetake et al. (2017) and unpublished data by the author (Svalbard).

ることがわかった．つまり，スンタルハヤタ地域でのみこの緑藻の暗色化の効果が現れたのは，*A. nordenskioldii* の大きな繁殖量が原因であると考えられる．なぜスンタルハヤタ地域で，この藻類のバイオマスが特別に大きいのか，その原因の特定には *A. nordenskioldii* の生態の理解が必要であるが，まだ不明なこと多い．Remias et al.（2011）は，*A. nordenskioldii* の暗色の色素の特定を試みているが，まだはっきりした色素名は不明である．*A. nordenskioldii* は，北極圏の氷河だけでなく北極海の海氷表面でも繁殖が確認されている（Melanikov, 1997）．このことは，この藻類が大気を介して北極圏に広く分散していることを示唆しているが，詳しい分散過程の研究もこれからの課題である．アラスカの氷河での季節変化の観測では，*A. nordenskioldii* は融解期間を通して繁殖しバイオマスが連続的に増加した（Takeuchi, 2013）．気温上昇によって融解期間が長くなれば，その分この藻類による氷河表面の暗色化が広がるかもしれない．

もう一つの暗色化のプロセスは，シアノバクテリアによるクリオコナイト粒の形成である．アラスカ，スバールバル，グリーンランドでは，氷河の反射率は全不純物量に依存した．つまり，クリオコナイト量が反射率を決めていることを示している．グリーンランドのクリオコナイト粒を形成するシアノバクテリア *P. priestleyi* は，北極圏全域に共通する種であることも明らかになってきている（Chrismas et al., 2016）．したがって，クリオコナイトによる暗色化の理解には，このシアノバクテリアの生態を知ることが必須である．グリーンランドの分析では，氷河表面への鉱物粒子の供給量がシアノバクテリアの繁殖量を決めていることが示唆された（Uetake et al., 2016）．それでは，氷河表面への鉱物粒子はどこから来るのだろうか．グリーンランドのアイスコア中のダスト粒子の分析では，鉱物粒子がアジアの砂漠に由来し，大気を介して長距離輸送されてきたものであることが示されている（Biscaye et al., 1997）．しかしながら，クリオコナイト中の鉱物粒子に含まれる微量元素 Sr と Nd の安定同位体比の分析から，これらの鉱物粒子の起源はアジアではなく氷床周囲の地表面であることがわかった（Nagatsuka et al., 2016）．ただし，単に氷河の周囲から鉱物粒子が供給されるのであれば，氷河の下流部ほど堆積量が増えることが予想されるが，実際にはどの氷河も鉱物粒子の堆積量が多いのは下流部よりもむしろ中流部である．さらに安定同位体の分析をすすめた結果，中流部の鉱物粒子は，大気から直接氷河表面に堆積したものではなく，もともと氷河の氷に含まれていた鉱物粒子が氷の融解とともに露出して堆積したものであることがわかった．中流部の暗色域には暗色の縞模様が見えることも，鉱物粒子が氷体内の層に由来することを示唆している（Takeuchi et al., 2014）．グリーンランド氷床の中西部でも，辺縁部よりも中流部に暗色域が広がっていること，暗色域に縞模様が見られることから，氷体内の鉱物粒子が暗色域形成の要因となっていることが示唆される（Wientjes et al., 2011）．以上のことから考えられるプロセスは，氷河周辺を起源とする鉱物粒子が，完新世の数百から数千年前のある時代に氷床上に堆積し，その堆積層が氷河流動によって下流に移動し，現在表面に現れたところでシアノバクテリアが繁殖しクリオコナイト粒が形成，暗色化が起きている，ということである．鉱物粒子の大気からの供給及び氷体内の物質の移動と表面への堆積過程については，簡単なモデルがつくられている

（Goelles et al., 2015）．グリーンランド氷床のような大規模な氷河では，このような氷体内の鉱物粒子の分布が暗色化に大きな役割をもつ可能性がある．氷体内の鉱物粒子は，いつ堆積したものなのか，毎年どれくらいの量が表面へ露出しているのか，観測とモデルを合わせて定量的に理解することが今後の重要な課題である．

緑藻の *A. nordenskioldii* とシアノバクテリア *P. priestleyi* は，同じ光合成微生物でも，それぞれの繁殖の特徴は大きく異なり，その違いはこの二つの暗色化のプロセスを理解するうえで重要である．アラスカの氷河の季節変化が示す通り，裸氷域が露出してから繁殖する速さは，シアノバクテリアに比べ緑藻の方が明らかに速い（Takeuchi, 2013）．このことは，緑藻はその融解期が始まるとともに繁殖を開始し，その年の条件によって最大繁殖量が決まることを示す．したがって，緑藻による暗色化は，各年の条件に依存することを意味する．一方，シアノバクテリアは，繁殖速度は遅いがクリオコナイト粒は氷河表面を流れる融解水に流されにくく，年を超えて表面に堆積していく．したがって，シアノバクテリアによる暗色化は，毎年生産された有機物が蓄積されていくプロセスを含む複数年をまたいだ長期的なものと考えられる．グリーンランド氷床中西部の裸氷域は流動方向に長さ 50 km 以上に渡る広大な領域であるため，氷河上に物質は融解水に流されながらも長期間滞在すると考えらえる．これは長さ数 km 規模の小型氷河と大きく異なる点である．クリオコナイト粒については，実験室での成長実験を行うことも成功しているが（Musilova et al., 2016），このような鉱物粒子の供給とシアノバクテリアの繁殖を合わせたクリオコナイトの長期的な変化の理解が今後必要である．

氷河表面のクリオコナイト量については長期的に変動すると考えられる一方，衛星画像からみた暗色化した表面は毎年大きく変化していることも明らかになっている．グリーンランド氷床中西部では，2000 年からの 15 年間で暗色化した裸氷の面積が 7 倍以上にまで増加していた一方，年々変動も大きい（図 8a，b，Shimada et al., 2016）．この年々変動は，クリオコナイト量というよりも，氷表面の微構造によるものと考えられる．氷河の氷表面は，純氷の平らな面が広がっているわけではなく，表面には細かい隙間が無数にある風化氷やクリオコナイトホールという円柱上の水たまりが発達している．このような氷が発達すると，表面の不純物が氷の隙間や穴の中に沈みこんで，広域的にみたアルベドは上昇する（図 8c，Bøggild et al., 2010）．このような氷の発達具合は Chandler et al.（2015）が明らかにしている通り季節単位で大きく変化する．Shimada et al.（2016）が，暗色域の面積と日射に負の相関があることを明らかにした通り，表面氷の構造は日射や気温が関わる表面の熱収支バランスの影響をうけると考えられ，そのプロセスを明らかにすることが実際の暗色域の変動の理解に欠かせない．さらに，表面氷の構造は，栄養塩を含む物質の循環や，緑藻を含む裸氷上の微生物の活動にも強く関わっている可能性が指摘されている（Irvine-Fynn and Edwards, 2014）．Cook et al.（2015）が Biocryomorphology という概念を提案しているように，アルベドと裸氷の構造，物質循環，微生物活動を総合した理解が，今後の大きな課題と言えるだろう．

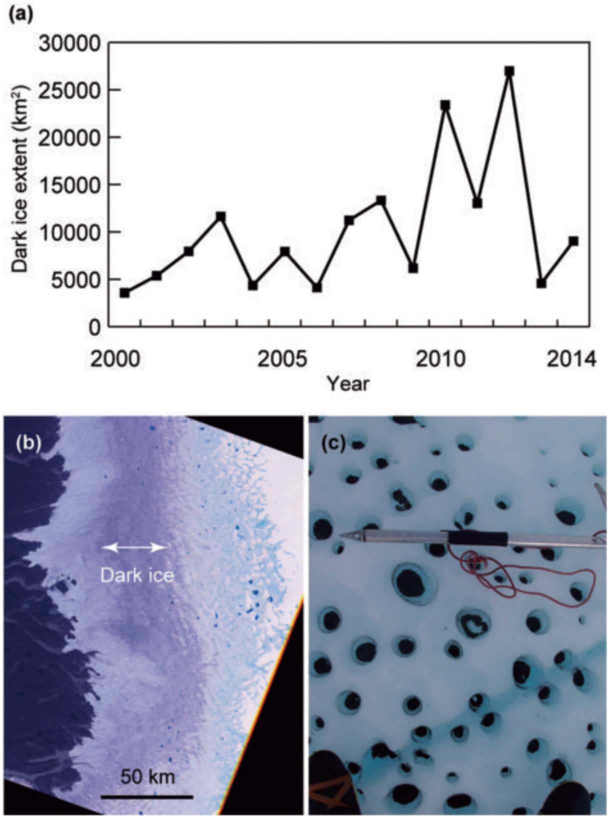

図 8：グリーンランド氷床の（a）暗色域面積（7 月平均）の経年変動，Shimada et al.（2016）から引用，（b）衛星画像からみた暗色域（Landsat 7, 2001.7.18），（c）暗色域面積の経年変動の要因の一つである裸氷域に発達したクリオコナイトホール．

Figure 8：(a) Inter-annual variation in the dark ice extent of the Greenland Ice Sheet (July mean) by Shimada et al. (2016), (b) the dark ice in the western Greenland Ice Sheet (Landsat 7, 18 July 2001), (c) cryoconite holes on the bare ice surface, which have an effect of hiding impurities from the surface and reducing the dark ice area.

北極域氷河の暗色化については裸氷域だけでなく，赤雪藻類による積雪域のアルベド低下も評価する必要がある．本稿で見た 4 地域では，積雪域に緑藻の *Chlamydomonas* sp. または *Chloromonas* sp. による赤雪現象が

見られた．赤雪は，衛星画像からも北極域に広く起きていることが確認されている（Hisakawa et al., 2015）．裸氷域と異なり冬期に降った積雪の表面で毎年繁殖が始まる．Lutz et al.（2016）は，北極域の広範囲（グリーンランド，スバルバール，アイスランド，スウェーデン）の赤雪の比較から，積雪上で繁殖するバクテリア群集は地域によって全く異なる一方，藻類群集は地域によらずほぼ同じであることを明らかにした．赤雪を引き起こす藻類が北極域で共通するとし，藻類によるアルベド低下量を求めグリーンランド融解量の見積もりを行っている．しかし，この融解量の見積もりに用いたのは，観測値に基づく経験的なアルベド低下量であり，BC やダスト，積雪粒径などの他の物理的要因の影響は考慮されていない．実際のアルベド低下の評価および将来予測には，藻類の繁殖の時間変化をモデル化し，他の不純物と合わせて物理モデルに基づきアルベドを計算することが必要である．表面の藻類量の増加に関しては，Onuma et al.（2016）が，日本の十日町の積雪で融解期に連続観測をすることによって，積雪表面に藻類が出現するタイミングおよび出現以降の増加する過程を明らかにした．この観測をもとに藻類量を時間の関数にしたモデルを提案している．SIGMA プロジェクトでも同様な赤雪の連続観測が行われ，グリーンランド上の藻類繁殖モデルも提案されている（大沼，2016）．このモデルによって計算された藻類量に加え，積雪に沈着する BC やダスト量をいれた Aoki et al.（2011）や（2013）に提案されているような放射伝達モデル PBSAM でアルベドを計算し，空間的時間的変動を求められれば，藻類の積雪アルベドへの影響の定量的な評価が可能となるだろう．

謝辞

本論文に関する観測，分析，議論に協力いただいた SIGMA および GRENE 北極プロジェクト関係者，千葉大学大学院理学研究科地球科学コース生物地球化学分野学生諸君に深く感謝する．本論文の成果の一部は，JSPS 科研費，26247078，26241020，16H1772 の助成を受けたものである．また本研究成果の一部は，低温科学研究所共同利用研究集会における発表と議論に基づくものである．本論文を書く機会を与えていただいた，杉山慎，飯塚芳徳，Ralf Greve の各氏に感謝する．

参考文献

Ananicheva, M. D. and M. M., Koreisha (2005) Glacial recession in northern and southern parts of Suntar-Khayata Mts. and Chersky Range. *Data of Glaciological Studies*, **99**, 18–25. [In Russian with English summary]

Aoki, T., K. Kuchiki, M. Niwano, Y. Kodama, M. Hosaka, and T. Tanaka (2011) Physically based snow albedo model for caluclating broadband albedos and the solar heating profile in snow pack for general circulation models. *J. Geophys. Res.*, **116**, D11114, doi: 10.1029/2010JD015507.

Aoki, T., K. Kuchiki, M. Niwano, S. Matoba, J. Uetake, K. Masuda, and H. Ishimoto (2013) Numerical simulation of spectral albedos of glacier surfaces covered with glacial microbes in Northwestern Greenland. *In* Radiation Processes in the Atmosphere and Ocean (IRS2012) *Proceedings of the International Radiation Symposium*, **1531** (1), 176–179.

Aoki, T., S. Matoba, J. Uetake, N. Takeuchi, and H. Motoyama (2014) Field activities of the “Snow Impurity and Glacial Microbe effects on abrupt warming in the Arctic” (SIGMA) Project in Greenland in 2011–2013. *Bull. Glaciol. Res.*, **32**, 3–20.

Bøggild, C. E., R. E. Brandt, K. J. Brown, and S. G. Warren (2010) The ablation zone in northeast Greenland: ice types, albedos and impurities. *J. Glaciol.*, **56** (195), 101–113.

Biscaye, P. E., F. E. Grousset, M. Revel, S. Van der Gaast, G. A. Zielinski, A. Vaars, and G. Kukla (1997) Asian provenance of glacial dust (stage2) in the Greenland Ice Sheet Project 2 Ice Core, Summit Greenland. *J. Geophys. Res.*, **102**, 26765–26781, doi: 10.1029/97JC01249.

Box, J. E., X. Fettweis, J. C. Stroeve, M. Tedesco, D. K. Hall, and K. Steffen (2012) Greenland ice sheet albedo feedback: thermodynamics and atmospheric drivers. *Cryosphere*, **6**, 821–839, doi: 10.5194/tc-6-821-2012.

Cameron, K. A., M. Stibal, J. D. Zarsky, E. Gözdereliler, M. Schostag, and C. S. Jacobsen (2016) Supraglacial bacterial community structures vary across the Greenland ice sheet. *FEMS Microbiol. Ecol.*, **92** (2), fiv164.

Chandler, D. M., J. D. Alcock, J. L. Wadham, S. L. Mackie, and J. Telling (2015) Seasonal changes of ice surface characteristics and productivity in the ablation zone of the Greenland Ice Sheet. *Cryosphere*, **9**, 487–504, doi: 10.5194/tc-9-487-2015.

Cook, J. M., A. J. Hodson, A. M. Anesio, E. Hanna, M. Yallop, M. Stibal, J. Telling, and P. Huybrechts (2012) An improved estimate of microbially mediated carbon fluxes from the Greenland ice sheet. *J. Glaciol.*, **58** (212), 1098–1108.

Cook, J., A. Edwards, N. Takeuchi, and T. Irvine-Fynn (2015) Cryoconite The dark biological secret of the cryosphere. *Prog. Phys. Geogr.*, **40** (1), 66–111.

Cook, J., A. Edwards, and A. Hubbard (2015) Biocryomorphology: Integrating Microbial Processes with Ice Surface Hydrology, Topography, and Roughness. *Front. Earth Sci.*, **3**, 78.

Goelles, T., C. E. Bøggild, and R. Greve (2015) Ice sheet mass loss caused by dust and black carbon accumulation. *Cryosphere*, **9**, 1845–1856, doi: 10.5194/tc-9-1845-2015.

Hisakawa, N., S. D. Quistad, E. R. Hester, D. Martynova, H. Maughan, E. Sala, M. V. Gavrilo, and F. Rohwer (2015) Metagenomic and satellite analyses of red snow in the Russian Arctic. *PeerJ*, **3**, e1491.

Hodson, A., K. Cameron, C. Bøggild, T. Irvine-Fynn, H. Langford, D. Pearce, and S. Banwart (2010) The structure, biological activity and biogeochemistry of cryoconite aggregates upon an Arctic valley glacier: Longyearbreen. Svalbard. *J. Glaciol.*, **56** (196), 349–362.

Hoham, R. W. and B. Duval (2001) Microbial ecology of snow and freshwater ice. *In* Snow Ecology. Cambridge University Press: Cambridge; 168–228.

Irvine-Fynn, T. D. L., E. Hanna, N. E. Barrand, P. R. Porter, J. Kohler, and A. J. Hodson (2014) Examination of a physically based, high-resolution, distributed Arctic temperature-index melt model, on Midtre Lovénbreen, Svalbard. *Hydrol. Processes*, **28**(1), 134–149.

Irvine-Fynn, T. D. and A. Edwards (2014) A frozen asset: The potential of flow cytometry in constraining the glacial biome. *Cytometry Part A*, **85**, 3–7, doi: 10.1002/cyto.a.22411.

Josberger E. G, W. R. Bidlake, R. S. March, and B. W. Kennedy (2007) Glacier mass-balance fluctuations in the Pacific Northwest and Alaska, USA. *Ann. Glaciol.* **46**, 291–296, doi: 10.3189/172756407782871314

Kol, E. (1942) The snow and ice algae of Alaska. *Smithsonian Miscellaneous Collections* 101, 1–36.

Kol, E. and S. Eurola (1974) Red snow algae from Spitsbergen. *Astarte*.

Kohshima, S., K. Seko, and Y. Yoshimura (1993) Biotic acceleration of glacier melting in Yala Glacier, Langtang region, Nepal Himalaya. Snow and Glacier Hydrology (*Proceeding of the Kathumandu Symposium*, November 1992), *IAHS Publication*, **218**, 309–316.

Koreisha, M. M. (1963) Present glaciers of the Suntar-Khayata Range (Moscow, Nauka).

Lutz, S., A. M. Anesio, R. Raiswell, A. Edwards, R. J. Newton, F. Gill, and L. G. Benning (2016) The biogeography of red snow microbiomes and their role in melting arctic glaciers. *Nat. Commun.*, **7**, 11968.

Melnikov, I. A. (1997) The Arctic Sea Ice Ecosystem. CRC Press, 80–88.

Murakami, T., T. Segawa, D. Bodington, R. Dial, N. Takeuchi, S. Kohshima, and Y. Hongoh (2015) Census of bacterial microbiota associated with the glacier ice worm Mesenchytraeus solifugus. *FEMS Microbiol. Ecol.*, **91**, fiv003, doi:10.1093/femsec/fiv003.

Musilova, M., M. Tranter, J. L. Bamber, N. Takeuchi, and A. M. Anesio (2016) Experimental evidence that microbial activity lowers the albedo of glaciers. *Geochem. Perspec. Let.*, **2**, 106–116, doi: 10.7185/geochemlet.1611.

Müller, T., W. Bleiss, C. D. Martin, S. Rogaschewski, and G. Fuhr (1998) Snow algae from northwest Svalbard: their identification, distribution, pigment and nutrient content. *Polar Biol.*, **20** (1), 14–32.

Müller, T., T. Leya, and G. Fuhr (2001) Persistent snow algal fields in Spitsbergen: field observations and a hypothesis about the annual cell circulation. *Arct. Antarct. Alp. Res.*, **33** (1), 42–51.

永塚尚子，竹内望，植竹淳（2015）グリーンランド氷床の生物学的研究．月刊地球，37（3），72–82.

Nagatsuka, N., N. Takeuchi, J. Uetake, R. Shimada, Y. Onuma, S. Tanaka, and T. Nakano (2016) Variations in Sr and Nd isotopic ratios of mineral particles in cryoconite in western Greenland. *Front. Earth Sci.,* **4**, 93, doi: 10.3389/feart.2016.00093.

Chrismas, N. A., G. Barker, A. M. Anesio, and P. Sánchez-Baracaldo (2016) Genomic mechanisms for cold tolerance and production of exopolysaccharides in the Arctic cyanobacterium Phormidesmis priestleyi BC1401. *BMC Genomics*, **17** (1), 533.

Onuma, Y., N. Takeuchi, and Y. Takeuchi (2016) Temporal changes in snow algal abundance on surface snow in Tohkamachi, Japan. *Bull. Glaciol. Res.*, **34**, 21–31, doi: 10.5331/bgr.16A02.

大沼友貴彦（2016）積雪観測に基づいた雪氷藻類の繁殖とそのアルベド効果のモデル化に関する研究．千葉大学大学院理学研究科，博士論文.

Remias D., A. Holzinger, and C. Lütz (2009) Physiology, ultrastructure and habitat of the ice alga Mesotaenium berggrenii (Zygnemaphyceae, Chlorophyta) from glaciers in the European Alps. *Phycologia*, **48** (4), 302–312, doi: 10.2216/08-13.1.

Remias, D., A. Holzinger, S. Aigner, and C. Lütz (2011) Ecophysiology and ultrastructure of Ancylonema nordenskiöldii (Zygnematales, Streptophyta), causing broun ice on glaciers in Svalbard (high arctic). *Polar Biol.*, **36** (6), 899–908, doi: 10.1007/s00300-011-1135-6.

Screen, J. A. and I. Simmonds (2010) The central role of diminishing sea ice in recent Arctic temperature amplification. *Nature*, **464**, 1334–7.

Segawa, T. and N. Takeuchi (2010) Cyanobacterial communities on Qiyi Glacier in the Qilian Mountains of China. *Ann. Glaciol.*, **51** (56), 153–162.

Shimada, R., N. Takeuchi, and T. Aoki (2016) Inter-annual and geographical variations in the extent of bare ice and dark ice on the Greenland ice sheet derived from MODIS satellite images. *Front. Earth Sci.*, **4**, 43, doi: 10.3389/feart.2016.00043.

Shirakawa, T., T. Kadota, A. Fedorov, P. Konstantinov, T. Suzuki, H. Yabuki, F. Nakazawa, S. Tanaka, M. Miyairi, F. Fujisawa, N. Takeuchi, R. Kusaka, S. Takahashi, H. Enomoto, and T. Ohata (2016) Meteorological and glaciological observations at Suntar-Khayata Glacier No. 31, east

Siberia, from 2012–2014. *Bull. Glaciol. Res.*, **34**, 33–40, doi: 10.5331/bgr.16R01.

Stibal M, M. Šabacká and K. Kaštovská (2006) Microbial communities on glacier surfaces in Svalbard: impact of physical and chemical properties on abundance and structure of cyanobacteria and algae. *Microbial Ecol.*, **52**, 644–654, doi: 10.1007/s00248-006-9083-3.

Stibal, M., M. Šabacká, and J. Žárský (2012) Biological processes on glacier and ice sheet surfaces. *Nat. Geosci.*, **5** (11), 771–774.

Sugiyama, S., D. Sakakibara, S. Matsuno, S. Yamaguchi, S. Matoba, and T. Aoki (2014) Initial field observations on Qaanaaq ice cap, northwestern Greenland. *Ann. Glaciol.*, 55 (66), **25**, doi: 10.3189/2014AoG66A102.

Takahashi, S., K. Sugiura, T. Kameda, H. Enomoto, Y. Kononov, M. D. Ananicheva, and G. Kapustin (2011) Response of glaciers in the Suntar-Khayata range, eastern Siberia, to climate change. *Ann. Glaciol.*, **52** (58), 185–192.

Takeuchi, N. (2001) The altitudinal distribution of snow algae on an Alaska glacier (Gulkana Glacier in the Alaska Range). *Hydrol. Processes*, **15** (18), 3447–3459.

Takeuchi, N., S. Kohshima, and K. Seko (2001) Structure, formation, darkening process of albedo reducing material (cryoconite) on a Himalayan glacier: a granular algal mat growing on the glacier. *Arct. Antarct. Alp. Res.*, **33** (2), 115–122.

Takeuchi, N. (2002) Surface albedo and characteristics of cryoconite on an Alaska glacier (Gulkana Glacier in the Alaska Range). *Bull. Glaciol. Res.*, **19**, 63–70.

Takeuchi, N., S. Koshima, and T. Segawa (2003) Effect of cryoconite and snow algal communities on surface albedo on maritime glaciers in south Alaska. *Bull. Glaciol. Res.*, **20**, 21–27.

Takeuchi, N., R. Dial, S. Kohshima, T. Segawa, and J. Uetake (2006) Spatial distribution and abundance of red snow algae on the Harding Icefield, Alaska derived from a satellite image. *Geophys. Res. Lett.*, **33** (21), doi: 10.1029/2006GL027819.

Takeuchi, N. and Z. Li (2008) Characteristics of surface dust on Ürümqi Glacier No.1 in the Tien Shan Mountains, China. *Arct. Antarct. Alp. Res.*, **40** (4), 744–750.

Takeuchi, N. (2009) Temporal and spatial variations in spectral reflectance and characterisitics of surface dust on Gulkana Glacier, Alaska Range. *J. Glaciol.*, **55** (192), 701–709.

Takeuchi, N. (2013) Seasonal and altitudinal variations in snow algal communities on an Alaskan glacier (Gulkana glacier in the Alaska range). *Environ. Res. Lett.*, **8**, 035002, doi: 10.1088/1748-9326/8/3/035002.

Takeuchi, N., N. Nagatsuka, J. Uetake, and R. Shimada (2014) Spatial variations in impurities (cryoconite) on glaciers in northwest Greenland. *Bull. Glaciol. Res.*, **32** (0), 85–94.

Takeuchi, N., Y. Fujisawa, T. Kadota, S. Tanaka, M. Miyairi, T. Shirakawa, R. Kusaka, A. N. Fedorov, P. Konstantinov, and T. Ohata (2015) The effect of impurities on the surface melt of a glacier in the Suntar-Khayata Mountain range, Russian Siberia. *Front. Earth Sci.*, **3** (82), doi: 10.3389/feart.2015.00082.

竹内望（2012）氷河の暗色化とクリオコナイト．低温科学，70，165–172.

Tanaka, S., N. Takeuchi, M. Miyairi, Y. Fujisawa, T. Kadota, T. Shirakawa, R. Kusaka, S. Takahashi, H. Enomoto, T. Ohata, H. Yabuki, K. Konya, A. Fedorov, and P. Konstantinov (2016) Snow algal communities on glaciers in the Suntar-Khayata Mountain Range in eastern Siberia, Russia. *Polar Sci.*, **10** (3), 227–238, doi: 10.1016/j.polar.2016.03.004.

Telling, J., M. Stibal, A. M. Anesio, M. Tranter, I. Nias, J. Cook, C. Bellas, G. Lis, J. L. Wadham, A. Sole, P. Nienow, and A. Hodson (2012) Microbial nitrogen cycling on the Greenland Ice Sheet. *Biogeosci.*, **9** (7), 2431–2442.

Uetake, J., S. Tanaka, T. Segawa, N. Takeuchi, N. Nagatsuka, H. Motoyama, and T. Aoki (2016) Microbial community variation in cryoconite granules on Qaanaaq Glacier, NW Greenland. *FEMS Microbiol. Ecol.*, **92** (9), fiw127; doi: 10.1093/femsec/fiw127.

Wientjes, I. G. M. and J. Oerlemans (2010) An explanation for the dark region in the western melt zone of the Greenland ice sheet. *Cryosphere*, **4** (3), 261–268.

Wientjes, I. G. M., R. S. W. Van de Wal, G. J. Reichart, A. Sluijs, and J. Oerlemans (2011) Dust from the dark region in the western ablation zone of the Greenland ice sheet. *Cryosphere*, **5** (3), 589–601.

Yallop, M L, A. M. Anesio, R. G. Perkins, J. Cook, J. Telling, D. Fagan, J. MacFarlane, M. Stibal, G. Barker, and C. Bellas (2012) Photophysiology and albedo-changing potential of the ice algal community on the surface of the Greenland ice sheet. *ISME J.*, **6**, 2302–2313, doi: 10.1038/ismej.2012.107.

低温科学 75 （2017） 67-75
doi: 10.14943/lowtemsci. 75. 67

Glacier/ocean interactions in Greenland and their impact on the climate system

Fiammetta Straneo[1]*

Received 18 November 2016, accepted 11 January 2017

Rapid mass loss from the Greenland Ice Sheet has increased interest in glacier/ocean interactions for two reasons. First, increased submarine melting of marine terminating glaciers is a likely trigger of the observed dynamic ice loss. Second, the increased freshwater discharge from Greenland has the potential to affect the regional and large-scale ocean circulation. While extensive progress has been made, over the last decade, in understanding glacier/ocean exchanges of heat and freshwater in Greenland's glacial fjords, an in-depth knowledge of these exchanges is hindered by the models' inability to resolve the wide range of dynamical scales involved and by the fact that observations that can only provide a partial description because of the intrinsic challenges of working at the glacier margins. Specifically, major challenges remain to understand the dynamics in the near-ice zone, which controls submarine melting and iceberg calving, and the different drivers of the fjord circulation that delivers heat to the glacier. On the ocean side, much progress has been made in showing how Greenland's meltwaters are exported into the ocean in the form of highly diluted glacially modified waters whose properties depend on the details of the glacier/ocean/iceberg interaction. Major challenges remain, however, to parameterize these processes in order to provide appropriate boundary conditions to ocean/climate models.

Keywords: Glacier/ocean interaction, Greenland, glacial fjords, submarine melt, Arctic freshwater

1. Introduction

Ice loss from the Greenland Ice Sheet (GrIS) quadrupled from 1992-2001 to 2002-2011 and contributed 7.5 ± 1.8 mm to sea level rise from 1992 to 2011 (Shepherd et al., 2012). The ice loss is focused around the marine margins (Pritchard et al., 2009) and is due to a combination of changes in surface mass balance (i. e. increased net melt; Hanna et al., 2011) and dynamic changes associated with the thinning, retreat and speed-up of marine terminating glaciers (Howat and Eddy, 2011; Rignot and Kanagaratnam, 2006). While changes in surface mass balance have been largely attributed to rising air temperatures over Greenland (Box et al., 2009) and positive feedbacks associated with changes in albedo (Box et al., 2012), there is less of a consensus on the triggers for the dynamic changes (Fig. 1; Straneo et al., 2013). Amongst the likely players, however, is increased submarine (or subaqueous) melting at the marine margins of the glaciers (Holland et al., 2008; Motyka et al., 2011; Straneo et al., 2013; Straneo and Heimbach, 2013; Sugiyama et al., 2015). This hypothesized role of the ocean in driving major changes in mass loss from the Greenland Ice Sheet (GrIS) has focused interest on the heat and freshwater exchanges at the margins of Greenland's glaciers and set the stage for rapid advances in a relatively new, interdisciplinary field: 'glacier/ocean interactions'. In parallel, there is growing interest for the fate of Greenland meltwater which,

---

*Corresponding author
e-mail：fstraneo@whoi.edu
1）Woods Hole Oceanographic Institution, Woods Hole, USA

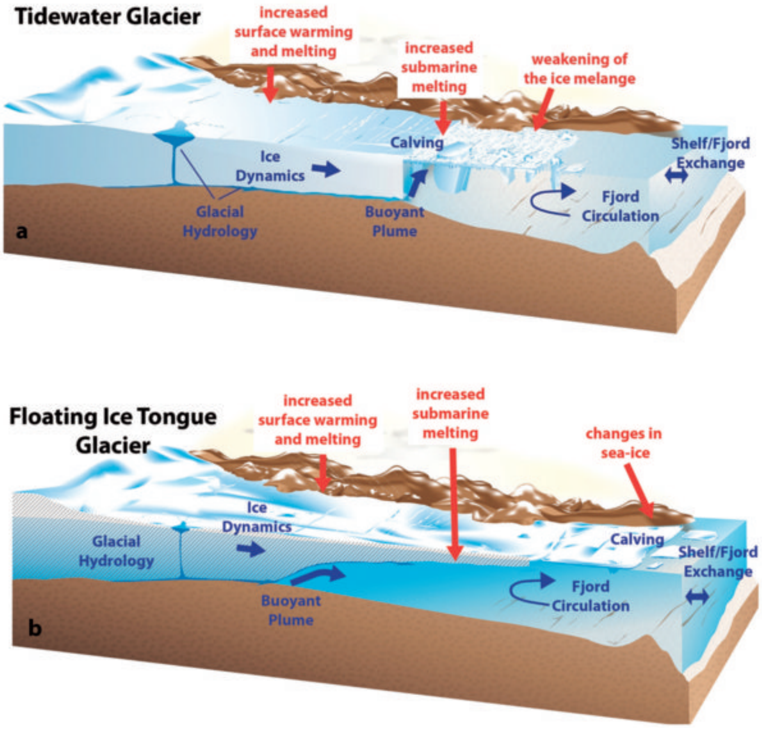

Figure 1 : Schematic of a) tidewater and b) floating tongue glaciers. The proposed mechanisms for the glacier retreat are shown in red and the key processes in blue. (Reproduced from Straneo et al., 2013.)

given the increasing discharge, has the potential to affect both the regional and large-scale ocean circulation, including the Atlantic Meridional Overturning Circulation (Boning et al., 2016; Lenaerts et al., 2015) and the regional marine ecosystems through the nutrient discharge (Bhatia et al., 2013). Given that both the ocean and air temperatures around Greenland are projected to increase over the next century, understanding glacier/ocean interactions is relevant to studies of ice sheet variability and its impact on the climate system including the biosphere. Here I summarize what we have learned over the last decade on ice sheet/ocean interactions in Greenland and outline what questions remain ahead.

2. Submarine melting of Greenland glaciers

Greenland glacier/ocean exchanges occur inside glacial fjords, which act as the connectors between the ocean waters flowing around Greenland's continental shelves and the ice sheet margins. As a result, glacier/ocean exchanges of heat and freshwater are regulated not only by the far-field ocean and glacier, but also by the ice/ocean boundary layer as well as the fjord dynamics. Key to understanding these dynamics is knowledge of the fjord's geometric characteristics including the presence of a sill, the width, the length, and the geometry of the glacier terminus. In Greenland, the terminus can vary from a floating ice tongue, similar to Antarctica's floating ice shelves, which covers most or all of the fjord (e.g. Nioghalvfjerdsbrae or 79 North Glacier) to mostly vertical glacial termini (e.g. Helheim Glacier in southeast Greenland). Depending on these characteristics (Fig. 1), the dynamics at the ice/ocean interface and within the fjord can be vastly different. In summarizing the relevant dynamics for glacier/ocean exchanges, we consider three different regions: the turbulent ice-ocean 'mixed' layer, the fjord system and the large-scale ocean. Processes within the near-ice zone regulate the exchange of heat and mass across the ice-ocean interface. The fjord dynamics supply the warm water to the glacier and export the freshwater from the fjord to the continental shelf region.

2.1 Oceanic heat content

Submarine melting is a result of a heat flux from the ocean to the glacier. Its magnitude is thus controlled by the available heat in the ocean waters next to the glacier and by the turbulent processes which affect the heat exchange across the oceanic boundary layer at the ice edge (Jenkins, 2011). The available heat in the ocean is expressed in terms of the thermal forcing, ΔT, a measure of the temperature above freezing of the ocean waters in contact with the ice:

$$\Delta T = T_a(x,y,z) - T_f(z,S),$$

where T_a is the spatially varying ocean temperature adjacent to the boundary layer and T_f is the freezing point temperature which varies mostly with pressure and weakly with salinity, S.

Ocean conditions near or under Greenland's marine terminating glaciers are largely unknown because of the challenges associated with making measurements next to the ice edge; however, some inferences can be made by considering water properties on Greenland's continental shelves and, where measurements exist, near the glaciers. Water properties around Greenland's continental shelves are characterized by the confluence of cold, relatively fresh water of Arctic origin (Polar Water, PW) carried by the East and West Greenland Currents (Sutherland and Pickart, 2008; Myers et al., 2007), and of warm, salty water of Atlantic origin (Atlantic Water, AW) initially carried poleward by the North Atlantic Current (Fig. 2; Straneo et al., 2013). Depending on the distance from their Atlantic or Arctic source, the properties within these water masses vary but, generally speaking, PW are thicker and colder along the eastern coast of Greenland and Atlantic waters are warmer in southeast and western Greenland. PW are lighter than AW due to differences in salinity and, therefore, are found closer to the surface all around Greenland. Seasonally, PW warms due to solar insolation giving rise to a third, surface water mass 'Warm Polar Water' (Beaird et al., 2015).

Ocean properties inside glacial fjords with sills deeper than the Polar/Atlantic Water interface resemble those on the nearby continental shelves, with cold PW overlying warm, salty Atlantic waters. These deep-silled fjords include all of Greenland's largest glaciers including Jakobshavn Isbrae, Helheim, Kangerdlugssuaq, Petermann and 79 North Glaciers (Fig. 3; Holland et al., 2008; Straneo et al., 2010; Christoffersen et al., 2011; Johnson et al., 2011; Wilson and Straneo, 2015). For fjords whose outer or inner sills are shallower than the Atlantic/Arctic water interface, we expect the near-glacier properties to be closer to the PW layer since these sills effectively prevent the Atlantic waters from reaching the glacier (e.g. Beaird et al., 2015).

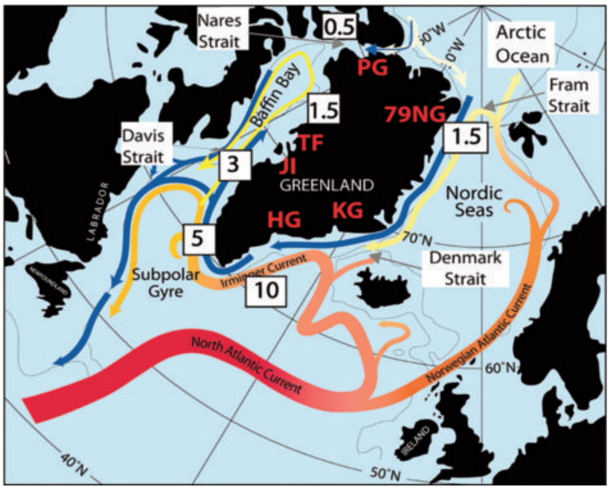

Figure 2：Schematic circulation of warm Atlantic (red to yellow) and cold Arctic (blue) water masses around Greenland. Numbers indicate the mean temperature (℃) of the Atlantic water on the shelf. (Redrawn from Straneo et al., 2012.)

The thermal forcing defined above requires knowledge of the ocean temperature distribution along the entire glacier face, which is challenging to obtain. Instead, to compare thermal forcings for several Greenland glaciers I estimate these in two approximate ways. For the first estimate, I assume that the ocean temperature near the glacier face is horizontally uniform and vertically varying like that of the closest profile of temperature (and salinity) obtained near the glacier. For most glacial fjords this is a profile taken 5 to 80 km from the glacier face (see Straneo et al., 2012). For the second estimate, I assume that the temperature near the glacier face is uniform and equal to the temperature at the grounding line depth observed closest to the grounding line (effectively the grounding line depth temperature from the profile used in the first method). The need for these partly empirical formulations reflect the lack of appropriate data in the near-ice zone.

The results of this calculation for profiles taken close to Greenland's five largest systems are shown in Fig. 3

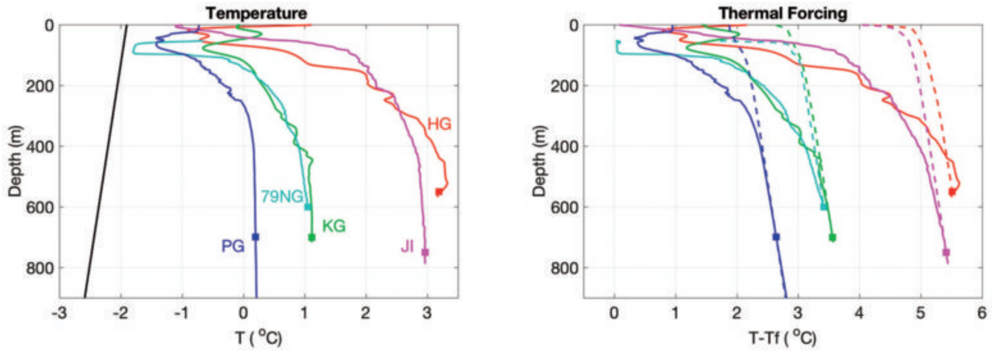

Figure 3：Left: Temperature profiles near Greenland's largest glaciers: HG (Helheim Glacier), JI (Jakobshavn Isbrae), KG (Kangerdlugssuaq Glacier), 79NG (79 North Glacier), PG (Petermann Glacier). Black line shows freezing point temperature for constant salinity of 34.9. Right: Temperature above freezing for the 5 glaciers above for the same profile as shown in left (solid) or for a constant temperature equal to that at the grounding line depth (dashed). Squares show grounding line depths. Data described in Straneo et al. (2012).

(see Straneo et al., 2012, for a more in-depth description of the profiles). Clear from the figure is that all of these large systems are associated with maximum temperatures at depth (the AW) and that the AW characteristics vary around Greenland depending on the distance and transformation from the Atlantic source. For example, waters at Helheim Glacier are the warmest and those at Petermann Glacier are the coldest. In terms of thermal forcing, this is largest at depth both because of the maximum ocean temperatures at depth but, also, because of the decrease in the freezing point temperature with pressure. Broadly speaking, differences in thermal forcing (estimated as described above) around Greenland are largely set by the temperature of the inflowing Atlantic waters but are also sensitive to changes in the freezing point temperatures. The two methods provide fairly different results except at the grounding line (where they are forced to be equal, Fig. 3). This highlights the need to improve our understanding of what governs melt rates at the margins of Greenland's glaciers. In general, the extent to which thermal forcing alone is responsible for differences in melt rate at Greenland's glaciers, however, is unknown. Likely dynamical factors such as the flow speed, the ice topography and the ocean stratification also play an important role.

2.2 Circulation at the glacier edge and in the fjord

Observations near the glacier fronts are scarce, but the dynamics is conceptualized as follows. Within a few meters of the ice, the ice-ocean boundary layer consists of a turbulent region (a few meters thick) where the turbulence is unaffected by the boundary and, closer to the ice, a viscous sublayer (a few millimeters thick) where the turbulent eddies are suppressed and molecular processes dominate the exchanges (Holland and Jenkins, 1999; Jenkins, 2011). Farther away, the flow is given by a system of rising buoyant plumes driven by submarine melting and subglacial discharge (surface melt above sea level). The seasonality in the discharge of surface melt, in particular, is thought to impart a large seasonal cycle to the dynamics at the ice/ocean edge. This discharge enters the fjord waters through channels discharging at the base of the glacier fronts whose number, sizes, and geometries are mostly unknown and possibly influenced by the complex networks of drainage channels and crevasses in the glaciers (for a review, see Chu, 2014). Observations of plumes consist of visual observations of turbid waters that surface at the edge of a glacier (e.g. Chauché et al., 2014) and a limited number of surveys of plume characteristics (Chauché et al., 2014; Bendtsen et al., 2015; Mankoff et al., 2016). A recent study of a west Greenland glacier mapped the volume flux within a surfacing plume and showed that, within 100 m of the glacier face, the plume's characteristics matched those predicted by plume theory (Mankoff et al., 2016). The study also highlighted, however, that the plume itself is very narrow (~30 m) compared to the width of the glacier (~5 km), raising the question of how much submarine melt actually occurs in the plume/glacier contact area. More likely, the important contribution is how the plumes influence the fjord-scale circulation and, as such, the supply of ocean heat to the glacier face. No doubt, however, plumes also play an important role in glacier mass balance by impacting calving processes (O'Leary and Christoffersen, 2013).

Numerical studies have greatly improved our understanding of buoyant plumes by showing that submarine melt rates are strongly influenced by the volume of subglacial discharge (and hence its seasonality; Sciascia et al., 2013, Xu et al., 2012, 2013) and the distribution of plumes (Slater et al., 2015). In particular, these studies have highlighted one important result: that melting is enhanced in the presence of subglacial discharge. The implication is that submarine melting can increase as a result of increases in surface melting even if the ocean conditions near the margin do not change. To this day, however, quantitative results from these models are largely untested because of the limited data from the ice/ocean interface. In particular, the coefficients used in the melt parameterization have not been validated by direct measurements (Straneo and Cenedese, 2015). In general, estimates of submarine melt from ocean measurements for Greenland's glacial fjords are highly uncertain because of the temporal variability, of the need to compute both heat and freshwater fluxes, and because of our inability to separate glacier and iceberg melt (Jackson and Straneo, 2016).

Key questions remain about the role of plumes in driving the fjord-scale circulation and, in turn, the melting of the glacier. In part these are being addressed by models in which the plumes are being parameterized (Cowton et al. 2015; Carroll et al. 2015) but cross-validation with field experiments will be key to determine if all the relevant dynamics are appropriately resolved.

Beyond the buoyancy-driven circulation resulting from glacial melting and discharge, glacier/ocean interactions are also affected by the fjord circulation forced by local or regional winds and by exchanges with the continental shelves. Examples of external drivers for glacial fjords include along-fjord winds (Moffat, 2014), tidal-mixing and flows (Mortensen et al., 2011 and 2013), shelf-forced flows (Jackson et al., 2014) and buoyancy-driven flows (Gladish et al., 2014). At present there is no simple model that can account for the fjord dynamics or even identify which regime may dominate in one particular fjord (Sutherland et al., 2014a; Jackson and Straneo, 2016). Yet either resolving or understanding how changing atmospheric and oceanic conditions will affect the circulation and properties within a fjord and, in turn, glacial melt will be key to understanding ice sheet variability. To date, studies analyzing correlations between ocean data and glacier variability (where both exist) over 1–10 year timescales show that there is no simple model that can link glacier variability, subglacial discharge variability and oceanic changes (e.g. Straneo et al., 2016). Likely, this is because other factors, including bedrock configuration, surface melt and other glaciological processes, play a role in glacier stability.

3. Discharge of meltwater

One important consequence of GrIS mass loss is an increased discharge of freshwater into the North Atlantic and Arctic Ocean and thus the potential to impact the Atlantic Meridional Overturning Circulation, the regional circulation, sea-ice formation and air-sea exchanges. Key to understanding this impact is our ability to track the pathways of Greenland meltwater into the ocean and, also, to provide appropriate boundary conditions from Greenland to ocean models investigating the impact of increased Greenland discharge (e.g. Boning et al., 2016).

In terms of budget, total discharge from the GrIS is due to the sum of ice discharge (icebergs and submarine melting) and runoff of ice melting above sea level. From 1961 to 1990, the GrIS was mostly stable, with an estimated ice discharge of 497 ± 50 km^3/y and runoff of 416 ± 57 km^3/y (Bamber et al., 2012). Both these components have increased over the past two decades, and a recent study estimated that the additional (ice and runoff combined) freshwater discharge in 2012 was 378 ± 50 km^3/y (Enderlin et al., 2014), resulting in a total freshwater discharge of 1,291 ± 50 km^3/y.

Most of Greenland's freshwater is discharged at the margins of the subpolar North Atlantic and the connected Baffin Bay (Bamber et al., 2012) and enters the ocean through calved icebergs, submarine melt, and subglacial discharge occurring in the glacial fjords. Thus, the fjords are the conduits through which this freshwater reaches Greenland's continental shelves. It is important to note that this freshwater discharge is not distributed evenly around Greenland but is localized into discrete locations, corresponding to the glacial fjords. Furthermore, a significant fraction is discharged at depth (either because of subglacial discharge or deep submarine melt) and, as such, behaves in a very different manner from a surface freshwater discharge like a river.

Tracking Greenland meltwater is challenging because its fresh signature is rapidly lost due to mixing with ocean waters. Some progress has been made by taking into account that melting of ice transforms ocean waters in specific ways given the thermodynamic change associated with the phase change (Jenkins, 1999). A comparison of winter and summer water temperatures and salinities in one major fjord have shown, furthermore, the large impact of the seasonal addition of subglacial discharge (Straneo et al., 2011). In general these studies show that Greenland meltwater is exported in the form of glacially modified waters which are distributed over a thick upper layer (at times ～200 m) and with salinities close to those of the PW (e.g. Beaird et al., 2015; Straneo et al., 2011; Jackson and Straneo, 2016; Mortensen et al. 2011, 2013). Quantitative tracking of meltwater requires additional tracers, however. One promising avenue is the use of noble gases (Beaird et al., 2015) which, for a mid-sized glacier in West Greenland, show that glacially modified waters contain fractions of subglacial discharge and submarine melt that are less than a few percent even within a kilometer of the glacier's terminus.

In order to provide appropriate boundary conditions to the large-scale ocean models, the mixing processes that dilute Greenland's meltwater must be understood and accounted for. For models which do not resolve the ice/ocean boundary layer dynamics, the plumes and even the fjords, this means that they need to be parameterized. Based on our present knowledge, one expects Greenland's meltwater to be exported in a strongly diluted form, over the upper 100–200 m, and that this export have a strong seasonal modulation (given the summer release of subglacial discharge). Icebergs released from Greenland are also highly problematic for models. Recent studies show that a significant fraction of the icebergs melt inside some of the fjords (Enderlin et al., 2016) but, also, that many icebergs are exported from the fjords after a non-trivial time lag (Sutherland et al., 2014b).

4. Summary

Major advances in understanding glacier/ocean interactions in Greenland have been made over the last decade as interest for the role of the ocean in triggering Greenland's dynamic changes and the impact of increased Greenland freshwater discharge into the ocean has grown. These studies collectively have shown that Atlantic waters reach the margins of large glaciers at depth and drive substantial submarine melt. They have also shown that the glacier/ocean exchange is strongly modulated by the seasonal release of surface melt which, in turn, has a big impact on submarine melt. In terms of melt-water export, these studies have shown that Greenland's meltwater is exported in the form of highly diluted glacially modified waters and that their properties are set by the processes at the ice edge, including subglacial discharge, and by fjord processes. In general, we expect the meltwater export to have a strong seasonality and the meltwaters to be distributed over the upper 100–200 m.

Key questions pertaining to glacier/ocean interactions in Greenland remain, however, and we are far from being in a position to provide submarine melt rates to ice sheet models or meltwater forcing to ocean models. Specific issues that need to be addressed include:

1. Testing of melt rate parameterizations using high-resolution models and data.
2. Establishing the patterns and rates of subglacial discharge for marine terminating glaciers.
3. Understanding the role of externally forced fjord circulations in setting the submarine melt rate magnitude and in regulating the meltwater export.

In addition, it is important to remember that submarine melt rates affected, for example, by oceanic or atmospheric variability, are only one of the multiple factors influencing glacier stability. Thus prolonged measurements of multiple systems is key to unraveling the different dynamics at play and improving our understanding of ice sheet variability.

Acknowledgements

This research was supported by the National Science Foundation. The author gratefully acknowledges the invitation to the international workshop “Greenland ice sheet mass loss and its impact on global climate change” under the ArCS (Arctic Challenge for Sustainability) Project, the SIGMA (Snow Impurity and Glacial Microbe effects on abrupt warming in the Arctic) project and the Joint Research Program of the Institute of Low Temperature Science, Hokkaido University.

References

Bamber J., M. van den Broeke, J. Ettema, J. Lenaerts, and E. Rignot (2012) Recent large increases in freshwater fluxes from Greenland into the North Atlantic. *Geophys. Res. Lett.,* **39**, L19501.

Beaird, N., F. Straneo, and W. Jenkins (2015) Noble gases trace Greenland’s surface and submarine melt in the ocean. *Geophys. Res. Lett.*, **44**, 7705–7713.

Bendtsen, J., J. Mortensen, K. Lennert, and S. Rysgaard (2015) Heat sources for glacial ice melt in a West Greenland tidewater outlet glacier fjord: The role of subglacial freshwater discharge. *Geophys. Res. Lett.*, **42**, 4089–4095.

Bhatia, M. P., E. Kujawinski, S. D. Das, C. Breier, P. Henderson, and M. Charette (2013) Greenland meltwater as a significant and potentially bioavailable source of iron to the ocean. *Nat. Geosci.*, **6**, 274–278.

Böning, C. W., E. Behrens, A. Biastoch, K. Getzlaff, and J. L. Bamber (2016) Emerging impact of Greenland meltwater on deepwater formation in the North Atlantic Ocean. *Nat. Geosci.,* **9**, 523–528.

Box, J. E., L. Yang, D. H. Bromwich, and L. S. Bai (2009) Greenland ice sheet surface air temperature variability: 1840–2007. *J. Climate*, **22**, 4029–4049.

Box, J. E., X. Fettweis, J. C. Stroeve, M. Tedesco, D. K. Hall, and K. Steffen (2012) Greenland ice sheet albedo feedback: thermodynamics and atmospheric drivers. *Cryosphere*, **6**, 821–839.

Carroll, D., D. A. Sutherland, E. L. Shroyer, J. D. Nash, G. A. Catania, and L. A. Stearns (2015) Modeling turbulent subglacial meltwater plumes: Implications for fjord-scale buoyancy-driven circulation. *J. Phys. Oceanogr.*, **45**, 2169–2185.

Chauché, N., A. Hubbard, J.-C. Gascard, J. E. Box, R. Bates, M. Koppes, A. Sole, P. Christoffersen, and H. Patton (2014) Ice-ocean interaction and calving front morphology at two west Greenland tidewater outlet glaciers. *Cryosphere*, **8**, 1457–1468.

Christoffersen, P., R. I. Mugford, K. J. Heywood, I. Joughin, J. A. Dowdeswell, J. Syvitski, A. Luckman, and T. Benham (2011) Warming of waters in an East Greenland fjord prior to glacier retreat: mechanisms and connection to large-scale atmospheric conditions. *Cryosphere* **5**, 701–714.

Chu, V. W. (2014) Greenland Ice Sheet hydrology: a review. *Prog. Phys. Geogr.,* **38**, 19–54.

Cowton, T. R., D. Slater, A. Sole, D. Goldberg, and P. Nienow (2015) Modeling the impact of glacial runoff on fjord circulation and submarine melt rate using a new subgrid scale parameterization for glacial plumes. *J. Geophys. Res. Oceans*, **120**, 796–812.

Enderlin E. M., I. M. Howat, S. Jeong, M.-J. Noh, J. H. van Angelen, and M. R. van den Broeke (2014) An improved mass budget for the Greenland ice sheet. *Geophys. Res. Lett.,* **41**, 866–872.

Enderlin, E. M., G. S. Hamilton, F. Straneo, and D. Sutherland (2016) Iceberg meltwater fluxes dominate the freshwater budget in Greenland’s iceberg congested glacial fjords. *Geophys. Res. Lett.,* **43**, 11288–11294.

Gladish, C. V., D. M. Holland, A. Rosing-Asvid, J. W. Behrens, and J. Boje (2014) Oceanic boundary conditions for Jakobshavn Glacier: part I. Variability and renewal of Ilulissat Icefjord Waters, 2001–2013. *J. Phys. Oceanogr.*, **45**, 3–32.

Hanna, E., P. Huybrechts, J. Cappelen, K. Steffen, R. C. Bales, E. W. Burgess, J. R. McConnell, J. P. Steffensen, M. van den Broeke, L. Wake, G. R. Bigg, M. Griffiths, and D. Savas (2011). Greenland Ice Sheet surface mass balance 1870 to 2010 based on Twentieth Century Reanalysis, and links with global climate forcing. *J. Geophys. Res. Atmos.*, **116**, D24121.

Holland, D. M., and A. Jenkins (1999) Modeling thermodynamic ice-ocean interactions at the base of an ice shelf. *J. Phys. Oceanogr.,* **29**, 1787–1800.

Holland, D. M., R. H. Thomas, B. de Young, M. H. Ribergaard, and B. Lyberth (2008) Acceleration of Jakobshavn Isbræ triggered by warm subsurface ocean waters. *Nat. Geosci.,* **1**, 659–664.

Howat, I. M., and A. Eddy (2011) Multi-decadal retreat of Greenland’s marine-terminating glaciers. *J. Glaciol.*, **57**, 389–396.

Jackson, R. H., F. Straneo, and D. A. Sutherland (2014) Externally forced fluctuations in ocean temperature at Greenland glaciers in non-summer months. *Nat. Geosci.,* **7**, 503–508.

Jenkins A. (1999) The impact of melting ice on ocean waters. *J. Phys. Oceanogr.,* **29**, 2370–2381.

Jenkins A. (2011) Convection-driven melting near the grounding lines of ice shelves and tidewater glaciers. *J. Phys. Oceanogr.,* **41**, 2279–2294.

Johnson, H. L., A. Münchow, K. K. Falkner, and H. Melling (2011) Ocean circulation and properties in Petermann Fjord, Greenland. *J. Geophys. Res.,* **116**, C01003.

Lenaerts, J. T. M., D. Le Bars, L. van Kampenhout, M. Vizcaino, E. M. Enderlin, and M. R. van den Broeke (2015) Representing Greenland ice sheet freshwater fluxes in climate models. *Geophys. Res. Lett.*, **42**, 6373–6381.

Mankoff, K. D., F. Straneo, C. Cenedese, S. B. Das, C. G. Richards, and H. Singh (2016) Structure and dynamics of a subglacial plume in a Greenland fjord. *J. Geophys. Res. Oceans*, doi: 10.1002/2016JC011764.

Moffat, C. (2014) Wind-driven modulation of warm water supply to a proglacial fjord, Jorge Montt Glacier, Patagonia. *Geophys. Res. Lett.,* **41**, 3943–3950.

Mortensen, J., J. Bendtsen, R. J. Motyka, K. Lennert, M. Truffer, M. Fahnestock, and S. Rysgaard (2013) On the seasonal freshwater stratification in the proximity of fast-flowing tidewater outlet glaciers in a sub-Arctic sill fjord. *J. Geophys. Res. Oceans,* **118**, 1382–1395.

Mortensen, J., K. Lennert, J. Bendtsen, and S. Rysgaard (2011) Heat sources for glacial melt in a sub-Arctic fjord (Godthåbsfjord) in contact with the Greenland Ice Sheet. *J. Geophys. Res.,* **116**, C01013.

Motyka, R. J., M. Truffer, M. Fahnestock, J. Mortensen, S. Rysgaard, and I. Howat (2011) Submarine melting of the 1985 Jakosbhavn Isbræ floating tongue and the triggering of the current retreat. *J. Geophys. Res.,* **116**, F01007.

Myers, P. G., N. Kulan, and M. H. Ribergaard (2007) Irminger Water variability in the West Greenland Current. *Geophys. Res. Lett.*, **34**, L17601.

O'Leary, M., and P. Christoffersen (2013) Calving on tidewater glaciers amplified by submarine frontal melting. *Cryosphere*, **7**, 119–128.

Pritchard, H. D., R. J. Arthern, D. G. Vaughan, and L. A. Edwards (2009) Extensive dynamic thinning on the margins of the Greenland and Antarctic ice sheets. *Nature*, **461**, 971–975.

Rignot, E., and P. Kanagaratnam (2006) Changes in the velocity structure of the Greenland ice sheet. *Science,* **311**, 986–990.

Sciascia, R., F. Straneo, C. Cenedese, and P. Heimbach (2013) Seasonal variability of submarine melt rate and circulation in an East Greenland fjord. *J. Geophys. Res.,* **118**, 2492–2506.

Shepherd, A., E. R. Ivins, G. A, V. R. Barletta, M. J. Bentley, S. Bettadpur, K. H. Briggs, D. H. Bromwich, R. Forsberg, N. Galin, M. Horwath, S. Jacobs, I. Joughin, M. A. King, J. T. M. Lenaerts, J. Li, S. R. M. Ligtenberg, A. Luckman, S. B. Luthcke, M. McMillan, R. Meister, G. Milne, J. Mouginot, A. Muir, J. P. Nicolas, J. Paden, A. J. Payne, H. Pritchard, E. Rignot, H. Rott, L. S. Sørensen, T. A. Scambos, B. Scheuchl, E. J. O. Schrama, B. Smith, A. V. Sundal, J. H. van Angelen, W. J. van de Berg, M. R. van den Broeke, D. G. Vaughan, I. Velicogna, J. Wahr, P. L. Whitehouse, D. J. Wingham, D. Yi, D. Young, and H. J. Zwally (2012) A reconciled estimate of ice-sheet mass balance. *Science,* **338** (6111), 1183–1189.

Slater, D. A., P. W. Nienow, T. R. Cowton, D. N. Goldberg, and A. J. Sole (2015) Effect of near-terminus subglacial hydrology on tidewater glacier submarine melt rates. *Geophys. Res. Lett.*, **42**, 2861–2868.

Straneo, F., and C. Cenedese (2015) The dynamics of Greenland's glacial fjords and their role in climate. *Ann. Rev. Mar. Sci.*, **7**, 89–112.

Straneo, F., G. S. Hamilton, L. A. Stearns, and D. A. Sutherland (2016) Connecting the Greenland ice sheet and the ocean: a case study of Helheim Glacier and Sermilik Fjord. *Oceanography,* **29**, 34–45.

Straneo, F., R. G. Curry, D. A. Sutherland, G. S. Hamilton, C. Cenedese, K. Våge, and L. A. Stearns (2011) Impact of fjord dynamics and glacial runoff on the circulation near Helheim Glacier. *Nat. Geosci.,* **4**, 322–327.

Straneo, F., G. S. Hamilton, D. A. Sutherland, L. A. Stearns, F. Davidson, M. O. Hammill, G. B. Stenson, and A. Rosing-Asvid (2010) Rapid circulation of warm subtropical waters in a major glacial fjord in East Greenland. *Nat. Geosci.,* **3**, 182–186.

Straneo, F., and P. Heimbach (2013) North Atlantic warming and the retreat of Greenland's outlet glaciers. *Nature,* **504**, 36–43.

Straneo, F., P. Heimbach, O. Sergienko, G. Hamilton, G. Catania, S. Griffies, R. Hallberg, A. Jenkins, I. Joughin, R. Motyka, W. T. Pfeffer, S. F. Price, E. Rignot, T. Scambos, M. Truffer, and A. Vieli (2013) Challenges to understand the dynamic response of Greenland's marine terminating glaciers to oceanic and atmospheric forcing. *Bull. Am. Meteorol. Soc.,* **94**, 1131–1144.

Straneo, F., D. A. Sutherland, D. Holland, C. Gladish, G. S. Hamilton, H. L. Johnson, E. Rignot, Y. Xu, and M. Koppes (2012) Characteristics of ocean waters reaching Greenland's glaciers. *Ann. Glaciol.,* **53**, 202–210.

Sugiyama, S., D. Sakakibara, S. Tsutaki, M. Maruyama, and T. Sawagaki (2015) Glacier dynamics near the calving front of Bowdoin Glacier, northwestern Greenland. *J. Glaciol.*, **61**, 223–232.

Sutherland, D. A., and R. S. Pickart (2008) The East Greenland Coastal Current: structure, variability, and forcing. *Prog. Oceanogr.,* **78**, 58–77.

Sutherland, D. A., F. Straneo, and R. S. Pickart (2014a) Characteristics and dynamics of two major Greenland glacial fjords. *J. Geophys. Res.,* **119**, 3767–3791.

Sutherland, D. A., G. E. Roth, G. S. Hamilton, S. H. Mernild, L. A. Stearns, and F. Straneo (2014b) Quantifying flow regimes in a Greenland glacial fjord using iceberg drifters. *Geophys. Res. Lett.,* **41**, 8411–8420.

Wilson, N. J., and F. Straneo (2015) Water exchange between the continental shelf and the cavity of Nioghalvfjerdsbræ

(79 North Glacier). *Geophys. Res. Lett.*, **42**, 7648–7654.

Xu, Y., E. Rignot, D. Menemenlis, and M. Koppes (2012) Numerical experiments on subaqueous melting of Greenland tidewater glaciers in response to ocean warming and enhanced subglacial discharge. *Ann. Glaciol.,* **53**, 229–234.

Xu, Y., E. Rignot, I. Fenty, D. Menemenlis, and M. M. Flexas (2013) Subaqueous melting of Store Glacier, west Greenland from three-dimensional, high-resolution numerical modeling and ocean observations. *Geophys. Res. Lett.,* **40**, 4648–4653.

低温科学 75 （2017） 77-84
doi: 10.14943/lowtemsci. 75. 77

氷河融解水を起源とする高濁度水プルームの数値モデリング

松村 義正[1)]，大橋 良彦[2), 1)]，青木 茂[1)]，杉山 慎[1), 3)]

2016 年 11 月 14 日受付 2017 年 1 月 11 日受理

グリーンランド氷床の表面融解水は，氷河を貫通するムーランを通過して岩盤に到達し，陸上の堆積物を懸濁物質として取り込みながら氷河末端で海洋に流出する．淡水である融解水は海水より軽いため直ちに湧昇し，氷河末端で高濁度の融解水プルームを形成してフィヨルド内の鉛直循環を駆動する．本研究では粒子追跡法を組み込んだ非静力学海洋モデルによる理想化シミュレーションによってこの高濁度水プルームを再現し，特にフィヨルド内の懸濁物質輸送過程について解析した．

Modeling subglacial meltwater plumes and associated sediment transport

Yoshimasa Matsumura[1*], Yoshihiko Ohashi[2, 1], Shigeru Aoki[1], Shin Sugiyama[1, 3]

The surface meltwater of the Greenland ice sheet is drained through englacial channels called moulins that reach the bedrock, and hence it contains substantial amounts of terrestrial sediments. The meltwater runoff from marine-terminating glaciers form an upwelling turbid plume at the glacier front and drives overturning circulation in the fjord. We perform idealized numerical experiments on the turbid meltwater plume and associated sediment transport by using a non-hydrostatic ocean model coupled with a Lagrangian particle tracking system that simulates the dynamics of suspended sediments.

キーワード：融解水プルーム・懸濁物質輸送・粒子追跡法・非静力学海洋モデル
Meltwater plume, suspended sediment transport, Lagrangian particle tracking, non-hydrostatic ocean model

1．はじめに

温暖化に起因するとみられる南極大陸及びグリーンランド氷床の質量損失の加速が報告されており（Rignot et al., 2008; Pritchard et al., 2009），海洋-氷床間相互作用の理解は近年の海洋学・気候学において最も重要な課題の一つとなっている．海洋-氷床間相互作用の海洋への影響に関しては，海水温の上昇が棚氷の底面融解を加速させ，結果として淡水化および海面水位上昇が進行するという観点から議論されることが多い（Rignot et al., 2011）が，それらに加え氷床融解水の海洋への流入は海洋の物質循環や生物生産にも大きな影響力を持つ可能性がある．表面融解によって生じた融解水はムーラン（氷河内部を貫通する筒状の空洞）を通過して岩盤に到達し，氷河底面の岩盤上を河川のように流れて海洋に流出するが，この間に岩盤上の堆積物を懸濁物質として取り込み海洋に放出する（Chu, 2014）．このため融解期には氷河末端の沿岸域でしばしば高濁度水域が出現する（Ohashi

---

連絡先
松村 義正
北海道大学低温科学研究所
e-mail：ymatsu@lowtem.hokudai.ac.jp
１）北海道大学低温科学研究所
Institute of Low Temperature Science, Hokkaido University, Sapporo, Japan
２）北海道大学大学院環境科学院
Graduate School of Environmental Science, Hokkaido University, Sapporo, Japan
３）北海道大学北極域研究センター
Arctic Research Center, Hokkaido University, Sapporo, Japan

et al., 2016）．特に末端が海洋中に流入しているカービング氷河の場合には融解水の出水口は海面より深くに位置するが，流出する融解水は淡水であるため浮力を得て上昇し，同時に懸濁物質を鉛直に輸送する．実際に氷河末端で局所的に融解水が湧き上がる様子が濁度によって可視化され，ドローン等による現場直接観測からも捉えられている（杉山，私信）．

周りの海水と混合しながら湧昇した融解水は海面に達した後は河川水と同様に表層に広がりながら沖に向かって流出し，その補償流として下層では陸向きの流れが生じてフィヨルド内でエスチュアリ循環に類似した鉛直循環が駆動される（Carrol et al., 2015）．カービング氷河の接地線は密度躍層下部に達しているため，この鉛直循環は高温高塩の中層水をフィヨルド内部に引き込んで海洋の熱を氷河末端まで輸送し，氷河の融解を促進していることが指摘されている（Straneo et al., 2011）．また躍層下部からの融解水プルームの湧昇は中層の栄養塩を密度躍層を超えて表層に運ぶ役割も担っており，加えて懸濁物質中にも鉄分等の陸起源微量元素が含まれる可能性もあるため，物質輸送の観点からは融解水供給は近傍海域での生物生産に正の影響をもつと考えられる．一方で海面付近での高濁度域の出現は日射を遮るため光環境に対しては負に作用している可能性がある．

このように氷河融解に伴う高濁度水の供給は力学的な海洋循環とそれに伴う生物地球化学過程まで含む複雑なシステムを構築し，フィヨルド内及び近傍海域での生態系においても本質的に重要な役割を担っている（Lydersen et al., 2014）．しかしながら氷河融解水の海洋への流出に関する既往の研究の多くは主に熱収支に着目しており，氷河融解と懸濁物質供給の定量的な関係や，それが生態系に与える影響についてはほとんど解明されていない．大橋（2015）は氷床融解に伴って出現する高濁度水域を人工衛星データ（MODIS画像）から検知し，その面積変動と気象要素や海面クロロフィル濃度との関係を議論したが，人工衛星によって高濁度水域を検知できるのは懸濁物質がごく浅層に存在する場合に限られる．本研究ではグリーンランドカービング氷河末端に接続するフィヨルドを模した理想化設定の数値モデルによって融解水を起源とする高濁度水の上昇プルームを再現し，融解水及びそれに含まれる懸濁物質がフィヨルド内をどのように輸送されるかを調査する．

2．数値モデルと実験設定

実験には有限体積法に基づく非静力学海洋モデルkinaco（Matsumura and Hasumi, 2008）にオンライン粒子追跡を組み込み，海水中に浮遊する多数の懸濁物質粒子をラグランジュ的に扱うParticle-in-Cell（PIC）型の数値海洋モデル（Matsumura and Ohshima, 2015）を用いた．これにより上昇プルームの挙動と，それに含まれる懸濁物質の輸送及び沈降過程をパラメタ化に頼ることなく陽に表現することができる．図1にPIC型モデルの概念図を示す．

海洋流速はブジネスク近似を適用した3次元非圧縮ナビエ–ストークス方程式によって予報する．圧力は非圧縮の連続の式から導かれるポアソン方程式を，多重格子法を前処理とする共役勾配法を用いて解くことにより求まる．温位・塩分は格子平均量の移流拡散方程式を積分することにより予報され，海水密度は各格子での温位・塩分の予報値及び水深の関数として多項式で表現された

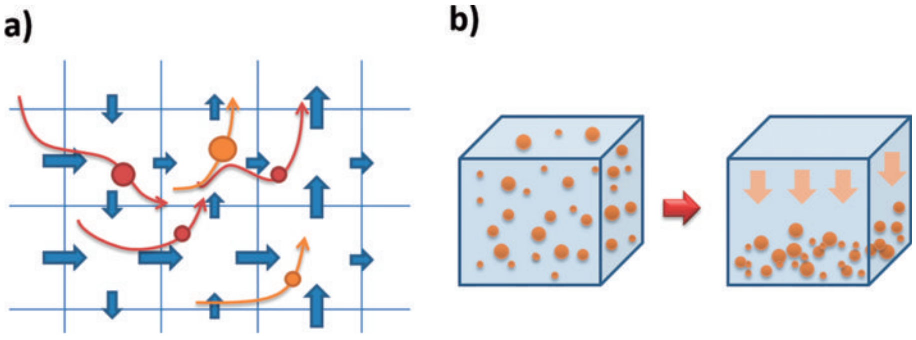

図1：PIC型海洋モデルの概念図．a）流速（青矢印）は格子面でオイラー的に予報され，個々の粒子（赤・黄）はラグランジュ的に軌跡が計算される（赤・黄矢印）．b）格子内における懸濁粒子沈降の様子．

Figure 1：Schematics of PIC-type ocean model. a) Velocity field (blue arrows) is predicted at the surfaces of each cell in the Eulerian form, while the trajectory of each individual particle (red and orange circles) is calculated in the Lagrangian form. b) Sub-grid scale settlement of the suspended sediment particles in a grid cell.

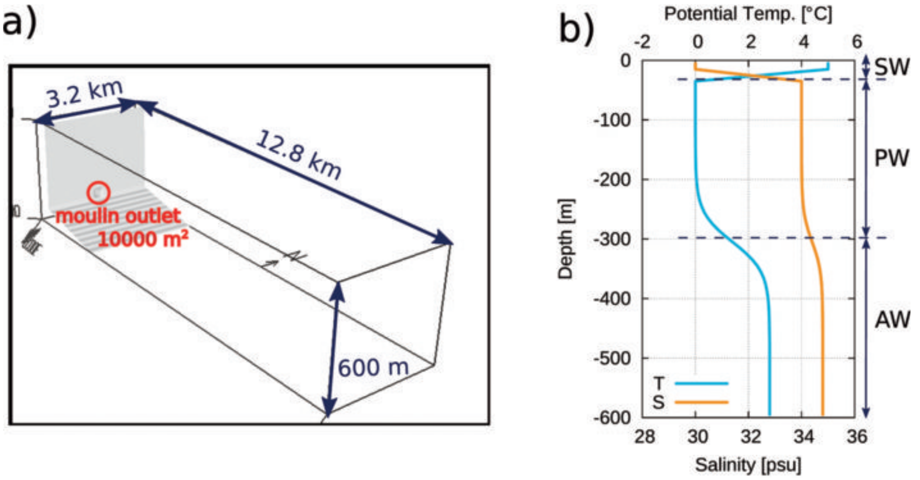

図 2：a）実験領域，および b）温位・塩分の初期成層構造.
Figure 2：a） Domain of the simulation and b） the initial stratification for potential temperature and salinity.

経験的な状態方程式により診断的に求める．浮遊する懸濁物質を表現する粒子の軌跡は海洋の予報流速の線形内挿値と粒子固有の沈降速度の和を用いて 4 次ルンゲ–クッタスキームによりラグランジュ的に計算される.

本研究では懸濁物質として微小な鉱物粒子を想定しており，個々の粒子がもつ慣性の影響はグリッドスケールの海水運動変動に比べ十分小さい．そこで全ての粒子について，海水に対する相対速度は重力と海水から受ける抵抗が平衡する終端速度にあると仮定した．海水中に浮遊する鉱物粒子の有効直径は高々数 100 μm 程度（それ以上のサイズの粒子は速やかに沈降して除去されてしまう）であり，このような微小粒子の運動方程式を陽に解いたとしても海洋流速に対する粒子の相対速度が収束するまでの時間スケールはモデルの時間刻み幅より十分小さいため，この仮定は妥当であると思われる．水中の鉱物粒子の沈降速度は Rubey の式（Rubey, 1933）等によって近似されるが，本研究で対象とする有効直径 10–100 μm の範囲では終端沈降速度は概ね次の Stokes 則に従う：

$$W=\frac{d^2}{18\nu}\frac{\rho_0-\rho_s}{\rho_0},$$

ここで d は粒子の有効直径，ν は海水の分子粘性係数，g は重力加速度の大きさ，ρ_0 は海水密度，ρ_s は懸濁物質を構成する鉱物の密度であり，それぞれの典型的な値を代入すると終端沈降速度はシルトに相当する直径 10 μm の粒子で $W\sim10^{-4}$ m s^{-1}，細かい砂粒に相当する直径 100 μm の粒子で $W\sim10^{-2}$ m s^{-1} と見積もることができる．実際の高濁度水中には様々な粒径の懸濁粒子が特徴的なサイズスペクトル分布に従って存在していると考えられるが，本研究では簡単のため全粒子の粒径（すなわち終端沈降速度）を一定とし，$W=10^{-2}$，10^{-3}，10^{-4} m s^{-1} の 3 ケースについて感度実験を実施した．実際に海水中に浮遊する懸濁粒子の個数は膨大であり，その全てを扱うことは現実的でないため，数値モデルの 1 粒子は同じ特性を持つ多数の粒子を代表しているとみなす．本研究では粒径に関わらず数値モデルでの 1 粒子が懸濁粒子 10 kg に相当するとしている．なお当モデルには浮遊する懸濁物質粒子自体の重さが海水の運動に影響を与える分散混相流としての力学的効果も含まれているが，本研究の実験設定ではプルームの浮力において塩分の寄与が支配的であり，この効果は無視できる.

実験領域としてグリーンランドのカービング氷河に接続する小規模なフィヨルドを想定した東西 12.8 km，南北 3.2 km，鉛直 600 m の矩形型海洋を設定し，領域西端に海底斜面に接する切り立った氷河末端（接地深度 500 m）を配置する．氷河末端接地面に氷河底面の水路を模した幅 200 m，高さ 50 m のトンネル様の融解水出水口を設け，ここから領域内に高濁度の融解水を供給する（図 2a）．なおこのトンネル構造は数値モデル上は海底地形と Losch（2008）に基づく棚氷モデルの組み合わせによって実現されているが，本研究の設定においては棚氷–海水間の熱力学的相互作用を無効化しているため，海洋の熱による氷河末端の融解は生じない.

温位・塩分の初期値は水平一様とし，Chauché et al.（2014）等を参考に夏季のグリーンランドフィヨルド域の典型的な成層構造を与えた（図 2b）．すなわち 300 m 以浅に北極海を起源とする低温低塩の Polar Water（PW：0℃，34 psu）が存在し，それより深くを大西洋からもたらされる相対的に高温高塩の Atlantic Water（AW：2.8℃，34.8 psu）が占める．PW と AW の間は

双曲正接関数により滑らかに接続した．また日射による加熱と海氷・氷山融解水の影響による極めて低密度の Surface Water（SW：5℃，30 psu）が表層 20 m 深までを覆っている．領域西端境界からトンネルを通過するように結氷温度の淡水（0℃，0 psu）を流入させ，同時にトンネル内で底面から堆積物粒子を継続的に投入することで出水口から高濁度氷河融解水を供給する．流出量として Q=100，300，1000 m^3 s^{-1} の 3 通りの実験を実施し，すべての実験において 1 個あたり 10 kg の懸濁物質に相当する堆積物粒子を毎秒 100 個投入した（10^3 kg s^{-1} の懸濁物質供給に相当）．格子解像度は水平 50 m×鉛直 10 m，水平境界は壁面とし，東端では温位・塩分を初期成層に緩和する．海面での熱フラックスや風応力は与えていない．静止状態から実験を開始し，積分期間は融解水プルームの沖方向への輸送が最も速い Q=1000 m^3 s^{-1} m，W=10^{-4} m s^{-1} のケース（実験 A1）において高濁度域が領域東端に達するまでの 8 時間とした．各実験における融解水供給量 Q と懸濁物質沈降速度 W の値を表 1 にまとめた．

なお流入する氷河融解水中に実際にどの程度の濃度で陸起源懸濁物質が含まれているかは定量的には明らかでなく，本研究で与えた 10^3 kg s^{-1}という値に特に根拠はない．また河川における出水イベントでは懸濁物質濃度が流出量に対し指数関数的に増加することが知られており，融解水流出量にかかわらず同量の堆積物粒子を投入するという設定も妥当性を欠く．したがって本稿で以後議論される懸濁物質含有量の定量値は，各実験において投入された堆積物総量に対する割合としての意味しか持たないことに注意されたい．

表 1：各実験における淡水流出フラックス Q および懸濁物質沈降速度 W．

Table 1：Values of the meltwater discharge flux Q and the sinking velocity of suspended sediments W for each experiment.

	Q[m^3 s^{-1}]	W[m s^{-1}]
A1	1000	10^{-4}
A2	1000	10^{-3}
A3	1000	10^{-2}
B1	300	10^{-4}
B2	300	10^{-3}
B3	300	10^{-2}
C1	100	10^{-4}
C2	100	10^{-3}
C3	100	10^{-2}

3．結果

はじめに最も流入量が大きく粒子沈降速度の遅い実験 A1 の結果を示す．図 3 は海水濁度に対応する懸濁粒子含有量の時間発展である．トンネル状出水口から流出した融解水は実験開始後直ちに氷河末端に沿って湧昇し，海面に到達する．海面に到達後は融解水は河川水と同様のバルジを形成して表層を広がり，1 時間後にはフィヨルド全幅を満たす．その後は融解水投入による浮力のコントラストが駆動する鉛直循環により表層で沖向きの流れが形成され，高濁度域が移流されていく．ただし高濁度水塊が海面に露出しているのは氷河末端近傍のみであ

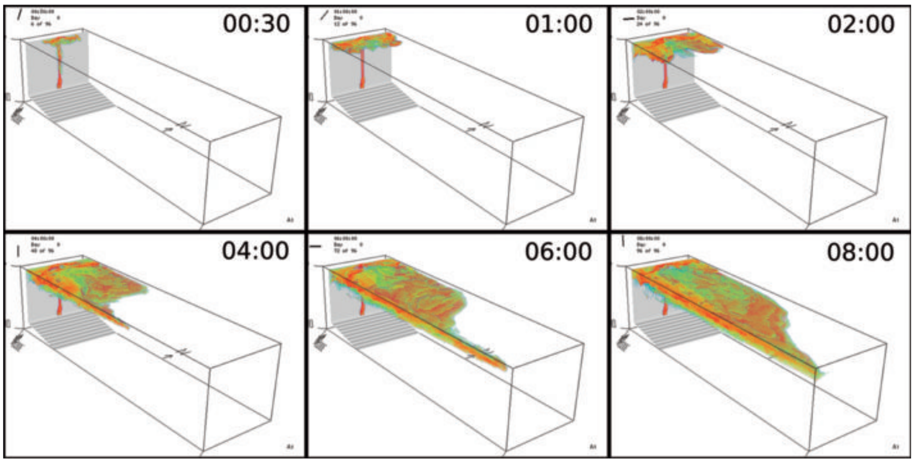

図 3：単位体積あたりの懸濁粒子含有量（濁度に相当）の 3 次元ボリュームレンダリング画像．赤い色ほど多量の懸濁粒子を含む．左上から順に実験開始から 0.5，1，2，4，6，8 時間後．

Figure 3：Three-dimensional volume-rendering images of suspended sediment concentration at 0.5, 1, 2, 4, 6, 8 hours. The red-colored regions contain a greater amount of suspended sediments.

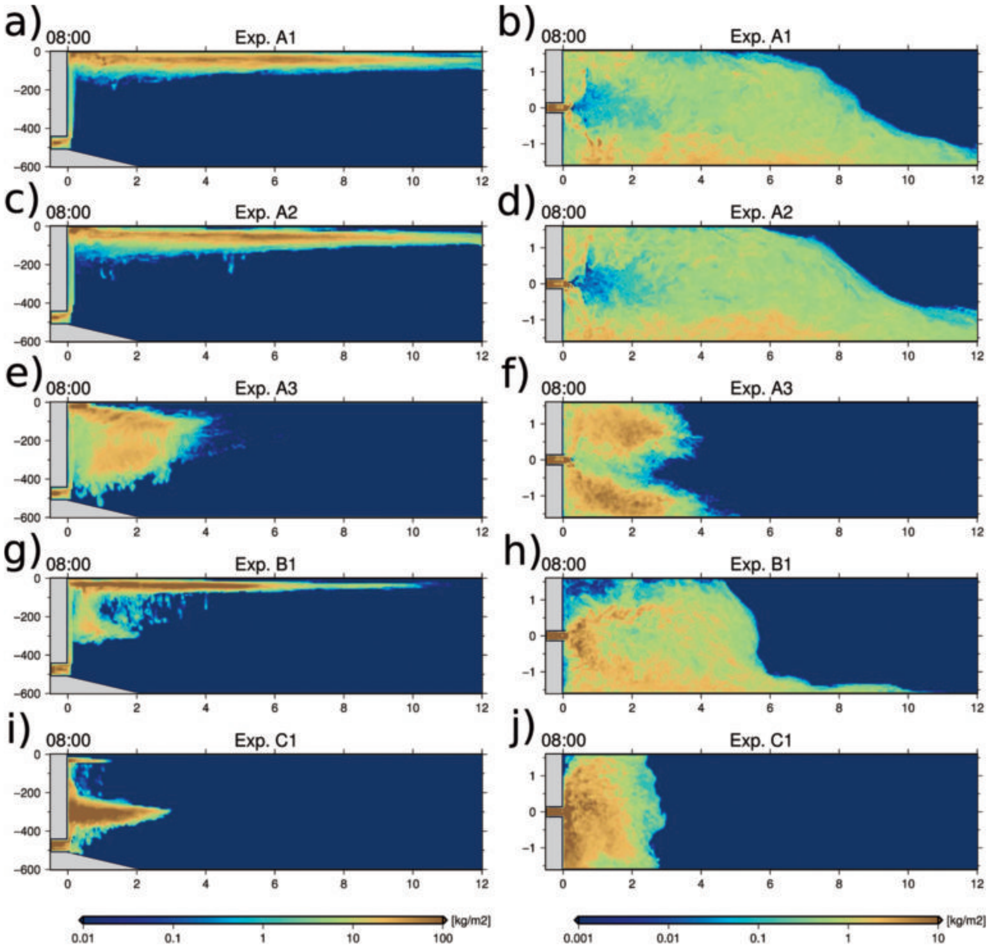

図4：フィヨルド横断方向（左列）及び鉛直方向（右列）に積算した懸濁物質量．上からそれぞれ実験A1，A2，A3，B1，C1の実験開始8時間後のスナップショット値．
Figure 4：Snapshots of cross-fjord integrated (left column) and vertically integrated (right column) suspended sediment content at hour 8 for cases A1, A2, A3, B1 and C1.

り，それより遠方では高温低塩のSW層の直下に潜り込むように拡がっていく．初期には高濁度域はフィヨルド全幅を一様に占めているが，4時間を経過すると地球自転の影響により，プルーム先端部分は沖に向かって右側の壁面に捕捉されている．右側壁面に沿ったプルーム先端は8時間後に領域東端に到達する．図4は各実験の8時間後における，フィヨルド横断方向及び鉛直方向に積算した懸濁物質含有量である．また図5は実験領域を氷河末端からの距離に応じて4つの区分に分割し，それぞれの区分について8時間経過後の懸濁物質存在量の鉛直プロファイルをプロットしたものである．図4-a，bおよび図5-aから実験A1においては概ねフィヨルド末端より2km以遠では懸濁物質含有量のピークが50m深に位置し，また投入された懸濁物質の大部分が領域南側（氷河末端から沖を見て右側）に存在していることがわかる．

次に融解水流出量はA1と同じで，粒子沈降速度を変化させた感度実験の結果を紹介する．実験A2は粒径が30 μm（粗めのシルト），A3は粒径が100 μm（細かい砂粒）にそれぞれ対応している．実験A2（図4-c，dおよび図5-b）では定量的にもA1とほぼ同様の結果が得られたのに対し，A3（図4-e，fおよび図5-c）はそれらとは全く異なる．A3においても氷河末端での湧昇流は沈降速度の速い懸濁粒子を海面まで上昇させることはできているが，湧昇域の外側では懸濁粒子は沖向き流の形成されている亜表層に留まることができず，結果として8時間後においても4kmより遠方には到達できていない．4km以内の海域では水深100-400mの層に広く懸濁物質が分布している．

続いて粒子沈降速度はA1と同じとし，融解水流出量を変化させた実験の結果を紹介する．流出量をA1の30%としたB1（図4-g，hおよび図5-d）においては，供給される浮力が全ての懸濁粒子を海面まで湧昇させるには十分でなく，一部の懸濁粒子はPWとAWの間に存在する成層を突破できずに200-300m深に留まっている．表層まで到達した懸濁粒子は定性的にはA1と同様

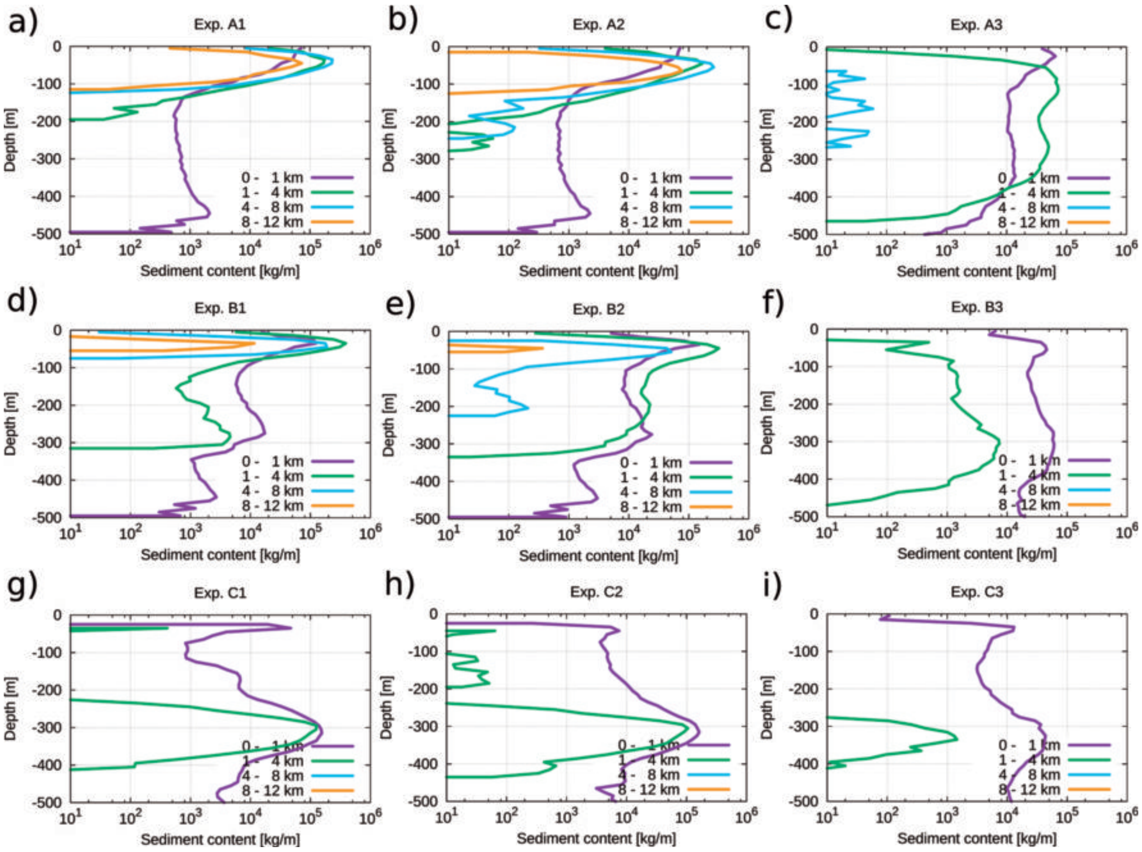

図5：各実験における実験開始8時間後の懸濁物質分布の鉛直プロファイル．氷河末端からの距離に応じて4つの区分を設け，それぞれについての水平積分値の鉛直分布を対数スケールでプロットした．
Figure 5：Vertical profiles of suspended sediment content at hour 8 for all cases. The domain is divided into four regions by the distance from the glacier front, and the vertical profile of horizontally integrated sediment content is plotted on a logarithmic scale for each region.

の高濁度域プルームを形成するが，浮力供給の減少に伴い鉛直循環もA1より弱化しているため，8時間後においても壁面に沿ったプルーム先端が10 kmまでしか到達しておらず，大半の懸濁物質は5 kmより近くに存在している．実験C1（図4-i，jおよび図5-g）では融解水供給量はA1の10％しかなく，ごくわずかの懸濁物質粒子しかAW-PW間の成層を突破できない．したがってほぼ全ての懸濁物質粒子が200-400 m深，氷河末端から2 km以内に留まるという結果となった．

4. まとめと今後の発展

海水中の懸濁物質をラグランジュ的に表現する粒子追跡を組み込んだ非静力学海洋モデルを用いて，グリーンランドカービング氷河末端から流出する融解水が形成する湧昇プルームと，それによってもたらされる陸起源懸濁物質の輸送過程を対象とした理想化数値シミュレーションを実施した．融解水流出量が大きい場合には湧昇プルームは海面まで到達し，氷河末端近傍で高濁度水域が形成される．その後融解水はSW層の下にもぐりこみながらフィヨルド内を広がり，それに伴って懸濁物質も亜表層を沖向きに輸送される．このような鉛直構造はフィヨルド内における海水濁度の現場観測ともよく整合する．実験開始直後には融解水プルームは扇状に等方的に広がるが，実験開始後6時間を超えると徐々にコリオリ力の影響でプルーム先端が沖を見て右側の壁面に補足され，懸濁物質も壁面近くにより多く存在する．一方流出量が小さい場合は湧昇プルームが海面まで到達することができず，融解水とそこに含まれる懸濁物質はPWとAWの中間層（～300 m深）に留まる．これらの結果は海面のみを対象とする衛星画像による見積もりでは氷河融解水に起因する陸起源懸濁物質の海洋への供給を正しく評価できないことを意味し，採水等による現場直接観測の重要性を再確認するに至った．また懸濁物質の沈降速度を変化させた感度実験においては，シルトサイズ（直径30 μm以下）に相当する粒子は10 km以上遠方まで輸送されるのに対し，砂粒として分類される直径100 μmの粒子の大半は氷河末端から4 km以内で沈降し，

それ以上遠方に輸送されることは稀であった．本研究では積分期間が8時間と短く，また領域も狭いため終端沈降速度 10^{-3} m s^{-1} と 10^{-4} m s^{-1}（それぞれ粒径約30 μm と10 μm に対応）の実験間には顕著な違いは見られなかった．今後はフィヨルド外との接続を含む，より広範囲・長い積分期間の実験を実施し，懸濁物質の輸送および沈降による除去・堆積過程を詳細に調査したい．本研究実施時点では筆者に具体的な懸濁物質濃度に関する知識が無かったため，恣意的かつ一定の堆積物粒子投入を与えるのみであったが，より現実的な懸濁物質濃度及び粒径分布を適用することが望まれる．特に濁度と実際の懸濁物質濃度との定量的な対応関係は数値モデルと衛星観測等を比較するためにも重要であり，現場観測研究と連携してこれらの課題に取り組みたい．本研究は海洋に流出する氷河末端での高濁度融解水を対象としているため，運動を駆動する密度差において塩分偏差の寄与が支配的であり，浮遊する懸濁粒子はほぼパッシブトレーサーとして振舞う．他方，淡水湖に流出する氷河においては浮遊する懸濁粒子の濃度自体が循環や成層構造の維持に大きく影響している（Sugiyama et al., 2016）．本研究で開発した数値モデルはこのような浮遊粒子が流体の運動に直接影響する状況を陽に扱うことが可能であり，今後は対象を淡水湖まで広げた発展的研究が期待できる．

湧昇プルームの形成は表層に栄養塩を供給する一方，懸濁物質の供給によって生じる高濁度域が日射を遮ることで光環境を悪化させるなど，氷河融解水の供給はグリーンランド周辺海域の生物地球化学環境において重要な役割を担っている．特に近年の氷床質量損失の加速による氷河融解水供給量の増大と，それに伴う環境変化が海洋生物資源に与える影響の解明は喫緊の課題である．筆者らが開発する非静力学海洋数値モデル kinaco には鉄分による制限項を含む低次生態系モデル（Shigemitsu et al., 2012）が組み込まれており，また現実的な懸濁物質濃度を与えることで格子内粒子集積度に基づく光制限要素を導入することも可能である．氷河融解水の供給が駆動する様々な物理及び生物地球化学過程を陽に表現するフィヨルド内海洋生態系シミュレーションの実現に向けて準備が整いつつあり，本研究をその端緒としたい．

謝辞

本研究は JSPS 科研費 16K12575，26247080 および文部科学省北極域研究推進プロジェクト（ArCS）の助成を受けた．北海道大学北極域研究センターの漢那博士には最新の現場直接観測からの知見並びに生物地球化学的見地から高濁度融解水の重要性に関する示唆を頂いた．東京大学大気海洋研究所の川崎博士からは高解像度海洋大循環モデルの出力に基づいたグリーンランド北西沿岸域の成層構造に関する助言を頂いた．また本研究成果の一部は，低温科学研究所共同利用研究集会における発表と議論に基づくものである．記してここに謝意を表する．

参考文献

Carroll, D., D. Sutherland, E. Shroyer, J. Nash, Ginny Catania and L. Stearns (2015) Modeling Turbulent Subglacial Meltwater Plumes: Implications for Fjord-Scale Buoyancy-Driven Circulation. *J. Phys. Oceanogr.*, **45**, 2169–2185.

Chauché, N., A. Hubbard, J. Gascard, J. Box, R. Bates, M. Koppes, A. Sole, P. Christoffersen and H. Patton (2014) Ice-ocean interaction and calving front morphology at two west Greenland tidewater outlet glaciers. *The Cryosphere*, **8**, 1457–1468.

Chu, V. (2014) Greenland ice sheet hydrology: A review. *Prog. in Phys. Geogr.*, **38**, 19–54.

Losch, M. (2008) Modeling ice shelf cavities in a z coordinate ocean general circulation model. *J. Geophys. Res.*, **113**, C08043

Lydersen, C., P. Assmy, S. Falk-Petersen, J. Kohler, K. M. Kovacs, M. Reigstad, H. Steen, H. Strøm, A. Sundfjord, Ø. Varpe, W. Walczowski, J. M. Weslawski and M. Zajaczkowski (2014) The importance of tidewater glaciers for marine mammals and seabirds in Svalbard, Norway. *J. Marine Sys.*, **129**, 452–471.

Matsumura, Y. and H. Hasumi (2008) A non-hydrostatic ocean model with a scalable multigrid Poisson solver. *Ocean Model.* **24**, 15–28.

Matsumura, Y. and K. Ohshima (2015) Lagrangian modelling of frazil ice in the ocean. *Ann. Glaciol.*, **56** (69), 373–382.

Ohashi, Y., T. Iida, S. Sugiyama and S. Aoki (2016) Spatial and temporal variations in high turbidity surface water off the Thule region, northwestern Greenland. *Polar Science*, **10**, 270–277.

Pritchard, H., R. Arthern, D. Vaughan and L. Edwards (2009) Extensive dynamic thinning on the margins of the Greenland and Antarctic ice sheets. *Nature*, **461**, 971–975.

Rignot, E., J. L. Bamber, M. R. van den Broeke, C. Davis, Y. Li, W. J. van de Berg and E. van Meijgaard (2008) Recent Antarctic ice mass loss from radar interferometry and regional climate modelling. *Nat. Geosci.*, **1**, 106–110.

Rignot, E. I. Velicogna, M. R. Van den Broeke, A. Monaghan, J. T. M. Lenaerts (2011) Acceleration of the contribution of the Greenland and Antarctic ice sheets to sea level rise. *Geophys. Res. Lett.*, **38**, L05503.

Rubey, W. W. (1933) Settling velocities of gravel, sand, and silt particles. *Am. J. Sci.*, **25**, 325–338.

Shigemitsu, M., T. Okunishi, J. Nishioka, H. Sumata, T. Hashioka, M. N. Aita, S. L. Smith, N. Yoshie, N. Okada and Y. Yamanaka (2012) Development of a one-dimensional ecosystem model including the iron cycle applied to the Oyashio region, western subarctic Pacific. *J. Geophys. Res.*, **117**, C06021.

Sugiyama, S., M. Minowa, D. Sakakibara, P. Skvarca, T. Sawagaki, Y. Ohashi, N. Naito and K. Chikita (2016) Thermal structure of proglacial lakes in Patagonia. *J. Geophys. Res. Earth Surf.*, doi:10.1002/2016JF004084.

Straneo, F., R. G. Curry, D. D. Sutherland, G. S. Hamilton, C. Cenedese, K. Vage and L. A. Stearns (2011), Impact of fjord dynamics and glaicial runoff on the circulation near Helheim Glacier. *Nat. Geosci.*, **4**, 322–327.

大橋良彦（2015）グリーンランド氷床北西部における高濁度海水域の変動．北海道大学大学院環境科学院地球圏専攻修士論文

低温科学 75 （2017） 85-90
doi: 10.14943/lowtemsci. 75. 85

Temperature observations from northernmost Greenland, 2006-2010

Anders Schomacker[1,2]*, Nicolaj K. Larsen[2,3], Anders A. Bjørk[2], Kurt H. Kjær[2]

Received 11 November, accepted 11 January 2017

Air-, surface-, and subsurface temperatures were recorded by automatic weather stations in Bliss Bugt and Moore Gletscher, Johannes V. Jensen Land, North coast of Greenland from 2006-2010. The mean annual surface temperature is −12.1 ℃ in Bliss Bugt and −13.8 ℃ at Moore Gletscher. In 20 cm depth below the surface at Moore Gletscher, the mean annual temperature is −13.2 ℃ (2007-2008). High-amplitude fluctuations of the winter temperature at the surface and in 20 cm depth at Moore Gletscher indicate that the surface has little or no snow cover, possibly due to catabatic winds from the glacier. In contrast, in Bliss Bugt, c. 5 km to the north, the surface temperature series only shows low-amplitude variations during the winters. This indicates a significant snow cover in Bliss Bugt, persisting throughout the winter. The surface temperature series reveals that the surface is snow free from mid-late June to late August in Bliss Bugt.

Keywords: Surface temperature, soil temperature, Bliss Bugt, Moore Gletscher, North Greenland

1. Introduction

Instrumental temperature records from the High Arctic are characterized by few observation points, very uneven geographical distribution of observation points, and short temporal coverage of the observations (Bekryaev et al., 2010). The instrumental temperature record of the north coast of Greenland only extends back to 1980 with data from an automatic weather station located at Kap Morris Jesup (Fig. 1; 83°39'N lat.; 33°22'W long., 4 m a.s.l.; WMO station ID 4301; Cappelen et al., 2000) and operated by the Danish Meteorological Institute. The temperature series from this station suffers from several data gaps and the completion is only 65% for the period 1980-1999 (Box, 2002). This means that additional short time series of air and ground temperature observations from this very remote region add important information that might be used for studies of the cryosphere, e.g. glacier mass balance, snow cover, the thermal state of permafrost, and validation of remotely sensed data (Braithwaite et al., 1998; Christiansen et al., 2008; Romanovsky et al., 2010; Urban et al., 2013; Williamson et al., 2014).

During a field campaign in North Greenland in 2006, two automatic weather stations were deployed in Bliss Bugt and in front of Moore Gletscher, both located in Johannes V. Jensen Land at the central north coast (Fig. 1). The stations were configured to measure air temperature 2.5 m above the ground, precipitation, surface temperature, and soil temperature in 20 cm depth (in front of Moore Gletscher). Data were recorded from 2006-2010, and retrieved during field work in the summer of 2016. The aim of this paper is to present the temperature data series from Bliss Bugt and

---

*Corresponding author
e-mail：anders.schomacker@uit.no
1）Department of Geosciences, UiT The Arctic University of Norway, Tromsø, Norway
2）Centre for GeoGenetics, Natural History Museum of Denmark, University of Copenhagen, Copenhagen, Denmark
3）Department of Geoscience, Aarhus University, Aarhus, Denmark

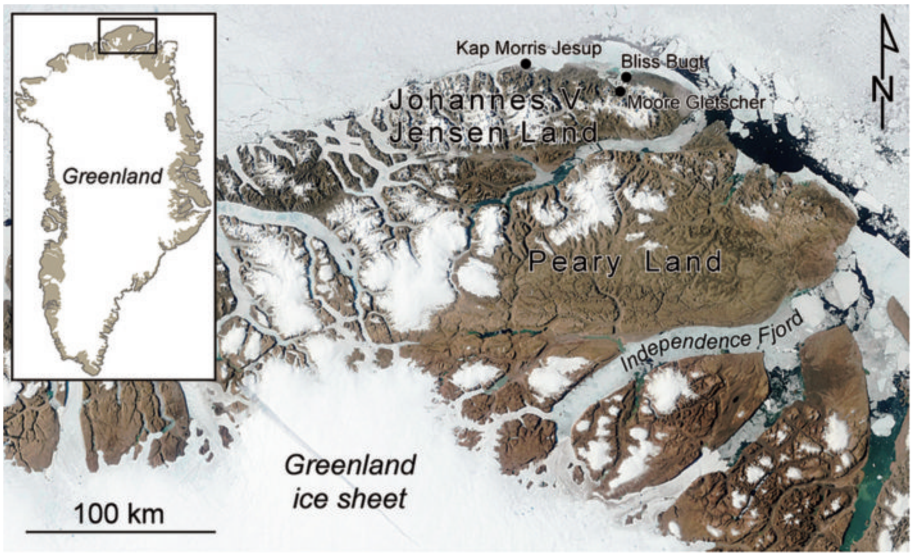

Figure 1 : Map of North Greenland. The two automatic weather stations were located in Bliss Bugt and Moore Gletscher in Johannes V. Jensen Land. The location of the meteorological station at Kap Morris Jesup is also shown.

Moore Gletscher.

2. Setting

The north coast of Greenland is characterized by a High Arctic, arid climate. There is perennial sea ice cover at the Arctic Ocean along the north coast. Kap Morris Jesup annually experiences 154 days of midnight sun and 143 days of polar night. Some of the coldest temperatures ever measured in Greenland (outside the Greenland Ice Sheet) are from North Greenland. The coldest temperatures recorded in Greenland in November and December in the period 1980–1999 were measured at Kap Morris Jesup with −45 ℃ and −48.9 ℃, respectively (Cappelen et al., 2000). The mean monthly temperatures at Kap Morris Jesup from 1980–2013 are presented in Fig. 2. Based on years with complete temperature records, the mean annual air temperature at Kap Morris Jesup is −17.3 ℃ from 1980–2013. Cappelen et al. (2000) report a mean annual air temperature of −18 ℃ at Kap Morris Jesup from 1980–1999. Positive mean monthly air temperatures only occur in June, July, and August (JJA). The mean summer (JJA) air temperature is 0.3 ℃ at Kap Morris Jesup based on months with a complete record in the period 1980–2013.

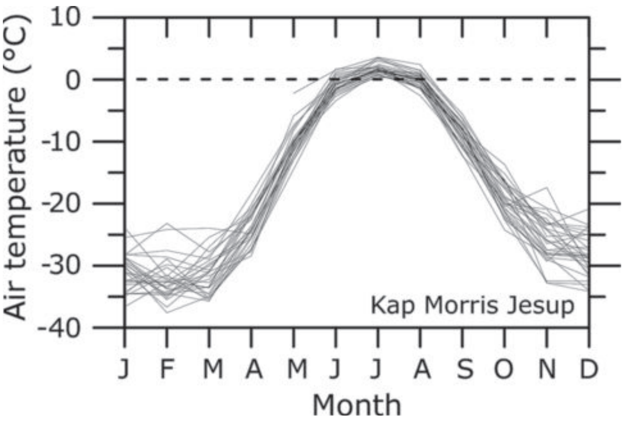

Figure 2 : Stacked curves of monthly mean air temperatures from Kap Morris Jesup from 1980–2013. Data from the Danish Meteorological Institute.

3. Data and methods

In Bliss Bugt, an automatic weather station was deployed at 83°31' N lat.; 28°47' W. long.; 17 m a.s.l. (Fig. 1). It was operated from July 30, 2006 and recorded hourly until April 19, 2010 when the datalogger memory was full. Air and ground surface temperatures were recorded with Gemini Data Loggers TinyTag Plus2 TGP-4020 with a PB-5001-1M5 10 K NTC thermistor. For positive temperatures, the accuracy of the sensor is 0.2 ℃, and for negative temperatures it ranges from 0.2–0.4 ℃. The air temperature was measured 2.5 m above the ground and the thermistor was mounted in a

Figure 3 : Photograph of the automatic weather station in front of Moore Gletscher, August 4, 2006. The surface and sub-surface temperature sensors are not visible. Persons for scale.

white plastic solar radiation shield. The ground surface thermistor was radiation shielded by well-ventilated rocks. Temperature range of the thermistors is reported to −40 to 125 ℃ by the manufacturer although they did return colder measurements. This station did not measure temperature below the surface.

A second automatic weather station was deployed c. 700 m from the Moore Gletscher terminus at 83°29'N lat.; 28°55'W long; 10 m a. s. l. (Figures 1 and 3). It was deployed on August 4, 2006 and recorded hourly until February 2, 2010 when the datalogger memory was full. This station was equipped with similar instruments as Bliss Bugt, but additionally it measured soil temperature at 20 cm depth below the surface.

Both stations were also equipped with an automatic precipitation gauge. However, one was missing when the stations were visited in 2016, and another did not return meaningful data. Table 1 provides an overview of the recovered data series from the two stations.

4. Results and discussion

The two air temperature sensors only recorded data from July/August 2006 to November 2006/April 2007, respectively (Table 1). They stopped recording data for unknown reasons. The Danish Meteorological Institute automatic weather station at Kap Morris Jesup was also not recording data from January 2006 to July 2009, and the only overlap between our temperature observations and Kap Morris Jesup is from July 2009–April 2010.

The air temperature data from Bliss Bugt reached a minimum of −43.2 ℃ on December 2006. This series also shows that the 2006–2007 winter air temperatures range between 0 ℃ and −43.2 ℃. The surface temperature in Bliss Bugt, however, is characterized by much smaller amplitude during the winters (Fig. 4A; Table 2). The four recorded winters all show a similar trend where temperature drops below zero in mid-late August and does not reach positive temperatures until mid-late June the following year. The lowest surface temperature of −28.7 ℃ in Bliss Bugt was recorded on March 12, 2007. We interpret the low-amplitude winter surface temperatures in Bliss Bugt as evidence of a significant snow cover that does not allow the short-lived air temperature fluctuations to penetrate to the ground surface (Christiansen et al., 2008). This is also supported by the slow transition from negative to positive ground surface temperatures in mid-late June each year. The ground surface temperature first rises steeply to 0 ℃ in June each year and stays at c. 0 ℃ for 1–2 weeks. This is interpreted as the final period of snowmelt.

The summer surface temperature in Bliss Bugt shows much larger amplitude than the winter temperature and follows closely the air temperature fluctuations in 2006. The maximum ground surface temperature was 24.7 ℃ recorded on August 1, 2008 and the

Table 1 : Overview of automatic temperature recordings in North Greenland, 2006–2010.

Station name	Position	Parameter	Start date	End date
Bliss Bugt	83°31'N; 28°47'W	2.5 m air temp.	July 30, 2006	April 24, 2007
Bliss Bugt	83°31'N; 28°47'W	Surface temp.	July 30, 2006	April 19, 2010
Moore Gletscher	83°29'N; 28°55'W	2.5 m air temp.	August 4, 2006	November 14, 2006
Moore Gletscher	83°29'N; 28°55'W	Surface temp.	August 4, 2006	February 2, 2010
Moore Gletscher	83°29'N; 28°55'W	20 cm soil temp.	August 10, 2006	December 3, 2009

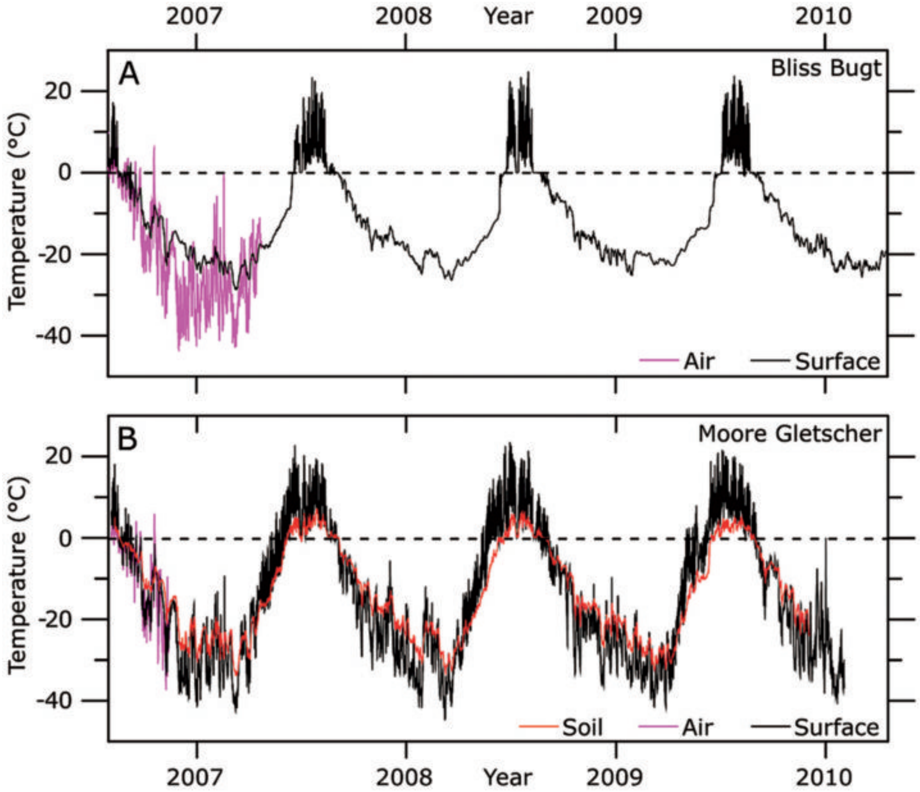

Figure 4 : Temperature records from 2006–2010 from the automatic weather stations at the North coast of Greenland. A. Bliss Bugt. B. Moore Gletscher.

Table 2 : Summary of data from automatic temperature recordings in North Greenland, 2006–2010.

Station name	Parameter	T_{mean} (2007; ℃)	T_{mean} (2008; ℃)	T_{mean} (2009; ℃)	T_{max} (℃; date)	T_{min} (℃; date)
Bliss Bugt	2.5 m air temp.	No data	No data	No data	10.5; August 10, 2006	−43.2; December 1, 2006
Bliss Bugt	Surface temp.	−12.0	−12.4	−11.8	24.7; August 1, 2008	−28.7; March 12, 2007
Moore Gletscher	2.5 m air temp.	No data	No data	No data	10.4; August 10, 2006	−37.3; November 8, 2006
Moore Gletscher	Surface temp.	−13.6	−13.9	−14.0	23.5; June 29, 2008	−44.6; March 8, 2007
Moore Gletscher	20 cm soil temp.	−12.8	−13.6	No data	7.0; July 27, 2007	−33.9; March 9, 2007

temperature ranges between 0 ℃ and 24.7 ℃ during the summers (Table 2). The mean annual ground surface temperature in Bliss Bugt is −12.1 ℃ based on the complete years 2007, 2008, and 2009.

The air temperature data from Moore Gletscher reached a minimum of −37.3 ℃ on November 8, 2006 before the instrument stopped recording data later that month (Fig. 4B; Table 2). The period of overlap with Bliss Bugt shows the same trend. The ground surface temperature series at Moore Glacier, however, differs significantly from Bliss Bugt (Fig. 4). The amplitude during the winters is much higher, and the ground surface temperature mimics closely the air temperature during the period of overlap in late 2006. Winter ground surface temperatures at Moore Glacier reach a minimum of −44.6 ℃ on March 8, 2007, and the amplitude reaches c. 40 ℃ in the winter of 2010. The similarity to the air temperature in late 2006 and the high amplitude of the ground surface temperature during winters compared to Bliss Bugt indicate that the surface at this locality does not have a significant snow cover (Christiansen et al., 2008). The transition from negative to positive temperatures is rapid in all three years, and there are no extensive periods with near-zero temperatures. This also suggests that there is almost no snow cover.

The summer surface temperature trend at Moore Gletscher is similar to Bliss Bugt. It closely follows the air temperatures in the late summer of 2006. The maximum ground surface temperature was 23.5 ℃ recorded on June 29, 2008 and the temperature ranges between 0 ℃ and 23.5 ℃ during the summers (Table 2). The mean annual ground surface temperature at Moore Gletscher is −13.8 ℃ based on the complete years 2007, 2008, and 2009.

The temperature at Moore Gletscher was also recorded 20 cm below the surface (Tables 1–2; Fig. 4B). The amplitude of this temperature series is smaller than at the surface and in the air but it follows the fluctuations recorded on the ground surface. Minimum temperature in 20 cm depth was −33.9 ℃ recorded on March 9, 2007, and maximum temperature was 7 ℃ recorded on July 27, 2007. The mean annual temperature 20 cm below the surface at Moore Gletscher is −13.2 ℃ based on the two complete years 2007 and 2008. We interpret the high-amplitude winter temperature variations in 20 cm depth as an indicator of a very limited insulating snow cover at the surface.

Notably, the ground surface temperature at Moore Glacier rises above zero 3–4 weeks earlier than in Bliss Bugt each year. Together with the high-amplitude winter temperature fluctuations, this indicates that the snow cover was limited throughout the observation period. We suggest that the limited snow cover in front of Moore Gletscher is due to catabatic winds from the glacier, blowing snow off the ground surface. The station in Bliss Bugt is located on the flat, open coastal plain at the north coast of Greenland (Larsen et al., 2010). Although this very open plain is not favorable for snow accumulation, our data show that the surface is, indeed, snow covered until mid-late June. The snow cover also explains the slightly higher mean annual ground surface temperatures in Bliss Bugt compared to Moore Gletscher (Table 2). Ground surface temperature data suggest that the surface is free of snow from mid-late June to late August in Bliss Bugt. Air, surface, and 20 cm depth temperatures all suggest that the study area hosts continuous permafrost (e. g. French, 2007; Christiansen et al., 2008). Only the upper 20–30 cm of the ground were thawed during installation of the thermistor at Moore Gletscher in August 2006.

5. Conclusions

- The mean annual ground surface temperature in Bliss Bugt is −12.1 ℃ (2007–2009) and −13.8 ℃ at Moore Gletscher (2007–2008).
- The mean annual temperature at 20 cm depth below the surface at Moore Gletscher is −13.2 ℃ (2007–2008).
- Snow free surface conditions extend from mid-late June to late August in Bliss Bugt (2007–2009).
- The lowest recorded temperature was −44.6 ℃ at the ground surface at Moore Gletscher on March 8, 2007. The highest temperature was 24.7 ℃ at the ground surface in Bliss Bugt on August 1, 2008.
- Bliss Bugt and Moore Gletscher experience very different snow cover conditions. The low-amplitude fluctuations of surface temperature in Bliss Bugt suggest that the surface is snow-covered throughout the winter. The forefield of Moore Gletscher experience high-amplitude variations in surface and subsurface temperature, indicating that the snow cover is absent or thin.

Acknowledgements

The Danish National Research Council (FNU) supported this study through the LongTerm project (grant to S. Funder). Funding from the Commission for Scientific Research in Greenland to K.H. Kjær during the International Polar Year 2007–08 endorsed APEX (Arctic Palaeoenvironments and its EXtremes) project is also acknowledged. We thank members of the 2006 LongTerm field campaign in North Greenland. K. H. Kjær acknowledges the invitation to the international workshop “Greenland ice sheet mass loss and its impact on global climate change” under the SIGMA (Snow Impurity and Glacial Microbe effects on abrupt warming in the Arctic) project, the ArCS (Arctic Challenge for Sustainability) Project and the Joint Research Program of the Institute of Low Temperature Science, Hokkaido University. Data from Bliss Bugt and Moore Gletscher

are available from the authors.

References

Bekryaev, R. V., I. V. Polyakov, and V. A. Alexeev (2010) Role of polar amplification in long-term surface air temperature variations and modern Arctic warming. *J. Climate*, **33**, 3888–3906.

Box. J. E. (2002) Survey of Greenland instrumental temperature records: 1873–2001. *Int. J. Climatol.,* **22**, 1829–1847.

Braithwaite, R. J., T. Konzelmann, C. Marty, and O. B. Olesen (1998) Reconnaissance study of glacier energy balance in North Greenland, 1993–94. *J. Glaciol.*, **44**, 239–247.

Cappelen, J., B. V. Jørgensen, E. V. Laursen, L. S. Stannius, and R. S. Thomsen (2000) The observed climate of Greenland, 1958–99 - with climatological standard normal, 1961–90. *Dan. Met. Inst. Techn. Rep.*, **00–18**, 1–151.

Christiansen, H. H., C. Sigsgaard, O. Humlum, M. Rasch, and B. U. Hansen (2008) Permafrost and periglacial geomorphology at Zackenberg. *Adv. Ecol. Res.*, **40**, 151–174.

French, H. M. (2007) *The periglacial environment.* John Wiley and Sons, England.

Larsen, N. K., K. H. Kjær, S. Funder, P. Möller, J. J. M. van der Meer, A. Schomacker, H. Linge, and D. A. Darby (2010) Late Quaternary glaciation history of northernmost Greenland - Evidence of shelf-based ice. *Quaternary Sci. Rev.,* **29**, 3399–3414.

Romanovsky, V. E., S. L. Smith, and H. H. Christiansen (2010) Permafrost thermal state in the Polar northern hemisphere during the International Polar Year 2007–2009: a synthesis. *Permafrost Periglac.*, **21**, 106–116.

Urban, M., J. Eberle, C. Hüttich, C. Schmullius, and M. Herold (2013) Comparison of satellite-derived land surface temperature and air temperature from meteorological stations on the pan-Arctic scale. *Remote Sens.,* **5**, 2348–2367.

Williamson, S. N., D. S. Hik, J. A. Gamon, J. L. Kavanaugh, and G. E. Flowers (2014) Estimating temperature fields from MODIS land surface temperature and air temperature observations in a sub-Arctic alpine environment. *Remote Sens.,* **6**, 946–963.

低温科学 75 （2017） 91-104
doi: 10.14943/lowtemsci. 75. 91

Numerical weather prediction system based on JMA-NHM for field observation campaigns on the Greenland ice sheet

Akihiro Hashimoto[1]*, Masashi Niwano[1], Teruo Aoki[2, 1], Shun Tsutaki[3], Shin Sugiyama[4], Tetsuhide Yamasaki[5], Yoshinori Iizuka[4], Sumito Matoba[4]

Received 25 October 2016, accepted 11 January 2017

As part of a research project titled, "Snow Impurity and Glacial Microbe effects on abrupt warming in the Arctic" (SIGMA), numerous observation campaigns were conducted on the Greenland ice sheet (GrIS) from FY2011 to FY2015. To support research activities in the field, the Japan Meteorological Agency Non-Hydrostatic Model (JMA-NHM) was applied to form a numerical weather prediction system covering all of Greenland. Before executing our numerical simulation using this model, however, we modified the model to better represent the meteorological processes over the GrIS, since the original model was adjusted to fit mid-latitude environments. Using our modified model, we performed numerical weather prediction twice per day such that expedition crews in the field could access the resulting prediction information in the morning and evening, which helped them plan and execute their daily missions. Further, we improved our model during these campaigns by referencing the daily reports obtained from the observation site on the GrIS. In this paper, we describe our weather prediction system and evaluate its performance in reference to surface meteorological observation data.

Keywords: Greenland, Weather prediction, Non-hydrostatic model

1. Introduction

Field observation campaigns, especially in polar regions, often face severe weather conditions. Since weather is indeed one of the strongest factors that influence field activities, accurate weather prediction is crucial for making a campaign successful and ensuring the safety of the individuals involved. In general, operational weather predictions have limited availability in such campaign areas. There are research-based prediction systems that target polar regions, in particular the Arctic Numerical Weather Prediction (Hines et al., 2008, Hines et al., 2011, Wilson et al., 2011) and Antarctic Numerical Weather Prediction (Powers et al., 2003, Bromwich et al., 2013) systems, both currently based on the Polar Weather Research and Forecasting (WRF) model, though previously on the Polar Fifth-generation Mesoscale Model (MM5) (Bromwich et al., 2005).

Unfortunately, these existing systems are not customized for particular campaigns. If expedition crews in the field are able to access prediction

---

*Corresponding Author
e-mail：ahashimo@mri-jma.go.jp
１）Meteorological Research Institute, Japan Meteorological Agency, Tsukuba, Japan
２）Graduate School of Natural Science and Technology, Okayama University, Okayama, Japan
３）Earth Observation Research Center, Japan Aerospace Exploration Agency, Tsukuba, Japan
４）Institute of Low Temperature Science, Hokkaido University, Sapporo, Japan
５）Avangnaq, Takatsuki, Japan

information customized for their specific campaigns, their activities become safer and more efficient. Further, observation data obtained during a campaign often include information regarding various phenomena that go undetected by operational observation systems, thus these data are useful for validation and improving existing weather prediction models.

In the summer seasons of 2011–2015, the "Snow Impurity and Glacial Microbe effects on abrupt warming in the Arctic" (SIGMA) project conducted glaciological, meteorological, and biological observation campaigns in Greenland (Aoki et al., 2014; Niwano et al., 2015). To support these campaigns, we created a specific weather prediction system in the summer season of 2013, then extended our system for campaigns held in successive years (Hashimoto et al., 2016). Weather prediction information was also shared with other cooperative field activities in Greenland, including the following: field observations of aerosol and frost flower at Siorapaluk, northwestern Greenland (Hara et al., 2014; Matoba et al., 2014); glacier dynamics observations on Bowdoin Glacier (Sugiyama et al., 2015) as part of the Green Network of Excellence Arctic Climate Change Research Project (GRENE-Arctic, 2011–2015); glaciological and meteorological observations at the southeastern dome (SE-Dome) site in southeastern GrIS (Iizuka et al., 2016); and maintenance of the Greenland Climate Network (GC-Net) Automatic Weather Station (AWS) by the Institute for Snow and Avalanches Research (SLF), Swiss Federal Institute for Forest, Snow and Landscape Research (WSL).

In the present paper, we describe our weather prediction system based on Hashimoto et al. (2016), showing prediction performance as evaluated with reference to surface meteorological observation data obtained from several field campaigns.

2. Meteorological data at field campaign sites

As part of the SIGMA project, an AWS was installed in the summer season of 2012 at a point called SIGMA-A on the northwest GrIS at 1,490 m above sea level (a.s.l.) (Aoki et al., 2014; Niwano et al., 2015), as shown in Fig. 1 (b). This AWS continues to measure meteorological parameters, including air temperature, humidity, air pressure, wind speed, and wind direction, as well as radiative properties, including downward and upward shortwave radiation and longwave radiation. Similarly, again shown in Fig. 1(b), as part of the GRENE-Arctic project, an AWS (WXT520, Vaisala) was installed on the eastern flank of Bowdoin Glacier at 100 m a.s.l to measure air temperature, humidity, air pressure, wind speed, and wind direction during expeditions conducted in the summers of 2013, 2014, and 2015.

Further, in a field campaign spanning from late May to early June 2015 at the SE-Dome at 3,170 m a.s.l., as shown in Fig. 1(c), air temperature, humidity, air pressure, wind speed, and wind direction were measured using a handheld meteorological meter (Kestrel 4500 NW). Cloud types, cloud coverage, and visibility were also recorded via visual observations. Specific explanations of the meteorological measurements from SIGMA-A, Bowdoin Glacier, and the SE-Dome are provided by Aoki et al. (2014), Sugiyama et al. (2015), and Iizuka et al. (2016), respectively. We compared our prediction results with these observation results to evaluate the accuracy of our prediction system.

3. Model description

We applied the Japan Meteorological Agency Non-Hydrostatic Model (JMA-NHM, Saito *et al.*, 2006) to our numerical experiments, essentially the same configuration as that of the operational weather prediction system implemented in Japan, with the following exceptions. First, instead of the original configuration, which adopts a double-moment scheme only for cloud ice and a single-moment scheme for other hydrometeors (i.e., snow and graupel), we applied a double-moment bulk cloud microphysics scheme to predict both the mixing ratio and concentration of particles of solid hydrometeors (i.e., cloud ice, snow, and graupel) and a single-moment scheme to predict only the mixing ratio of particles of liquid hydrometeors (i.e., cloud water and rain).

Second, for ice crystal formation in the atmosphere, we adopted a temperature-dependent parameterization instead of one that depends on the super-saturation ratio for ice and the updraft velocity of a grid from the original configuration. Third, we turned off the ice-saturation adjustment scheme (Tao et al., 1989) in the original

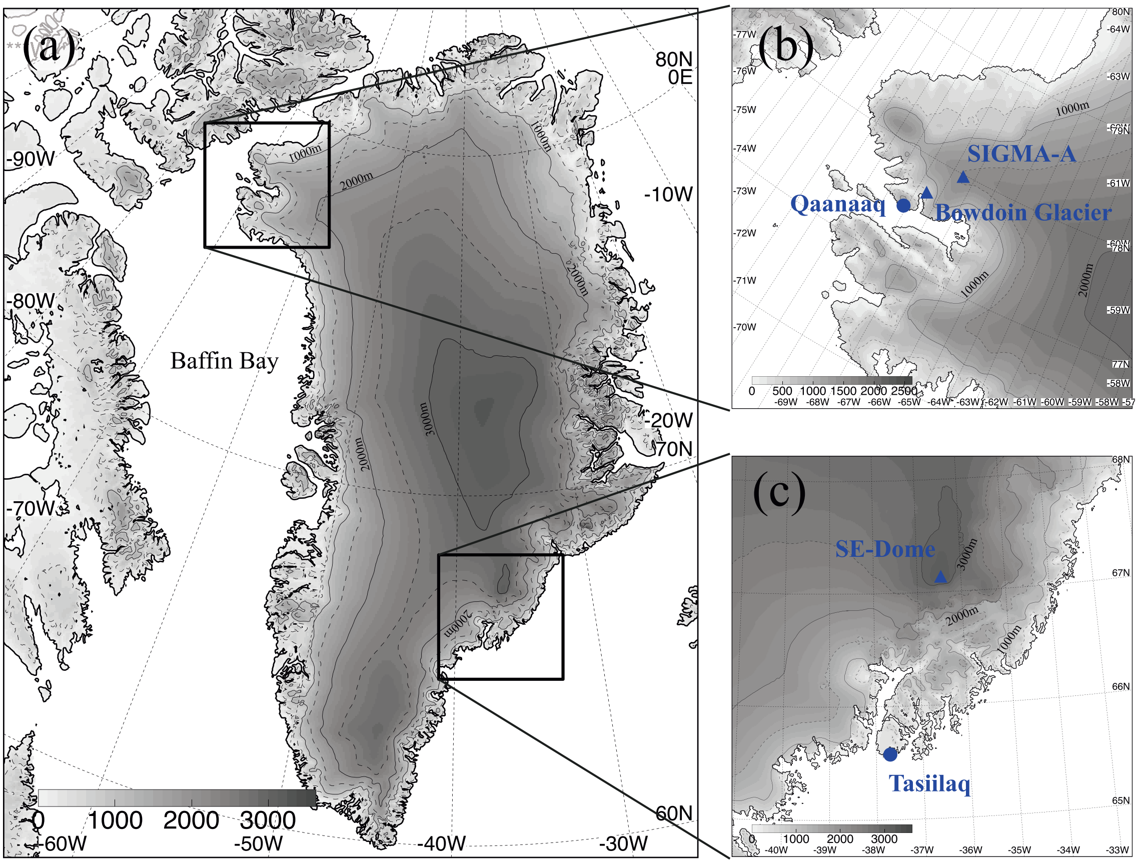

Figure 1 : (a) Calculation domain for our numerical weather prediction experiment, with enlarged views around (b) Qaanaaq and (c) Tasiilaq. Triangles and circles indicate camping sites and base towns, respectively.

configuration to avoid the unrealistic formation of ice clouds in the upper troposphere (Hashimoto et al. 2007). Similarly, we also turned off a cumulus parameterization.

JMA-NHM has four land surface classes, i.e., soil, snow, sea, and sea ice. In the original configuration, the surface temperature of a grid is allowed to rise higher than the freezing point even if the surface of the grid is classified as “snow”. Note that this considers the sub-grid scale heterogeneity of land surface characteristics (e.g., a mixture of soil and snow surface in a spatial scale less than the given grid spacing, i.e., several kilometers), which is usually included in domestic weather simulations (Hara, 2008). As our fourth alteration to the original model, we limited the surface temperature of a snow grid to be lower than the freezing point, since the heterogeneity of land surface characteristics is rarely seen on the GrIS.

4. Numerical experiments

Figure 1(a) shows the computational domain, with a domain size of 2250 × 2750 km in the horizontal plane and 22 km in the vertical direction. Horizontal grid spacing is set at 5 km, while vertical grid spacing is stretched from 40 m at the surface to 886 m at the top of the domain. We employ 50 variable vertical layers using a terrain-following coordinate system. Integration time is 42 hours for each simulation, with a timestep interval between 8 and 12 seconds. Computations of the radiative process are performed every 15 minutes at a horizontal grid spacing of 20 km. The initial and boundary conditions were obtained from the global forecast obtained via the Global Spectral Model (GSM) of JMA. Model topography was based on the 5-km-mesh surface elevation data from the digital elevation model of Greenland provided by Bamber et al. (2001). Simulations were performed twice per day with an initial time of 06 or 18 UTC throughout the various campaigns, with hourly output data used for our analysis.

5. Results

5.1 SIGMA-A

Figure 2 shows the observed and predicted meteorological parameters throughout the field campaign period of July 2012 at SIGMA-A. The model did well in terms of predicting downward shortwave and longwave radiant fluxes, except for occasional under- or overestimations of a daily maximum of downward shortwave radiant flux, as shown in Fig. 2(a). When the observed shortwave radiation showed a clear sine curve, which indicates almost no cloud coverage, our predictions agreed with observations. Conversely, when cloudy conditions were expected, our predictions showed a bias from the observations. The mean error (ME) and root mean square error (RMSE) were −28.2 W m^{-2} and 69.9 W m^{-2}, respectively, for the predicted downward shortwave radiant flux, and −2.2 W m^{-2} and 23.9 W m^{-2}, respectively, for the predicted downward longwave radiant flux (Fig. A1 in Appendix A).

Aoki et al. (2014) reported that it rained intermittently from the afternoon of July 10, 2012 through the morning of July 13, 2012. The measurement of precipitation was performed from 18 : 00 local time on 12 July to 09 : 00 local time on 14 July during the event. The measured rainfall was 20 mm. Based on this value, the total amount of rainfall during the event was estimated to be 60–100 mm (Aoki et al., 2014). Niwano et al. (2015) estimated the total rainfall amount as 100 mm on the basis of ERA-Interim reanalysis data with appropriate correction. Appearance of this rainfall event was certainly predicted by our system, as indicated by the blue line in Fig. 2(a), but the total rainfall amount was predicted as 10 mm at the SIGMA-A site. In general, quantitative accuracy of rainfall prediction is affected by many factors, including a shift of rainfall zone. This point will be the subject of future study. The wind speed and direction, shown in Fig. 2(b), as well as the temperature and water vapor mixing ratio, shown in Fig. 2(c), showed generally good agreement between

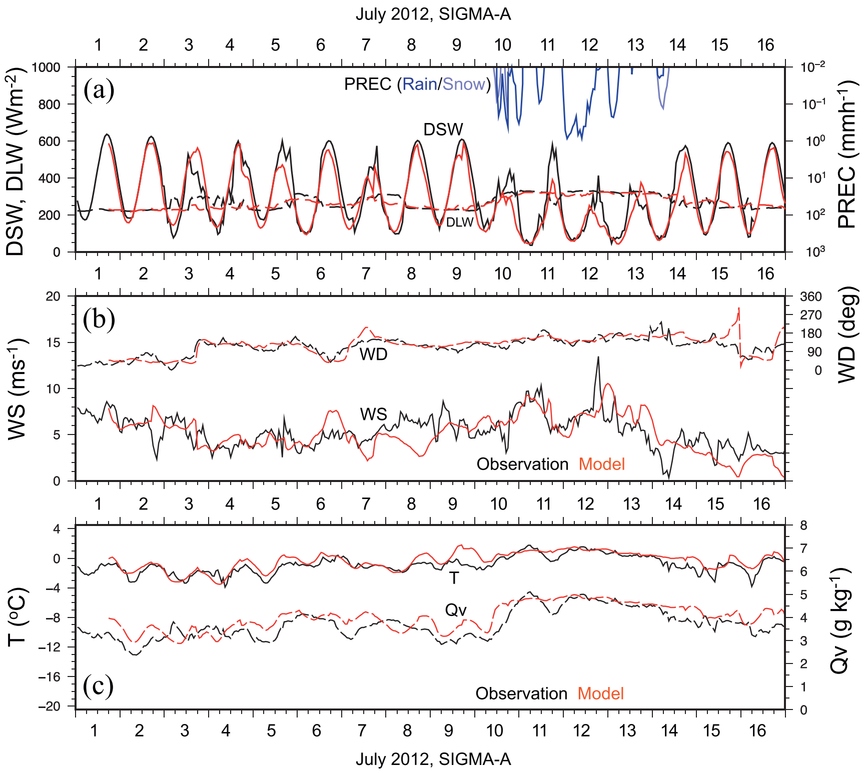

Figure 2 : (a) Observed (black) and predicted (red) downward shortwave (DSW, solid line) and longwave (DLW, broken line) fluxes at SIGMA-A for the campaign period of July 2012. (b) Same as (a), but solid and broken lines represent wind speed (WS) and direction (WD), respectively. (c) Same as (a), but solid and broken lines represent air temperature (T) and water vapor mixing ratio (Qv), respectively. Note that the blue line in (a) shows the predicted hourly precipitation amount.

observations and our predictions. According to the analysis of prediction error shown in Figs. A1 and A2(a)–(d), our prediction system has the same level of performance as in July 2012 throughout the campaigns in July 2013 (Fig. 3) and June 2014 (Fig. 4).

5.2 Bowdoin Glacier

Figure 5 shows the observed and predicted meteorological parameters through the field campaign period of July 2013 at Bowdoin Glacier (Sugiyama et al., 2015). Shown using solid lines in Fig. 5 (a), the wind speed showed generally good agreement between observations and our predictions, although a large overestimation occurred in some cases. Our model showed a systematic bias in wind direction, as indicated by the red broken line in Fig. 5(a). An easterly wind was predicted by our model most of the time, while westerly winds were actually observed, except for a few short-lived occurrences of an easterly wind. This discrepancy in wind direction between observations and our predictions points to the existence of local circulations that are not resolved with a grid spacing of 5 km in our simulations. These same features appeared in our predictions during the 2014 and 2015 campaigns, as shown in Figs. 6 and 7, respectively.

Figure 6, however, revealed another feature. Between July 18, 2014 and July 22, 2014, a strong easterly wind of up to approximately 10 $m\ s^{-1}$ was observed under the influence of a synoptic scale perturbation. During this period, in contrast with the other periods, our model accurately predicted both wind speed and direction. This remarkable turn for the better, accompanied by a strong wind, was also seen on July 25, 2013, as shown in Fig. 5. Figure 8 shows a scatter plot of the error of predicted wind direction and air temperature versus observed wind speeds. For 2013 and 2014, both Figs. 8(a) and 8(c) clearly indicate that the errors of predicted wind direction were never larger than 80 degrees when the observed wind speed was larger than 5 $m\ s^{-1}$.

For surface air temperature, our model showed a positive bias for most campaign periods in 2013 and 2015, as shown in Figs. 5(b) and 7(b), respectively, as well as better performance in 2014, as shown in Fig. 6(b). Figures 8(b), 8(d), and 8(f) provide scatter plots showing

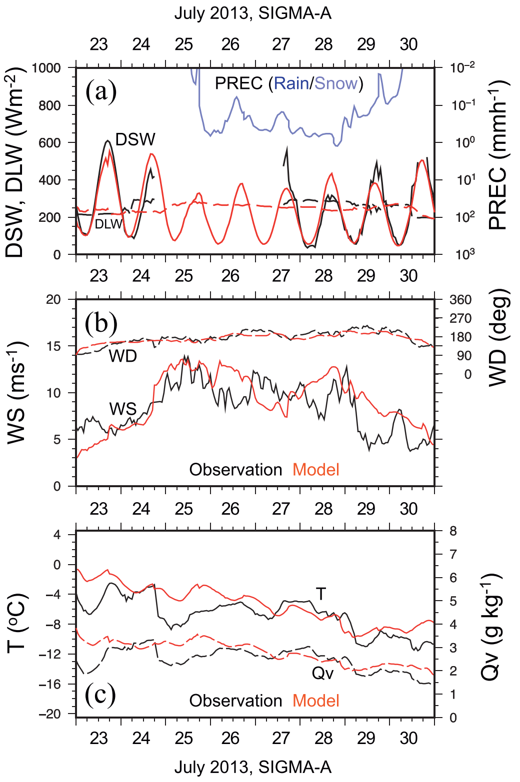

Figure 3: Same as Fig. 1, but for the campaign period of July 2013.

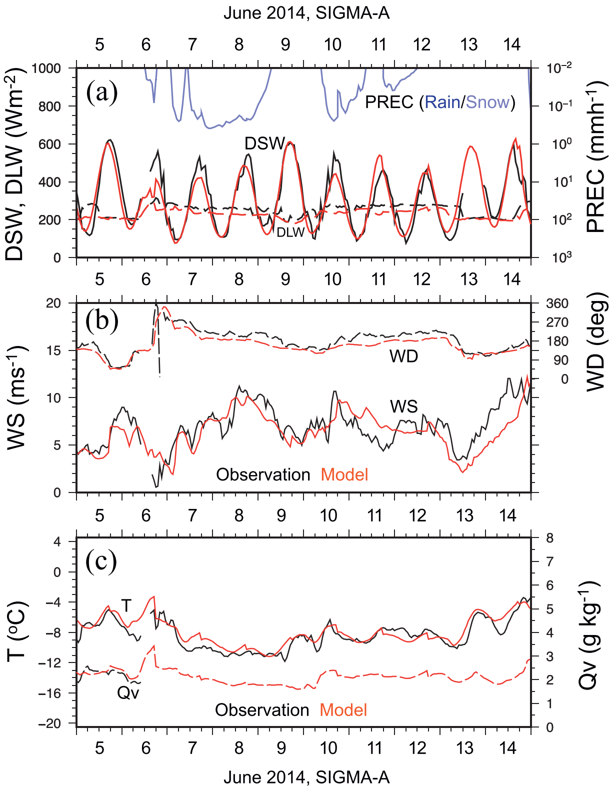

Figure 4: Same as Fig. 1, but for the campaign period of June 2014.

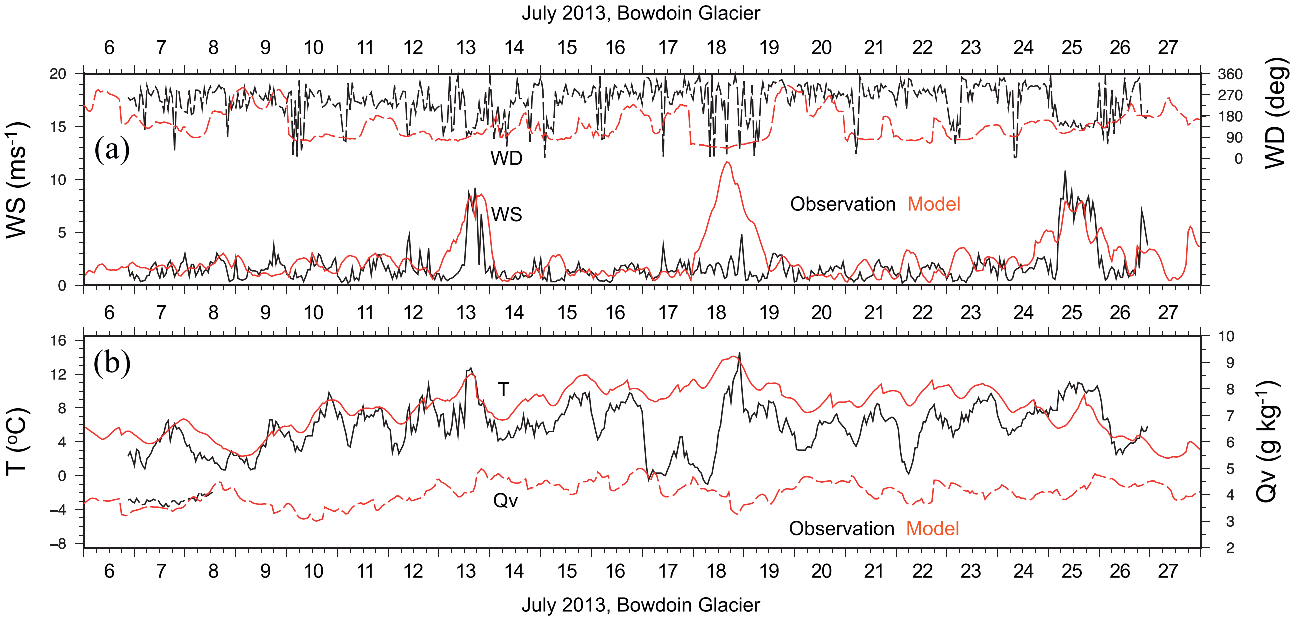

Figure 5: (a) Observed (black) and predicted (red) wind speed (WS, solid line) and direction (WD, broken line) at Bowdoin Glacier for the campaign period of July 2013. (b) Same as (a), but solid and broken lines represent air temperature (T) and water vapor mixing ratio (Qv), respectively.

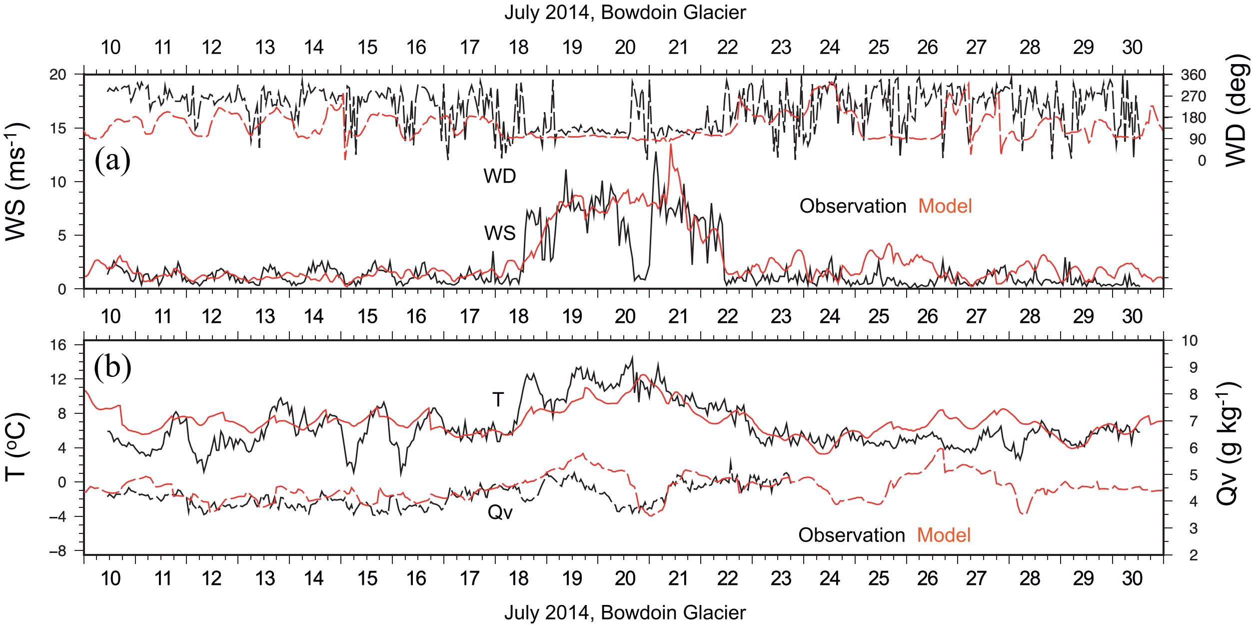

Figure 6: Same as Fig. 4, but for the campaign period of July 2014.

the errors of predicted air temperature versus observed wind speeds. Similar to wind direction, predicted air temperatures tended to agree with observed values when the observed wind speed was greater than 5 m s^{-1}.

Finally, for the mixing ratio of water vapor, our simulated results agreed with observed results throughout the three field campaigns at Bowdoin Glacier, though note that there were periods of time in which measurements were not available. The ME and RSME of predicted parameters at Bowdoin Glacier are summarized in Fig. A2(e)–(h) (Appendix A).

5.3 SE-Dome

Figure 9 shows observed and predicted wind speeds and surface air temperatures at the SE-Dome throughout an ice core drilling campaign conducted from May 19,

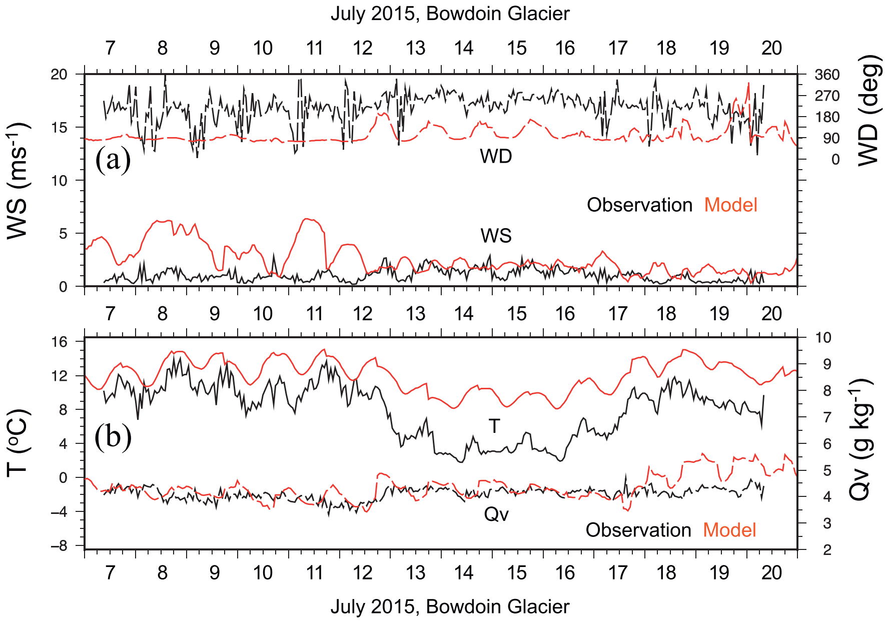

Figure 7 : Same as Fig. 4, but for the campaign period of July 2015.

2015 through June 2, 2015 (Iizuka et al., 2016). Our model accurately predicted strong winds of more than 10 m s^{-1} on May 20, May 29, and May 30, as shown in Fig. 9 (a), thus effectively warning the expedition team.

Conversely, predicted surface air temperatures showed defective behavior in that predicted values were much lower than observed values in the early predictions for each simulation, as is evident in Fig. 9(b). After examining our prediction system, we found a problematic procedure in the initiation of snow surface temperature. To correct the procedure, we provided an initial surface air temperature to initiate snow surface temperature. This correction yielded substantial improvements to our air temperature predictions, as shown in Fig. 9(d), without negatively impacting the accuracy of wind speed predictions, as is evident in Fig. 9(c). Note that we also updated the prediction system accordingly for the subsequent field campaign at Bowdoin Glacier in July 2015.

6. Discussion

6.1 Transmission of prediction results

When the expedition team stays at a nearby base town (e.g., Qaanaaq for the SIGMA and GRENE-Arctic projects and Tasiilaq for SE-Dome campaigns), they can browse visualized prediction results through the Internet; however, after leaving the base town for the camping site, the Internet is not available. A commercial satellite communication service is the only way to access weather information. Since satellite communication services are too expensive and have bit rates that are too small to use for obtaining large-scale images of weather prediction maps, our prediction results were translated into short documents and transmitted via e-mails through the satellite communication system.

When a research team had a weather analysis crew, in addition to the short document noted above, we also provided downsized data constructed by the procedure of Hashimoto et al. (2016) (see Appendix B for details). The crew retrieved prediction results from this data and shared them with the team. This means of transmission introduced only light loading on satellite communication, but was effective in updating the crew with necessary weather prediction information.

6.2 Effectiveness in field campaigns

Figure 10 shows the time evolution of sea level pressure based on the JMA's global objective analysis during the field campaign at SIGMA-A from July 24, 2013 through July 29, 2013. With the approach of an Arctic cyclone heading toward northern Greenland, Greenland high pressure weakened until its intensity started to recover after July 28, 2013. During this

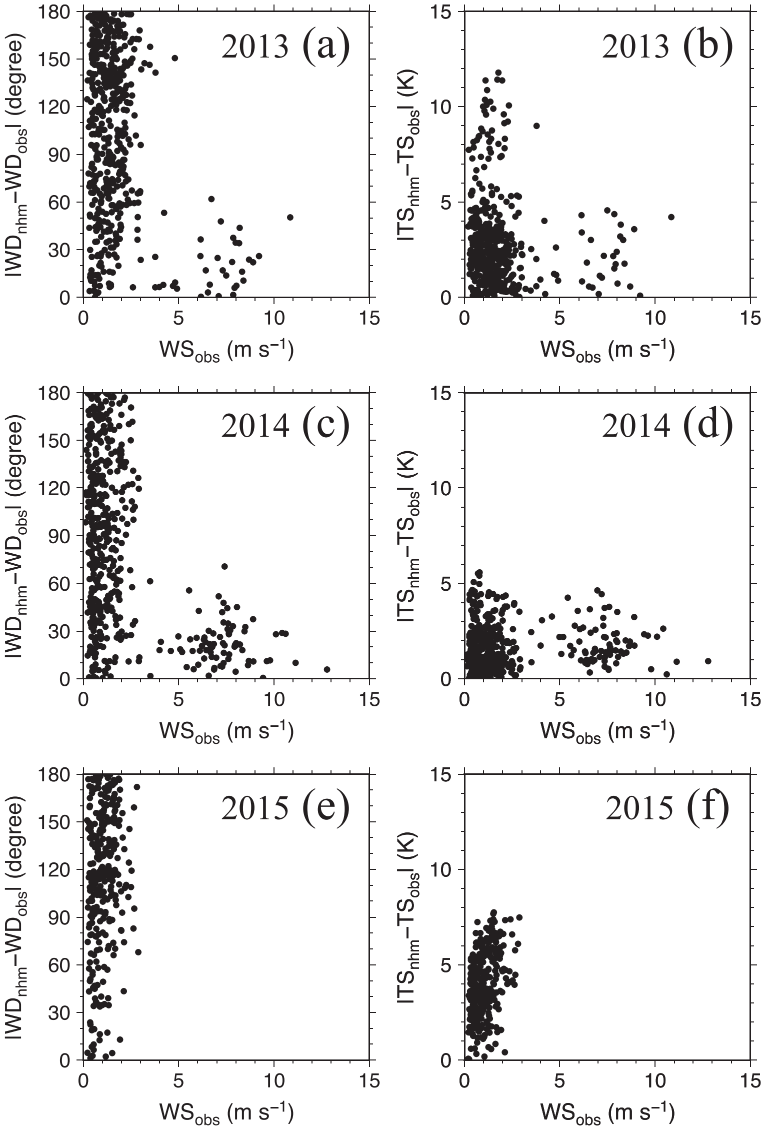

Figure 8 : Scatter plot of the error of (a) predicted wind direction and (b) predicted surface air temperature versus the observed wind speed in the 2013 field campaign at Bowdoin Glacier. Here (c) and (d), as well as (e) and (f), represent the same results as those of (a) and (b), but for the 2014 and 2015 field campaigns, respectively.

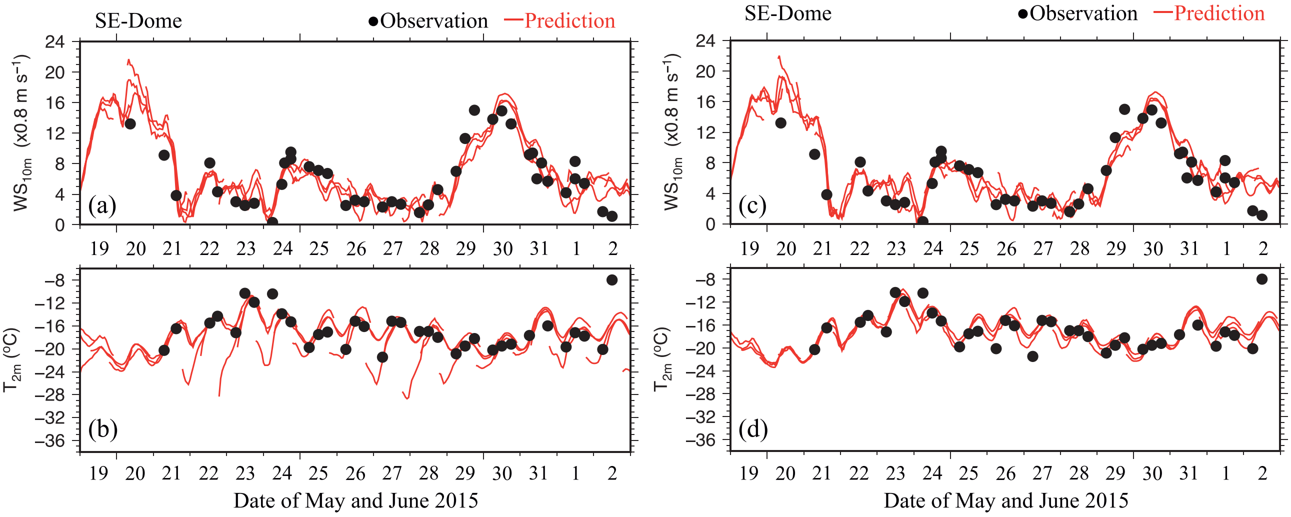

Figure 9 : (a) Observed (black dot) and predicted (red line) wind speed at the SE-Dome through the campaign period ranging from May 2015 through June 2015. (b) Same as (a), but for surface air temperature.

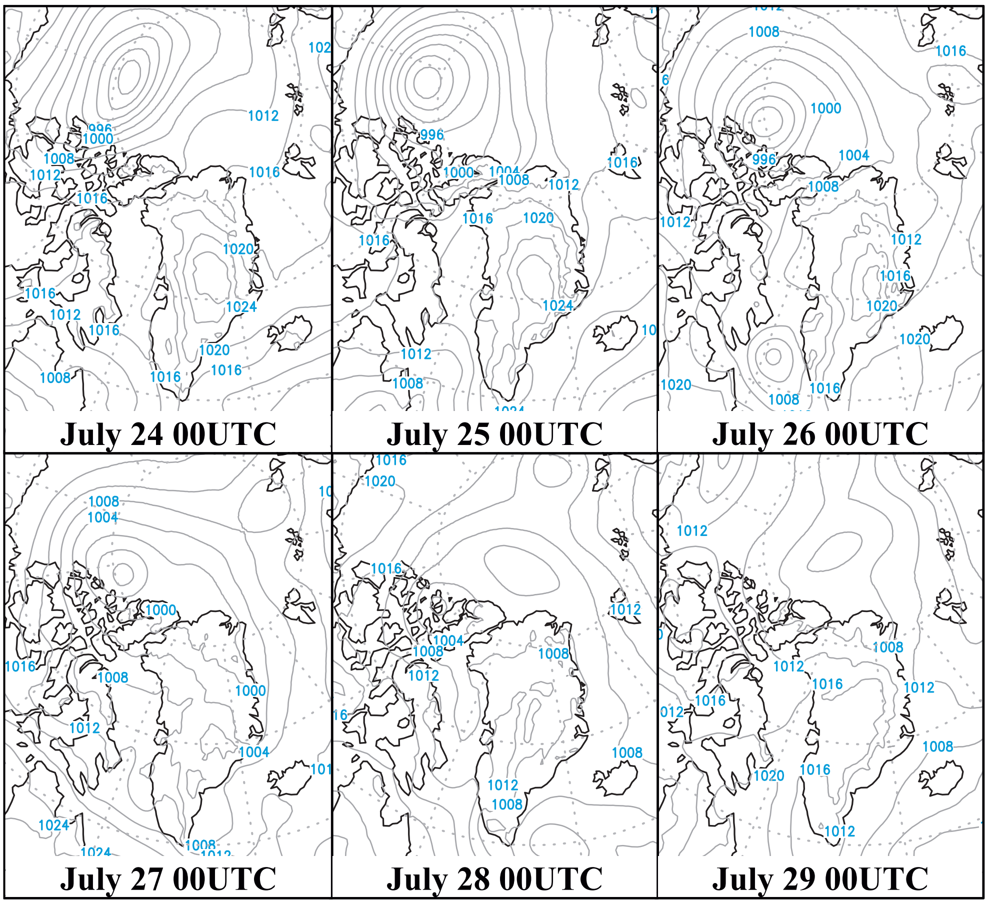

July 24 00UTC July 25 00UTC July 26 00UTC

July 27 00UTC July 28 00UTC July 29 00UTC

Figure 10 : Time evolution of sea level pressure from July 24, 2013 through July 29, 2013.

period, the expedition team experienced a blizzard at SIGMA-A, which forced them to cancel some of their scheduled measurements (Aoki et al., 2014). As shown in Fig. 3(b), our prediction system accurately predicted strong winds of up to approximately 10 m s^{-1} intermittently from July 25, 2013 through July 28, 2013. These predications helped the crew shift their plans for taking measurements and schedule a helicopter flight back to the base town of Qaanaaq.

In the field campaign at the SE-Dome in late May through early June 2015 (Iizuka et al., 2016), the crew successfully flew to the camping site on May 18, 2015, one day before a heavy storm hit the site, accompanied by an Icelandic low. Using predictions produced by our prediction system, the crew felt they would encounter strong winds of up to 20 m s^{-1} the next day, as indicated in Fig. 9(a). In a strategic sense, they gained time to prepare their ice core drilling operations at the site, owing to the flight on May 18, 2015. They started the drilling operation on May 21, 2015, soon after the storm left the site, thus completing all scheduled field studies on May 27, 2015. Unfortunately, for their flight back to their base town of Tasiilaq, they were stuck until June 2, 2015 due to another storm accompanied by an Icelandic low that was closest to the SE-Dome on May 30, 2015, as shown in Fig. 11. The pick-up flight was then done after the weather improved, which was accurately predicted by our prediction system, as shown in Fig. 9(a).

The field campaigns in Greenland depended on heliborne transportation, which is vulnerable to such weather conditions as strong winds, low visibility, and insufficient clearance from the surface of ice sheets to a cloud base, and so on. Through the use of our numerical weather prediction system during the campaigns, our results show the effectiveness of our prediction system for scheduling heliborne transportation and for supporting the safe collection of scientific measurements.

6.3 Implications to modeling

As shown by the comparisons between observed

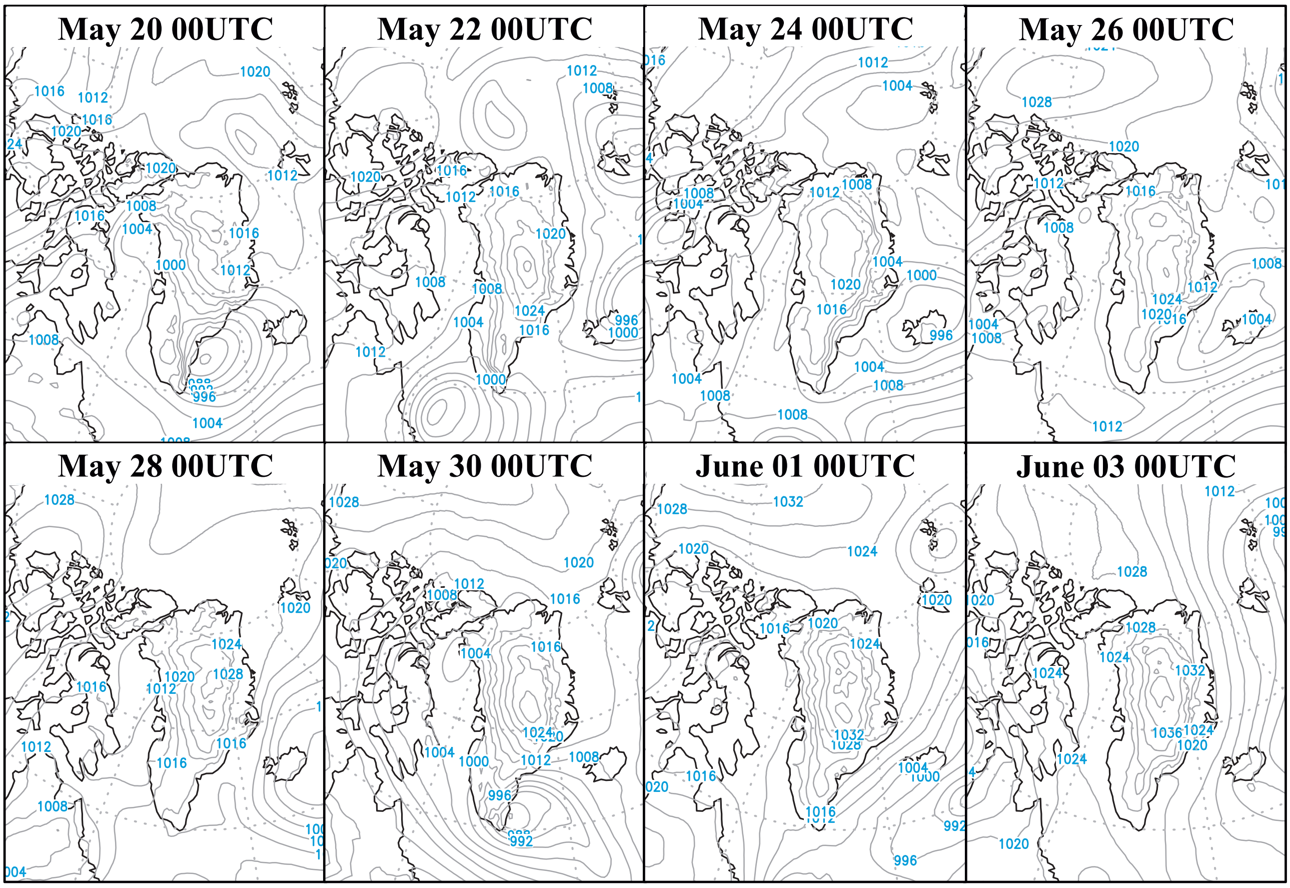
May 20 00UTC
May 22 00UTC
May 24 00UTC
May 26 00UTC
May 28 00UTC
May 30 00UTC
June 01 00UTC
June 03 00UTC

Figure 11: Same as Fig. 10, but for the period ranging from May 20, 2015 through June 3, 2015.

and predicted downward shortwave radiant flux at SIGMA-A, the prediction of shortwave radiation worsened on cloudy days. In our model, cloud radiation was influenced by cloud formations determined by the amount of energy and water vapor within a grid volume of atmosphere, hence it is necessary to further validate our model with cloud fraction observations, such as an all-sky camera observation system, and to modify parameters related to the cloud microphysics and the cloud radiation process.

Compared with SIGMA-A, the performance of our local weather prediction system was considerably inferior at Bowdoin Glacier in terms of wind direction and surface air temperature. We note that the errors in predicted wind direction and surface air temperature tended to be larger when the observed wind speed was less than 5 m s^{-1}, as shown in Fig. 8. A possible explanation for this is as follows. When a large-scale environmental force is weak, the local air circulation near the surface is expected to be separate from large-scale winds, but more influenced by local effects, such as topographic or thermodynamic effects from the surface. The topography and land surface characteristics around Bowdoin Glacier are entangled at a horizontal scale less than that of the grid spacing of our model, i.e., 5 km (Fig. 1 in Sugiyama et al., 2015), thus small-scale local air circulation patterns are not represented by our model.

In contrast, when the environmental force is stronger, surface air circulation is expected to be more affected by a large-scale wind that is resolvable with our model rather than by unresolvable local effects. Figure 12 shows that the pressure gradient over northwest Greenland increased from July 19, 2014 through July 21, 2014 in conjunction with a low pressure system approaching, which corresponds to the period in which our prediction showed good performance for wind direction, as shown in Fig. 6. Since a larger pressure gradient generally brings stronger winds, this synoptic scale feature in the focused period is consistent with the expectation that the accuracy of the predicted wind direction improves when a strong wind brought by a large-scale force is observed.

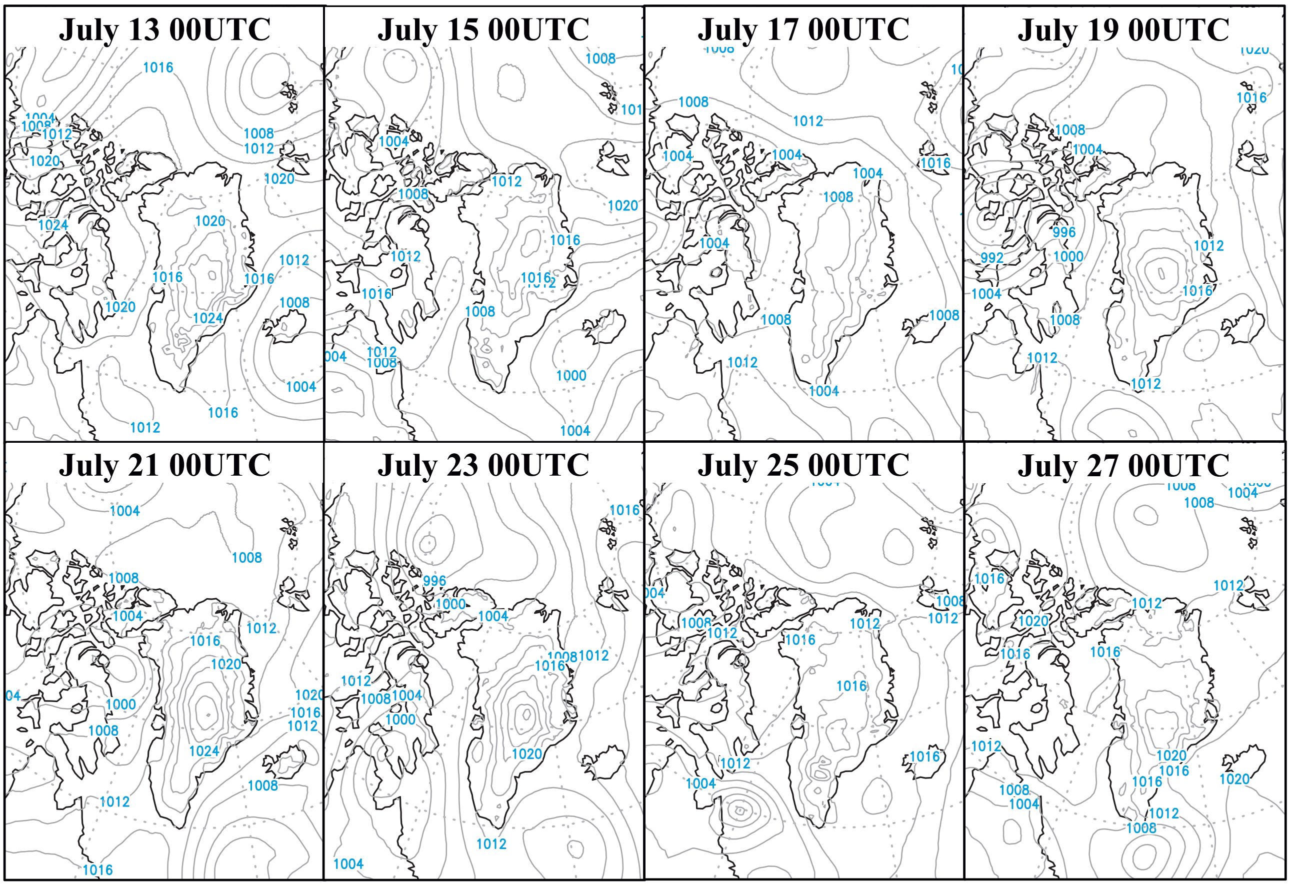

Figure 12：Same as Fig. 10, but for the period ranging from July 13, 2014 through July 27, 2014.

Further, the surface air temperature is affected by both a local surface heat flux and a heat advection across a wide spatial range. For weaker winds, the air temperature is more influenced by the local surface heat flux, which includes sub-grid scale heterogeneity, due to topography and land surface characteristics; otherwise, it is more influenced by the large-scale heat advection resolvable with our model. Therefore, we can extend the same explanation for wind direction to surface air temperature. From the viewpoint of modeling, heat exchange at the land surface in a meteorological model is strongly dependent on the implemented land surface model and land surface characteristics, hence we need a high level of sophistication in the land surface model and a finer expression of topography and land surface characteristics to improve our prediction performance at Bowdoin Glacier.

7. Conclusions

In this paper, we described our efforts and results of developing a weather prediction system based on JMA-NHM to support field research activities in Greenland with customized prediction information. Through feedback obtained from the expedition crews, we confirmed the effectiveness of our system in relation to field activities in terms of supporting scientific measurements and heliborne transportation. We updated our system during the selected campaigns by a collaboration between field and modeling researchers.

We validated our prediction results in relation to ground-based meteorological observation data collected at SIGMA-A, Bowdoin Glacier, and the SE-Dome during the field campaigns over the summer seasons from 2012 to 2015. Our system accurately predicted local weather parameters at these three sites, except for the downward shortwave radiation at SIGMA-A and the wind direction and surface air temperature at Bowdoin Glacier. To improve performance, our system needs to be improved in terms of its cloud radiation and land surface processes. We plan to maintain and refresh our system to support field activities in Greenland, including those planned in upcoming projects named Post-SIGMA and the Arctic Challenge for Sustainability (ArCS).

In our paper, we also described the set up of our weather prediction system in Greenland. Our system can be extended for other weather prediction environments, including other Arctic or Antarctic regions, mountain glaciers, and so on according to available computational resource. In addition, Niwano et al. (2016) are currently attempting to perform climate simulations by a coupled model constructed by our system and the physical snowpack model SMAP (Snow Metamorphism and Albedo Process) applied in polar regions (Niwano et al., 2015). We believe such a system promotes more collaborative work among glaciologists and meteorologists to produce new and deeper understandings of the cryosphere-atmosphere system.

Acknowledgements

This work was partly supported by JSPS KAKENHI Grant Numbers JP16H01772, JP23221004, 26257201. The field observation campaign at Bowdoin Glacier was carried out under the Green Network of Excellence Program Arctic Climate Change Research Project. The ice core drilling campaign at the SE-Dome was carried out partly with the support of the Joint Research Program of the Institute of Low Temperature Science, Hokkaido University.

Appendix A

1. Errors of predicted parameters

The ME and RMSE of downward shortwave and longwave radiant fluxes are shown in Fig. A1 for the field campaigns at SIGMA-A. Figs. A2(a)–(d) show the ME and RMSE of wind speed, wind direction, surface air temperature and water vapor mixing ratio for the field campaigns at SIGMA-A, and (e)–(h) for the campaign at Bowdoin Glacier.

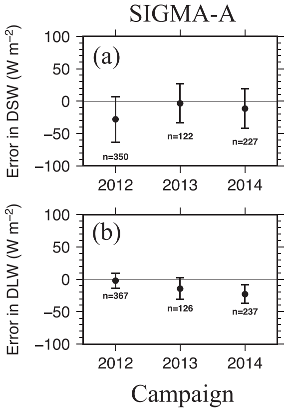

Figure A1 : The ME of (a) predicted downward shortwave radiant flux and (b) predicted downward longwave radiant flux. Bar indicates RMSE. “n” indicates the sample number.

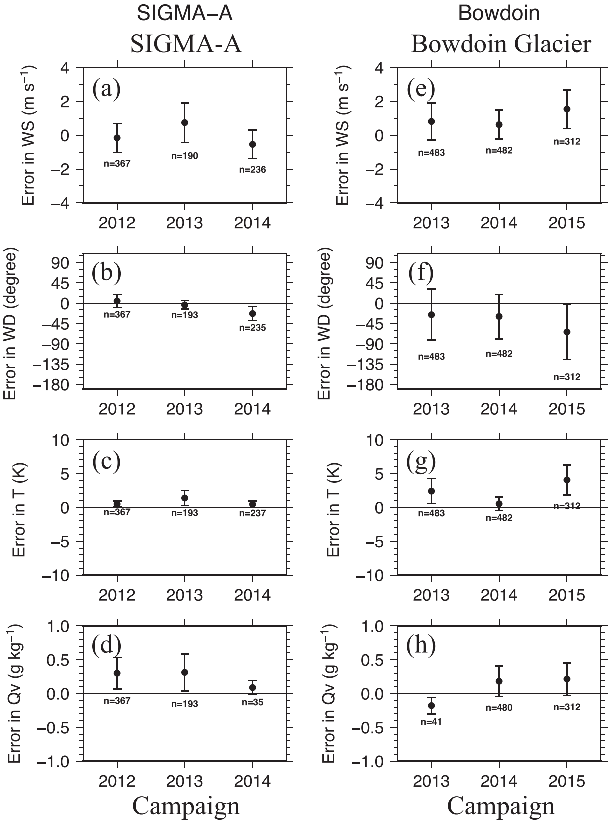

Figure A2 : The ME of (a) predicted wind speed, (b) predicted wind direction, (c) predicted surface air temperature and (d) predicted water vapor mixing ratio at SIGMA-A. (e)–(h) are same as (a)–(d), respectively, but for Bowdoin Glacier. Bar indicates RMSE. “n” indicates the sample number.

Appendix B

1. Downsized data

To provide an expedition team isolated from the Internet results of numerical weather prediction, from the output of each simulation, we extracted 10 meteorological parameters — i.e., air pressure, air temperature, humidity, cloud fractions of low, middle, and high layers, wind speed and direction, a rain/snow flag, and precipitation amount — at the surface and a height of 5 km a.s.l. at four predetermined locations, including the

Table B1：Specifications of the downsized data, reproduced from Hashimoto et al. (2016) with permission.

	VARIABLE	UNIT	MIN	MAX	INCREMENT	TONE	SIZE	DIGIT
Station ID	VAR 0^U	(height) km	0	15	1	16	upper 4 bits	DIG 0^U
	VAR 0_L		0	15	1	16	lower 4 bits	DIG 0_L
Time	VAR 1	*day UTC	0	63.75	0.25	256	full 8 bits	DIG 1
Pressure	VAR 2	hPa	100	1120	4	256	full 8 bits	DIG 2
Temperature	VAR 3	℃	-100	27.5	0.5	256	full 8 bits	DIG 3
Humidity	VAR 4^U	%	25	100	5	16	upper 4 bits	DIG 4^U
High-cloud coverage	VAR 4_L		0	1	0.0625	16	lower 4 bits	DIG 4_L
Middle-cloud coverage	VAR 5^U		0	1	0.0625	16	upper 4 bits	DIG 5^U
Low-cloud coverage	VAR 5_L		0	1	0.0625	16	lower 4 bits	DIG 5_L
Wind velocity scale	VAR 6^U		0	15	1	16	upper 4 bits	DIG 6^U
16-direction wind scale	VAR 6_L		0	15	1	16	lower 4 bits	DIG 6_L
Flag (if snow<rain)	VAR 7^U		0	1	1	2	upper 1 bit	DIG7^U
Precipitation scale	VAR 7_L		0	5.1	0.04	128	lower 7 bits	DIG 7_L

camp site, up to four times every 12 hours (i.e., 6, 18, 30, and 42 hours after the initial time). The output eight-byte datum of each parameter is then converted to a sub-byte datum via tone scale processing. After this processing is complete, the total data size, including the extracted data, the station ID, and the forecast time, is downsized to approximately one-tenth the original size, i. e., only 256 bytes.

Using the above algorithm, we converted and transmitted the downsized data through the satellite communication system to the expedition team. These transmitted data are then converted to their original values by applying the following:

$$VARn_L^U = MINn_L^U + \frac{DIGn_L^U}{TONEn_L^U - 1}\left(MAXn_L^U - MINn_L^U\right),$$

$$\left(n_L^U = 0^U, 0_L 1, 2, 3, 4^U, 4_L, 5^U, 5_L, 6^U, 6_L, 7^U, 7_L\right) \qquad (B1)$$

Here, $VARn_L^U$ represents the locations, forecast times, and the 10 meteorological parameters (i. e., eight-byte data), while $DIGn_L^U$ represents the downsized data. Further, $DIGn$ represents an integer datum with a one-byte length; $DIGn^U$ and $DIGn_L$ represent the upper four bits (upper one bit for n=7) and the lower four bits (lower seven bits for n=7), respectively, within $DIGn$. Finally, $MINn_L^U$, $MAXn_L^U$, and $TONEn_L^U$ represent the maximum and minimum values of $VARn_L^U$ and the number of tones, respectively. Specific values for these parameters are listed in Table B1.

References

Aoki, T., S. Matoba, J. Uetake, N. Takeuchi, and H. Motoyama (2014) Field activities of the "Snow Impurity and Glacier Microbe effects on abrupt warming in the Arctic" (SIGMA) Project in Greenland in 2011–2013. *Bull. Glaciol. Res.*, **32**, 3–20, doi: 10.5331/bgr32.3.

Bamber, J., S. Ekholm, and W. Krabill (2001), A new, high resolution digital elevation model of Greenland fully validated with airborne laser altimeter data. *J. Geophys. Res.*, **106**, 6733–6745.

Bromwich, D. H., A. J. Monaghan, K. W. Manning, and J. G. Powers (2005) Real-time forecasting for the Antarctic: An evaluation of the Antarctic Mesoscale Prediction System (AMPS). *Mon. Wea. Rev.*, **133**, 579–603.

Bromwich, D. H., F. O. Otieno, K. M. Hines, K. W. Manning, and E. Shilo (2013) Comprehensive evaluation of polar weather research and ofrecasting performance in the Antarctic. *J. Geophys. Res.*, **118**, 274–292, doi: 10.1029/2012JD018139.

Hara, T., 2008: Prediction of land surface quantities. The JMA Nonhydrostatic Model II, *Japan Meteorological Agency Annual Rep.*, **54**, 176–180. (in Japanese)

Hara, K., S. Matoba, and T. Yamasaki (2014) Aerosol measurements at Siorapaluk, Greenland, The Fifth Symposium on Polar Science, Tokyo, 2–5 December 2014. http://www.nipr.ac.jp/symposium2014/program/abstract/OM_Hara_00355_01.pdf

Hashimoto A., M. Murakami, T. Kato and M. Nakamura (2007) Evaluation of the Influence of Saturation Adjustment with Respect to Ice on Meso-scale Model Simulations for the Case of 22 June, 2002. *SOLA*, **3**, 085–088, doi: 10.2151/sola.2007-022.

Hashimoto, A., M. Niwano, and T. Aoki (2016) Numerical weather prediction supporting cryospheric field observation campaign on the Greenland Ice Sheet. *Seppyo*, **78**, 205–214. (in Japanese with English abstract)

Hines, K. M., and D. H. Bromwich (2008) Development and Testing of Polar WRF. Part I. Greenland Ice Sheet Meteorology. *Mon. Wea. Rev.*, **136**, 1971–1989, doi: 10.1175/2007MWR2112.1.

Hines, K. M., D. H. Bromwich, L.-S. Bai, M. Barlage, and A. G. Slater (2011) Development and testing of Polar WRF. Part III. Arctic land. *J. Clim.*, **24**, 26–48, doi: 10.1175/2010JCLI3460.1.

Iizuka, Y., S. Matoba, T. Yamasaki, I. Oyabu, M. Kadota, and T. Aoki (2016) Glaciological and meteorological observations at the SE-Dome site, southeastern Greenland Ice Sheet. *Bull. Glaciol. Res.*, **33**, doi: 10.5331/bgr.15R03.

Matoba, S., K. Hara, and T. Yamasaki (2014) Chemical compositions of frost flower at Siorapaluk in northwestern Greenland. The Fifth Symposium on Polar Science, Tokyo, 2–5 December 2014. http://www.nipr.ac.jp/symposium2014/program/abstract/OM_Matoba_00172_01.pdf

Niwano, M., T. Aoki, S. Matoba, S. Yamaguchi, T. Tanikawa, K. Kuchiki, and H. Motoyama (2015) Numerical simulation of extreme snowmelt observed at the SIGMA-A site, northwest Greenland, during summer 2012. *The Cryosphere*, **9**, 971–988, doi: 10.5194/tc-9-971-2015.

Niwano, M., T. Aoki, A. Hashimoto, T. Tanikawa, M. Hosaka, M. Hori, R. Shimada, S. Matoba, S. Yamaguchi, K. Fujita, and H. Motoyama (2016) Initial evaluation of the NHM-SMAP regional climate model in the Greenland ice sheet during 2012. JSSI & JSSE Joint Conference, Nagoya, 28 September to 2 October 2016. (in Japanese)

Powers, J. G., A. J. Monaghan, A. M. Cayette, D. H. Bromwich, Y. -H. Kuo, and K. W. Manning (2003) Real-time mesoscale modeling over Antarctica: The Antarctic Mesoscale Prediction System (AMPS). *Bull. Amer. Meteor. Soc.*, **84**, 1533–1545, doi: 10.1175/BAMS-84-11-1533.

Saito K, T. Fujita, Y. Yamada, J. Ishida, Y. Kumagai, K. Aranami, S. Ohmori, R. Nagasawa, S. Kumagai, C. Muroi, T. Kato, H. Eito, Y. Yamazaki (2006) The Operational JMA Nonhydrostatic Mesoscale Model. *Mon. Wea. Rev.*, **134**, 1266–1297.

Sugiyama, S., D. Sakakibara, S. Tsutaki, M. Maruyama, and T. Sawagaki (2015) Glacier dynamics near the calving front of Bowdoin Glacier, northwestern Greenland. *J. Glaciol.*, **61**, 223–232, doi: 10.3189/2015JoG14J127.

Tao, W. -K., J. Simpson, and M. McCumber (1989) An ice-water saturation adjustment. *Mon. Wea. Rev.*, **117**, 231–235.

Wilson, A. B., D. H. Bromwich, K. M. Hines (2011) Evaluation of Polar WRF forecasts on the Arctic System Reanalysis domain: Surface and upper air analysis. *J. Geophys. Res.*, **116**, D11112, doi: 10.1029/2010JD015013.

低温科学 75 （2017） 105-115
doi: 10.14943/lowtemsci. 75. 105

Surface mass balance of the Greenland ice sheet in the regional climate model HIRHAM5: Present state and future prospects

Ruth Mottram[1]*, Fredrik Boberg[1], Peter Langen[1], Shuting Yang[1], Christian Rodehacke[1], Jens Hesselbjerg Christensen[1], Marianne Sloth Madsen[1]

Received 1 February 2017, accepted 9 February 2017

Surface mass balance (SMB) is the builder of the Greenland ice sheet and the driver of ice dynamics. Quantifying the past, present and future state of SMB is important to understand the drivers and climatic processes that control SMB, and to both initialize and run ice sheet models which will help clarify sea level rise, and how likely changes in ice sheet extent feedback within the climate system.

Regional climate models (RCMs) and climate reanalysis are used to quantify SMB estimates. Although different models have different spatial and temporal biases and may include different processes giving significant uncertainty in both SMB and the ice sheet dynamic response to it, all RCMs show a recent declining trend in SMB from the Greenland ice sheet, driven primarily by enhanced melt rates. Here, we present new simulations of the Greenland ice sheet SMB at 5 km resolution from the RCM HIRHAM5. The RCM is driven by the ERA-Interim reanalysis and the global climate model (GCM) EC-Earth v2.3 to make future projections for climate scenarios RCP8.5 and RCP4.5.

Future estimates of SMB are affected by biases in driving global climate models, and feedbacks between the ice sheet surface and the global and regional climate system are neglected, likely resulting in significant underestimates of melt and precipitation over the ice sheet. These challenges will need to be met to better estimate the role climate change will have in modulating the surface mass balance of the Greenland ice sheet.

Keywords: Greenland ice sheet, surface mass balance, climate, climate modelling, ice sheet modelling

1. Introduction

The Greenland ice sheet is famously the second largest land ice mass on the planet, containing around 2.85 million km^3 of ice over an area of 1.71 million km^2, equivalent to 7.2 m sea level rise (IPCC, 2013). Results from remote sensing missions such as the GRACE gravimetry satellites indicate a recent significant negative mass budget, with around −234 ± 20 Gt of net mass (Barletta et al., 2013) being lost each year including both the contribution from precipitation and surface mass balance and the dynamic contribution of calving from icebergs and submarine melt (Shepherd et al., 2012). The surface mass balance component is by far the most important component of the mass budget since it includes both positive (accumulation by precipitation) and negative (melt and runoff) terms, though around one third to one half of the mass lost by the ice sheet is from calving glaciers (Enderlin et al., 2014).

---

*Corresponding author
e-mail：rum@dmi.dk
1）Danish Meteorological Institute, Copenhagen, Denmark

Table 1 : Comparison of surface mass balance components calculated for the present day using different models. Note that, as Vernon et al. (2013) point out, these models also have different resolutions and different ice masks, so that the numbers are not quite comparable. Therefore, we include in the right most column values from that study that compare the RACMO and MAR models using the same ice mask and forcing data, though with differing model resolution.

Model	Mean annual surface mass balance (Gt year^{-1})	Mean annual precipitation (Gt year^{-1})	Mean annual runoff (Gt year^{-1})	Mean annual surface mass balance (Gt year^{-1}) 1960–2008, from Vernon et al. (2013)
HIRHAM5 (1980–2014) (this study)	360 ± 134	866 ± 70	446 ± 109	—
RACMO (1991–2015) (van den Broeke et al., 2016)	306 ± 120	712 ± 70	363 ± 102	470
MAR (1980–2015) (Fettweis et al., 2016)	480 ± 87	711 ± 61	220 ± 52	432

SMB is not only important in itself, but is also important for ice sheet modelling studies where SMB, or the degree day approximation of it based on temperature and precipitation, is used to drive ice sheet dynamics. We thus use high-resolution regional climate models to clarify both the current state of the ice sheet surface mass balance and its future prospects under climate change scenarios with the aim of also providing SMB forcing for dynamical ice sheet models.

Previous work on Greenland ice sheet mass balance has used the regional climate models MAR and RACMO as well as HIRHAM5 to determine the present-day and future surface mass balance (Lucas-Picher et al., 2012; Rae et al., 2012; Langen et al., 2015). Other models, such as SnowModel (Mernild et al., 2009) or Hanna et al.'s (2013) dECMWF model are not strictly regional climate models, but use either model output to drive a separate snow scheme (SnowModel) or use statistical methods to downscale output that is then used to calculate SMB based on temperature index methods (dECMWF) (Church et al., 2013).

These models have previously estimated the mean annual SMB to be in the range 340 to 470 Gt per year (see Table 1), though note that both forcing data, time period, resolution as well as processes and ice mask all vary in these estimates, and this can have a significant effect on any one models SMB estimate when compared to the others, as shown by Vernon et al. (2013). An earlier version of HIRHAM5 showed an average annual SMB of 188 Gt year^{-1} over the whole ice sheet for the period 1990 to 2008 (Rae et al., 2012). However, this version was run at a coarser resolution of 25 km and with a significantly simplified snow model to calculate surface mass balance. Our current version of HIRHAM5 is run at 5 km resolution and was used by Langen et al. (2015) to show regional changes in Greenland. Here we use a further updated version of the model (Langen et al., 2017) to calculate SMB across the Greenland ice sheet and to make future projections when forced with a global climate model.

The high resolution of the HIRHAM5 model in this set of simulations means that we can assess the performance of the model on both the narrow ablation zone and on small outlet glaciers and peripheral ice caps without needing to statistically account for elevation changes, as performed for example by Noël et al. (2016). Results by Langen et al. (2017) show that the model performs well in these marginal areas, even without elevation correction, when compared with ablation and weather station measurements predominantly in the ablation zone compiled by Machguth et al. (2016). Similarly, analysis by Schmidt et al. (submitted) shows that the model works very well over the small Icelandic ice cap Vatnajökull, which is analogous to peripheral glaciers in Greenland. At the present day up to 10% of the mass loss from Greenland is currently contributed by these small glaciers and ice caps (Bolch et al., 2013) and it is therefore important to be able to account for their surface mass balance correctly in model projections.

In this study we use a separate dataset of shallow firn cores from around the accumulation zone in Greenland compiled by Buchardt et al. (2012) to evaluate how the model performs at higher elevations. In the future, dynamically driven changes in ice sheet altitude, due to increasing melt rates and projected increases in precipitation, will likely have important feedbacks on both orographic precipitation and melt rates. In this sense the use of high-resolution simulations offers additional value in both identifying and quantifying feedbacks between ice and atmosphere.

The combination of surface mass balance modelling with estimates of total mass budget derived from both altimetry and flux gate calculations (Rignot et al., 2011) and the satellite gravimetry mission GRACE offers the possibility of estimating the relative importance of surface mass processes and calving dynamics (Shepherd et al., 2012). In this paper we focus on the surface mass budget contribution both at the present day and in the future.

2. Regional climate model HIRHAM5

In this study we use the latest version of the RCM HIRHAM5 (Langen et al., 2017) for a domain covering Greenland, Iceland and parts of Arctic Canada (Figure 1). The RCM was developed at the Danish Meteorological Institute (DMI) (Christensen et al., 2006) from the HIRLAM7 numerical weather prediction model (Eerola, 2006) and the ECHAM5 global climate model (Roeckner et al., 2003). The model is very similar in set-up to that fully described in Langen et al. (2015, 2017) and Lucas-Picher et al. (2014) run on a $0.05^\circ \times 0.05^\circ$ rotated polar grid for a 35 year period (1980–2014). For the present-day simulations HIRHAM5 was forced on the lateral boundaries by the ERA-Interim reanalysis product (Dee et al., 2011) every 6 hours. On the lower boundary, sea surface temperatures (SSTs) and sea ice concentration were statistically interpolated from the ERA-Interim data format to the model resolution and prescribed daily. The model runs freely within the boundaries and only temperature, pressure, relative humidity and wind velocities are used in lateral boundary forcing. The current set-up of HIRHAM5 has 31 vertical levels in the atmosphere, 5 vertical levels in the soil, including glaciers and snow and a 90 second dynamical time step. A 32 layer snow pack model is applied offline over glacier points to calculate surface mass balance using more detailed snowpack processes (Langen et al., 2017; see below). The topography of Greenland is taken from Bamber et al. (2001), and it should be noted that although snow is allowed to accumulate without limits over glaciers and ice sheets, the elevation of the ice sheet surface remains fixed during the simulation such that there are no feedbacks between surface mass balance and ice dynamics. The ice mask used in this simulation is updated from that used by Langen et al. (2015) to that produced by Citterio and Ahlstrøm (2013) with additional data for Iceland provided by the Icelandic Met Office (Figure 1).

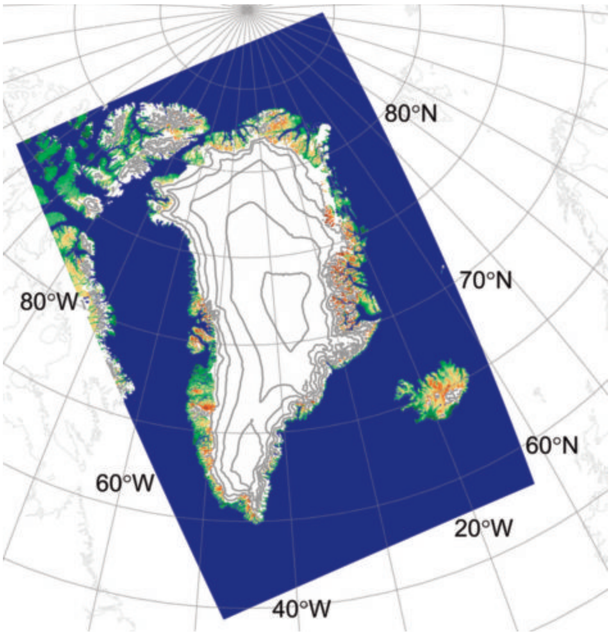

Figure 1: The domain, topography and ice mask used in all HIRHAM5 simulations for Greenland.

Using this same set-up we also forced HIRHAM5 on the lateral boundaries with fields from the EC-Earth v2.3 GCM (Hazeleger et al., 2012) in order to produce future climate simulations of the surface mass balance of Greenland. In this set-up, EC-Earth was run at a resolution of 125 km using the historical emissions and RCP4.5 and 8.5 climate scenarios in the CMIP5 set-up (Taylor et al., 2012). Both the lateral boundaries and the ocean SSTs and sea ice were provided by the driving GCM to the HIRHAM5 model for downscaling experiments. The future projections were run as transient 20 year time slices for the mid and end of the 21st century using RCP4.5 and RCP8.5 scenarios, as well as a simulation using historical emissions for the period 1991–2010, used as a control run to assess performance of the EC-Earth model at the present day.

Prior to running the simulations, the inclusion of the full snowpack model as detailed below meant that an adequate spin-up was required in particular for the snow and ice properties to reach equilibrium with the climate. For this purpose we ran the HIRHAM5 model for one year, and then used the atmospheric output to run the surface scheme offline repeatedly until decadal means of runoff and subsurface temperatures ceased to show transient variability (in this case, after 70 years of simulation time).

The full details of the surface mass balance calculation in HIRHAM5 are given in Langen et al. (2017), but a quick summary is given here to assist in interpreting results. Surface mass balance is calculated from the sum of the precipitation and the runoff (a negative term). Runoff is calculated from the melt of surface snow and ice, accounting for the effects of retention and refreezing within any snowpack that overlies the glacier ice. Rain on snow is similarly accounted for, though rain on bare ice is assumed to runoff directly. There is currently no runoff routing scheme from the model and therefore no superimposed ice formation on bare glacier ice. However, with the introduction of a sophisticated firn model, processes now include densification, snow grain growth, snow state-dependent hydraulic conductivity, superimposed ice formation at the base of the snow pack on glacier ice, and irreducible water saturation. The accommodation for water retention in excess of the irreducible saturation means that formation of both perennial firn aquifers and perched ice lenses occurs within the snowpack (Langen et al., 2017).

The HIRHAM5 surface scheme uses a standard energy balance scheme to calculate the melt of snow and underlying glacier ice:

$$Q_m = S_{in}(1-\alpha) + L_{in} - L_{out} + Q_H + Q_L$$

$$M = \frac{Q_m}{\rho_w L_f} \qquad (1)$$

where Q_m is the total energy flux at the surface, S_{in} is the incoming shortwave radiation, α is the surface albedo, L_{in} and L_{out} are the incoming and outgoing longwave radiative fluxes, respectively, and Q_H and Q_L are the sensible and latent heat fluxes. As the skin temperature cannot rise above the freezing point of 273.15° K on a glacier surface, the excess energy is instantaneously used for melt, M, accounting for the density of water, ρ_w, and the release of latent heat, L_f.

Meltwater and rain that falls over glaciers are grouped together in the model as the liquid water fraction. Where there is a snow layer overlying the glacier surface, the liquid water percolates into the deeper layers according to a given threshold of irreducible water saturation and, if there is a sufficient cold content, refreezes within the snowpack. In the sub-surface scheme over glaciers, there are 32 layers of unequal thickness of snow or ice or some combination of the two depending on the depth of surface snow. The thickness of the layers in the subsurface scheme over glaciers or snow-covered land is calculated in metres of water equivalent to allow for the easy calculation of mass change, with different heat diffusion and conductivity parameter values used for water, ice and snow within the snowpack. As surface melting and rainfall occur, the water percolates into the lower layers and retention is calculated by allowing liquid water in excess of the density-dependent irreducible water saturation within the layer to percolate to the layer below. Ice is formed in the snowpack layers based on the "cold content" in each layer. The cold content determines how much liquid water can freeze within that layer based on the energy required to heat the snow and ice mass to the freezing point in each layer. This is used to instantaneously freeze as much liquid water as is available or as the cold content allows, within a single time step. This mass is then transferred to the ice fraction and the temperature of the layer is calculated taking into account the latent heat release to conserve energy.

As the subsurface scheme extends to a depth of 60 metres water equivalent (mwe), if there is less than 60 mwe snow on the glacier surface then the layers of the subsurface scheme have the properties of ice. No percolation of meltwater is allowed through ice layers, but energy fluxes are diffused through all the layers. We assume that the ice layers from the glacier coming into the column at the base of the subsurface scheme have a temperature equivalent to the annual mean

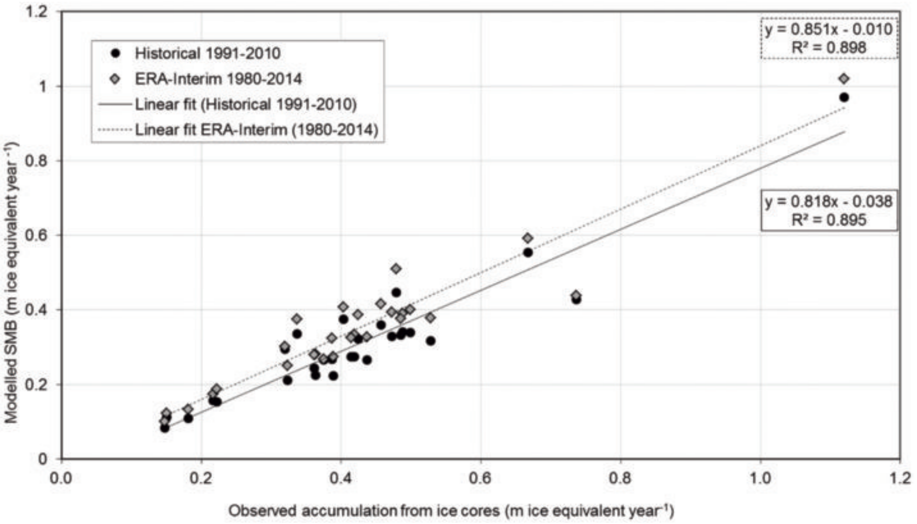

Figure 2 : Comparison of observed SMB from shallow core data compiled by Buchardt et al. (2012) with modelled values from the ERA-Interim forced simulation and the historical emissions scenario of EC-Earth.

temperature of that grid square location.

As Langen et al. (2017) discuss, the albedo of the model is one of the largest sources of uncertainty in the mass balance estimate. In the simulations we present here, we use the internally derived albedo scheme, rather than an externally forced albedo product based on MODIS as also described in Langen et al. (2017). This allows us to make a direct comparison of the present-day SMB with the future projections where data such as MODIS is of course unavailable. The albedo scheme in the model has a cold (< −5°C) snow albedo of 0.85, linearly decreasing to 0.65 as temperature increases from −5°C to 0°C. The albedo for bare ice is fixed at 0.4 with a linear function for thin (<3 cm) snow between the two values. Broadband values lower than 0.4 do occur as shown in measurements at the PROMICE automatic weather stations (van As et al., 2016) and MODIS data products (Stroeve et al., 2006). Similarly, freshly exposed ice can have much brighter values for surface albedo, but the values in the current scheme were optimized over the ice sheet by Nielsen-Englyst (2015). Langen et al. (2017) show that significant biases still persist in albedo values over the ice sheet; however, partly due to processes such as dust accumulation and biological activity that are not currently included. Recent work by Stibal et al. (2015) demonstrates the importance of microorganisms and melted out dust on the Greenland ice sheet, and the development of appropriate parameterizations is an area of active research.

The HIRHAM5 model performance is comprehensively evaluated in Langen et al. (2015, 2017) using weather station data, shallow firn cores and historical SMB observations from Machguth et al. (2016). Their results show that the model performs extremely well over Greenland, reproducing air temperatures and accumulation rates well on average. However, some biases in radiation suggest that cloud cover or cloud optical thickness may not be fully captured in the model. Similarly, HIRHAM5 is not able to capture deep cold inversion layers over the ice sheet, and evidence from Fausto et al. (2016) suggests that during extreme melt events, such as were observed in 2012, the model underestimated the sensible heat flux by up to 75% in some locations.

Analysis of the same ERA-Interim simulation by Schmidt et al. (submitted) over Icelandic glaciers shows that HIRHAM5 also performs well over small glaciers and ice caps, particularly with regard to accumulation rates. However, Schmidt et al. (submitted) also identify that orographically forced precipitation is overestimated on the upslope with a possible small dry bias downwind. This is a common problem in hydrostatic models where the dynamical scheme means that precipitation is handled diagnostically (Forbes et al., 2011).

3. Results and discussion

3.1 Surface mass balance

In Figure 2 we complement the model analysis of Langen et al. (2017) by comparing observed surface mass balance from stake measurements and shallow firn cores (Buchardt et al., 2012) with those calculated from the same grid cell in HIRHAM5. Figure 2 shows that the model is able to reproduce the pattern of SMB over the ice sheet when forced with both ERA-Interim ($R^2 = 0.898$) and EC-Earth ($R^2 = 0.895$), though with a very slightly more pronounced dry bias in the historical simulation. For this comparison we took the decadal mean SMB from firn cores that cover all or part of the period of the ERA-Interim driven simulation. Although the model reproduces the observed SMB pretty well, it is important to note that observed SMB rates are determined by short- and medium-term climate variability that may not be captured by climate models, thus leading to the poorer fit against these point measurements. This point is underlined in Table 2 where there are large differences in SMB calculated on a decadal timescale and compared across the full 1980–2014 simulation period. However, note that in Table 1 the total SMB for Greenland is close to, but not exactly the same as comparable simulations using other RCMs.

Table 2 : SMB calculated using the ERA-Interim driven simulation in different decades and overall. The choice of period can make a large difference in the estimated annual mean SMB.

Period	Mean annual SMB (Gt year^{-1})
1980–2014	360 ± 134
1980–1990	375 ± 130
1991–2010	346 ± 132
2000–2014	277 ± 101

As we plot both model simulations against the same core data for comparison, it is interesting to see that the pattern of high and low accumulation rates across Greenland are reflected in both simulations (see also Figure 5), but the magnitude differs slightly with the EC-Earth historical run having a generally lower value. This suggests that in the accumulation zone at least, both models have a dry bias, though that in the EC-Earth simulation is somewhat stronger. Observational data from the south-east of Greenland, the region with highest precipitation, are too sparse to assess how well the model reproduces it. For the only core data we have from south-east Greenland, the model under-estimates SMB in both simulations, though to a lesser extent in the ERA-Interim simulation. More observations in this region would be helpful in both evaluating the model and comparing results from this simulation with other models.

3.2 Surface mass balance components

Figure 3 shows the surface mass balance of Greenland as a whole for the period 1980 to 2014. There

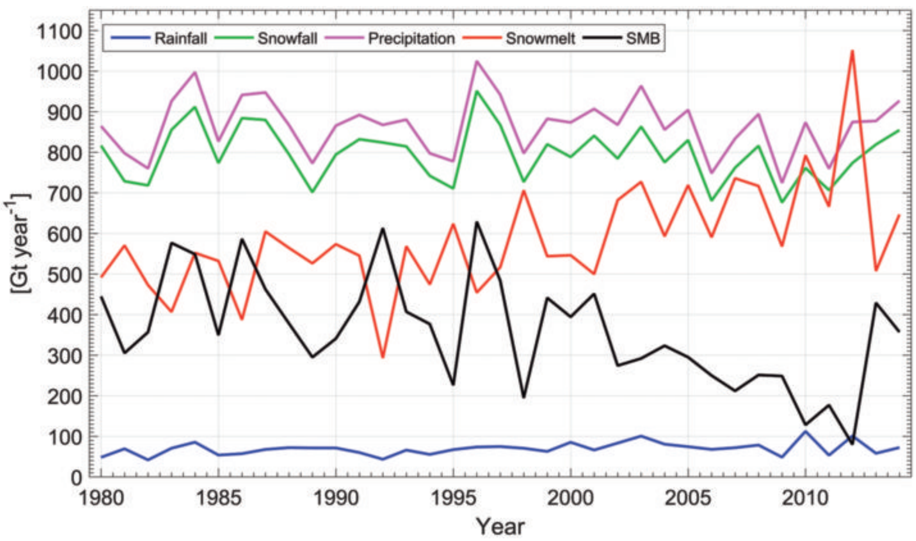

Figure 3 : Annual mean components of surface mass balance for the present day in the ERA-Interim simulation.

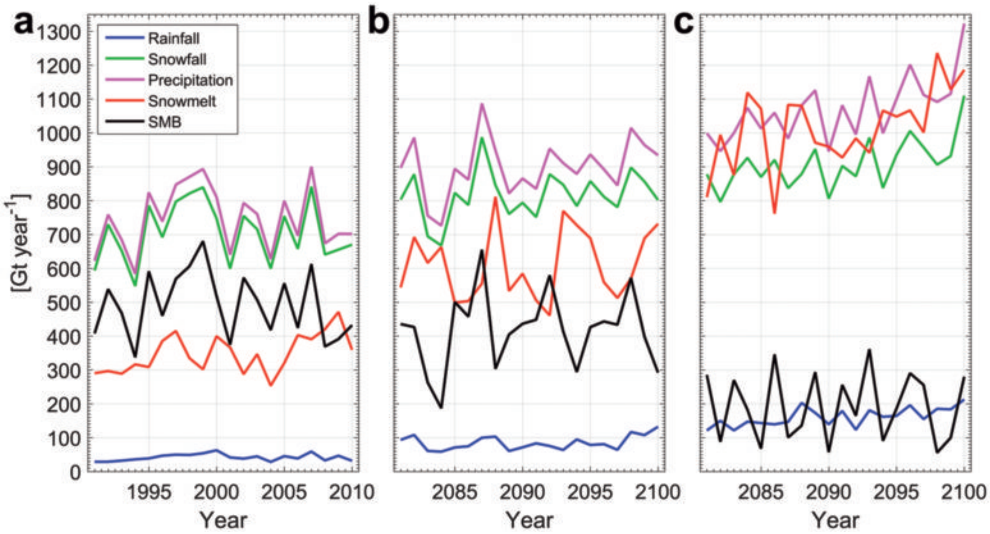

Figure 4：Annual mean components of surface mass balance for a) the historical emissions simulation, and the end of the century under b) RCP4.5 and c) RCP8.5 scenarios.

is a strong declining trend in SMB in the most recent decade driven largely by increased melt and runoff rates. The interannual variability is however also large and shows the importance of long time series in analyzing the SMB trends. There has also been an increase in rainfall events over Greenland, though this is barely discernable over the whole ice sheet. However, work by Doyle et al. (2015), analyzing the ERA-Interim simulation, shows that in western Greenland, rainfall events occurring more frequently at higher altitudes over the ice sheet have a distinct impact on the dynamics of the ice sheet.

Comparison between Figures 3 and 4a shows that the EC-Earth historical simulation underestimates snowfall across the whole ice sheet compared to ERA-Interim; however, melt rates are also lower and these two components compensate for each other to some extent when estimating total SMB. Note that the firn core observations in Figure 2 are confined to the higher accumulation zone where differences in melt and runoff rates between the two historical period simulations are minor.

Figures 4b and 4c show the end of the 21st century under two different climate scenarios. A comparison between Figures 3 and 4b show that under the RCP4.5 scenario, the model expects a similar, though still higher mean annual SMB to that of the last decade in ERA-Interim, with both higher precipitation and higher melt rates than the historical simulation. It is important to note that in Figure 5 both the pattern of precipitation and melt appear comparable with that given by the ERA-interim simulation, suggesting that EC-Earth does not simulate significant changes in circulation.

There is a documented bias in EC-Earth v2.3, which is colder in the Arctic region during the historical period than observations suggest (Hazeleger et al., 2012). This is partly attributable to a larger area covered by sea ice than observed and possibly also to the albedo scheme in Greenland (Helsen et al., 2016) in the standard EC-Earth set-up. Ongoing work to couple EC-Earth to an ice sheet model (Madsen et al., in preparation) may improve this in the future.

On the other hand, the sources of high melt rates observed over the ice sheet in recent years appear to be persistent blocking high pressure systems that may simply reflect internal variability within the climate system (Fettweis et al., 2013). Although recent work by Hanna et al. (2016) suggests that some of the recent increases in persistent anomalies could be a climate change signal, analysis of data from a wide range of climate models within the CMIP5 archive does not seem to indicate this is an expected signal of climate change. The higher SMB in the EC-Earth simulations suggests that the cold bias in EC-Earth observed historically in the Arctic persists through the 21st century. Assuming that the ERA-Interim driven SMB is accurate, it suggests that the EC-Earth climate simulations may be under-estimating the rate of climate change in the Arctic over this century. However, the much lower SMB in

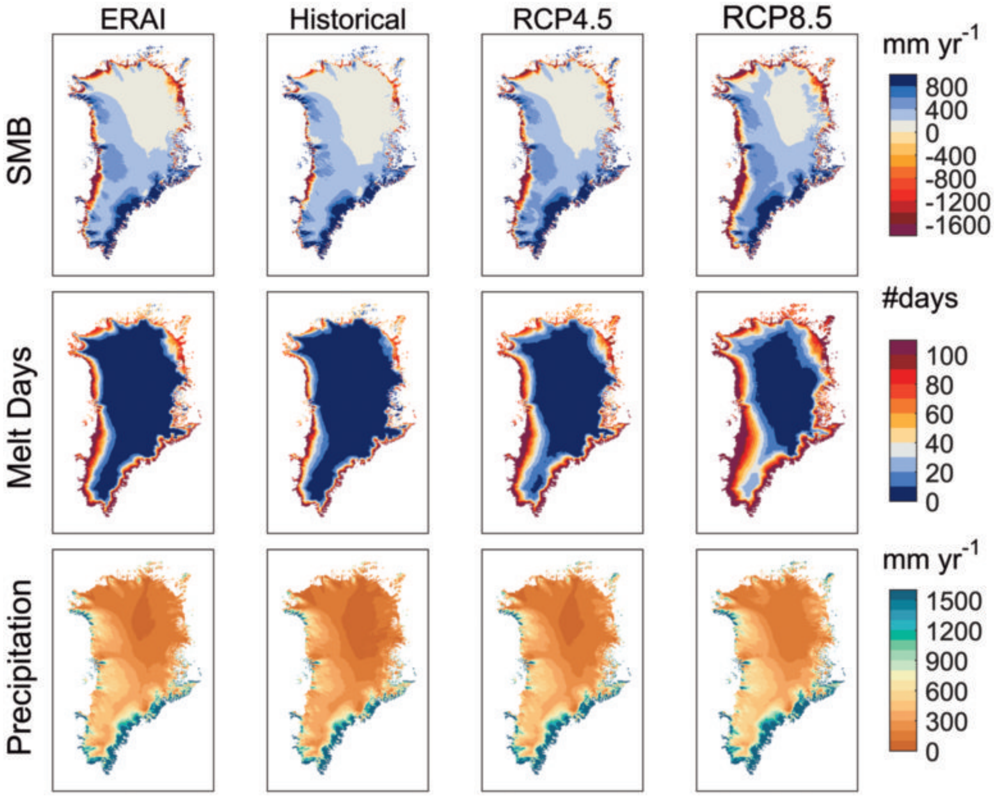

Figure 5: SMB, precipitation and the number of melt days for the ERA-Interim and historical emissions scenario as well as the end of the 21st century RCP4.5 and RCP8.5 scenarios.

the RCP8.5 simulation at the end of the 21st century reflects a much greater enhancement to Arctic warming in the higher RCP8.5 emissions scenario.

The change in ice sheet SMB expected under climate scenarios RCP4.5 and RCP8.5 both show increased precipitation and a significant increase in melt compared in melt rates compared to the historical simulation. These increases are scaled by scenario so that RCP4.5 has a lower increase in melt than RCP8.5.

Table 3 summarizes the projected change in SMB for the mid-century and end of the century simulations for the two different climate scenarios. The plots in Figure 5 show that, while the precipitation pattern remains similar through the projections, the melt area will expand, particularly in western and northern Greenland and over the saddle region in the south, with the magnitude of this expansion determined by the scenario. The increase in precipitation projected by the model is largely confined to the south-east, with a very small increase in northern Greenland, this represents an intensification of existing precipitation patterns.

One potential source of uncertainty in this study is the fixed ice sheet mask during the simulations. Neither the ablation — elevation feedback, which leads to lowering of the ice sheet margin and thus increased ablation rates, nor the potential migration of orographic precipitation as the ice sheet margin retreats are included. Similarly, with high ablation rates, the lower ablation zone and peripheral glaciers will be lost at some point, but these are still in the ice mask at the end of century when SMB is calculated in these simulations. This suggests that the very low annual SMB under RCP8.5 may be an understimate. Further analysis of the difference between ice sheet and peripheral glaciers

Table 3: SMB from historical, mid-century and end of the century simulations for two different climate scenarios, RCP4.5 and RCP8.5 dynamically downscaled from EC-Earth using the HIRHAM5 set-up. Note that the historical emissions scenario is used for the period 1990-2006 and RCP4.5 for the remaining four years.

	Mean annual surface mass balance (Gt year^{-1})		
Simulation period	Historical	RCP4.5	RCP8.5
1991-2010	492 ± 94	—	—
2031-2050	—	460 ± 79	414 ± 65
2081-2100	—	418 ± 109	193 ± 99

is required to account for this. A dynamical ice sheet model run coupled with the climate model is also required to answer these questions fully, and sensitivity experiments planned for future work will also help to determine whether these effects are important.

4. Conclusions

In this paper we present a summary of the present-day surface mass balance in Greenland. Our results and those reported in Langen et al. (2017) show that the ice sheet and peripheral glaciers are well represented at the present day, but biases from global climate model forcing underestimate the amount of melt and precipitation currently in Greenland compared to reanalysis driven simulations.

In the future, downscaling global climate model simulations suggest that an increase in melt and runoff, only partially balanced by a small increase in precipitation, is likely to lead to increasing mass loss from the ice sheet, with the total magnitude determined by the forcing due to greenhouse gas emissions.

The small size of peripheral glaciers means that many of them may disappear entirely in this century. However, the fixed ice mask in this simulation means that neither the changing distribution of ice nor elevation-related feedbacks such as ablation area increase due to declining elevation, nor precipitation migration due to changes in orography, are considered here. These are areas for future study.

Data availability

HIRHAM5 simulation output is freely available at http: //prudence. dmi. dk/data/temp/RUM/HIRHAM/GL2 (or contact the authors directly).

Acknowledgements

Research reported in this paper was supported in part by the ERC Synergy project ice2ice (ERC grant 610055) from the European Community's Seventh Framework Programme (FP7/2007–2013) and the RETAIN project, funded by the Danish Council for Independent research (Grant no. 4002-00234). Ruth Mottram gratefully acknowledges the invitation to the international workshop “Greenland ice sheet mass loss and its impact on global climate change” under the SIGMA (Snow Impurity and Glacial Microbe effects on abrupt warming in the Arctic) project, the ArCS (Arctic Challenge for Sustainability) Project and the Joint Research Program of the Institute of Low Temperature Science, Hokkaido University. We thank Ralf Greve for a thorough review which substantially improved the paper.

References

Bamber, J. L., R. L. Layberry, and S. P. Gogineni (2001) A new ice thickness and bed data set for the Greenland ice sheet: 1. Measurement, data reduction, and errors. *J. Geophys. Res. Atmos.*, **106**, 33773–33780, doi: 10.1029/2001JD900054.

Barletta, V. R., L. S. Sørensen, and R. Forsberg (2013) Scatter of mass changes estimates at basin scale for Greenland and Antarctica. *Cryosphere*, **7**, 1411–1432, doi: 10.5194/tc-7-1411-2013.

Bolch, T., L. Sandberg Sørensen, S. B. Simonsen, N. Mölg, H. Machguth, P. Rastner, and F. Paul (2013) Mass loss of Greenland's glaciers and ice caps 2003–2008 revealed from ICESat laser altimetry data. *Geophys. Res. Lett.*, **40**, 875–881, doi: 10.1002/grl.50270.

Buchardt, S. L., H. B. Clausen, B. M. Vinther, and D. Dahl-Jensen (2012) Investigating the past and recent δ^{18}O-accumulation relationship seen in Greenland ice cores. *Clim. Past*, **8**, 2053–2059, doi: 10.5194/cp-8-2053-2012.

Christensen, O. B., M. Drews, J. H. Christensen, K. Dethloff, K. Ketelsen, I. Hebestadt, and A. Rinke (2006) The HIRHAM regional climate model version 5. DMI Technical Report 06-17, URL: https: //www. dmi. dk/fileadmin/Rapporter/TR/tr06-17.pdf.

Church, J. A., P. U. Clark, A. Cazenave, J. M. Gregory, S. Jevrejeva, A. Levermann, M. A. Merrifield, G. A. Milne, R. S. Nerem, P. D. Nunn, A. J. Payne, W. T. Pfeffer, D. Stammer, and A. S. Unnikrishnan (2013) Sea level change. In: T. F. Stocker, D. Qin, G.-K. Plattner, M. Tignor, S. K. Allen, J. Boschung, A. Nauels, Y. Xia, V. Bex, and P. M. Midgley (Eds.), *Climate Change 2013: The Physical Science Basis. Contribution of Working Group I to the Fifth Assessment Report of the Intergovernmental Panel on Climate Change*. Cambridge University Press, Cambridge, United Kingdom and New York, NY, USA, pp.1137–1216.

Citterio, M., and A. P. Ahlstrøm (2013) Brief communication “The aerophotogrammetric map of Greenland ice masses”. *Cryosphere*, **7**, 445–449, doi: 10.5194/tc-7-445-2013.

Dee, D. P., S. M. Uppala, A. J. Simmons, P. Berrisford, P. Poli, S.

Kobayashi, U. Andrae, M. A. Balmaseda, G. Balsamo, P. Bauer, P. Bechtold, A. C. M. Beljaars, L. van de Berg, J. Bidlot, N. Bormann, C. Delsol, R. Dragani, M. Fuentes, A. J. Geer, L. Haimberger, S. B. Healy, H. Hersbach, E. V. Hólm, L. Isaksen, P. Kållberg, M. Köhler, M. Matricardi, A. P. McNally, B. M. Monge-Sanz, J.-J. Morcrette, B.-K. Park, C. Peubey, P. de Rosnay, C. Tavolato, J.-N. Thépaut, and F. Vitart (2011) The ERA-Interim reanalysis: configuration and performance of the data assimilation system. *Q. J. R. Meteorol. Soc.*, **137**, 553–597, doi: 10.1002/qj.828.

Doyle, S. H., A. Hubbard, R. S. W. van de Wal, J. E. Box, D. van As, K. Scharrer, T. W. Meierbachtol, P. C. J. P. Smeets, J. T. Harper, E. Johansson, R. H. Mottram, A. B. Mikkelsen, F. Wilhelms, H. Patton, P. Christoffersen, and B. Hubbard (2015) Amplified melt and flow of the Greenland ice sheet driven by late-summer cyclonic rainfall. *Nat. Geosci.*, **8**, 647–653, doi: 10.1038/ngeo2482.

Eerola, K. (2006) About the performance of HIRLAM version 7.0. *HIRLAM Newsl.*, **51**, 93–102.

Fausto, R. S., D. van As, J. E. Box, W. Colgan, P. L. Langen, and R. H. Mottram (2016) The implication of nonradiative energy fluxes dominating Greenland ice sheet exceptional ablation area surface melt in 2012. *Geophys. Res. Lett.*, **43**, 2649–2658, doi: 10.1002/2016GL067720.

Fettweis, X., E. Hanna, C. Lang, A. Belleflamme, M. Erpicum, and H. Gallée (2013) Important role of the mid-tropospheric atmospheric circulation in the recent surface melt increase over the Greenland ice sheet. *Cryosphere*, **7**, 241–248.

Forbes, R., A. M. Tompkins, and A. Ungatch (2011) A new prognostic bulk microphysics scheme for the IFS. Technical Memorandum No.649, ECMWF.

Hanna, E., T. Cropper, R. Hall, and J. Cappelen (2016) Greenland Blocking Index 1851–2015: a regional climate change signal. *Int. J. Climatol.*, **36**, 4847–4861, doi: 10.1002/joc.4673.

Hanna, E., F. J. Navarro, F. Pattyn, C. M. Domingues, X. Fettweis, E. R. Ivins, R. J. Nicholls, C. Ritz, B. Smith, S. Tulaczyk, P. L. Whitehouse, and H. J. Zwally (2013) Ice-sheet mass balance and climate change. *Nature*, **498**, 51–59.

Hazeleger, W., X. Wang, C. Severijns, S. Ştefănescu, R. Bintanja, A. Sterl, K. Wyser, T. Semmler, S. Yang, B. van den Hurk, T. van Noije, E. van der Linden, and K. van der Wiel (2012) EC-Earth V2.2: description and validation of a new seamless earth system prediction model. *Clim. Dyn.*, **39**, 2611–2629, doi: 10.1007/s00382-011-1228-5.

IPCC (2013) *Climate Change 2013: The Physical Science Basis. Contribution of Working Group I to the Fifth Assessment Report of the Intergovernmental Panel on Climate Change* (Eds. T. F. Stocker, D. Qin, G.-K. Plattner, M. Tignor, S. K. Allen, J. Boschung, A. Nauels, Y. Xia, V. Bex, and P. M. Midgley). Cambridge University Press, Cambridge, United Kingdom and New York, NY, USA.

Langen, P. L., R. H. Mottram, J. H. Christensen, F. Boberg, C. B. Rodehacke, M. Stendel, D. van As, A. P. Ahlstrøm, J. Mortensen, S. Rysgaard, D. Petersen, K. H. Svendsen, G. Aðalgeirsdóttir, and J. Cappelen (2015) Quantifying energy and mass fluxes controlling Godthåbsfjord freshwater input in a 5 km simulation (1991–2012). *J. Climate*, **28**, 3694–3713, doi: 10.1175/JCLI-D-14-00271.1.

Langen, P. L., R. S. Fausto, B. Vandecrux, R. H. Mottram, and J. E. Box (2017) Liquid water flow and retention on the Greenland ice sheet in the regional climate model HIRHAM5: Local and large-scale impacts. *Front. Earth Sci.*, **4**, 110, doi: 10.3389/feart.2016.00110.

Lucas-Picher, P., M. Wulff-Nielsen, J. H. Christensen, G. Aðalgeirsdottir, R. Mottram, and S. B. Simonsen (2012) Very high resolution regional climate model simulations over Greenland: Identifying added value. *J. Geophys. Res. Atmos.*, **117**, D02108, doi: 10.1029/2011JD016267.

Machguth, H., H. H. Thomsen, A. Weidick, A. P. Ahlstrøm, J. Abermann, M. L. Andersen, S. B. Andersen, A. A. Bjørk, J. E. Box, R. J. Braithwaite, C. E. Bøggild, M. Citterio, P. Clement, W. Colgan, R. S. Fausto, K. Gleie, S. Gubler, B. Hasholt, B. Hynek, N. T. Knudsen, S. H. Larsen, S. H. Mernild, J. Oerlemans, H. Oerter, O. B. Olesen, C. J. P. P. Smeets, K. Steffen, M. Stober, S. Sugiyama, D. van As, M. R. van den Broeke, and R. S. W. van de Wal (2016) Greenland surface mass-balance observations from the ice-sheet ablation area and local glaciers. *J. Glaciol.*, **62**, 861–887, doi: 10.1017/jog.2016.75.

Mernild, S. H., G. E. Liston, C. A. Hiemstra, K. Steffen, E. Hanna, and J. H. Christensen (2009) Greenland Ice Sheet surface mass-balance modelling and freshwater flux for 2007, and in a 1995–2007 perspective. *Hydrol. Process.*, **23**, 2470–2484, doi: 10.1002/hyp.7354.

Noël, B., W. J. van de Berg, H. Machguth, S. Lhermitte, I. Howat, X. Fettweis, and M. R. van den Broeke (2016) A daily, 1 km resolution data set of downscaled Greenland ice sheet surface mass balance (1958–2015). *Cryosphere*, **10**, 2361–2377, doi: 10.5194/tc-10-2361-2016.

Nielsen-Englyst, P. (2015) *Impact of Albedo Parametrizations on Surface Mass Balance Runoff on the Greenland Ice Sheet.* Master Thesis, University of Copenhagen.

Rae, J. G. L., G. Aðalgeirsdottir, T. L. Edwards, X. Fettweis, J. M. Gregory, H. T. Hewitt, J. A. Lowe, P. Lucas-Picher, R. H. Mottram, A. J. Payne, J. K. Ridley, S. R. Shannon, W. J. van de Berg, R. S. W. van de Wal, and M. R. van den Broeke (2012) Greenland ice sheet surface mass balance: evaluating simulations and making projections with regional climate models. *Cryosphere*, **6**, 1275–1294, doi: 10.5194/tc-6-1275-2012.

Rignot, E., I. Velicogna, M. R. van den Broeke, A. Monaghan, and J. T. M. Lenaerts (2011) Acceleration of the contribution of the Greenland and Antarctic ice sheets to sea level rise. *Geophys. Res. Lett.*, **38**, L05503, doi: 10.1029/2011GL046583.

Roeckner, E., G. Bäuml, L. Bonaventura, R. Brokopf, M. Esch, M. Giorgetta, S. Hagemann, I. Kirchner, L. Kornblueh, E. Manzini, A. Rhodin, U. Schlese, U. Schulzweida, and A. Tompkins (2003) The atmospheric general circulation model ECHAM 5. Part I: Model description. Technical Report No.349, Max Planck Institute.

Schmidt, L. G. Aðalgeirsdóttir, S. Guðmundsson, P. L. Langen, F. Pálsson, R. Mottram, S. Gascoin, and H. Björnsson (submitted) Evaluating the surface energy balance in the HIRHAM5 regional climate model over Vatnajökull, Iceland, using automatic weather station data. *Cryosphere* (submitted MS No. tc-2017-14).

Shepherd, A., E. R. Ivins, G. A, V. R. Barletta, M. J. Bentley, S. Bettadpur, K. H. Briggs, D. H. Bromwich, R. Forsberg, N. Galin, M. Horwath, S. Jacobs, I. Joughin, M. A. King, J. T. M. Lenaerts, J. Li, S. R. M. Ligtenberg, A. Luckman, S. B. Luthcke, M. McMillan, R. Meister, G. Milne, J. Mouginot, A. Muir, J. P. Nicolas, J. Paden, A. J. Payne, H. Pritchard, E. Rignot, H. Rott, L. S. Sorensen, T. A. Scambos, B. Scheuchl, E. J. O. Schrama, B. Smith, A. V. Sundal, J. H. van Angelen, W. J. van de Berg, M. R. van den Broeke, D. G. Vaughan, I. Velicogna, J. Wahr, P. L. Whitehouse, D. J. Wingham, D. Yi, D. Young, and H. J. Zwally (2012) A reconciled estimate of ice-sheet mass balance. *Science*, **338**, 1183-1189, doi: 10.1126/science.1228102.

Stibal, M., E. Gözdereliler, K. A. Cameron, J. E. Box, I. T. Stevens, J. K. Gokul, M. Schostag, J. D. Zarsky, A. Edwards, T. D. L. Irvine-Fynn, and C. S. Jacobsen (2015) Microbial abundance in surface ice on the Greenland Ice Sheet. *Front. Microbiol.*, **6**, 225, doi: 10.3389/fmicb.2015.00225.

Van As, D., R. S. Fausto, J. Cappelen, R. S. W. van der Wal, R. J. Braithwaite, H. Machguth, C. Charalampidis, J. E. Box, A. M. Solgaard, A. P. Ahlstrøm, K. Haubner, M. Citterio, and S. B. Andersen (2016) Placing Greenland ice sheet ablation measurements in a multi-decadal context. *Geol. Surv. Den. Greenl. Bull.*, **35**, 71-74.

Vernon, C. L., J. L. Bamber, J. E. Box, M. R. van den Broeke, X. Fettweis, E. Hanna, and P. Huybrechts (2013) Surface mass balance model intercomparison for the Greenland ice sheet. *Cryosphere*, **7**, 599-614, doi: 10.5194/tc-7-599-2013.

低温科学 75　(2017)　117-129
doi: 10.14943/lowtemsci. 75. 117

Projecting the response of the Greenland ice sheet to future climate change with the ice sheet model SICOPOLIS

Ralf Greve[1]*, Reinhard Calov[2], Ute C. Herzfeld[3]

Received 13 January 2017, accepted 16 January 2017

Numerical modelling has become established as an important tool for understanding ice sheet dynamics in general, and in particular for assessing the contribution of the Greenland and Antarctic ice sheets to future sea level change under global warming conditions. In this paper, we review related work carried out with the ice sheet model SICOPOLIS (SImulation COde for POLythermal Ice Sheets). As part of a group of eight models, it was applied to a set of standardised experiments for the Greenland ice sheet defined by the SeaRISE (Sea-level Response to Ice Sheet Evolution) initiative. A main finding of SeaRISE was that, if climate change continues unabatedly, the ice sheet may experience a significant decay over the next centuries. However, the spread of results across different models was very large, mainly because of differences in the applied initialisation methods and surface mass balance schemes. Therefore, the new initiative ISMIP6 (Ice Sheet Modeling Intercomparison Project for CMIP6) was launched. An early sub-project is InitMIP-Greenland, within which we showed that two different initialisations computed with SICOPOLIS lead indeed to large differences in the simulated response to schematic future climate scenarios. Further work within ISMIP6 will thus focus on improved initialisation techniques. Based on this, refined future climate simulations for the Greenland ice sheet, driven by forcings derived from AOGCM (atmosphere-ocean general circulation model) simulations, will be carried out. The goal of ISMIP6 is to provide significantly improved estimates of ice sheet contribution to sea level rise in the coming years.

Keywords: Greenland, ice sheet, climate change, sea level rise, modelling

1. Introduction

Ice sheets are grounded ice masses of sub-continental to continental size (e.g., Molnia, 2004). The two ice sheets on the present-day Earth are those of Greenland and Antarctica. Most of the terrestrial freshwater reserves are stored in these two ice sheets, amounting to ~ 65 m of sea level equivalent (Antarctica ~ 58 m, Greenland ~ 7.4 m; Vaughan et al., 2013).

Like the smaller ice caps and glaciers, ice sheets show gravity-driven creep flow ("glacial flow"), sustained by the underlying land. This leads to thinning and horizontal spreading, which is essentially compensated by snow accumulation in the higher (interior) areas and melting and calving in the lower (marginal) areas (Fig. 1). Any imbalance of this dynamic equilibrium leads to either growing or shrinking ice masses.

The Greenland ice sheet is significantly warmer than the Antarctic ice sheet. Therefore, the regions close to the ice margin experience a considerable amount

---

*Corresponding author
e-mail：greve@lowtem.hokudai.ac.jp
１）Institute of Low Temperature Science, Hokkaido University, Sapporo, Japan
２）Potsdam Institute for Climate Impact Research, Potsdam, Germany
３）Department of Electrical, Computer and Energy Engineering, University of Colorado, Boulder, USA

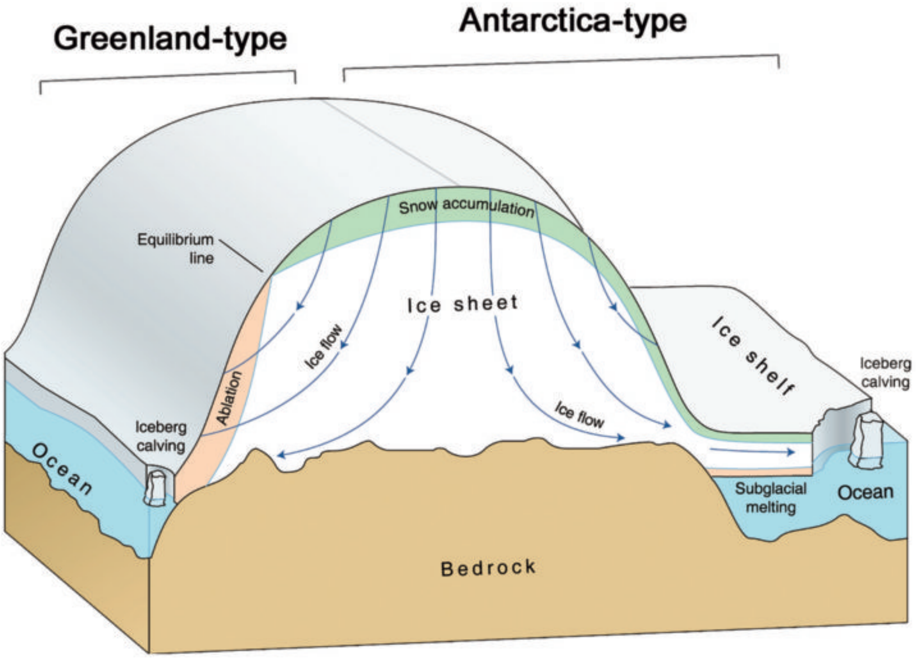

Figure 1 : Main processes that govern the evolution and dynamics of the Greenland and Antarctic ice sheet. Modified from lima.nasa.gov/antarctica/.

of surface melting (ablation) during the summer season, so that the mass loss of the Greenland ice sheet is divided roughly equally between melting and calving (left part of Fig. 1; van den Broeke et al., 2009). In contrast, for the much colder Antarctic ice sheet surface melting is virtually non-existing, and it loses mass mainly through basal melting under its attached, floating ice shelves and calving at the fronts of the ice shelves (right part of Fig. 1; Rignot et al., 2013).

Observations indicate that both the Greenland and Antarctic ice sheets have already shown strong, and accelerating, reactions on global warming (Shepherd et al., 2012; Hanna et al., 2013; Enderlin et al., 2014; Khan et al., 2015). The average rate of ice loss from the Greenland ice sheet has increased substantially from 34 ± 40 Gt a^{-1} over the period 1992–2001 to 215 ± 59 Gt a^{-1} for 2002–2011 (IPCC, 2013a) and 341 ± 22 Gt a^{-1} for 2011–2014 (Helm et al., 2014), and the average rate of ice loss from the Antarctic ice sheet has increased from 30 ± 67 Gt a^{-1} over the period 1992–2001 to 147 ± 75 Gt a^{-1} for 2002–2011 (IPCC, 2013a) and 116 ± 76 Gt a^{-1} for 2011–2014 (Helm et al., 2014). According to the most recent figures for 2011–2014 (Helm et al., 2014), which were determined by CryoSat-2 altimetry, Greenland contributes nearly 75% to the combined mass loss of the two ice sheets.

Modelling the response of the Greenland and Antarctic ice sheets to anthropogenic climate change has been undertaken for more than two decades. Among the older studies are, e.g., Huybrechts and Oerlemans (1990), Huybrechts et al. (1991), de Wolde et al. (1997), Greve (2000) and Ridley et al. (2005). More recently, this has become a fairly hot topic in climate science because, in the Fourth Assessment Report (AR4) of the United Nations Intergovernmental Panel on Climate Change (IPCC), it was explicitly stated that *"Dynamical processes related to ice flow not included in current models but suggested by recent observations could increase the vulnerability of the ice sheets to warming, increasing future sea level rise. Understanding of these processes is limited and there is no consensus on their magnitude"* (IPCC, 2007). The scientific community responded by launching two major ice sheet modelling initiatives, namely SeaRISE (Sea-level Response to Ice Sheet Evolution; tinyurl.com/srise-umt) and Ice2sea (www.ice2sea.eu). Both projects are meanwhile completed and provided valuable input for the Fifth Assessment Report (AR5) of the IPCC (IPCC, 2013b, and references therein). Efforts towards further improved assessments of the expected contribution from the Greenland and Antarctic ice sheets to sea level rise are continued within the ongoing ISMIP6 project (Ice Sheet Modeling

Intercomparison Project for CMIP6; Nowicki et al., 2016). In this paper, we focus on the Greenland ice sheet and review the contributions to SeaRISE and ISMIP6 with the ice sheet model SICOPOLIS.

2. Ice sheet model SICOPOLIS

SICOPOLIS (SImulation COde for POLythermal Ice Sheets; www.sicopolis.net) is a dynamic/thermodynamic ice sheet model that was originally created by Greve (1995, 1997) in a version for the Greenland ice sheet. Since then, SICOPOLIS has been developed continuously and applied to problems of past, present and future glaciation of Greenland (e. g., Robinson et al., 2012), Antarctica (e. g., Kusahara et al., 2015), the entire northern hemisphere, the polar ice caps of the planet Mars and others. A list of the > 100 peer-reviewed papers that use or describe SICOPOLIS can be found at www.sicopolis.net/publ.

The model simulates the large-scale dynamics and thermodynamics (ice extent, thickness, velocity, temperature, water content and age) of ice sheets three-dimensionally and as a function of time. It is based on the shallow ice approximation for grounded ice (Hutter, 1983; Morland, 1984) and the shallow shelf approximation for floating ice (Morland, 1987; MacAyeal, 1989). Recently, hybrid shallow-ice/shelfy-stream dynamics has been added as an option for ice streams (Bernales et al., 2017). The rheology is that of an incompressible, heat-conducting, power-law fluid (Glen's flow law; e.g., Greve and Blatter, 2009). Isostatic depression and rebound of the lithosphere due to changing ice load is modelled by either the local-lithosphere-relaxing-asthenosphere (LLRA) or the elastic-lithosphere-relaxing-asthenosphere (ELRA) approach with an isostatic time lag (Le Meur and Huybrechts, 1996). External forcing is specified by (1) the air temperature at the ice surface, (2) the surface mass balance (precipitation minus runoff), (3) the sea level surrounding the ice sheet (that defines the land area available for glaciation), and (4) the geothermal heat flux prescribed at the bottom of the lithospheric thermal boundary layer.

A particular feature of SICOPOLIS is its very detailed treatment of ice thermodynamics. A variety of different thermodynamics solvers are available, namely the polythermal two-layer method, two versions of the one-layer enthalpy method, the cold-ice method and the isothermal method (Greve and Blatter, 2016). The polythermal and enthalpy methods account in a physically adequate way for the possible co-existence of cold ice (with a temperature below the pressure-melting point) and temperate ice (with a temperature at the pressure-melting point) in the ice body, a condition that is referred to as "polythermal". It is hereby assumed that cold ice makes up the largest part of the ice volume, while temperate ice exists as thin layers overlying a temperate base. In the temperate ice layers, the water content is computed, and its reducing effect on the ice viscosity is taken into account.

SICOPOLIS is coded in Fortran and uses finite difference discretisation techniques on a staggered Arakawa C grid, the velocity components being taken between grid points (Arakawa and Lamb, 1977). For the simulations of the Greenland ice sheet discussed here, all computations are carried out in a stereographic plane (standard parallel at 71°N, central meridian at 39°W), spanned by the Cartesian coordinates x and y. The distortions due to the stereographic projection are corrected by appropriate metric coefficients. Floating ice is ignored, and only the shallow ice approximation is used. A sketch of the model is shown in Fig. 2.

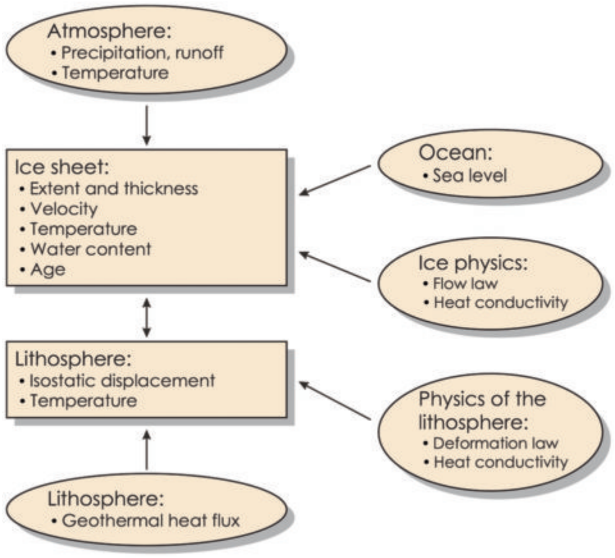

Figure 2 : Sketch of the ice sheet model SICOPOLIS. The rectangular boxes denote prognostic model components, while the ovals indicate required model input (boundary conditions etc.).

3. SeaRISE-Greenland

Sea-level Response to Ice Sheet Evolution (SeaRISE) was a community-organised effort to explore the sensitivity of the available ice sheet models to external forcing, and to gain insight into the potential future contribution to sea level from the Greenland and Antarctic ice sheets (Bindschadler et al., 2013; Nowicki et al., 2013a, b). The main characteristics of SeaRISE were (1) the use of multiple models, (2) standardisation of datasets that describe the physical setting, model initialisation and sensitivity experiments, and (3) application of an 'experiment minus control' method to isolate ice-sheet sensitivity to any environmental-forcing experiment. Results served as input for the Fifth Assessment Report (AR5) of the IPCC (IPCC, 2013b).

3.1 Paleoclimatic spin-up

Here, we only discuss the SeaRISE experiments with SICOPOLIS for the Greenland ice sheet. The strategy for model initialisation (i.e., obtaining a suitable present-day configuration of the Greenland ice sheet that can serve as initial condition for the future climate experiments) was to carry out a paleoclimatic spin-up over a full glacial cycle. However, it is difficult to reproduce the observed geometry by an unconstrained, freely evolving simulation without heavy tuning (e. g., Greve et al., 2011). For this reason, we carried out the spin-up simulation in four steps, each run using the result of the previous run as the initial condition (Greve and Herzfeld, 2013):

1. An initial relaxation run with freely evolving ice topography over 100 years, starting from the present-day geometry and isothermal conditions at −10℃ everywhere, in order to avoid spurious noise in the computed velocity field. The ice sheet is not allowed to extend beyond its present-day margin. The surface temperature and the sea level are those of today; the surface mass balance and basal sliding are set to zero.
2. A steady-state run from 250 ka BP (before present) until 125 ka BP, with the entire topography (surface, bed, ice margin) kept fixed over time. The surface temperature is that of 125 ka BP; the surface mass balance is unspecified (due to the fixed topography). The purpose of this run is to bring internal and basal temperatures to near equilibrium for the climate conditions at 125 ka BP.
3. A transient run from 125 ka BP until 100 years BP; with the entire topography kept fixed over time in order to enforce a good fit between the simulated and observed present-day topographies. The surface temperature varies over time, reflecting the sequence of the Eemian interglacial, the Weichselian glacial and the Holocene; the surface mass balance is unspecified.
4. A short transient run from 100 years BP until the present, with evolving ice topography in order to avoid transition shocks at the beginning of the subsequent future climate experiments. The climatic forcing (surface temperature, surface mass balance) and the sea level are kept steady at today's conditions, and the ice sheet is not allowed to extend beyond its present-day margin.

The horizontal resolution is 10 km prior to 5 ka BP and 5 km from 5 ka BP until today. For further details of the set-up cf. Greve and Herzfeld (2013).

3.2 Future climate experiments

The future climate experiments discussed here are a subset of the suite defined by SeaRISE for the Greenland ice sheet (Bindschadler et al., 2013):

- CTL — constant climate control run; beginning at present (more precisely, the year 2004, corresponding to $t=0$) and running for 500 years, holding the climate steady to the present climate.
- C2 — 1.5 × A1B climate forcing [mean annual temperature, mean July temperature and precipitation anomalies derived from an ensemble average from 18 of the Intergovernmental Panel on Climate Change's Fourth Assessment Report (IPCC AR4) models, run under the A1B emission scenario; see Fig. 2 and accompanying text by Bindschadler et al. (2013)] until 2098, then held steady.
- S1 — constant climate forcing, 2 × basal sliding.
- M2 — constant climate forcing, 20 m w.e. a^{-1} ocean-induced marginal melting (applied at grounded ice cells that have a base below the sea level and are adjacent to ocean).
- R8 — combination experiment approximating

IPCC's RCP (Representative Concentration Pathway) 8.5 scenario; 1.5×A1B climate forcing (extrapolated beyond 2098 over the entire 500 years) plus 1.5×basal sliding plus ocean-induced marginal melting increasing over time to a maximum of 70 m w.e. a^{-1} (for details of this set-up and its rationale see Fig. 14 and accompanying text by Bindschadler et al. (2013)).

The reason for the selection of C2, S1 and M2 is that they are closest to the settings of the combination experiment R8. The horizontal resolution is 5 km for all experiments. For further details see Greve and Herzfeld (2013).

3.3 Results

The results of the paleoclimatic spin-up run (Section 3.1) for the present are shown in Figs. 3 and 4. Comparison of the simulated (Fig. 3a) and observed (Fig. 3b; data by Joughin et al., 2010, 2016) surface velocities reveals that the general pattern with the low-velocity (<10 m a^{-1}) 'backbone', the general acceleration towards the coast and the organisation into drainage systems is reproduced well. As it was discussed in detail by Greve and Herzfeld (2013), on a more local scale, the Jakobshavn Ice Stream, Helheim and Kangerdlugssuaq Glaciers are also reproduced reasonably well despite the applied shallow ice dynamics. In contrast, the North-East Greenland Ice Stream (NEGIS) and the Petermann Glacier are only weakly pronounced in the simulation.

Owing to the fixed-topography constraint during most of the spin-up run, the simulated and observed ice thickness distributions (Fig. 4) agree very well, the misfit being generally small (<100 m). However, some areas stick out, and one of them is the NEGIS area, where simulated ice thicknesses are too large as a consequence of the underpredicted drainage towards the coast. The same holds for the area of Petermann Glacier in the northwest. In contrast, along the south-eastern ice margin simulated ice thicknesses are often too small, which may be due to over-predicted ice flow or to inaccuracies in the surface mass balance. Most of the rapid topographic adjustments that lead to these local misfits arise early during the short transient run over 100 years at the end of the spin-up sequence (step 4; see Section 3.1). After these 100 years, the ice-sheet geometry has largely stabilised, and no spurious rapid adjustments occur in the future climate runs.

Figure 5 depicts the simulated evolution of the volume V of the Greenland ice sheet (panel a) and the volume relative to CTL (panel b) for the five different future climate experiments (Section 3.2). The control run CTL shows a small, but notable drift towards a

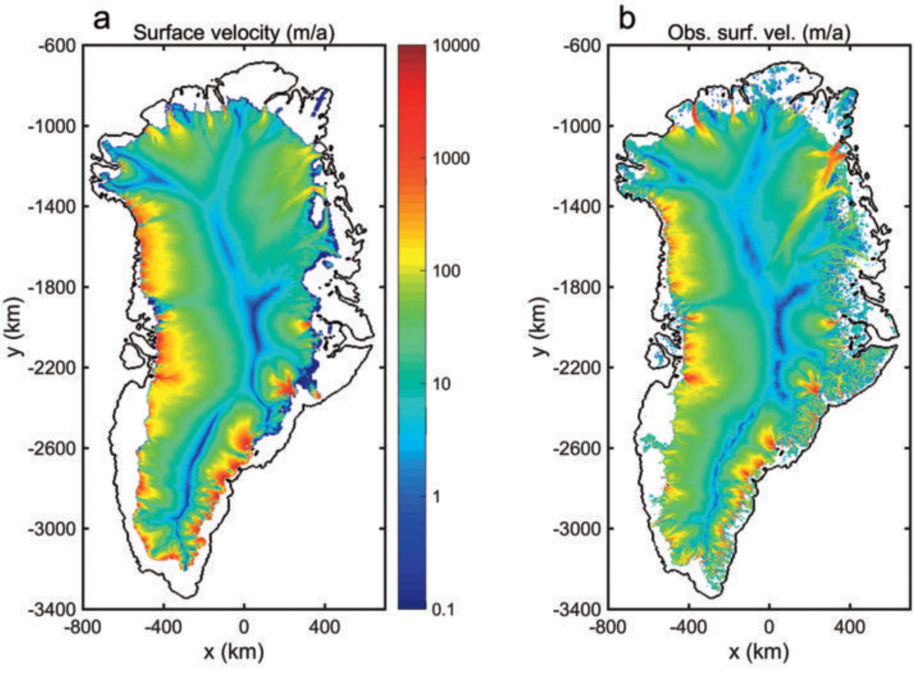

Figure 3 : SeaRISE paleoclimatic spin-up. (a) Simulated present-day surface velocity. (b) Observed present-day surface velocity (Joughin et al., 2010, 2016).

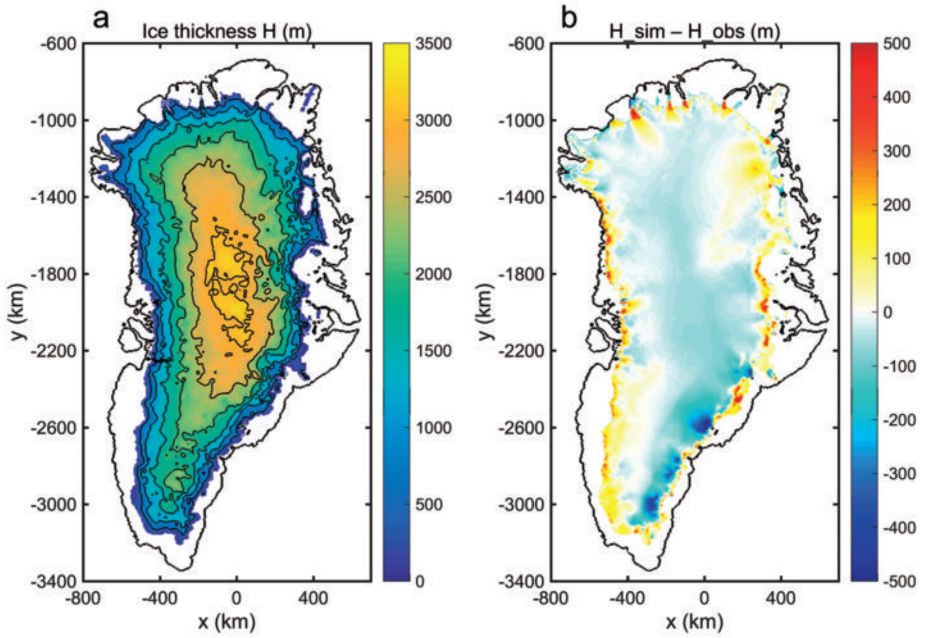

Figure 4: SeaRISE paleoclimatic spin-up. (a) Simulated present-day ice thickness. (b) Difference of simulated and observed present-day ice thickness (the latter is the difference of the surface topography by Bamber (2001) and the "JakHelKanPet" bed topography by Herzfeld et al. (2011, 2012)).

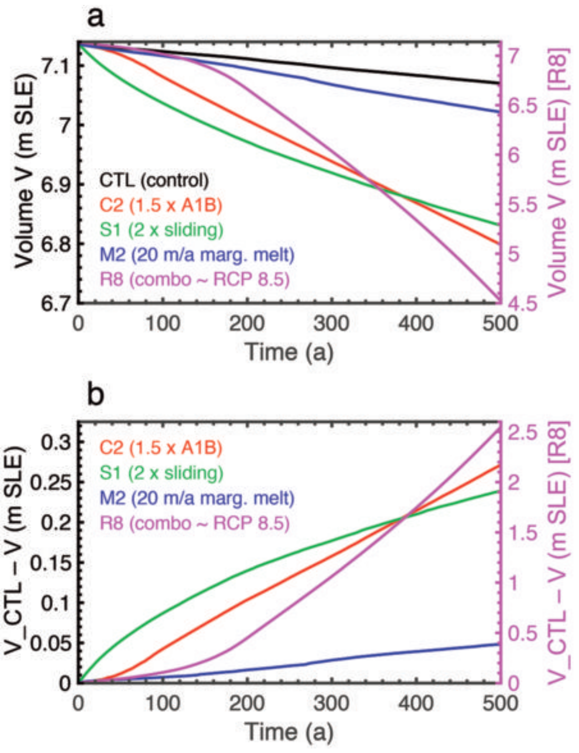

Figure 5: SeaRISE future climate runs. (a) Ice volumes for experiments CTL (control), C2 (1.5×A1B climate forcing until 2098, then held steady), S1 (2×basal sliding), M2 (20 m w.e. a^{-1} ocean-induced marginal melting and R8 (combination experiment approximating an IPCC RCP 8.5 scenario). (b) Ice volume differences (CTL minus experiment) for C2, S1, M2 and R8. All volumes are given in metres of sea level equivalent (m SLE). Note the two different y-axes (left for CTL, C2, S1, M2; right for R8).

smaller ice volume (positive contribution to sea level, on average ~ 0.13 mm a^{-1} during the 500 model years), which is still a reaction to the release of the fixed-topography constraint 100 years before the end of the spin-up sequence. However, all other experiments produce a stronger ice volume decrease than CTL. Of the three sensitivity experiments (C2, S1, M2), S1 (2× basal sliding) has by far the strongest initial reaction with an experiment-minus-control sea-level contribution ($V_{\mathrm{CTL}}-V$, panel b) of ~ 1.3 mm a^{-1} during the first 10 years (but then steadily decreasing). Run C2 (1.5× A1B climate forcing) shows a much weaker, but increasing initial reaction, and approximately stabilises at an average experiment-minus-control sea-level contribution of ~ 0.57 mm a^{-1} from 100 years on until the end of the simulation, ultimately outperforming the impact of run S1. Run M2 (20 m a^{-1} marginal melting) produces the weakest reaction of the sensitivity experiments because the contact of the Greenland ice sheet with the ocean is not that pronounced on the large scale (this is radically different for the Antarctic ice sheet).

As mentioned above, the experiment R8 was designed in order to simulate roughly the response of the Greenland ice sheet to the RCP 8.5 greenhouse gas concentration scenario (a rather pessimistic, 'business-

Table 1 : Simulated sea-level contribution of the Greenland ice sheet for SeaRISE experiment R8 after 100, 200 and 500 years model time. “Min”, “Mean” and “Max” denote the minimal, mean and maximal values across the participating models (Bindschadler et al., 2013). In addition, the SICOPOLIS results are shown.

	Min	Mean	Max	SICOPOLIS
100 a	0.045 m	0.223 m	0.663 m	0.101 m
200 a	0.096 m	0.532 m	0.889 m	0.450 m
500 a	0.181 m	2.016 m	4.097 m	2.549 m

as-usual’ scenario for which it is assumed that emissions continue to rise throughout the 21st century) via a combination of surface climate forcing, enhanced basal sliding and increased ocean-induced marginal melting. The response of the ice sheet to this experiment is very strong and accelerating with time: the experiment-minus-control cumulative sea-level contribution is ~ 0.10 m after 100 years, ~ 0.45 m after 200 years and ~ 2.5 m after 500 years. This means that, after 500 years, approximately one third of the entire ice sheet has disintegrated.

The SeaRISE-Greenland experiments were carried out by a total of eight different ice sheet models, of which five (including SICOPOLIS) completed the R8 experiment with all three forcings as specified above (Bindschadler et al., 2013). An important finding of this multiple-model approach is that the spread of results is very large. For the R8 experiment, the difference of simulated sea-level contributions is as large as an order of magnitude (Table 1). Saito et al. (2016) investigated this problem further and found that the two largest sources for the spread of results are (1) differences in the initialisation methods and (2) differences in the surface mass balance schemes.

4. ISMIP6 InitMIP-Greenland

4.1 ISMIP6

The Ice Sheet Modeling Intercomparison Project for CMIP6 (ISMIP6, www.climate-cryosphere.org/activities/targeted/ismip6) is the successor of the completed SeaRISE and Ice2sea initiatives, and the primary activity within the Coupled Model Intercomparison Project Phase 6 (CMIP6) focusing on the Greenland and Antarctic ice sheets. ISMIP6 was established in autumn 2014, and was endorsed by CMIP6 in mid-2015. A crucial approach is to integrate ISMIP6 in CMIP6. In the past, sea-level projections made by the glaciological community have been lagging behind the projections considered by the wider climate modelling community. For instance, for the IPCC AR5, the SeaRISE and Ice2sea ice sheet modelling initiatives predominantly worked with the old AR4 scenarios, while the CMIP5 community already used the new Representative Concentration Pathways (RCP) scenarios. By linking ISMIP6 to CMIP6, this long-standing disadvantage will be overcome because the latest climate change scenarios simulated by AOGCMs within CMIP6 will be available without delay as drivers for ice sheet modelling studies. This will allow to improve both sea level projections due to changes in the cryosphere and our understanding of the ice sheets in a changing climate. These goals map into the “Changes in Cryosphere” Grand Challenge relevant to Climate and Cryosphere (CliC) and the World Climate Research Program (WCRP) (www.climate-cryosphere.org/activities/grand-challenges). ISMIP6 is described in further detail by Nowicki et al. (2016).

4.2 InitMIP-Greenland experiments

Earlier large-scale Greenland ice sheet experiments, e.g., those run for the SeaRISE initiative, have shown that ice sheet initialisation has a large effect on future sea-level projections and gives rise to important uncertainties (Saito et al., 2016). In order to compare and evaluate the initialisation methods used in the ice sheet modelling community and estimate the uncertainty associated with initialisation, the ice sheet model initialisation experiments for Greenland (InitMIP-Greenland) were devised as an early sub-project within ISMIP6 (H. Goelzer, personal communication, 2016). InitMIP-Greenland comprises three experiments:

- init — Initialisation of the Greenland ice sheet to present day. Modellers can use the method of their choice to achieve this (typically either assimilation methods or paleoclimatic spin-up methods). Further, the exact meaning of “present day” is at the modeller’s discretion.
- ctrl — Control run 100 years into the future, starting from the final state of run init and holding the climate steady to the present-day state.

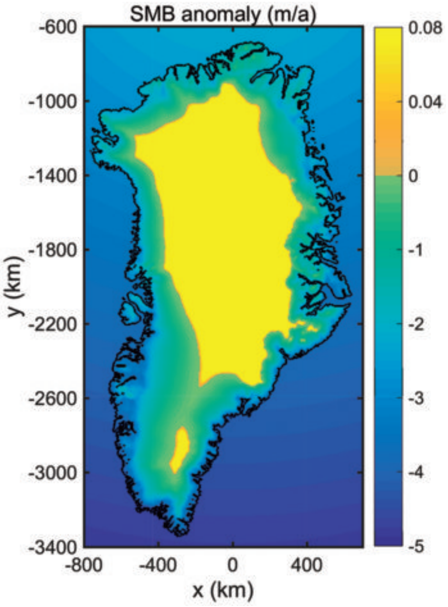

Figure 6 : Schematic surface mass balance anomaly used for the InitMIP-Greenland experiment asmb after 40 years model time (in metres of ice equivalent per year) (H. Goelzer, personal communication, 2016).

- asmb — Run 100 years into the future, starting from the final state of run init with a prescribed, schematic surface mass balance (SMB) anomaly. The SMB anomaly starts from zero, increases stepwise every full year over the first 40 years and remains steady thereafter (Fig. 6).

We contribute to InitMIP-Greenland with the ice sheet model SICOPOLIS and two different spin-up techniques for the run init:

- Spin-up #1 — a SeaRISE-legacy spin-up with essentially fixed topography (as described in Section 3.1).
- Spin-up #2 — a new spin-up over 135 ka with freely evolving topography.

For both cases, we used the recently developed melting-CTS enthalpy method ("ENTM"; Greve and Blatter, 2016) as the solver for ice sheet thermodynamics. Our reference year ("present day") is 1990. New methods applied for spin-up #2 are monthly-mean (rather than mean annual) input data for the present-day precipitation (Robinson et al., 2010), a sub-grid-scale ice discharge parameterisation (Calov et al., 2015) and an iterative correction of the present-day precipitation based on the misfit between the simulated and observed present-day ice thickness. Details of this procedure will be published elsewhere. The horizontal resolution for spin-up #1 is the same as for SeaRISE (10 km prior to 5 ka BP, 5 km from 5 ka BP until today), and for spin-up #2 it is 10 km prior to 9 ka BP and 5 km from 9 ka BP until today. The two future climate scenarios ctrl and asmb are run with freely evolving ice topography for either spin-up method, and the horizontal resolution is 5 km.

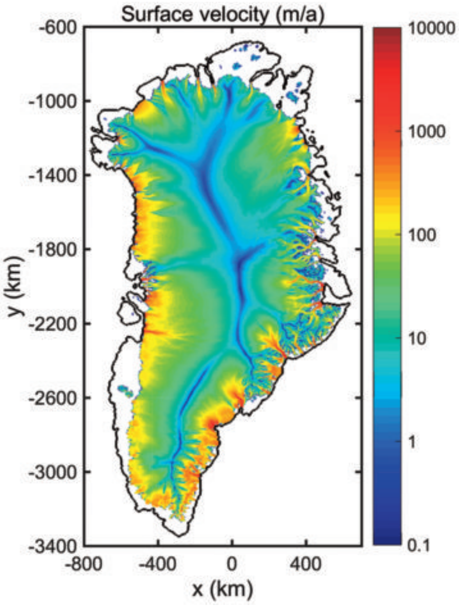

Figure 7 : InitMIP-Greenland paleoclimatic spin-up #2 with freely evolving topography. Simulated present-day surface velocity (for the observed counterpart see Fig. 3b).

4.3 Results

The present-day surface velocity and ice thickness produced by spin-up #1 are almost identical to those obtained by the original SeaRISE spin-up (Figs. 3 and 4) and thus not shown again. The surface velocity produced by spin-up #2 is shown in Fig. 7. While there are some differences in detail, it shares the same main features with the result of spin-up #1: the low-velocity 'backbone', the general acceleration towards the coast, the organisation into drainage systems and most of the major ice streams and outlet glaciers agree well with the observed pattern (Fig. 3b). The Petermann Glacier is even reproduced better by spin-up #2 than by spin-up #1, while the problem with the generally too slow flow in the area of the NEGIS remains.

The agreement between simulated and observed ice topography is naturally better for the fixed-topography case #1 (Fig. 4) than for the freely evolving case #2 (Fig. 8). As for the interior ice sheet simulated by spin-up #2, thicknesses are generally too large in the south-

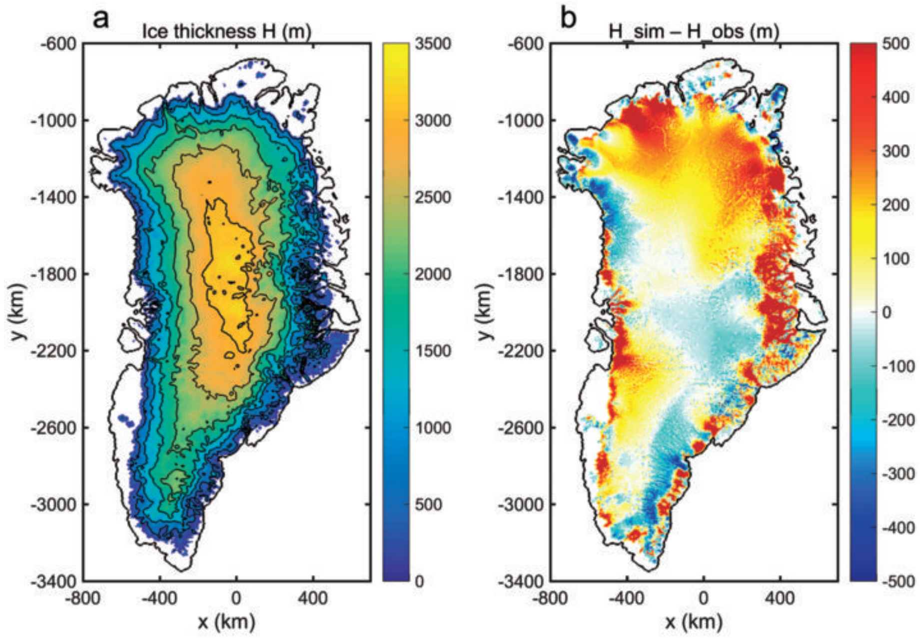

Figure 8: InitMIP-Greenland paleoclimatic spin-up #2 with freely evolving topography. (a) Simulated present-day ice thickness. (b) Difference of simulated and observed present-day ice thickness (the latter is by Bamber et al. (2013)).

west, north and north-east, while they are too small in the south-east, centre and north-west. Near the ice margin, a number of areas exhibit distinctly overpredicted ice thicknesses, and they often coincide with areas of fast ice flow. The latter is likely mainly due to the employed shallow ice dynamics that does not describe the dynamics of ice streams adequately. The reason for the pattern of disagreement in the interior is more difficult to assess as lacking accuracy of several input data or boundary conditions (surface mass balance, basal sliding, geothermal heat flux) may contribute.

Total ice volumes and areas for the two spin-ups are shown in Table 2 along with their observational counterparts. In line with the discussion above, the volume produced by spin-up #1 matches the observed volume very closely, while the volume produced by spin-up #2 is ～ 8% too large. The ice-sheet area simulated by spin-up #2 is also larger than for spin-up #1; however, in contrast to the ice volume, the result of spin-up #2 is closer to the observation than that of spin-up #1. This is so because the SeaRISE-legacy fixed-topography spin-up #1 is based on older topographic data (surface topography by Bamber (2001), bed topography by Herzfeld et al. (2011, 2012)) that lead to a smaller ice-covered area than the newer data by Bamber et al. (2013).

Table 2: Simulated volume and area of the present-day Greenland ice sheet for InitMIP-Greenland. The simulations are the fixed-topography spin-up #1 and the freely-evolving-topography spin-up #2 carried out with SICOPOLIS (see main text for details). Observational data are also shown (volume by Bamber et al. (2013), area by Kargel et al. (2012)).

	Volume (km^3)	Area (km^2)
Spin-up #1	2.92×10^6	1.66×10^6
Spin-up #2	3.21×10^6	1.86×10^6
Observed	2.96×10^6	1.80×10^6

For the two future climate scenarios ctrl (constant-climate control run) and asmb (schematic SMB anomaly), Fig. 9 depicts the sea-level contribution (initial volume V_{init} minus actual volume V, expressed in sea-level equivalents) of the Greenland ice sheet. As discussed above (Section 3.3), for spin-up #1, ctrl shows a notable drift towards a smaller ice volume (positive sea-level contribution) due to the release of the fixed-topography constraint 100 years before the end of the spin-up. In contrast, for spin-up #2, such a transition shock does not occur, so that the drift is very small. The response of the ice sheet to the asmb forcing is, in absolute terms, ～ 50% larger for spin-up #2 than for spin-up #1, and relative to the respective control run even ～ 85% larger. This demonstrates impressively that, even with the same ice sheet model, different initialisation methods can lead to a major spread of results of future climate

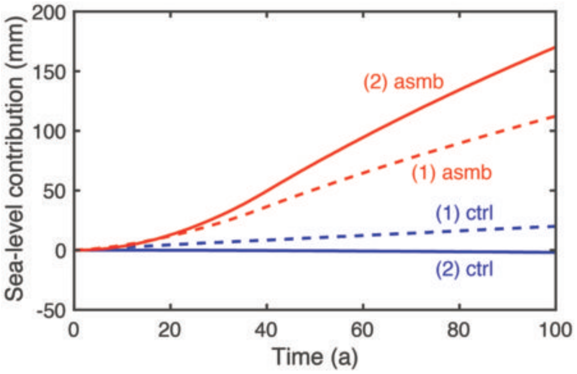

Figure 9 : InitMIP-Greenland future climate runs. Sea-level contribution (due to ice volume change) of the Greenland ice sheet for the runs ctrl (control) and asmb (schematic surface mass balance anomaly). (1) Initialisation by the fixed-topography spin-up #1, (2) initialisation by the freely-evolving-topography spin-up #2.

experiments.

5. Summary and outlook

Climate change constitutes a major challenge for humankind. One of the most severe consequences of climate change is sea level rise, currently (1993–2010) occurring at a global mean rate of 3.2 ± 0.4 mm a^{-1} (IPCC, 2013a), for which the two main contributors are the melting of land ice masses (ice sheets and glaciers) and the thermal expansion of ocean water. The largest potential for future sea level rise lies in the ice sheets of Antarctica and Greenland with their combined volume of ∼ 65 m of sea level equivalent.

Numerical modelling has become an important tool for assessing the response of ice sheets to climate change and thus their contribution to sea level rise. In this paper, we focused on the Greenland ice sheet and reviewed related work conducted with the ice sheet model SICOPOLIS. Within the SeaRISE initiative, SICOPOLIS was part of a group of eight models that were applied to a set of standardised experiments for the Greenland ice sheet. These experiments comprised sensitivity studies to changes in the surface climate, basal sliding and marginal (ocean-induced) melting as well as a combination experiment approximating IPCC's 'business-as-usual' RCP 8.5 scenario. Results of the latter showed that there is potential for a significant decay of the Greenland ice sheet over the next centuries if climate change progresses unabatedly. However, the spread of results across the different models was very large, clearly indicating the need for further efforts in this direction.

Therefore, as a post-AR5 initiative, the scientific community devised ISMIP6, which is still in an early stage. A first sub-project is InitMIP-Greenland, in which the influence of model initialisation on schematic future climate simulations is investigated. Results obtained with SICOPOLIS for two different initialisation methods, namely (1) a spin-up with essentially fixed topography, and (2) a spin-up with freely evolving topography (both run over a full glacial-interglacial cycle) showed that the influence of these different spin-ups on the evolution of the ice sheet in the future is indeed very pronounced. Within the ongoing research project "ProGrIS" (Projecting discharge from the Greenland Ice Sheet using climatic forcings derived from atmosphere-ocean models; Grant-in-Aid for Scientific Research A, provided by the Japan Society for the Promotion of Science (JSPS)), we will therefore continue our efforts towards improving the quality of the spin-up for the Greenland ice sheet with the models SICOPOLIS and IcIES (the latter operated by F. Saito and A. Abe-Ouchi; e.g., Abe-Ouchi et al., 2013). Based on this, we will project the total discharge from the Greenland ice sheet, and thus its contribution to sea level rise, with the models SICOPOLIS and IcIES. In close cooperation with the ISMIP6 community, forcings for the atmospheric and oceanic climate over and surrounding the Greenland ice sheet will be derived from the suite of CMIP6 AOGCM (atmosphere-ocean general circulation model) simulations. These combined efforts will hopefully lead to significantly improved estimates of ice sheet contribution to sea level rise in the coming years.

6. Code and data availability

The ice sheet model SICOPOLIS is available as free and open-source software (under the GNU General Public License) via www.sicopolis.net. The data produced by SICOPOLIS for this study can be obtained by contacting the corresponding author.

Acknowledgements

We thank all organisers and steering committee members of the SeaRISE and ISMIP6 initiatives, in particular Robert A. (Bob) Bindschadler, Sophie Nowicki and Heiko Goelzer, for their efforts in managing these projects. Further, we thank Ayako Abe-Ouchi and Fuyuki Saito for continued, fruitful exchange on ice sheet modelling issues, and the numerous colleagues who have contributed to the development of the ice sheet model SICOPOLIS over the last ～ 20 years. Shin Sugiyama kindly proofread the manuscript.

Ralf Greve was supported by Grants-in-Aid for Scientific Research A (Nos. 22244058, 25241005 and 16H02224) of the Japan Society for the Promotion of Science (JSPS), and by the Green Network of Excellence (GRENE) Arctic Climate Change Research and Arctic Challenge for Sustainability (ArCS) projects of the Japanese Ministry of Education, Culture, Sports, Science and Technology (MEXT). Reinhard Calov was supported by Leibniz Society grant SAW-2014-PIK-1 GreenRise. Support for research of Ute Herzfeld through NASA Cryospheric Sciences awards NNX11AP39G and NNX16AP71G and U. S. National Science Foundation Geography and Spatial Sciences Awards 1553133 and 1553134 (BCS 1504533) is thankfully acknowledged.

References

Abe-Ouchi, A., F. Saito, K. Kawamura, M. E. Raymo, J. Okuno, K. Takahashi, and H. Blatter (2013) Insolation-driven 100,000-year glacial cycles and hysteresis of ice-sheet volume. *Nature,* **500** (7461), 190–193.

Arakawa, A., and V. R. Lamb (1977) Computational design of the basic dynamical processes of the UCLA general circulation model. In: J. Chang (ed.), *Methods in Computational Physics Vol.17,* pp.173–265. Academic Press, New York, NY, USA.

Bamber, J. L. (2001) Greenland 5 km DEM, ice thickness, and bedrock elevation grids, Version 1. NASA National Snow and Ice Data Center Distributed Active Archive Center, Boulder, Colorado, USA. doi: 10.5067/01A10Z9BM7KP.

Bamber, J. L., J. A. Griggs, R. T. W. L. Hurkmans, J. A. Dowdeswell, S. P. Gogineni, I. Howat, J. Mouginot, J. Paden, S. Palmer, E. Rignot, and D. Steinhage (2013) A new bed elevation dataset for Greenland. *Cryosphere,* **7** (2), 499–510.

Bernales, J., I. Rogozhina, R. Greve, and M. Thomas (2017) Comparison of hybrid schemes for the combination of shallow approximations in numerical simulations of the Antarctic Ice Sheet. *Cryosphere,* **11** (1), 247–265.

Bindschadler, R. A., S. Nowicki, A. Abe-Ouchi, A. Aschwanden, H. Choi, J. Fastook, G. Granzow, R. Greve, G. Gutowski, U. C. Herzfeld, C. Jackson, J. Johnson, C. Khroulev, A. Levermann, W. H. Lipscomb, M. A. Martin, M. Morlighem, B. R. Parizek, D. Pollard, S. F. Price, D. Ren, F. Saito, T. Sato, H. Seddik, H. Seroussi, K. Takahashi, R. Walker, and W. L. Wang (2013) Ice-sheet model sensitivities to environmental forcing and their use in projecting future sea level (the SeaRISE project). *J. Glaciol.,* **59** (214), 195–224.

Calov, R., A. Robinson, M. Perrette, and A. Ganopolski (2015) Simulating the Greenland ice sheet under present-day and palaeo constraints including a new discharge parameterization. *Cryosphere,* **9** (1), 179–196.

De Wolde, J. R., P. Huybrechts, J. Oerlemans, and R. S. W. van den Wal (1997) Projections of global mean sea level rise calculated with a 2D energy-balance climate model and dynamic ice sheet models. *Tellus,* **49A**, 486–502.

Enderlin, E. M., I. M. Howat, S. Jeong, M.-J. Noh, J. H. van Angelen, and M. R. van den Broeke (2014) An improved mass budget for the Greenland ice sheet. *Geophys. Res. Lett.,* **41** (3), 866–872.

Greve, R. (1995) *Thermomechanisches Verhalten polythermer Eisschilde - Theorie, Analytik, Numerik.* Doctoral thesis, Department of Mechanics, Darmstadt University of Technology, Germany. Berichte aus der Geowissenschaft, Shaker Verlag, Aachen, Germany.

Greve, R. (1997) Application of a polythermal three-dimensional ice sheet model to the Greenland ice sheet: Response to steady-state and transient climate scenarios. *J. Climate,* **10** (5), 901–918.

Greve, R. (2000) On the response of the Greenland ice sheet to greenhouse climate change. *Clim. Change,* **46** (3), 289–303.

Greve, R., and H. Blatter (2009) *Dynamics of Ice Sheets and Glaciers.* Springer, Berlin etc., Germany.

Greve, R., and H. Blatter (2016) Comparison of thermodynamics solvers in the polythermal ice sheet model SICOPOLIS. *Polar Sci.,* **10** (1), 11–23.

Greve, R., and U. C. Herzfeld (2013) Resolution of ice streams and outlet glaciers in large-scale simulations of the Greenland ice sheet. *Ann. Glaciol.,* **54** (63), 209–220.

Greve, R., F. Saito, and A. Abe-Ouchi (2011) Initial results of the SeaRISE numerical experiments with the models SICOPOLIS and IcIES for the Greenland ice sheet. *Ann. Glaciol.,* **52** (58), 23–30.

Hanna, E., F. J. Navarro, F. Pattyn, C. M. Domingues, X. Fettweis, E. R. Ivins, R. J. Nicholls, C. Ritz, B. Smith, S. Tulaczyk, P. L. Whitehouse, and H. J. Zwally (2013) Ice-sheet mass balance and climate change. *Nature,* **498** (7452), 51–59.

Helm, V., A. Humbert, and H. Miller (2014) Elevation and elevation change of Greenland and Antarctica derived from CryoSat-2. *Cryosphere,* **8** (4), 1539–1559.

Herzfeld, U. C., B. F. Wallin, C. J. Leuschen, and J. Plummer (2011) An algorithm for generalizing topography to grids while preserving subscale morphologic characteristics - creating a glacier bed DEM for Jakobshavn trough as low-resolution input for dynamic ice-sheet models. *Comput. Geosci.,* **37** (11), 1793–1801.

Herzfeld, U. C., J. Fastook, R. Greve, B. McDonald, B. F. Wallin, and P. A. Chen (2012) On the influence of outlet glaciers in Greenland bed topography on results from dynamic ice sheet models. *Ann. Glaciol.,* **53** (60), 281–293.

Hutter, K. (1983) *Theoretical Glaciology; Material Science of Ice and the Mechanics of Glaciers and Ice Sheets.* D. Reidel Publishing Company, Dordrecht, The Netherlands.

Huybrechts, P., and J. Oerlemans (1990) Response of the Antarctic ice sheet to future greenhouse warming. *Clim. Dynam.,* **5** (2), 93–102.

Huybrechts, P., A. Letreguilly, and N. Reeh (1991) The Greenland ice sheet and greenhouse warming. *Palaeo3,* **89**, 399–412.

IPCC (2007) Summary for Policymakers. In: S. Solomon, D. Qin, M. Manning, Z. Chen, M. Marquis, K. B. Averyt, M. Tignor, and H. L. Miller (eds.), *Climate Change 2007: The Physical Science Basis,* pp.1–18. Cambridge University Press, Cambridge, United Kingdom and New York, NY, USA.

IPCC (2013a) Summary for Policymakers. In: T. F. Stocker, D. Qin, G.-K. Plattner, M. Tignor, S. K. Allen, J. Boschung, A. Nauels, Y. Xia, V. Bex, and P. M. Midgley (eds.), *Climate Change 2013: The Physical Science Basis,* pp.3–29. Cambridge University Press, Cambridge, United Kingdom and New York, NY, USA.

IPCC (2013b) *Climate Change 2013: The Physical Science Basis* (eds. T. F. Stocker, D. Qin, G.-K. Plattner, M. Tignor, S. K. Allen, J. Boschung, A. Nauels, Y. Xia, V. Bex, and P. M. Midgley). Cambridge University Press, Cambridge, United Kingdom and New York, NY, USA.

Joughin, I., B. Smith, I. Howat, T. Scambos, and T. Moon (2010) Greenland flow variability from ice-sheet-wide velocity mapping. *J. Glaciol.,* **56** (197), 415–430.

Joughin, I., B. Smith, I. Howat, and T. Scambos (2016) MEaSUREs multi-year Greenland ice sheet velocity mosaic, Version 1. NASA National Snow and Ice Data Center Distributed Active Archive Center, Boulder, Colorado, USA. doi: 10.5067/QUA5Q9SVMSJG.

Kargel, J. S., A. P. Ahlstrøm, R. B. Alley, J. L. Bamber, T. J. Benham, J. E. Box, C. Chen, P. Christoffersen, M. Citterio, J. G. Cogley, H. Jiskoot, G. J. Leonard, P. Morin, T. Scambos, T. Sheldon, and I. Willis (2012) Greenland's shrinking ice cover: "fast times" but not that fast. *Cryosphere,* **6** (3), 533–537.

Khan, S. A., A. Aschwanden, A. A. Bjørk, J. Wahr, K. K. Kjeldsen, and K. H. Kjær (2015) Greenland ice sheet mass balance: a review. *Rep. Prog. Phys.,* **78**, 046801.

Kusahara, K., T. Sato, A. Oka, T. Obase, R. Greve, A. Abe-Ouchi, and H. Hasumi (2015) Modelling the Antarctic marine cryosphere at the Last Glacial Maximum. *Ann. Glaciol.,* **56** (69), 425–435.

Le Meur, E., and P. Huybrechts (1996) A comparison of different ways of dealing with isostasy: examples from modelling the Antarctic ice sheet during the last glacial cycle. *Ann. Glaciol.,* **23**, 309–317.

MacAyeal, D. R. (1989) Large-scale ice flow over a viscous basal sediment: theory and application to ice stream B, Antarctica. *J. Geophys. Res.,* **94** (B4), 4071–4087.

Molnia, B. F. (2004) *Glossary of Glacier Terminology: A Glossary Providing the Vocabulary Necessary to Understand the Modern Glacier Environment.* USGS Open-File Report 2004–1216.

Morland, L. W. (1984) Thermomechanical balances of ice sheet flows. *Geophys. Astrophys. Fluid Dyn.,* **29**, 237–266.

Morland, L. W. (1987) Unconfined ice-shelf flow. In: Van der Veen, C. J. and J. Oerlemans (eds.), *Dynamics of the West Antarctic Ice Sheet.* D. Reidel Publishing Company, Dordrecht, The Netherlands, 99–116.

Nowicki, S., R. A. Bindschadler, A. Abe-Ouchi, A. Aschwanden, E. Bueler, H. Choi, J. Fastook, G. Granzow, R. Greve, G. Gutowski, U. C. Herzfeld, C. Jackson, J. Johnson, C. Khroulev, E. Larour, A. Levermann, W. H. Lipscomb, M. A. Martin, M. Morlighem, B. R. Parizek, D. Pollard, S. F. Price, D. Ren, E. Rignot, F. Saito, T. Sato, H. Seddik, H. Seroussi, K. Takahashi, R. Walker, and W. L. Wang (2013a) Insights into spatial sensitivities of ice mass response to environmental change from the SeaRISE ice sheet modeling project I: Antarctica. *J. Geophys. Res. Earth Surf.,* **118** (2), 1002–1024.

Nowicki, S., R. A. Bindschadler, A. Abe-Ouchi, A. Aschwanden, E. Bueler, H. Choi, J. Fastook, G. Granzow, R. Greve, G. Gutowski, U. C. Herzfeld, C. Jackson, J. Johnson, C. Khroulev, E. Larour, A. Levermann, W. H. Lipscomb, M. A. Martin, M. Morlighem, B. R. Parizek, D. Pollard, S. F. Price, D. Ren, E. Rignot, F. Saito, T. Sato, H. Seddik, H. Seroussi, K. Takahashi, R. Walker, and W. L. Wang (2013b) Insights into spatial sensitivities of ice mass response to environmental change from the SeaRISE ice sheet modeling project II: Greenland. *J. Geophys. Res. Earth Surf.,* **118** (2), 1025–1044.

Nowicki, S. M. J., A. Payne, E. Larour, H. Seroussi, H. Goelzer, W. Lipscomb, J. Gregory, A. Abe-Ouchi, and A. Shepherd (2016) Ice Sheet Model Intercomparison Project (ISMIP6) contribution to CMIP6. *Geosci. Model Dev.,* **9** (12), 4521–4545.

Ridley, J. K., P. Huybrechts, J. M. Gregory, and J. A. Lowe (2005) Elimination of the Greenland ice sheet in a high CO_2

climate. *J. Climate,* **18**, 3409–3427.

Rignot, E., S. Jacobs, J. Mouginot, and B. Scheuchl (2013) Ice-shelf melting around Antarctica. *Science,* **341** (6143), 266–270.

Robinson, A., R. Calov, and A. Ganopolski (2010) An efficient regional energy-moisture balance model for simulation of the Greenland Ice Sheet response to climate change. *Cryosphere,* **4** (2), 129–144.

Robinson, A., R. Calov, and A. Ganopolski (2012) Multistability and critical thresholds of the Greenland ice sheet. *Nat. Clim. Change,* **2** (6), 429–432.

Saito, F., A. Abe-Ouchi, K. Takahashi, and H. Blatter (2016) SeaRISE experiments revisited: potential sources of spread in multi-model projections of the Greenland ice sheet. *Cryosphere,* **10** (1), 43–63.

Shepherd, A., E. R. Ivins, G. A, V. R. Barletta, M. J. Bentley, S. Bettadpur, K. H. Briggs, D. H. Bromwich, R. Forsberg, N. Galin, M. Horwath, S. Jacobs, I. Joughin, M. A. King, J. T. M. Lenaerts, J. Li, S. R. M. Ligtenberg, A. Luckman, S. B. Luthcke, M. McMillan, R. Meister, G. Milne, J. Mouginot, A. Muir, J. P. Nicolas, J. Paden, A. J. Payne, H. Pritchard, E. Rignot, H. Rott, L. S. Sørensen, T. A. Scambos, B. Scheuchl, E. J. O. Schrama, B. Smith, A. V. Sundal, J. H. van Angelen, W. J. van de Berg, M. R. van den Broeke, D. G. Vaughan, I. Velicogna, J. Wahr, P. L. Whitehouse, D. J. Wingham, D. Yi, D. Young, and H. J. Zwally (2012) A reconciled estimate of ice-sheet mass balance. *Science,* **338** (6111), 1183–1189.

Van den Broeke, M., J. Bamber, J. Ettema, E. Rignot, E. Schrama, W. J. van de Berg, E. van Meijgaard, I. Velicogna, and B. Wouters (2009) Partitioning recent Greenland mass loss. *Science,* **326** (5955), 984–986.

Vaughan, D. G., J. C. Comiso, I. Allison, J. Carrasco, G. Kaser, R. Kwok, P. Mote, T. Murray, F. Paul, J. Ren, E. Rignot, O. Solomina, K. Steffen, and T. Zhang (2013) Observations: Cryosphere. In: T. F. Stocker, D. Qin, G.-K. Plattner, M. Tignor, S. K. Allen, J. Boschung, A. Nauels, Y. Xia, V. Bex, and P. M. Midgley (eds.), *Climate Change 2013: The Physical Science Basis,* pp.317–382. Cambridge University Press, Cambridge, United Kingdom and New York, NY, USA.

低温科学 75 （2017） 131-141
doi: 10.14943/lowtemsci. 75. 131

The human dimension of climate change research in Greenland: Towards a new form of knowledge generation

Naotaka Hayashi[1]*

Received 24 January 2017, accepted 30 January 2017

In the field of climate change research, social sciences have lagged behind natural sciences and have not yet mustered enough recognition from the public. Studies on the human dimension of climate change commonly use the concepts of 'vulnerability' and 'resilience'. The 'resilience' approach investigates the capacity of a community that absorbs environmental disturbances, so as to retain essential social, cultural, and economic structures, while the 'vulnerability' approach seeks to identify factors that make the community in question vulnerable to ongoing or future climate change. The term 'resilience' tends to give an impression that a system may remain static, and because of this, I adopt the term 'vulnerability' in this essay. 'Vulnerability' does not mean that Arctic communities are always "vulnerable" to environmental changes but may be negatively impacted by the associated social and political changes. Accordingly, vulnerability means the social and political "characteristics" of the community that is experiencing the changes. This concept helps researchers direct their attention not only to environmental changes, but also to the societal situation of the community. In the second half of this essay, I exemplify how the vulnerability approach works, drawing data from my fieldwork conducted in Siorapaluk, in 2009. More local communities want scientific data in order to plan a course of action and to shape their political and economic policies in the rapidly changing environment. In future, it will be increasingly important for natural scientists to work closely with local communities, and this may lead to a new form of knowledge generation.

気候変動といえば自然科学の分野が先行し，社会科学的調査の認知度は低い．社会科学の分野には，「復元性（resilience）」と，「脆弱性（vulnerability）」に注目する手法がある．復元性とは，環境攪乱がおきても，社会，文化，経済構造を維持できる地域の包容力であり，脆弱性とは，調査地が現在または未来の気候変動に対して，脆弱になる可能性である．「復元性」という言葉は，社会が変わらないという印象を与えるため，筆者は，脆弱性に注目した手法を本稿で解説する．脆弱性という言葉は，北極圏に住んでいる人たちが，単に環境変化に「脆弱である」という意味ではなく，環境変化に伴っておきる社会的，経済的，政治的変化に対応できないために，脆弱になるということを意味している．つまり，「脆弱性」とは，変化にさらされている調査地の社会的，政治的「特徴」を表していると考えてよい．この概念は，環境変化だけでなく，調査地の社会状況をも考慮する必要性を喚起する．後半では，筆者が2009年に行ったシオガパルクでの現地調査を紹介し，気候変動の社会科学的な調査がどのように行われたか解説する．現在，多くの町や村では，将来の政治経済方針や事業方針を定めるのに有用な科学的データが必要とされている．今後，自然科学者はますます，調査地の社会と連携を図る必要性が出てくるであろう．そしてそれは，新しい知識の形成に繋がるのである．

---

*Corresponding author
e-mail：naotaka.hayashi@ucalgary.ca

1）Department of Anthropology and Archaeology, University of Calgary, Calgary, Canada

キーワード：脆弱性，回復性，現地観察，地域密着型研究，知識形成
Vulnerability, resilience, local observation, community-based research, knowledge generation

1. Introduction

The purpose of this essay is to introduce the study of the human dimension of climate change, along with commonly used ‘vulnerability’ and ‘resilience’ approaches in this field, to review the relevant existing literature, and to make suggestions to natural scientists working in Greenland on climate change research.

2. The social dimension in climate change research

2.1 Changing Arctic environment

When it comes to climate change in the Arctic, people’s attention tends to be directed towards changes in the natural environment. For example, the summer of 2012 saw an extreme melt, in which almost the entire surface of the Greenland ice sheet started to melt, and this continued over four days. According to researchers, this phenomenon was a first in the past 120 years (Nghiem et al., 2012). The most striking feature of Greenland is snow and ice; these are dwindling. The Arctic environment is definitely changing at a much faster pace than was expected.

2.2 As climate changes, so does people’s life: An example from Ilulissat

These changes matter for natural scientists, but for us who live a life on the planet of the Earth, the question to be asked is: “What is going to happen next, if snow and ice continue to melt?” Unless the change is not affecting our life, we do not necessarily care about that. For example, during my stay in Greenland in 2008, I heard that local fishers in Ilulissat were having trouble fishing halibut because hooks and baits were more often washed away by sediments discharged by the melting glaciers (see also Mølgaard, 2007). Scientific reports produced by glaciologists indicate that Jakobshavn Glacier is flowing faster and is calving more ice into the ocean (Holland et al., 2008). Putting together this kind of scientific reports with local stories, it clearly shows that as the environment changes, people’s livelihoods are going to be significantly affected by them. This is more important to deal with, and this is the question that social scientists are tackling.

2.3 Physical environmental change ── ecological change ── human impacts

Internationally speaking, the human component in climate change studies lagged behind natural sciences such as climatology, glaciology, marine sciences, and geology. Much attention was, but still now is, paid to the impacts on the natural environments. In 1990, the Intergovernmental Panel on Climate Change (IPCC) produced one volume separately, as part of their first assessment report, on the social implications of climate change. It was around this period that the journal of *Global Environmental Change* was established, which covers wide ranging issues of social impacts of climate change. In the beginning of the 21st century, the human dimension of climate change began to draw more attention from the international arena. The Millennium Ecosystem Assessment (MEA), a project triggered by a speech given by then Secretary-General of the United Nations, Kofi Annan, in 2000, concluded in 2005 that the change in the ecosystem will very likely impact the livelihoods of Arctic communities (Chapin et al., 2005). Also, in a similar fashion, the Arctic Climate Impact Assessment (ACIA), carried out under the auspices of the Arctic Council and the International Arctic Science Committee (IASC), emphasized implications of climatic change on human society (Huntington et al., 2005; Nuttall et al., 2005). The latest version of knowledge synthesis on the human dimension of climate change can be available at the IPCC website. The Working Group II of the Fifth Assessment Report is specialized for the social implications of climatic and environmental changes (https://www.ipcc.ch/report/ar5/wg2/). In these reports, the mechanism of climate change impact was laid out that changes in the physical environment (such as the climatic system) will lead to ecosystem changes, and subsequently be translated into societal changes.

2.4 Adaptation in climate change studies

Although still being debated in a political arena, among natural scientists a consensus was already made that climate is changing (Oreskes, 2004). Furthermore, scientists have reached a common understanding that the Earth's climate has been affected by human activities and that the rate of change is unexpectedly faster. By 2006, in academia, whether climate was changing owing to human activities or a natural cycle was no longer a question. The focus in climate change studies had been shifted to a question of whether we can possibly adapt to the changing climate. The arising theme was "adaptation" to climate change, and "sustainable development" began to be discussed in the context of climate change.

2.5 Japanese research in the international arena in climate change studies

Japan has lagged behind the international arena. As late as 2015, as part of a new national-flagship ArCS (Arctic Challenge for Sustainability) project, one research project team (led by Dr. Sugiyama) included the social component in their research objectives to tackle with environment change problems along with this vein.

3. Research framework

3.1 Various impacts in different places

What we first keep in mind is that the impact of climate change varies from place to place. Accordingly, it is not prudent to make a sweeping generalization about influences of climate change. A certain impact in one place may be manifested differently in other areas. Greenland is the world's largest island, and the distance between the northern and the southern tips of Greenland is the same as the distance between Sapporo of Japan and Taipei of Taiwan. It is not reasonable to think of the weather of Taipei with reference to that of Sapporo. In North Greenland, the sea is covered by sea ice for extended winter months, and dogsleds are important for local people for hunting and transporting. Yet, in South Greenland, where the sea freezes, locals drive a car on the ice. (Actually, by law, one is not allowed to keep sled dogs south of Disko Bay.) As one passes down the Arctic Circle, bushes and trees start to appear. Willows and birches form bushes in the inner parts of the fjords in South Greenland. Some lands are arable; it is possible to grow crops such as potatoes and turnips; and there are about forty sheep farms along the shorelines of the inner fjords. Even plantation (mainly spruce trees transplanted from Alaska) has been promoted since the 1950s in South Greenland (Ødum, 1990; Hayashi, 2011).

Climate change has been manifesting differently, reflecting differences between these areas. In 2007, I heard that a hunter in Qeqertarsuaq, Disko Bay, sold off his sled dogs because as climate became warmer, the mushing season was becoming shorter. This means that he decided to stop hunting.

On the other hand, a warming temperature has made it possible for sheep farmers to grow more crops in South Greenland. The local agricultural advisory office indicates that sheep farmers in South Greenland produced over 100 tons of potatoes in 2012 and 2013 (Frederiksen, 2015). In the 1970s, it was not possible to grow potatoes in the region, but now vegetable growing is promising. The agricultural experimental station in Upernaviarsuk has been continuing experiments to grow lettuces, turnips, and even strawberries (KNR, 2011).

Another example for a positive impact of climate change may be fishing in South Greenland. Cod fishing collapsed in the 1970s due to a decline in the sea water temperature, but people are expecting that cod are coming back to the Greenland water due to the current warming trend. They began to see species that had never appeared in Greenland's coast such as mackerel (Tallaksen, 2014).

The media are usually quick to snatch these "hot spots" in climate change. *The New York Times* published an article with a headline "Climate Change Greens up Greenland" (Lyall, 2007). It described how sheep farmers might benefit by a warming trend because more hay could grow faster. The *National Geographic* featured Greenland in a similar vein in its volume of "Greenland: ground zero for global warming" (Folger, 2010). Yet, a closer look at the local community revealed that the impact of climate change was not so simple as generally thought (Hayashi, n.d.). My long-term fieldwork clarified that farmers are suffering from drier summers, being unable to produce enough winter fodder. In fact, a couple of sheep farmers closed their farms due to the changing climate conditions, economic problems, or perhaps a change in their course of action.

3.2 Societal factors for the manifestation of climate change

As outlined above, the influence of climate change varies from place to place. Yet, it is not only physical and ecological conditions, but also societal factors that influence local manifestation of climate change. Sociocultural and political contexts are intertwined with natural phenomenon to create very complicated impacts on local communities. Here lies the difficulty of the study of the human dimension of climate change. For example, even though the same level of earthquakes hit two similar environments, people who live in the areas may not have the same impact. At one place, where buildings were designed to cope with quakes and residents were well trained to evacuate, residents are likely to be inflicted less than those in another area that are not like that. This is because social, cultural, political, technological conditions of a locality inform the degree of the impact of environmental change (Fisher and Feinman, 2005). In another words, societal characteristics of the place in question matter. Therefore, climate change is not just an environmental disaster, but also a human-caused disaster.

3.3 Theoretical framework in the human dimension of climate change

When looking into journals on the human dimension of climate change or natural disasters, such as *Global Environmental Change* and *Ecology and Society*, one soon runs into technical terms such as 'vulnerability' and 'resilience'. These two terms indicate the concepts that have often been used in this research field. The resilience approach looks into characteristics of the community that absorb disturbances, so as to retain essential social, cultural, and economic structures (Adger et al., 2005), while the vulnerability approach tries to identify factors that make the community in question vulnerable towards ongoing or future climate change (Kelly and Adger, 2000). Simply speaking, these concepts are used in the same context, and it is just that researchers are seeing communities from opposite directions. If increasing the resilience, it means that a community has reduced its vulnerability towards a harm, and by reducing vulnerability, it can build a resilient community in the course of climate change. Basically, these concepts are based on a systems thinking, and human society and the environment in which the society is located are viewed as systems, and these are interlocked. It is meaningless to determine which approach is better, but for the following reasons, I use the vulnerability concept in this essay. I hasten to add that I do not blindly support vulnerability approach.

Originally, the concept of resilience was brought from ecology, in which an ecological system tries to organize itself around a single equilibrial state. When receiving a disturbance such as a fire, an ecosystem like a boreal forest is supposed to bring itself back to the original state. The Canadian zoologist and ecologist C. S. Holling developed this idea and applied it to human society (Holling, 1986, 2001). According to his "panarchy" doctrine, there could be several equilibrial states, and an ecosystem at one stable point can jump to another stable point when recovering itself after a disturbance (Gunderson and Holling, 2002). So does a human society. When disturbed, a society may catastrophically collapse, but with resources that it can resort to (technology, knowledge, social institutions, or collective actions), a society can rebuild itself like the same way as they were or in a different way (Folk et al., 2003). As seen in the websites of the Resilience Alliance and the journal *Ecology and Society*, social scientists such as Fikret Berkes, Carl Folke, Elinor Ostrom and Brian Walker extended this ecological thinking to the study of environmental change. The concept as such is very informative and inspiring when seeing the interaction between humans and the environment in which they live and when thinking of environmental change from the wider perspective (Walker and Salt, 2006, 2012); however, I think that this term is prone to emphasize that a system tries to remain static. Arctic landscapes are always changing, and it is not comprehensible to think that a system, ecological or social, remains at a stable point. The vulnerability approach may give more practical insights when constructing a problem-solving approach towards climate change research.

The concept of vulnerability was developed in the fields of natural disaster studies, human geography, and sustainability science (Wisner et al., 2004). It is not within the scope of this essay to review the development of the vulnerability concept. In 2003, Turner and his colleagues (2003) outlined the coupled human-environment systems model with a tangible diagram. This model facilitates the capture reciprocal interactions between humans and the environment and influences of the feedback from the environment on human society and vice versa. This model and the associated idea can be seen in the MEA (Kasperson et al., 2005) and the ACIA (McCarthy et al., 2005). Already, a forerunner of this model can be seen in the Third Assessment Report of IPCC (McCarthy et al., 2001). An extensive review on the development of the vulnerability conceptis done by W. Neil Adger (Adger, 2006), who is also one of the leading scholars in the field of *Global Environmental Change* and has been working in Southeast Asia.

At present, the Climate Change Adaptation research group at McGill University, led by James Ford (http://www.jamesford.ca/), is a leading research team in the vulnerability study, conducting extensive research in NWT and Nunavut (Ford et al., 2015).

What was new about the vulnerability approach was that it turned over the conventional notion of vulnerability. When it comes to the assessment of the vulnerability of a community towards the current and future climate change, it will often start with a projection of a future climate trend, move to the biophysical impacts studies, proceed to the identification potential adaptive options for the community, and will finally define any residual, adverse consequences as “social vulnerability” (Adger and Kelly, 1999; Kelly and Adger, 2000). In other words, natural scientists tend to place social vulnerability at the end point of their impact assessment.

Two points need to be made for this type of scientific assessment. First, this type of assessment is based on predicted future climate changes. The physical system of the Arctic region is dynamic, and even with advanced atmosphere-ocean general circulation models (AOGCMs), it is not possible to predict precisely the dynamics of the atmospheric and ocean currents that interact within and outside the region in a complex way. Therefore, this dynamism limits our understanding of the climate system. Now that it is widely regarded that the reduction of CO_2 emission from industrial activities prevents global warming, a primary driving force behind the work of the IPCC is to mobilize the broader community, and to put pressure on political arena. (This seems obvious when looking at summaries of its assessment reports, in which plain language, such as “very likely”, are used.) Yet, because of a sense of uncertainty and doubt that reside in any well-crafted climate scenarios, it is hard to convince policymakers to take an appropriate action to combat anthropogenic change. Truly, there are a lot of possibilities that concrete numeric values derived from research, such as “+3℃” and “next 50 years”, convince politicians; however, (natural) climate sciences have a limitation. Consequently, it is becoming more important to show local situations, where Arctic communities are actually being affected by climate change.

Second, as discussed above, since mitigation measures and coping options are selected based on predicted scientific scenarios, these do not always fit the actual situation of the community in question. Accordingly, mitigation and coping measures need to be determined by actually observing actual situations of Arctic communities.

Taking into account these two points, if we see a community actually being exposed to ongoing climate change, we can see that residents there are not just “passive actors” in the course of climate change, but that they are actively responding to unusual weather patterns and climate anomalies (Duerden, 2004). When exposed, individuals and groups in the affected community begin to cope with changes in a short term, by making use of a bundle of social resources, and their action will develop into the long-term adaptation to reduce vulnerability. Therefore, it appears that it is not appropriate to see vulnerability as a residue derived from the adaptation process. Accordingly, social scientists stopped placing “vulnerability” at the endpoint of the assessment, but began to view that vulnerability resides in a community before it goes through climate change (Kelly and Adger, 2000). In other words, vulnerability means the pre-existing constraints that limit the capacity to respond (the “adaptive capacity” often used in *Global Environmental Change*) to external environmental changes (“stress” and “stressor” often used in GEC). By defining vulnerability like this, we can start research by actually observing the current (vulnerable) state of a community.

This conceptual shift has brought researchers' attention to actually observing a community. Here I organize terms that I have used above. 'Coping' is the action that takes place within existing structure (e.g., production systems), while 'adaptation' is changing the framework within which coping takes place (Adger and Kelly, 1999). Coping is rather a bundle of short-term responses to a situation that threatens livelihood systems, while coping may develop into long-term adaptation. Therefore, a short-term 'coping' and long-term 'adaptation' are processes that human-environment systems go through environmental changes, while 'resilience' and 'vulnerability' are associated with the capacity of systems in the course of the changes (Eriksen et al., 2005).

A community has resources (or assets) that can be used for coping with and adapting to environmental changes. Vulnerability is the potential to adversely affect a community's capacity to respond to the changes (Adger, 2000). As discussed above, resources include knowledge, techniques, technologies, local regulations and institutions, human networks, and infrastructure (Adger, 2003). Yet, there are resources that a community lacks, or factors that constrain local efforts from adapting to changes. A constellation of these resources and constraints is termed 'vulnerability', and what needs to be emphasized is that the constellation is conditioned by societal, political, and economic situations of the subject community. According to the vulnerability approach, in order to assess the impact of climate change, researchers only need to identify the above-mentioned resources and constraints (Pearce et al., 2010). In this respect, I have stated above that the vulnerability concept is more practical and more suitable for a problem-solving research. I suspect that by streamlining a research approach, other factors that inform local residents' responses, such as an historical context of a community, environmental and temporal perceptions of residents, may elude from the research framework. Yet, the vulnerability approach is significant in that it directs our attention to the current conditions of local communities. For example, livelihoods, food security, and social well-being are closely related to societal, political, and economic contexts of a community (Gerlach et al., 2011), and these are significantly affected by climate change. The vulnerability approach has brought these issues under the examination of climate change.

4. Observations at Siorapaluk

4.1 Siorapaluk

Drawing a concrete example, let me show how the study of the human dimension of climate change can be conducted with a vulnerability approach (Hayashi, 2015). I conducted my fieldwork in Siorapaluk in the spring of 2009. Siorapaluk is the northernmost village in Greenland, located north of Qaanaaq, North Greenland.

In this village, there were more dogs than residents in 2009 (some 70 residents to over 200 dogs). This fact shows how important dogsleds are for hunting and transportation. Hunting is deeply rooted in the culture of North Greenland. In other words, hunting is an integral part of local people's lives.

4.2 A rising trend in temperature

Recently in this village, dramatic changes are being observed in the climate and the ecosystem. First of all, the temperature has risen by 2–3℃ (Danmarks Meteorological Institut [DMI], n. d.). When I visited Siorapaluk on April 30, 2009, the sea north of the village was already open. When hunting, two hunters hauled a motorized vessel by their dogsled to the edge of the ice, and then they changed vehicles from dogsleds to the boat. After a couple of hours of sailing to the north, they shot two walruses basking in the sunlight on the ice floe from the boat. Here, I found a notable change in the way the local residents hunt walruses.

During the 1970s, the sea used to freeze in late October and the ice would continue to cover the sea until June and even July (Iwashita, 1977). This means that local hunters could use dogsleds for seven to eight months for hunting, until late spring.

Traditionally, walrus is an important animal in this village. A walrus which may weigh 1,200 kg when maturing is a very important source of food for humans and dogs (Born, 2005). When hunting walrus, a couple of hunters would be teamed up, travelling by dogsled to

Table 1 : Hunting seasons for various animals in Siorapaluk, North Greenland

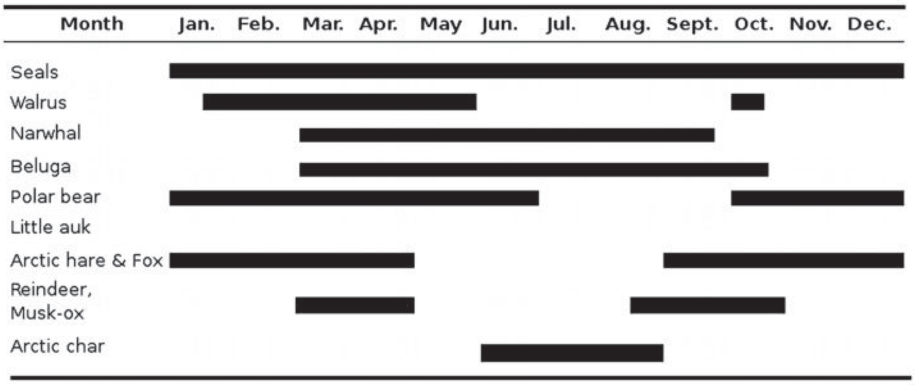

The table shows *potential* hunting seasons for several animals. Theoretically speaking, walrus can be hunt during winter months, but now hunters hunt only in spring. Therefore, the walrus hunting season was shortened from five months to one month. N. B. Compiled based on data obtained in 2015.

search for a breathing hole, wait for an animal to surface, and would harpoon it by the breathing hole (Iwashita, 1978; Ôshima, 1989). Yet, this is not the case any more. At present, the sea does not freeze until mid-December, while the sea ice starts to break up in late April. Unstable sea ice deters local hunters from mushing even during cold winter months. Consequently, nowadays, local hunters go hunting only in spring by boat. In other words, walrus is the one hunters kill on the sea, rather than on ice. Virtually, the hunting season for walrus was reduced from four months (February to May) to one month (May). Therefore, changing climate has changed the way local hunters procure animals.

As this shows, a temperature rise has significant implications for the environment —— namely, later freeze-up and early thaw. What is often reported is that these changes immediately make the winter hunting period shorter, make travel on ice dangerous, and make access to some living resources difficult. It can be said that local hunters are “victims” of climate change (Huntington et al., 2005). Let us look at closely this phenomenon. Table 1 shows hunting seasons for different animals in this village (Hayashi, n. d.). According to this table, it is clear that local hunters have a wide range of hunting options.

If it is difficult to hunt walruses, they can hunt seals because seals are accessible all year around. If hunting on ice is difficult, they can hunt reindeer and musk-ox on land. Other terrestrial animals such as fox and Arctic hare are still accessible. As for dragging a boat for walrus hunting, if viewed from a different angle, it can be thought that local hunters are flexible enough to change a means of transportation and travelling routes. Local hunters are vigilant and careful enough to avoid a dangerous situation, so that they hunt walrus only in spring these days. That said, I do not mean that climate change and the associated environmental changes are not significant. The point being here is local people’s flexibility, adaptability, and ingenuity that take part in local climate change. Hunters are not just vulnerable to a changing environment. The coping strategy of hunters is mainly based on flexibility.

4.3 Traditional ecological knowledge (TEK)

What makes it possible for local hunters to exercise these abilities is their precise understanding of the local environment. Through a long-term observation of the landscape, local residents have accumulated a breadth of environmental knowledge (Freeman and Carbyn, 1988; Inglis, 1993). Some environmental knowledge are passed on from previous generations, and some kinds of knowledge are shared by fellow hunters. This is what is often called traditional environmental knowledge (TEK). The word “traditional” may be elusive and may make the readers misunderstand the scope of TEK. By actually engaging in their surroundings through hunting and everyday life, they have learnt how things work and how to live fully and effectively in their environment (Wenzel, 1999; Usher, 2000). Therefore, TEK is not about old knowledge, but TEK is one constantly being updated, modified, and readjusted, according to a changing environment (Stevenson, 1996). This knowledge guides locals through their life and livelihood.

4.4 Other TEK examples

For example, in narwhal hunting, they decided not to use motorized vessels for hunting within the fjords of Qaanaaq in order to avoid scaring the narwhals and other animals (Lykke Thomsen, 1993). In addition, municipal bylaws require hunters to harpoon (with a rope at the other end) before shooting because the shot animals will sink immediately. A sunken animal will be wasted and is bad for the ecosystem. Like this, hunters have set up local regulations to keep a healthy animal stock. This is the case in dogsleding. As snowmobiles make a big noise to disturb animals, they have regulations prohibiting the use of snowmobiles for hunting (Born, 2008). These examples show that local hunters are knowledgeable about ecological processes and how they can maintain animal populations and the environment.

4.5 Assets and constraints: From a vulnerability point of view

These TEK and local environmental regulations based on TEK are good examples of resources and assets (social capital) that can be used for coping with climatic and environmental changes.

What the vulnerability approach tries is to find what constrains local effort to cope with and adapt to environmental changes. It has been a long time since the Greenland government introduced the quota system to hunting in the area. When I talked to local hunters, many complained about the introduction of this not because they are egoistic but because annual allowable hunts are not reasonably established.

The levels of allowable hunt are determined unilaterally by biologists' (i.e., natural scientists') recommendations, with little input from local residents. Consequently, the quota system is not so much useful for maintaining a balance between animal conservation and local households' economy. Here we can see a chasm between local hunters and natural sciences. I have stated above that the hunting season for walruses has been shortened from four months to one months. This is not just because of climate change. Since the walrus quota is so strict, hunters will max out their allowable hunt in a couple of hunting trips. Consequently, they do not need to take the risk of going out to unstable ice in the winter. They only need to go out to the sea by boat in spring (Hayashi, n.d.).

Another constraint is anti-sealskin campaigns in Europe (Wenzel, 1991). The harmed image of hunting seal has significantly affected the import of animal furs in European countries. Because of this, the Greenland national tannery could not clear the stockpile. When I was staying in 2009, the tannery stopped buying furs from hunters throughout Greenland for two months. Hunters earn money by selling sealskins to the tannery, and the two-month closure of the tannery was detrimental to many households in Greenland. Therefore, in order to facilitate hunters to cope with climate change, it is needed to provide a system or regulations to get rid of this kind of constraints. This kind of perspective cannot be drawn if only look at climate and environmental changes. As discussed above, constraints are conditioned by social, political, and cultural situations of a community. The vulnerability approach help understand the nature of constraints to local adaptation to climate change.

5. Concluding remarks

As demonstrated above, this essay has tried to clarify the importance of the observation of a local community that is actually experiencing climate change. In order to effectively combat a local manifestation of global climate change, it is necessary to see what climate change really means to local residents, and how it is intertwined to a local situation to create social, political, and economic problems for residents.

Recently, more communities are engaging in scientific research projects in the Arctic. This means that more communities want to participate in decision-making processes and two-way communications with authorities such as government. Also, they expect scientists to provide useful data and recommendations to mobilize authorities. This is why community-based research is becoming more important these days, and in near future (natural) scientists working in Greenland, such as researchers from the Institute of Low Temperature Science, will need to work more closely with local residents in their research projects, and this may lead to a new form of knowledge generation.

Acknowledgements

I acknowledge the invitation to the international workshop "Greenland ice sheet mass loss and its impact on global climate change" under the ArCS (Arctic Challenge for Sustainability) Project, the SIGMA (Snow Impurity and Glacial Microbe effects on abrupt warming in the Arctic) project and the Joint Research Program of the Institute of Low Temperature Science, Hokkaido University. This paper draws on my PhD dissertation at the University of Alberta, Canada, and my recent research project at the University of Calgary. My doctoral research project was financially supported by the Social Sciences and Humanities Research Council of Canada (SSHRC), the Faculty of Graduate Studies and Research (FGSR) of the University of Alberta (U of A), the Canadian Circumpolar Institute (CCI) of the U of A, and the then Department of Indian and Northern Affairs of Canada (DINAC). My recent research was funded by the University of Calgary internal research grants. I am grateful to the hunters in Siorapaluk and Qaanaaq for their kindness and patience during the interviews, despite my poor western Greenlandic (*Sioarapalummi Qaanaamilu piniartunnut qujanarujussuaq oqaloqatigiik-katta silaannaap allangoriantornera pillugit!*). Dr. Robert MacDonald helped me shape the structure of this paper.

References

Adger, W. N. (2000) Social and ecological resilience: Are they related? *Prog. Hum. Geog.*, **24**, 347–364.

Adger, W. N. (2003) Social capital, collective action and adaptation to climate change. *Econ. Geogr.*, **79**, 387–404.

Adger, W. N. (2006) Vulnerability. *Global Environmental Change*, **16**, 268–281.

Adger, W. N., T. P. Hughes, C. Folke, S. R. Carpenter, and J. Rockström (2005) Social-ecological resilience to coastal disasters. *Science*, **309**, 1036–1039.

Adger, W. N., and P. M. Kelly (1999) Social vulnerability to climate change and the architecture of entitlements. *Mitig. Adapt. Strateg. Glob. Change*, **4**, 253–266.

Born, E. W. (2005) *The Walrus in Greenland*. Ilinniusiorfik Education, Nuuk, Greenland.

Born, E. W. (2008) *The White Bears of Greenland*. Ilinniusiorfik Education, Nuuk, Greenland.

Chapin, F. S., III, M. Berman, T. V. Callaghan, P. Convey, A. S. Crépin, K. Danell, H. Ducklow, B. Forbes, G. Kofinas, A. D. McGuire, M. Nuttall, R. Virginia, O. Young, and S. A. Zimov (2005) Polar systems. In: R. M. Hassan et al. (eds.) Ecosystems and Human Well-Being: Current State and Trends, Volume 1: Findings of the Condition and Trends Working Group of the Millennium Ecosystem Assessment, 717–743. Island Press, Washington, DC.

Danmarks Meteorologiske Institut (DMI) (n.d.) *Vejret i Grønland*. http://www.dmi.dk/dmi/index/gronland.htm

Duerden, F. (2004) Translating climate change impacts at the community level. *Arctic*, **57**, 204–212.

Eriksen, S. H., K. Brown, and P. M. Kelly (2005) The dynamics of vulnerability: Locating coping strategies in Kenya and Tanzania. *Geogr. J.*, **171**, 287–305.

Fisher, C. T., and G. M. Feinman (2005) Introduction to landscapes over time. *Am. Anthropol.*, **107**, 62–69.

Folger, T. (2010) The changing face of Greenland: Viking weather. *Natl. Geogr.*, **217**, 48–67.

Folke, C., J. Colding, and F. Berkes (2003) Synthesis: Building resilience and adaptive capacity in social-ecological systems. In: F. Berkes et al. (eds.) Navigating Social-Ecological Systems: Building Resilience for Complexity and Change, 353–387. Cambridge University Press, Cambridge, UK.

Ford, J. D., G. McDowell, and T. D. Pearce (2015) The adaptation challenge in the arctic. *Nat. Clim. Change*, **5**, 1046–1053.

Frederiksen, A. (2015) *Siunnersortit ulluat 2015*. Unpublished manuscript.

Freeman, M. M. R., and L. N. Carbyn (Eds.) (1988) *Traditional Knowledge and Renewable Resource Management in Northern Regions*. Boreal Institute for Northern Studies, University of Alberta, Edmonton, AB, Canada.

Gunderson, L. H. and C. S. Holling (2002) *Panarchy: Understanding Transformations in Human and Natural Systems*. Island Press, Washington, DC.

Gerlach, S. C., P. A. Loring, A. Turner, and D. E. Atkinson (2011) Food systems, environmental change, and community needs in rural Alaska. In: A. L. Lovecraft, and H. Eicken (eds.) *North by 2020*, 89–109. University of Alaska Press, Fairbanks, AK.

Hayashi, N. [林直孝] (2011) Jisedai ni kanôsei wo tsunageru kôdô [次世代に可能性をつなげる行動 ── 南グリーンランドの植林事業 ──]. *Hôppô Ringyô[北方林業]*, **63**, 341–345.

Hayashi, N. (2015) Environmental knowledge in motion: Ingenuity and perseverance of hunters among north Greenland. In: S. Böhm et al. (eds.) Ecocultures: Blueprints for Sustainable Communities, 62–77. Routledge, London, UK.

Hayashi, N. (n.d.) It's climate change... but it's more than that: Political ecology of walrus hunting and sheep farming in

Greenland. [under review]

Holland, D. M., R. H. Thomas, B. deYoung, M. H. Ribergaard, and B. Lyberth (2008) Acceleration of Jakobshavn Isbrae triggered by warm subsurface ocean waters. *Nat. Geosci.*, **1**, 659–664.

Holling, C. S. (1986) The resilience of terrestrial ecosystems: Local surprise and global change. In: W. C. Clark and R. E. Munn (eds.) *Sustainable Development of the Biosphere*, 292–320. Cambridge University Press, Cambridge, UK.

Holling, C. S. (2001) Understanding the complexity of economic, ecological, and social systems. *Ecosystems*, **4**, 390–405.

Huntington, H. P., Weller, G., Bush, E., Callaghan, T. V., Kattsov, V. M., & Nuttall, M. (2005) An introduction to the arctic climate impact assessment. In: C. Symon, L. Arris & B. Heal (Eds.) *Arctic Climate Impact Assessment (ACIA)*, 1–19. Cambridge University Press, Cambridge, UK.

Inglis, J. T. (ed.) (1993) *Traditional Ecological Knowledge: Concepts and Cases*. International Program on Traditional Ecological Knowledge and International Development Research Centre, Ottawa, ON, Canada.

Iwashita, K. [岩下莞爾] (Dir.) (1977) Hyôgaki ni idonda 415 nichi *[氷河期に挑んだ415日]*. [Motion Picture] Nippon Television Network Corporation [日本テレビ], Tokyo. [in Japanese].

Iwashita, K. [岩下莞爾] (eds.) (1978) *Esukimô no michi [エスキモーの道：地球最北の村・4年間の記録]*. Nippon Television Network Corporation [日本テレビ], Tokyo.

Kasperson, R. E., K. Dow, E. R. M. Archer, D. Cáceres, T. E. Downing, T. Elmqvist, T., S. H. Eriksen, C. Folke, G. Han, K. Iyengar, C. Vogel, K. A. Wilson, and G. Ziervogel (2005) Vulnerable peoples and places. In: R. M. Hassan et al. (eds.) *Ecosystems and Human Well-being: Current State and Trends, Volume 1: Findings of the Condition and Trends Working Group of the Millennium Ecosystem Assessment*, 143–164. Island Press, Washington, DC.

Kelly, P. M., and W. N. Adger (2000) Theory and practice in assessing vulnerability to climate change and facilitating adaptation. *Climatic Change*, **47**, 325–352.

Lyall, S. (2007) Climate change greens up Greenland; farmers experiment with vegetable crops. [Newspaper] *Edmonton Journal*, October 28, A9.

Lykke Thomsen, M. (1993) *Local Knowledge of the Distribution, Biology, and Hunting of Beluga and Narwhal: A Survey among Inuit Hunters in West and North Greenland*. Greenland Hunters' and Fishermen's Association, Greenland Home Rule Government, and Inuit Circumpolar Conference, Nuuk, Greenland.

McCarthy, J. J., O. F. Canziani, N. A. Leary, D. J. Dokken, and K. S. White (eds.) (2001) *Climate Change 2001: Impacts, Adaptation, and Vulnerability: Contribution of Working Group II to the Third Assessment Report of the Intergovernmental Panel on Climate Change*. Cambridge University Press, Cambridge, UK.

McCarthy, J. J., M. L. Martello, R. W. Corell, N. E. Selin, S. Fox, G. Hovelsrud-Broda, S. D. Mathiesen, C. Polsky, H. Selin, and N. J. C. Tyler (2005) Climate change in the context of multiple stressors and resilience. In: C. Symon et al. (eds.) *Arctic Climate Impact Assessment (ACIA)*, 945–988. Cambridge University Press, Cambridge, UK.

Mølgaard, A. (2007) Piniartoq ilinniartunngorniartoq: Piniartuuneq inuuniutigisinnaajunnaarpara. [Newspaper] *Atuagagdliutit/Grønlandsposten*, Sept. 6, P5.

Mølgaard, N. (2011) Kujataani jordbærit. *Kalaallit Nunaata Radioa (KNR)*, Nov. 25. http://knr.gl/kl/nutaarsiassat/kujataani-jordbærit, Retrieved on Dec. 31, 2016.

Nghiem, S. V., D. K. Hall, T. L. Mote, M. Tedesco, M. R. Albert, K. Keegan, C. A. Shuman, N. E. DiGirolamo, G. Neumann (2012) The extreme melt across the Greenland ice sheet in 2012. *Geophys. Res. Lett.*, **39**, L20502.

Nuttall, M., F. Berkes, B. Forbes, G. Kofinas, T. Vlassova, and G. W. Wenzel (2005) Hunting, herding, fishing, and gathering: Indigenous peoples and renewable resource use in the arctic. In: C. Symon et al. (eds.) *Arctic Climate Impact Assessment*, 649–690. Cambridge University Press, Cambridge, UK.

Oreskes, N. (2004) The scientific consensus on climate change. *Science*, **306**, 1686–1686.

Ôshima, I. [大島育雄] (1989) *Esukimô ni natta nihonnjin [エスキモーになった日本人]*. Bungei Shunjû [文芸春秋], Tokyo.

Ødum, S. (1991 [1990]) *Choice of Species and Origins for Arboriculture in Greenland and the Faroe Islands*. Dansk Dendrologisk Forening, Copenhagen, Denmark.

Pearce, T. D., B. Smit, F. Duerden, J. D. Ford, A. Goose, and F. Kataoyak (2010) Inuit vulnerability and adaptive capacity to climate change in Ulukhaktok, Northwest Territories, Canada. *Polar Rec.*, **46**, 157–177.

Stevenson, M. G. (1996) Indigenous knowledge in environmental assessment. *Arctic*, **49**, 278–291.

Tallaksen, E. (2014) Greenland ups 2014 mackerel quota by 66% to 100,000t. *Undercurrent News*, February 24, Retrieved from https://www.undercurrentnews.com/2014/02/24/greenland-ups-2014-mackerel-quota-by-66-to-100000t/

Turner II, B. L., R. E. Kasperson, P. A. Matson, J. J. McCarthy, R. W. Corell, L. Christensen, N. Eckley, J. X. Kasperson, A. Luers, M. L. Martello, C. Polsky, A. Pulsipher, and A. Schiller (2003) A framework for vulnerability analysis in sustainability science. *P. Natl. Acad Sci. USA*, **100**, 8074–8079.

Usher, P. J. (2000) Traditional ecological knowledge in environmental assessment and management. *Arctic*, **53**, 183–193.

Walker, B., and D. Salt (2006) *Resilience Thinking: Sustaining Ecosystems and People in a Changing World*. Island Press, Washington, DC.

Walker, B., and D. Salt (2012) *Resilience Practice: Building*

Capacity to Absorb Disturbance and Maintain Function. Island Press, Washington, DC.

Wenzel, G. W. (1991) *Animal Rights, Human Rights: Ecology, Economy and Ideology in the Canadian Arctic*. University of Toronto Press, Toronto, ON, Canada.

Wenzel, G. W. (1999) Traditional ecological knowledge and Inuit: Reflections on TEK research and ethics. *Arctic*, **52**, 113–124.

Wisner, B., P. M. Blaikie, T. Cannon, and I. Davis (2004) *At Risk: Natural Hazards, People's Vulnerability, and Disasters* (2nd edition). Routledge, London, UK.